The excited state intramolecular hydrogen transfer mechanism of *ortho*-Nitrobenzaldehyde: A quantum chemical and molecular dynamics study

Dissertation

zur Erlangung des akademischen Grades doctor rerum naturalium

(Dr. rer. nat.)

vorgelegt dem Rat der Chemisch-Geowissenschaftlichen Fakultät der

Friedrich-Schiller-Universität Jena

von Verónica Leyva Novoa

geboren am 21.09.1980 in Ciudad de México, México

Gutachter:

1. . . . .

2. . . . .

3. . . . .

Tag der öffentlichen Verteidigung:

Abstract

This thesis is a theoretical analysis of the photorelaxation mechanism of *o*-NBA. O-NBA is a photolabile protecting group, used in chemical synthesis, in which an excited state intramolecular H-transfer takes place. Recent experiments suggest that this photoreaction might proceed *via* ketene intermediates. Yet, little is known about the mechanism of this photoreaction at molecular level. To shed some light into the relaxation mechanism of *o*-NBA, first highly accurate MS-CASPT2/CASSCF (multi-state complete active space second order perturbation over complete active space self-consistent field) calculations of *o*-NBA UV-spectrum in gas phase have been performed. The excited state S_5 has been assigned as the spectroscopic state from where the experimental wavelength at 260 nm initiates the H-transfer photoreaction. The effects of different positional isomers and of solute-solvent interactions are also addressed along this thesis. The transitions obtained are very similar to those obtained for *o*-NBA in gas phase, although solvation was found to induce a blue-shift. Once the UV-spectrum has been characterized, the deactivation mechanism of *o*-NBA has been deciphered by MS-CASPT2/CASSCF calculations. The location of different stationary points has suggested two deactivation pathways. The first path, non-Kasha, relaxes from the S_5 state to the ketene intermediate through a cascade of conical intersections along which a H-atom from the CHO is progressively transferred to the nitro group. The second path, Kasha, relaxes directly, by means of internal conversion, from the S_5 to the S_1 state, in which the hydrogen is transferred. In order to discern which of the two photoreaction mechanisms is preferred, mixed quantum-classical dynamics (MQCD) simulations have been performed. The MQCD simulations from the high-lying S_5 spectroscopic state are done with the time-dependent density functional theory method. None of the trajectories launched from the S_5 show a H-transfer along deactivation. Thus, it is assumed that the Kasha path is the operative one in the deactivation of *o*-NBA from the S_5. The last step of the Kasha path has been investigated with MQCD simulations starting from the S_1 state performed at the CASSCF level of theory. These simulations predict that the complete yield of the reaction is determined in its earliest step, with a conical intersection governing the competition between the creation of the ketene and the regeneration of the starting *o*-NBA material.

Resume

Molecular systems derived from 2-nitrobenzyl compounds, such as *ortho*-Nitrobenzaldehyde (*o*-NBA), are extensively used to protect the groups of a target molecule in chemical synthesis.[8] This is due to the fact that their inactive form can easily be transferred into an active form by irradiation of light.[3,9] The protecting properties of *o*-NBA are due to its ability, in the presence of light, of undergoing an intramolecular hydrogen transfer while shielding a functional group.[9] This photoreaction yields the formation of *ortho*-nitrosobenzoic acid and the release of the protected active moiety, see Figure 1. Recent experiments[33,35,36] suggest that this photoreaction might proceed *via* ketene intermediates. Many attempts have been made to explain the mechanism of this transformation, but up to date it is not understood at molecular level. For this reason, this PhD research is devoted to provide the theoretical foundations behind the excited state intramolecular H-transfer reaction of *o*-NBA that yields the main intermediate ketene. This work has been performed in collaboration with the experimental group of Peter Gilch, presently at the Heinrich Heine Universität Dusseldorf, and the theoretical group of Lluís Blancafort from Girona's University in Spain.
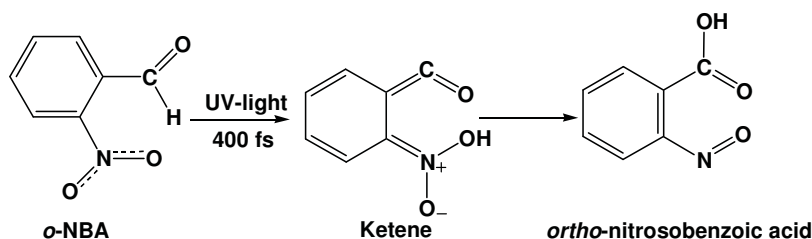

Figure 1. Photoredox reaction of *o*-NBA.

With the aim of understanding the photodeactivation mechanism of *o*-NBA, two types of studies have been performed: **a)** Quantum chemical (QC) calculations, which allow obtaining a global Potential Energy Surface of the photodeactivation of the *o*-NBA, and **b)** Reaction dynamical calculations which provide time-resolved mechanistic information. Prior to these calculations, we started by investigating the UV-absorption spectrum of *o*-NBA.[106] This has been done with the help of monoreferential (TD-DFT, RI-CC2) and multiconfigurational (MS-CASPT2/CASSCF) methods. The obtained results indicate that for wavelengths larger than 280 nm, the absorption spectrum of *o*-NBA is dominated by a series of weak $n\pi^*$ absorptions from the NO_2 and CHO groups. These weak transitions are followed in energy by a more intense band, peaking at 250 nm with charge transfer (CT) $\pi\pi^*$ character, involving mainly the benzene and the nitro group. In this band one might expect to find the reactive state, since the photoreaction is initiated experimentally upon excitation at 260 nm. Therefore, at MS-CASPT2 level of theory, the spectroscopic state is assigned to the S_5. Finally, the most intense band centred at 220 nm has its origin in the overlap of two

different absorptions: the first one localized in the NO_2 substituent and the second one arising from a CT excitation involving the NO_2 and the CHO fragments, respectively. The effect of one molecule of water on the vertical excitation energies of o-NBA has also been analyzed. The UV-absorption spectrum of the 1:1 o-NBA-H_2O complex is characterized by three main bands, similar to the ones predicted by MS-CASPT2 in o-NBA in gas phase, but blue-shifted. The vertical spectra in gas phase of the non-reactive isomers, m-NBA and p-NBA, have also been examined and compared with the o-NBA spectrum in gas phase. Interestingly, the spectra of both isomers are found to be characterized by three bands with similar transitions as those observed in the o-NBA,[107] although an excited H-transfer is not possible in these cases.

Using QC calculations, two photodeactivation mechanisms connecting the spectroscopic state with the main intermediate ketene have been considered. Minimum energy path calculations at MS-CASPT2/CASSCF level of theory have allowed the location of stationary points involved in both pathways. One path, non-Kasha, relaxes from the S_5 state (with $\pi\pi^*$ character) through a cascade of conical intersections (CIs) along which a H-atom from the aldehyde is progressively transferred to the nitro group. This non-Kasha relaxation pathway involves three phases: planarization, H-transfer, and rotation of the newly formed enol. A second path, Kasha, relaxes directly by means of internal conversion from the S_5 to the S_1 state (with $n\pi^*$ character) in which the H-transfer occurs. In this thesis, it is concluded that the Kasha relaxation mechanism plays a prominent role in the photochemistry of the o-NBA. This is in agreement with the experimental fact that the same quantum yield of 50% is observed upon excitation wavelengths of 260 and 388 nm.[33,35,36,109]

The time-resolved information about the photoreaction mechanism has been obtained using mixed quantum-classical dynamic (MQCD) simulations. These calculations have pursued two aims: **a)** To model the 260 nm excitation by starting the simulation from the spectroscopic S_5 state. **b)** To model the 388 nm excitation by starting the simulation from the S_1 state. The MQCD simulations from the high-lying S_5 spectroscopic state are done at TD-DFT level of theory. None of the trajectories launched from the S_5 show transfer of the aldehyde hydrogen to the NO_2 group along deactivation, confirming that the Kasha path is operative in the deactivation of o-NBA from the S_5. Along the relaxation to the S_1 state negligible changes in the NO_2 dihedral angle relative to the arene plane or changes in bond lengths are observed. Due to the nature of the TD-DFT method, it is not possible to describe the $S_1 \rightarrow S_0$ deactivation. Therefore, from the S_1 state CASSCF MQCD simulations have been performed. These simulations have shown that the deactivation from the S_1 state is a very efficient channel for the H-transfer reaction in o-NBA.[110] The H-transfer leads to a biradical that is converted to the ketene. Moreover, once the H-transfer is initiated, the tautomerization is completed on the femtosecond time scale, in agreement with the experimental results.[33,35,36] The semiclassical propagations predict a quantum yield for the formation of the ketene of ca. 30%. The discrepancy with the 50% observed experimentally is attributed to the initial conditions considered in the MQCD simulations and the absence of solvent. Yet, the qualitative agreement confirms the assumption that the complete yield of the reaction is determined in its earliest step, with a CI governing the competition between the creation of the

ketene and the regeneration of the starting o-NBA material. The H-transfer is irreversible once the trajectories have reached the biradical transient.

In summary, the analysis of the obtained static and dynamical calculations suggests that, upon 260 nm excitation o-NBA is excited to the S_5 excited state (with $\pi\pi^*$ character). Deactivation from this state occurs *via* a Kasha path through different CIs until the S_1 excited state (with $n\pi^*$ character), in which the hydrogen is transferred, hence yielding the main intermediate ketene.

Zusammenfassung

Molekulare Systeme, die sich von 2-Nitrobenzylverbindungen, wie etwa *ortho*-Nitrobenzaldehyd (*o*-NBA), ableiten, werden umfangreich genutzt, um in der chemischen Synthese die funktionellen Gruppen eines Zielmoleküls zu schützen.[8] Dies beruht auf der Tatsache, dass die inaktive Form der Schutz-gruppe leicht durch Lichtanregung in eine aktive Form umgewandelt werden kann.[3,9] Die schützenden Eigenschaften von *o*-NBA gehen auf dessem Fähigkeit zurück, einen lichtinduzierten intramolekularen Wasserstofftransfer im angeregten Zustand durchzuführen, während eine funktionelle Gruppe geschützt wird.[9] Diese Photoreaktion ergibt die Bildung von ortho-Nitrobenzoesäure und die Abspaltung der geschützten aktiven Gruppe, siehe Bild 1. Neueste Experimente[33,35,36] zeigen, dass diese Photoreaktion über Keten-Intermediate abläuft. Viele Versuche wurden unternommen, um den Mechanismus dieser Umwandlung zu erklären, aber auf molekularer Ebene wurde er bis jetzt nicht verstanden. Aus diesem Grunde widmen sich die Untersuchungen dieser Doktorarbeit den theoretischen Grundlagen hinter der intramolekularen H-Transferreaktion von *o*-NBA, das als Hauptintermediat das Keten erhält. Diese Arbeit wurde in Zusammenarbeit mit der experimentellen Gruppe um Peter Gilch, zur Zeit an der Heinrich-Heine-Universität Düsseldorf, und der theoretischen Gruppe um Lluís Blancafort, an der Universität von Girona in Spanien, durchgeführt.
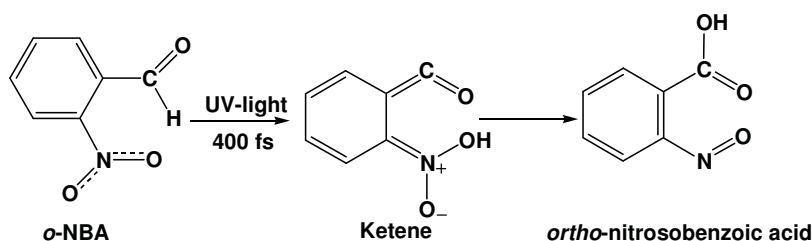

Bild 1: Photoredoxreaktion von *o*-NBA

Mit dem Ziel, den Photoaktivierungsmechanismus von *o*-NBA zu verstehen, wurden zwei Arten von Studien durchgeführt: **a)** Quantenchemische (QC) Rechnungen, die es ermöglichen, eine globale Potentialfläche der Photodeaktivierung von *o*-NBA zu erhalten, und **b)** reaktionsdynamische Rechnungen, die zeitaufgelöste mechanistische Informationen liefern. Vor diesen Rechnungen begannen wir, das UV-Absorptionsspektrum von *o*-NBA zu untersuchen.[106] Dies wurde mithilfe von Monoreferenz- (TD-DFT, RI-CC2) und Multikonfigurationsmethoden (MS-CASPT2/CASSCF) durchgeführt. Die erzielten Ergebnisse zeigen, dass das Absorptionsspektrum bei Wellenlängen, die größer als 280 nm sind, von einer Reihe von schwachen $n\pi^*$-Absorptionen von der NO_2- und der CHO-Gruppe dominiert wird. Diesen schwachen Übergängen folgt eine intensivere Bande mit ihrem Peak bei 250 nm mit Charge-Transfer (CT) $\pi\pi^*$-Charakter, der vor allem den Benzolring und die Nitrogruppe umfasst. In dieser Bande würde man erwarten, den reaktiven Zustand zu finden, denn die Photoreaktion wird experimentell durch die Anregung bei

260 nm initiiert. Auf dem MS-CASPT2-Theorieniveau wird dieser spektroskopische Zustand daher zum S_5 zugeordnet. Schließlich hat die intensivste Bande, deren Mitte bei 220 nm liegt, ihren Ursprung in der Überlappung von zwei verschiedenen Absorptionen: Die erste ist lokalisiert im NO_2-Substituenten und die zweite entsteht von einer CT-Anregung, die das NO_2- und das CHO-Fragment beinhaltet. Der Effekt eines Wassermoleküls auf die vertikalen Anregungsenergien von o-NBA wurde ebenso analysiert. Das UV-Absorptionsspektrum eines 1:1-o-NBA-H_2O-Komplexes ist durch 3 vorwiegende Banden gekennzeichnet, ähnlich denen, die im o-NBA durch MS-CASPT2 in Gasphase vorausgesagt wurden, aber blau-verschoben. Die vertikalen Spektra in Gasphase der nichtreaktiven Isomere, m-NBA und p-NBA, wurden außerdem untersucht und mit dem o-NBA-Spektrum in Gasphase verglichen. Interessanterweise sind die Spektren dieser beiden Isomere durch 3 Banden gekennzeichnet, ähnlich denen, die bei o-NBA beobachtet wurden, obwohl in diesen Fällen kein angeregter H-Transfer möglich ist.

Für die QC-Rechnungen wurden zwei Photodeaktivierungsmechanismen, die den spektroskopischen Zustand mit dem Keten-Intermediat verknüpft sind, berücksichtigt. "Minimum-Energy-Path"-Rechnungen auf dem MS-CASPT2/CASSCF-Niveau haben die Ortung stationärer Punkte ermöglicht, die in den beiden Pfaden enthalten sind. Ein Pfad, nicht-Kasha, relaxiert vom S_5-Zustand (mit $\pi\pi^*$-Charakter) über eine Reihe von konischen Durchschneidungen ("Conical Intersections", CIs), entlang derer ein H-Atom vom Aldehyd stufenweise zur Nitrogruppe wandert. Dieser nicht-Kasha-Relaxationspfad enthält drei Phasen: Planarisierung, H-Transfer und Rotation des neu entstandenen Enols. Ein zweiter Pfad, Kasha, relaxiert durch "Internal Conversion" direkt vom S_5- zum S_1-Zustand (mit $n\pi^*$-Charakter), in welchem der H-Transfer vorkommt. Diese Arbeit kommt zu dem Schluss, dass der Kasha-Relaxationsmechanismus eine bedeutende Rolle in der Photochemie von o-NBA spielt. Dies stimmt mit der experimentellen Erkenntnis, dass die selbe Quantenausbeute von 50% nach Anregung bei Wellenlängen von 260 und 388 nm erhalten wird, überein.[33,35,36,109]

Die zeitaufgelösten Informationen über den Photoreaktionsmechanismus wurden durch Ausführung von nichtadiabatischen "Mixed-Quantum-Classical-Dynamics"-(MQCD)-Simulationen erhalten. Diese Berechnungen verfolgten zwei Ziele: **a)** um die Anregung bei 260 nm zu modellieren, indem die Simulation vom spektroskopischen S_5-Zustand aus gestartet wurde, und **b)**, um die Anregung bei 388 nm zu modellieren, indem die Simulation vom S_1-Zustand aus gestartet wurde. Die MQCD-Simulationen vom hochliegenden spektroskopischen S_5-Zustand wurden auf dem TD-DFT-Niveau durchgeführt. Keine der Trajektorien, die vom S_5-Zustand starteten, zeigen während der Deaktivierung einen Transfer vom Aldehydwasserstoff zur NO_2-Gruppe und bestätigen, dass der Kasha-Pfad in der Deaktivierung des o-NBA vom S_5 wirksam ist. Entlang der Relaxation zum S_1-Zustand wurden vernachlässigbare Änderungen im NO_2-Diederwinkel bezüglich der Ebene des Arens oder in den Bindungslängen festgestellt. Aufgrund der Eigenschaft der TD-DFT-Methode ist es nicht möglich, die $S_1{\rightarrow}S_0$-Deaktivierung zu beschreiben. Daher wurden vom S_1-

Zustand aus CASSCF-MQCD-Simulationen durchgeführt. Diese Simulationen haben gezeigt, dass die Deaktivierung vom S_1-Zustand ein sehr effizienter Kanal für die H-Transferreaktion im *o*-NBA ist.[110] Die H-Wanderung führt zu einem Biradikal, das zum Keten umgewandelt wird. Außerdem wird, sobald der H-Transfer einmal initiiert wurde, die Tautomerisierung auf der Femtosekundenskala komplettiert, welches mit experimentellen Ergebnissen übereinstimmt. [33,35,36] Die semiklassischen Propagationen sagen eine Quantenausbeute von der Bildung des Ketens von 30% voraus. Die Abweichung von den experimentell gefundenen 50% ist auf die Anfangsbedingungen in den MQCD-Simulationen und das Fehlen des Lösungsmittels zurückzuführen. Trotzdem bestätigt die qualitative Übereinstimmung, dass die komplette Reaktionsausbeute durch ihren allerersten Schritt bestimmt wird, wobei eine CI den die Konkurrenz zwischen der Bildung des Ketens und der Regeneration des Ausgangs-*o*-NBA-Materials lenkt. Die H-Wanderung ist irreversibel, wenn die Trajektorien einmal den biradikalischen Transienten erreicht haben.

Abschließend legt die Analyse der durchgeführten statischen und dynamischen Berechnungen nahe, dass nach Anregung bei 260 nm, *o*-NBA in den S_5-Zustand (mit ππ*-Charakter) angeregt wird. Deaktivierung von diesem Zustand erfolgt über einen Kasha-Pfad durch verschiedene Cis bis zum S_1-Zustand (mit nπ*-Charakter), zu welchem der Wasserstoff gewandert ist, und somit das Keten-Intermediat liefert.

Contents

Abbreviations used in the thesis

AIM = Atoms in Molecules
ANO = Atomic Natural Orbital
ANO-L = Atomic Natural Orbital Large
ANO-S = Atomic Natural Orbital Small
AS = Active Space
BIR = Biradical
BO = Born-Oppheiemer
CC = Coupled Cluster
CASSCF = Complete Active Space Self-consistent Field
CASPT2 = Complete Active Space second order Perturbation
CI = Conical Intersection
$\mathbb{CI}$ = Configuration Interaction
CIS, CID, … CI-*th* = Configuration Interaction Singlets, Doubles, … *th*
CSF = Configuration State Function
CT = Charge Transfer
DFT = Density Functional Theory
FC = Franck-Condon
FCI = Full Configuration Interaction
GGA = Generalized Gradient Approximation
GTO = Gaussian-type Orbital
HF = Hartree-Fock
HF-SCF = Hartree Fock Self-consistent Field
HK = Hohenberg Kohn
HOMO = Highest Occupied Molecular Orbital
IR = Infrared region
IRC = Intrinsic Reaction Coordinates
KS = Kohn-Sham
LCAO = Linear Combination of Atomic Orbitals
LDA = Local Density Approximation
LIC = Linear Interpolation Coordinates
LS-CASPT2 = Level-shift Complete Active Space second order Perturbation
LSDA = Local Spin Density Approximation
LUMO = Lowest Unoccupied Molecular Orbital
LYP = Lee-Yang-Parr
m-NBA = *meta*-nitrobenzaldehyde
MCSCF = Multiconfigurational Self-consistent Field
MEP = Minimum Energy Path
MO = Molecular Orbital
MPn = Møller-Plesset
MQCD = Mixed Quantum-classical Dynamics
MRCI = Multireference Configuration Interaction
MRCIS, MRCID, … MRCI-*th* = Multireference Configuration Interaction Singlets, Doubles, …*th*
MS-CASPT2 = Multi-State Complete Active Space second order Perturbation
NB = Nitrobenzene

o-NBA = *ortho*-nitrobenzaldehyde
o-nitrobenzoic = *ortho*-nitrobenzoic
o-nitrobenzyl = *ortho*-nitrobenzyl
o-nitroso = *ortho*-nitroso
p-NBA = *para*-nitrobenzaldehyde
PES = Potential Energy Surface
Post-HF = Post Hartree-Fock
QM = Quantum Mechanics
RASSCF = Restricted Active Space Self-consistent Field
RAS1, RAS2, RAS3 = Restricted Active Space1, 2, 3
RG = Runge Gross
RHF = Restricted Hartree-Fock
RI = Resolution of the Identity
SA-CASSCF = State-average Complete Active Space Self-consistent Field
SCF = Self-consistent Field
SS-CASPT2 = Single-State Complete Active Space second order Perturbation
STO = Slater-type Orbital
TDSE = Time-dependent Schrödinger Equation
TD-DFT = Time-dependent Density Functional
TISE = Time-independent Schrödinger Equation
TS = Transition State
UHF = Unrestricted Hartree-Fock
UV = Ultraviolet
VWN = Vosko Wilk Nusair

Nomenclature

Ψ = Total wave function from the Time-dependent Schrödinger Equation
$\hat{H}^{mol}$ = Total Hamiltonian operator
ϕ = Total wave function from the Time-independent Schrödinger Equation
$\vec{r}$ = x,y and z; Vector position that denotes the set of electrons coordinates
x,y and z = Cartesian Coordinates
$\vec{R}$ = Vector position that denotes the set of nuclear coordinates
t = Time
E = Total molecular energy
$\hat{T}$ = Kinetic energy operator
$\hat{V}$ = Potential energy operator
$\hbar$ = Planck's constant in reference to the shape of a wave
N^{el} = Number of electrons
M^{nu} = Number of nuclei
$\boldsymbol{m}$ = Mass of the electrons
$\boldsymbol{\mathcal{M}}$ = Mass of the nuclei
i,j = Counters for electrons
I,J = Counters for nuclei
Z = Atomic number
∇ = Laplacian operator
$\hat{H}^{el}$ = Electronic Hamiltonian operator
$\hat{T}^{el}$ = Electronic Kinetic energy operator
$\hat{T}^{nu}$ = Nuclear Kinetic energy operator
$\hat{V}^{el,el}$ = Potential electron-electron energy operator
$\hat{V}^{el,nu}$ = Potential electron-nuclear energy operator
$\hat{V}^{nu,nu}$ = Potential nuclear-nuclear energy operator
ϕ^{el} = Total electronic wave function
ε^{el} = Electronic eigenenergy
$\hat{H}^{nu}$ = Nuclear Hamiltonian operator
ϕ^{nu} = Total nuclear wave function
ε^{nu} = Nuclear eigenenergy
$\psi(\vec{r})$ = Spatial orbital
$\alpha(\omega)$ and $\beta(\omega)$ = alfa and beta spin functions
α and β = Alfa and Beta electrons
$\chi(x)$ = One-electron function; where: x is in function of $\vec{r}, \omega$
ω = Spin coordinate
$\varphi(\vec{r})$ = Spatial basis function
$\hat{V}^{HF}$ = Hartree-Fock potential
E^{HF} = Hartree-Fock energy
ε^{corr} = Correlation energy
$\hat{\mathcal{J}}$ = Coulomb operator
$\hat{\mathcal{K}}$ = Exchange operator
$\hat{h}$ = single electron Hamiltonian or core Hamiltonian
$\mathcal{N}$ = Number of coordinates
$\boldsymbol{F}$ = Fock matrix

S = Matrix that represents the overlap between k and i functions
C = Matrix that contains the coefficients for the molecular orbitals χ_i in columns
ϵ = Matrix
c =Coefficient of the one-electron basis function
C = Coefficient of the Linear expansion wave functions (from CI method)
a, b, c, r, s and t = Spatial orbitals (pueden ser denominados también como simplemente contadores)
k = Counter of basis functions
K = Counter for spatial orbitals
$|S\rangle$ = Determinant representing single excitations
$|D\rangle$ = Determinant representing double excitations
$|T\rangle$ = Determinant representing triple excitations
n = Counter for orbitals in CASSCF (N^{el},n)
m = Number of roots in the SAm-CASSCF approach
λ = Parameter that determines the strength of a perturbation
ℓ = counter of corrections of the perturbation
ψ_0^{el} = Ground state one-determinant HF
$\hat{H}_0^{el}$ =Reference Hamiltonian Operator
$\hat{H}'$ = Perturbed Hamiltonian Operator
$\hat{T}$ = exctitation operator
ρ = Denisty
ρ^{TR} = Trial Charge Denisty
v^{ext} = external potential
$v^{Hartree}$ = Classical part of the electron-electron interaction
v^{xc} = exchange correlation potential
A^{xc} = Action operator
∇E^{pot} = Gradient of the pontetial
v =velocity
f = oscillator strength

CHAPTER 1

Introduction

In this chapter, the concept of photolabile protecting molecules is presented. Among them, we focus on the photochemistry of photolabile protecting groups containing the nitrobenzyl group. Then, the antecedents of a nitrobenzyl derivative, which is at the core of this PhD thesis, *ortho*-nitrobenzaldehyde (*o*-NBA), are scrutinized.

1.1 Photolabile protecting groups

Photolabile protecting groups are light sensitive molecules which are able to control the biological/chemical activity of a certain molecule. Photolabile protecting groups, also called *caging compounds,*[1] are employed in multistep syntheses of biomolecules[2-5] where many functional groups of equivalent reactivity exist, see Figure 1.1. Other applications of the photolabile protecting groups are: the ability to investigate the kinetics of pH controlled processes such as protein folding,[6,7] or the obtention of the correct characterization of DNA chips.[8,9] For these reasons, caging compounds offer experimental advantages which are otherwise very difficult to achieve.

The idea behind the photolabile caging technique is that a target functional group is blocked, i.e. *caged*, by the covalent attachment of the caging compound, see Figure 1.1b. This strategy is often used with biological compounds, since the activity of a specific moiety is switched on, i.e. *uncaged*, see Figure 1.1.c, by photochemically removing the protecting group with light of the appropriate wavelength. Hence, the caging/uncaging procedure so far based on the formation/breaking of a simple covalent bond.[3]
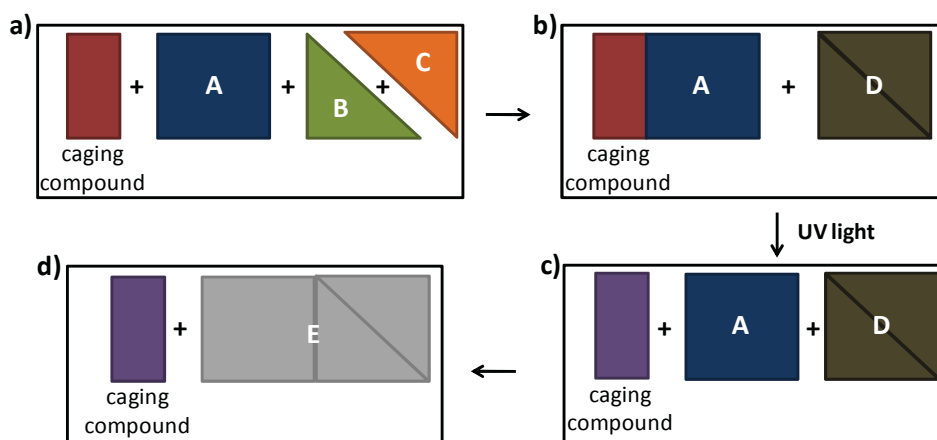
Figure 1.1. General description of a caging process in multistep syntheses. Usually, this kind of syntheses involves poly-functional molecules like peptides and saccharides.[10] A caging compound works in the following way: **a)** The caging compound and reactants, **A**, **B** and **C**, are present at the beginning of a multistep synthesis. **b)** The caging compound cages the target molecule, here **A**, meanwhile **B** and **C** react producing the **D** compound. **c)** Upon irradiation of light the caging compound is removed, allowing the compound **A** to be "switched on". **d)** At last, compound **A** is able to react with the **D** compound, forming **E**.

To be useful in biological experiments, caging compounds must satisfy, at least partially, the following criteria: They should be water soluble, hydrolytically stable, biologically inert,[11] and they must exhibit a bathochromic absorption when compared with amino acids and DNA bases.[12] Additionally, the photoreaction should proceed with a high quantum yield, so that any other released photoproducts different from the desired biomolecule do not interact or interfere with the biological system. Moreover, the release of the active compound should be faster than the process being studied.[13] Therefore, the rate of uncaging is an important issue for chemists to clarify through photochemistry.[4,5,10,12,14-16]

One of the most widely employed photolabile protecting group class is by far that of the *ortho*-nitrobenzyl (*o*-nitrobenzyl) derivatives.[4] This is due to their advantages,[14] which include the compatibility with a wide variety of functional groups, the easiness to synthesize, their reasonable light sensitivity[13] and the fact that the side products of the photo-cleavage, nitroso by-products, are generally biologically inert.[12] Nevertheless, the positive aspects of the nitrobenzyl caging compounds are shadowed by some adversities present in the photochemistry of mainly the nitroarenes derivatives, since these molecules can become potential pollutants.[17] Therefore, an insight into the rich photochemistry of the nitrobenzyl molecules is essential to understand their environmental impact[17,18] as well as their mechanism in the multistep synthesis.

1.2 Photochemistry of nitrobenzyl caging compounds

In the latest 1960's, Baltrop et al.[19,20] explored the photochemistry of 2-nitrobenzyl compounds, mainly the *o*-nitrobenzyl substituents.[21] The hydrogen in *ortho* position to the nitro group in the *o*-nitrobenzyl molecules allows to photochromism, a process that facilitates its use as caging compound in biochemical synthesis.[2] The photochemical reaction that confers the adequate photochromism to the *o*-nitrobenzyl compound is an internal redox reaction that gives an *ortho*-nitroso (*o*-nitroso) by-product.[10]

Aiming at explaining the photochemistry of *o*-nitrobenzyl compounds, Schaper et al. have stated through experimental and theoretical studies,[22] that after the excitation of the *o*-nitrobenzyl derivative, the low-lying states from the singlet manifold, e.g. S_1 and S_2 states, have a large contribution of local $n \rightarrow \pi^*$ excitations within the nitro group. Higher excited states, e.g. S_3 and S_4 states, can be described as *charge transfer* (CT) transitions from the π-orbitals of the aromatic ring to the π^*-orbitals of the nitro group. As well, it has been found that some contribution of a local excitation in the aromatic ring is associated with the S_3.

Another important characteristic traced in the *o*-nitrobenzyl derivatives was that the first excited state, either in the singlet or triplet manifold, might be photoreactive, where the relaxation from the S_1 or T_1 will depend on the functional groups located on the benzene ring.[22] In order to explain this, Schaper et al. have suggested to consider Kasha´s rule.[23,24] Kasha's rule states that vibrational relaxation takes place between excited levels towards the lowest-lying excited level, from where emission of a photon takes place, allowing the system to go back to its fundamental state.

The photochemistry of the nitrobenzene (NB) compounds, derivatives from the nitrobenzyl group, has already been experimentally analyzed[25] and theoretically studied[26] by Takezaki et al. They found similar transitions to those ones found in the *o*-nitrobenzyl compounds. Namely, in the low-energy states, local $n \rightarrow \pi^*$ excitations within the NO_2 group are present. Moreover, CT $\pi \rightarrow \pi^*$ excitations from the benzene moiety to the nitro group are located at higher energy. As well, internal conversion is observed until the first excited state. Therefore, the NBA deactivation mechanism proceeds according to Kasha's rule.

In the next section the molecule studied in this thesis, *o*-NBA, a NBA derivative which possesses a CHO in *ortho*- position to the nitro group NO_2, is presented. The characteristics that the arrangement of the two functional groups entails will be explained in detail.

1.3 *ortho*-Nitrobenzaldehyde

In the present section, the background known until now in the photoreaction of *o*-NBA is given.

The photoreaction of *o*-NBA, which gives the *ortho*-nitrosobenzoic (*o*-nitrosobenzoic) acid and the corresponding nitroso ester[27] in the presence of light, see Figure 1.2, has been investigated since the very beginning of modern organic photochemistry. In 1901, Ciamician and Silber[27] tried to describe this photochemical reaction. However, they did not have the adequate technology and the details of the reaction had to wait for the upcoming of time resolved spectroscopy.
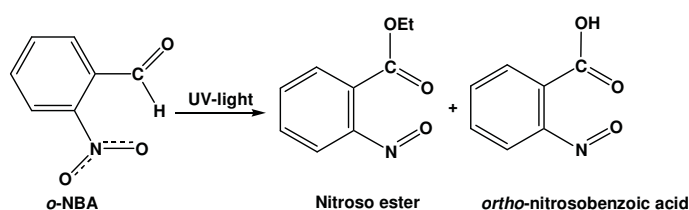

Figure 1.2. Photoreaction of *o*-NBA leads to the formation of *o*-nitrosobenzoic acid and the corresponding nitroso ester.[27]

In 1980, George and Scaiano used laser flash photolysis with a time resolution of some nanoseconds and found transients with solvent-dependent lifetimes around 0.6 ns. They reported that these transients come from triplet state transitions.[28] George and Scaiano rationalized the presence of a triplet state from the De Mayo and Reid studies.[29] The latter studies stated that after the transfer of an *ortho* H-atom to the nitro-group, which is the primary step in the photoinduced deprotection process in *o*-nitrobenzyl molecules,[3,18] a ketene intermediate is produced. Moreover, George and Scaiano found that the photo-rearrangement of *o*-NBA gives the *o*-nitrosobenzoic acid with quantum yields around 0.5, nearly irrespective of the solvent properties.[28]

In 1989, a pump-probe experiment for *o*-NBA, in aqueous acetonitrile and in THF solution, with a time resolution of 35 ps was reported by Yip and Sharma.[30] This experiment, with better time resolution in comparison with the one of George and Scaiano, revealed a transient with an absorption spectrum at ca. 440 nm for both solvents. Besides the similar absorption, a difference in the decay time was observed, i.e. *o*-NBA in THF solution was 2.4 ns shorter than *o*-NBA in acetonitrile. Furthermore, Yip and Sharma did not locate the characteristic triplet absorption band at 625-650 nm, observed for *o*-nitrobenzylic compounds under the same experimental conditions.[18,31] For this reason, Yip and Sharma attributed the observed transient to a ketene intermediate formed from the singlet rather than the triplet excited state for the photo-rearrangement of *o*-NBA. Nevertheless, Yip and Sharma still considered the possibility of the

existence of a triplet excited state absorption, which is formed either in low yield, or the triplet excited state is very short-lived. Therefore, a main ketene or a negligible biradical will lead to the nitrosobenzoic acid, see Figure 1.3.
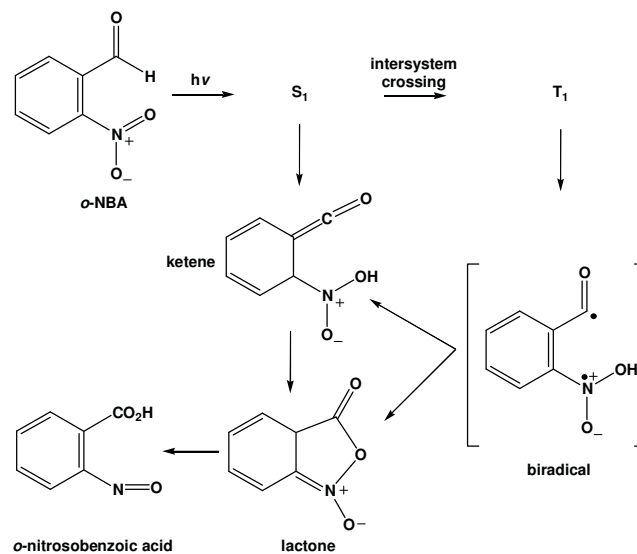

Figure 1.3. Photoreaction mechanism of the *o*-NBA proposed by Yip and Sharma.[30] The ketene intermediate is mostly formed by the first state of the singlet manifold, S_1, than the first state of the triplet manifold, T_1.

Yip and Sharma's consideration of the weak presence of a triplet excited state was based on precedent investigations on different *o*-NBA molecules[32] whose "ketene" intermediate is postulated to be formed from both the singlet as well as the triplet excited state. Consequently, dual singlet and triplet excited-state pathways are supposed to be operative.[18,32] The condition that will give preference for either of the pathways is the presence of the functional groups added on the benzene ring,[32] as already seen before by Barltrop et al.[20]

Summarizing, Yip and Sharma reported that the photorearrangement reaction of *o*-NBA, either in THF or acetonitrile solution, proceeds from the short-lived excited singlet state S_1 (t < 10 ps), or from negligible triplet excited state T_1, which undergoes through a biradical. A ketene intermediate is then formed by a H-abstraction of the aldehydic hydrogen, which mainly occurs within the excited singlet manifold of the nitro group.

Until 2005, all the experiments on the *o*-NBA photoreaction were limited by the time resolution of the used spectroscopic techniques. On 2005, the group of Gilch,[33] using femtosecond vibrational spectroscopy, was able to identify for the first time the presence of the ketene intermediate which until then had only been assumed. Along the photorearrangement of *o*-NBA, the ketene was

identified within the first 400 fs, after excitation with 260 nm. The ketene intermediate was identified by characteristic absorptions at 450 nm (UV/Vis) and a band appearing at 2100 cm^{-1}(IR), which is a characteristic band of ketenes.[34] Immediately after its formation, the ketene, which has a high degree of vibrational excitation, is relaxed through a cooling process in times > 10 ns. In this time, the ketene intermediate is completely formed and the ground state is partially recovered. In order to monitor the ketene formation, low excitations with 388 nm[35] were performed and then compared with high energy excitations,[33] and it has been observed that at both excitations, the same quantum yield is observed, i.e. 50% of ketene is formed.
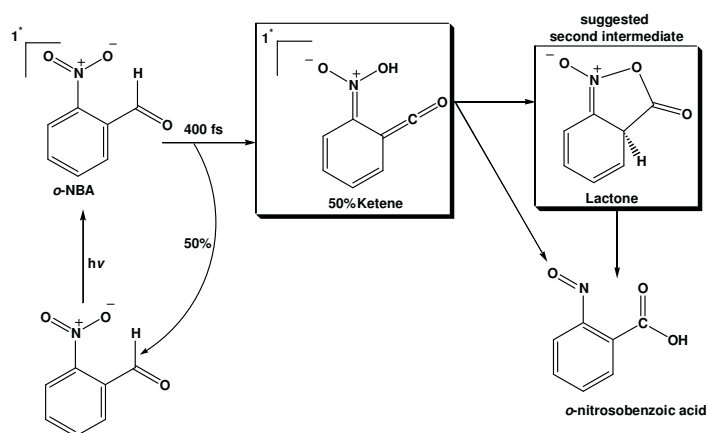

Figure 1.4. Intermediates of the photoredox reaction of *o*-NBA proposed by Laimgruber et al.[33].

In the experiments performed by Gilch et al. in organic and mixed solvents, a second intermediate has been reported,[36] as it has been stated by Yip et al.[30] and George et al.[28] The proposed arrangements of this intermediate differ in some details, but all structures in water feature a lactone, as sketched in Figure 1.4. Taking into account the solvent dependence effects with the observed transients Gilch et al. have postulated the following facts:

a) The quantum yield for the formation of the nitroso product is close to 50% irrespective of the solvent, as reported in Ref. 28.

b) The lifetime of the ketene intermediate strongly depends on the solvent[30,33] and can be interpreted as a signature of the reaction. The lifetimes of the ketene intermediate span a wide range of times according to the solvent used: in protic solvents, one that contains dissociable H^{+}, the existence of the ketene is of ~90 ps or less, whereas it is of 200 ps in aprotic solvent. For that reason, the experiments were mainly performed in aprotic solvents, such as acetonitrile, where the structural details of the vibrationally relaxed ketene can be examined.[37]

Gilch et al. tried to explain the photoreaction of the *o*-NBA suggesting two channels for the formation of the ketene.[35,36,38] For the predominating first channel, the formation of the ketene takes 0.4 ps. They assumed this would be the decay from the initially singlet CT $\pi \rightarrow \pi^*$ excited state with a concomitant twist of the nitro group. The second channel, a slower process with ~200 ps, is supposed to involve population of a negligible $n \rightarrow \pi^*$ triplet state. Due to the "long" time of the process and 0.5 of ketene quantum yield,[39] they assumed that the second channel decays to reform the *o*-NBA ground state or goes along with the formation of the ketene. The 50% of quantum yield in the can indicate that the formation of this intermediate is the key step of the photoreaction irreversibility.
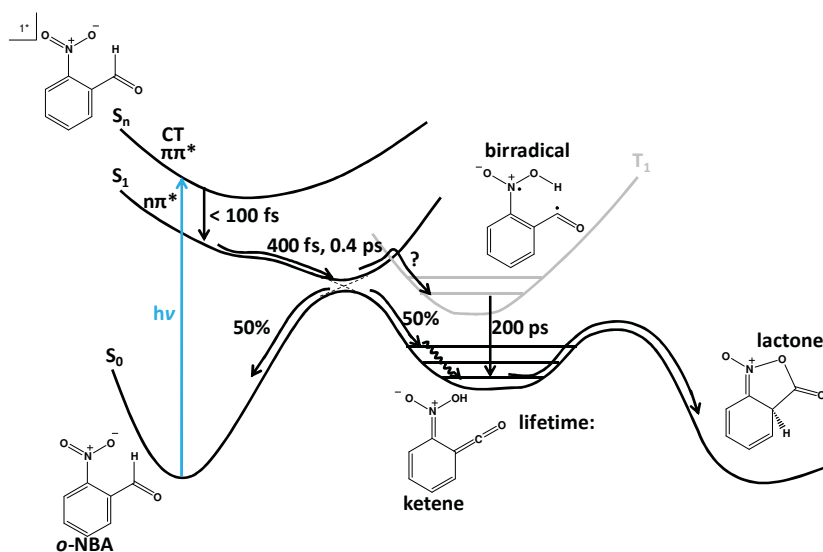

Figure 1.5. Kinetic scheme proposed by the group of Gilch of the photo-reaction of *o*-NBA in acetonitrile. The formation of the ketene intermediate in protic solvents is completed after less than 100 fs, on the contrary, in aprotic solvents, the time increases until $\leq$ 10ns.[33,35,36]

Summarizing the research done by the group of Gilch, upon irradiation of *o*-NBA at 260 nm, it is assumed that a bright CT $\pi \rightarrow \pi^*$ state is populated, and *o*-nitrosobenzoic acid is formed *via* a ketene intermediate. Moreover, internal conversion to the S_1 is expected to take place due to the detection of a weakly fluorescent signal after 100 fs of the excitation. Then, after 400 fs upon excitation, the ketene is formed through a H-transfer from the aldehyde group to the nitro group with a quantum yield of 50%, see Figure 1.5. In order to monitor the ketene formation at low-energy states, due the presence of internal conversion, a femtosecond UV/Vis transient absorption experiment at low energies, i.e. at 388 nm, has been performed. With this pump probe experiment it has been demonstrated that the ketene is formed with both wavelengths,[35] i.e. at high-energy 260 nm and at low-energy 388 nm. Furthermore, the likely participation of a "slow" pathway to the ketene formation due to the weak presence of a triplet biradical,[40] with $n \rightarrow \pi^*$ character, is considered.

Despite the many attempts that have been made to explain the photoreaction of *o*-NBA, very little is known about its molecular mechanism. For this reason, a theoretical analysis is mandatory and it constitutes the core of this thesis. This work has focused on *o*-NBA, where we have posed the following questions: Which excited states are experimentally populated? What is the character of the bright excited states? And how is the relaxation taking place from the populated state to the main ketene intermediate? i.e. is the hydrogen from the CHO group transferred to the nitro group in high-energy excited states (non-Kasha path) or is the hydrogen transferred in the lowest-energy excited state (Kasha path)?.

1.4 Objective and Outline of this thesis

As hinted above, this thesis is devoted to understand the mechanism of the phototransformation of *o*-NBA at molecular level, from the Franck-Condon (FC) point to the formation of the first intermediate ketene. To this aim we shall employ quantum mechanical methods and *ab initio* molecular dynamics. Since the production of the main ketene intermediate represents the key-step on the *o*-NBA photoreaction we assume that it will determine the quantum yield of the formation of the *o*-nitrobenzoic acid. It is foreseen that the insight into *o*-NBA photochemistry will give insights on the mechanisms of related molecules.

In order to elucidate the photodeactivation mechanism towards the *o*-nitrobenzoic acid, the following more specific tasks have been accomplished:

a) The study of the vertical spectrum of the *o*-NBA in order to discern the character of the corresponding excited states. This calculation has been done by means of quantum mechanical methods in gas phase and with solvation. The influence of solvation over the *o*-NBA is studied mainly with one molecule of water. The results will be shown in the chapter of Results, in the section #, and can be found in full detail in the article 3.4.1.

b) The calculation of the mechanistic path between the equilibrium FC *o*-NBA and the ketene. For the construction of the path, the most important stationary points, i.e. minima, transition states and conical intersections, have been located. This has been done through minimum energy path (MEP) calculations. These studies are summarized in the chapter of Results, in the section 3.3, and can be found in full detail in the article 3.4.4.

c) Guided by the quantum mechanical calculations of the *o*-NBA photodeactivation path, the natural dynamics of the system has been examined using high energy, i.e. 260 nm, and excitation at the low-energy, i.e. at 388 nm. This is done in order to have a time-dependent view of the photochemistry. Since the involved process is multi-dimensional, the dynamics have been studied using *ab initio* molecular dynamics calculations. The results are summarized in the section 3.4, and can be found in detail in the article 3.4.5.

Before the main results achieved in this thesis are presented, the next chapter, i.e. chapter 2, gives a brief explanation of the methods used in this thesis. Chapter 3 has a resume of the results obtained, including the articles published during the accomplishment of this thesis. This chapter is followed by the conclusions and outlook.

CHAPTER 2

Theoretical background

In an effort to depict nature, physicists through years had developed sophisticated equations in order to fit the phenomena in them, and yet, besides there is are a long path to achieve equations that can be accurate and suitable enough, several equations are used nowadays describe the behavior of atoms and molecules. The purpose of this chapter attempts to describe these latter equations that build the theoretical background of the methods used in this work.

2.1 The Schrödinger equation

In quantum mechanics, the *Time-dependent Schrödinger equation* (TDSE), formulated in 1926 by the Austrian physicist Erwin Schrödinger, describes how a *quantum state* (*wave function*) of a *physical system*, evolves in time:

$$i\hbar \frac{\partial}{\partial t} |\Psi(\vec{r}, \vec{R}, t)\rangle = \hat{H} |\Psi(\vec{r}, \vec{R}, t)\rangle,$$

... eq. 2.1

where $|\Psi\rangle$ is the total non-relativistic *wave function*, and $\hat{H}$ is the total non-relativistic Hamiltonian of the system. For a molecular system, those quantities depend on the electronic coordinates $\vec{r}$, nuclear coordinates $\vec{R}$, and time t.

Stationary properties of the TDSE can be obtained by solving the *Time-independent Schrödinger equation* (TISE):

$$\hat{H}^{mol} |\phi(\vec{r}, \vec{R})\rangle = E |\phi(\vec{r}, \vec{R})\rangle,$$

... eq. 2.2

which provides the eigenstates and eigenvalues of the system. In eq. 2.2 E is the total energy of the system, and $\hat{H}^{mol}$ is formed by the kinetic energy operator $\hat{T}$ and the potential energy operator $\hat{V}$:

$$\hat{H}^{mol} = \hat{T} + \hat{V}. \qquad\qquad \text{... eq. 2.3}$$

In a system with N-electrons (N^{el}) and M-nuclei (M^{nu}), $\hat{T}$ is defined as[i]:

$$\hat{T} = -\sum_{i=1}^{N^{el}} \frac{1}{2} \nabla_{\vec{r}i}^2 - \sum_{I=1}^{M^{nu}} \frac{1}{2\boldsymbol{\mathcal{M}}_I} \nabla_{\vec{R}I}^2. \qquad\qquad \text{... eq. 2.4}$$

The first sum in the eq. 2.4 runs over all electrons i, giving the electron kinetic energy: $\hat{T}^{el}$; the second sum runs over all nuclei I, giving the nuclear kinetic energy: $\hat{T}^{nu}$. $\boldsymbol{\mathcal{M}}_I$ is the mass of the I nuclei. ∇_i^2 and ∇_I^2 represent the Laplacian operators for the ith-electron and the Ith-nucleus, respectively.

Formally, $\hat{V}$ describes the Coulomb interactions between N-electrons and M-nuclei and takes the form:

$$\hat{V} = \sum_{i=1}^{N^{el}} \sum_{i<j}^{N^{el}} \frac{1}{|\vec{r}_i - \vec{r}_j|} - \sum_{i=1}^{N^{el}} \sum_{I=1}^{M^{nu}} \frac{Z_I}{|\vec{r}_i - \vec{R}_I|} + \sum_{I=1}^{M^{nu}} \sum_{I<J}^{M^{nu}} \frac{Z_I Z_J}{|\vec{R}_I - \vec{R}_J|}, \qquad \text{... eq. 2.5}$$

where the double sum runs over distinct pairs of particles: The first term concerns the interaction between electrons (repulsion): $\hat{V}^{el,el}$, the second term belongs to nuclear-electron interaction (attraction): $\hat{V}^{el,nu}$ and the last term corresponds to nuclear interaction (repulsion): $\hat{V}^{nu,nu}$. Z_I and Z_J represents the atomic number of the nuclei I and J. Relativistic effects, such as spin-orbit coupling, are neglected in this approximation. Then, the total molecular $\hat{H}^{mol}$ can be written as:

$$\hat{H}^{mol} = \hat{T}^{el} + \hat{T}^{nu} + \hat{V}^{el,el} + \hat{V}^{el,nu} + \hat{V}^{nu,nu} \qquad\qquad \text{... eq. 2.6}$$

Since we are interested in finding solutions of the stationary properties of a system, for example: the geometry in different stationary states, it is necessary to solve the TISE (or *stationary equation*) eq. 2.2. In order to do so, it is necessary to consider all the coordinates of all N-electrons and M-nuclei in the system with the total $\hat{H}^{mol}$ eq. 2.6. This leads to a ($3M^{nu} + 3N^{el}$)-degrees of freedom problem, for which, in practice, it is almost impossible to obtain analytical solutions.[41] Therefore, approximations, such as the *Born-Oppenheimer* (BO), have been developed in order to

---

[i] The following terms are expressed in atomic units, that is $e = \boldsymbol{m}_e = \hbar = 1$, where $\boldsymbol{m}_e$ is the mass of the electron.

11

simplify the mentioned *many-body* problem. A short description of the BO approximation will be provided in the following section.

The Born-Oppenheimer approximation

The BO (or "*adiabatic*" since it completely neglects the influence of nuclear motion on the electronic properties) approximation[42] was introduced by M. Born and R. Oppenheimer in 1927. It is based upon the fact that the timescale associated with the motion of nuclei is usually much slower than that associated with electrons, what allows separating the motion of the nuclei from the motion of the electrons. This is possible since nuclei are much heavier than electrons ($M \approx 10^{-27}$kg >> $m \approx 10^{-31}$kg). For this reason, one can consider the electrons in a molecule to be moving in the field of fixed nuclei where $\hat{V}^{nu,nu}$ is a constant and the $\hat{T}^{nu}$ can be neglected (since $\hat{T}^{nu} \ll \hat{T}^{el}$ by a factor of M_I/m_i). Therefore, the total wave function $|\phi\rangle$ of equation 2.2, can be expressed as a product of the nuclear function $|\phi^{nu}(\vec{R})\rangle$ and the electronic function $|\phi^{el}(\vec{r};\bar{R})\rangle$:

$$|\phi\rangle \approx |\phi^{nu}(\vec{R})\rangle|\phi^{el}(\vec{r};\bar{R})\rangle, \qquad \text{... eq. 2.7}$$

where for the $|\phi^{el}(\vec{r};\bar{R})\rangle$ eigenvalue, the electron cloud $\vec{r}$ adjusts instantly to a fixed nuclear configuration $\bar{R}$ (denoted by the semicolon in the 2.7 equation). The $\hat{H}^{mol}$ can be also separated into the nuclear $\hat{H}^{nu}$ and electronic $\hat{H}^{el}$ Hamiltonian operators:

$$\hat{H}^{mol} = \hat{H}^{el} + \hat{H}^{nu}. \qquad \text{... eq. 2.8}$$

The separation of eq. 2.8 leads to two eigenvalue equations for each stationary state: the electronic and the nuclear Schrödinger equations, which are explained below.

Time-independent Electronic Schrödinger Equation

As a consequence of the BO approximation, the *electronic Schrödinger equation* can be written as:

$$\hat{H}^{el}|\phi^{el}(\vec{r};\bar{R})\rangle = \varepsilon^{el}(\bar{R})|\phi^{el}(\vec{r};\bar{R})\rangle, \qquad \text{... eq. 2.9}$$

where the total electronic wave function $|\phi^{el}(\vec{r};\bar{R})\rangle$, depends directly on $\vec{r}$ and parametrically on $\bar{R}$. The $\hat{H}^{el}$ is defined as:

$$\hat{H}^{el} = \hat{T}^{el} + \hat{V}^{el,el} + \hat{V}^{el,nu}. \qquad \text{... eq. 2.10}$$

The solutions of eq. 2.9 give the electronic wave functions $|\phi^{el}\rangle$ with its associated electronic eigenenergies ε^{el} for a particular nuclear configuration $\bar{R}$.

Time-independent Nuclear Schrödinger equation

For the nuclear part of a system, the BO approximation results in the approximate nuclear Schrödinger equation, see Ref. 43:

$$\hat{H}^{nu}|\phi^{nu}(\vec{R})\rangle = \varepsilon^{nu}|\phi^{nu}(\vec{R})\rangle, \qquad \text{... eq. 2.11}$$

$\hat{H}^{nu}$ is defined by the sum of the electronic terms: the effective electronic energy $\varepsilon^{el}(\vec{R})$ and the nuclear repulsion $\hat{V}^{nu,nu}$, i.e. the potential energy $E(\bar{R})$, along with the kinetic energy operator for the nuclei $\hat{T}^{nu}$:

$$\hat{H}^{nuc} = \hat{T}^{nu} + \varepsilon^{el}(\vec{R}) + \hat{V}^{nu,nu}. \qquad \text{... eq. 2.12}$$

The solutions of the equation 2.11 for a given electronic state are a set of nuclear wave functions $|\phi^{nu}\rangle$ that depend on the nuclear coordinates $\vec{R}$ and describe the vibrations, rotations and translations of a molecule. The nuclear energy ε^{nu} now represents the total energy, E (recall eq. 2.2), in the BO approximation.

Potential Energy Surface

The potential energy $E^{pot}(\bar{R})$ for a given electronic state is given by:

$$E^{pot}(\bar{R}) = \varepsilon^{el}(\bar{R}) + V^{nu,nu}(\bar{R}). \qquad \text{... eq. 2.13}$$

In equation 2.13, different molecular arrangements of atoms in a molecule will give different values of $E^{pot}(\bar{R})$, which together form the Potential Energy Surface (PES), that is used to model chemical reactions and interactions in simple systems. A nuclear configuration in a PES where the derivation of the energy with respect to all nuclear displacements is zero is called *stationary point*.

Some of the main stationary points that help to build the PES are: the equilibrium geometry or *global minimum* which corresponds to the most stable nuclear configuration, the *saddle points* or *local maxima* (which correspond to *transition states* -TS-), and *local minima* (which correspond to *reactive intermediates*). All of which serve to follow a *reaction coordinate*, i.e. the path in the PES where the atoms "*travel*" along during a chemical reaction, as an example see Figure 2.1.
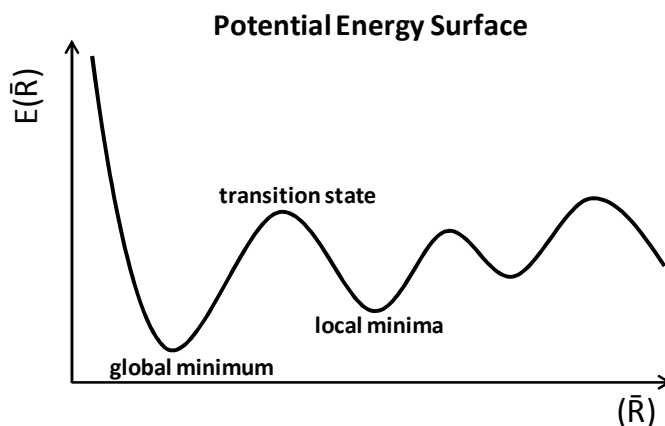

Figure 2.1. Different stationary points that are localized along the reaction coordinate of a PES.

Since the energy obtained by solving the electronic Schrödinger equation, eq. 2.9, provides the framework to solve the nuclear Schrödinger equation, eq. 2.11, it is therefore essential to represent adequate electronic wave functions $|\phi^{el}\rangle$ for the electronic part. Hence, in order to do so, a summary of some methods used to solve for the $|\phi^{el}\rangle$, with emphasis in those employed in this thesis, will be presented in the next section.

2.2 Solution to the Time-independent Electronic Schrödinger Equation

In this section we will focus on the electronic problem, i.e. the solution of the electronic Schrödinger equation 2.9 with quantum mechanical methods that are used in this thesis.

This section will be divided in two parts. First *ab initio* quantum mechanical approaches will be discussed. Then, as an alternative to the wave function method, an approach based on the *electronic density* will be presented.

2.2.1 *Ab initio* methods

The energy evaluation of a molecule, either in their electronic ground state or in a higher excited state, can be achieved through the use of approximations, e.g. within the frame of *ab initio* molecular orbital theory.

The *ab initio* term in its modern meaning ("from first principles of quantum mechanics") was used by Chen[44] (when quoting an unpublished MIT report from Allen and Nesbet), by Roothaan[45] and, in the title of an article, by Allen and Karo,[46] who also clearly define it.

The simplest type of *ab initio* electronic structure calculation for a molecule in the ground state is the Hartree–Fock self-consistent field (HF-SCF) scheme[ii]. HF does not specifically take into account the instantaneous Coulombic electron-electron repulsion, instead, uses the average of non-interaction electron-electron potential.

In order to recover electron-electron interaction, many types of methods begin with a HF calculation which is subsequently improved. Hence, in this section, the HF method will shortly be introduced as a start, then, some approaches that consider electronic interaction, the so-called *post-Hartree-Fock methodS* [47,48] (post-HF), will briefly be described.

A. Variational Principle in the ground state

A system that is localized in the lowest-energy state along its PES, it is said to be in the electronic *ground state*, i.e. we consider $\widehat{H}_0^{el}$.

As a first step in solving the electronic Schrödinger equation, eq. 2.9, in the *ab initio* methods, it is important to consider the *variational principle*:[41]

$$\varepsilon_0^{el} \leq \frac{\langle \phi_0^{el} | \widehat{H}_0^{el} | \phi_0^{el} \rangle}{\langle \phi_0^{el} | \phi_0^{el} \rangle}, \qquad \dots 2.14$$

which states that the energy (here of the ground state) ε_0^{el} of an electronic trial wave function $|\phi_0^{el}\rangle$ calculated as the expectation value of the $\widehat{H}_0^{el}$ divided by the norm of the $|\phi_0^{el}\rangle$ is always

---

[ii] Here, just the abbreviation Hartree-Fock (HF) will be used in order to simplify the nomenclature.

greater than or equal to the exact electronic energy ε^{el}. This gives the best trial wave function, since it is the one with the lowest energy possible.

The goal of the quantum chemical approximations described in the further sections is to solve the TISE by finding the most appropriate parameters for the trial wave function $|\phi^{el}\rangle$, thus obtaining the ε^{el}.

Slater determinant for N-electrons in a molecule on the ground state (Description of a wave function)

In order to solve the electronic TISE, eq. 2.9, the $|\phi^{el}\rangle$ must be antisymmetric with respect to the interchange of any two electron coordinates, following the Pauli principle. An expression representing the simplest antisymmetrized wave function, of an N-electron system is a *Slater determinant*:

$$|\phi^{el}\rangle = \frac{1}{\sqrt{N^{el}!}}\begin{vmatrix} \chi_1(x_1) & \chi_2(x_1) \cdots & \chi_N(x_1) \\ \chi_1(x_2) & \chi_2(x_2) \cdots & \chi_N(x_2) \\ \vdots & \ddots & \vdots \\ \chi_1(x_N) & \chi_2(x_N) \cdots & \chi_N(x_N) \end{vmatrix}, \qquad \text{… eq. 2.15}$$

which comprises N ortho-normalized *one-electron-functions* (or *spin orbitals*) $|\chi_i(x_i)\rangle$. The lower energy spin orbitals are occupied and the higher energized, $2k - N^{el}$ virtual orbitals, are not, following the basic Aufbau principle. The spin orbitals $|\chi_i(x_i)\rangle$ can be defined as the product of the spatial orbitals $|\psi_i(\vec{r}_i)\rangle$ with the so called *spin functions*, $|\alpha(\omega_i)\rangle$ and $|\beta(\omega_i)\rangle$:

$$|\chi_i(x_i)\rangle = |\chi_i(\vec{r}_i, \omega_i)\rangle = |\psi_i(\vec{r}_i)\rangle \cdot \begin{cases} |\alpha(\omega_i)\rangle \\ |\beta(\omega_i)\rangle \end{cases}, \qquad \text{… eq. 2.16}$$

in which, the $|\psi_i(\vec{r}_i)\rangle$ depends on the position of the electrons, and the spin functions: $|\alpha(\omega_i)\rangle$ and $|\beta(\omega_i)\rangle$ depend on the *spin coordinate ω*. It is assumed that the spin eigenfunctions are orthonormal, i.e. $\langle\alpha|\alpha\rangle = \langle\beta|\beta\rangle = 1$ and $\delta_{\alpha\beta} = \langle\alpha|\beta\rangle = \langle\beta|\alpha\rangle = 0$.

Hartree-Fock theory

The easiest solution of the electronic TISE, eq. 2.9, is achieved when the variational principle, eq. 2.14, is applied on the wave function, eq. 2.15, for the ground state where different sets of

$|\chi_i(x_i)\rangle$ will provide different eigenvalues until the minimal energy for the ground state, ε_0^{el}, is achieved. This latter procedure is the basis of the HF method.[49,50] The HF equations are:

$$\hat{f}(x_i)|\chi_i(x_i)\rangle = \varepsilon_i|\chi_i(x_i)\rangle, \qquad \text{... eq. 2.17}$$

where $\hat{f}$ is the Fock operator and will give as solutions of the one-electron eigenenergies ε_i and the optimal spin orbitals $|\chi_i(x_i)\rangle$. The $\hat{f}$ consists of two terms:

$$\hat{f}(x_i) = \hat{h}(x_i) + \hat{V}^{HF}(x_i). \qquad \text{... eq. 2.18}$$

The first term, $\hat{h}(x_i)$, in the eq. 2.18 is the *single-* or *one-electron operator*, and represents the Coulomb interaction of one electron in the fixed-field of M-nuclei:

$$\hat{h}(x_i) = \hat{T}_i^{el}(x_i) - \sum_{I=1}^{M^{nu}} \frac{Z_I}{|\vec{r_i} - \vec{R_I}|}. \qquad \text{... eq. 2.19}$$

The second term, $\hat{V}^{HF}(x_i)$, of the eq. 2.18 is the *Hartree-Fock potential* and describes the interaction of the ith-electron in the effective potential of all other electrons. $\hat{V}^{HF}(x_i)$ is composed of two terms: the *Coulomb operator* $\hat{J}_j(x_i)$, and the *Exchange operator* $\hat{K}_j(x_i)$,

$$\hat{V}^{HF}(x_i) = \sum_{j}^{N^{el}} [\hat{J}_j(x_i) - \hat{K}_j(x_i)]. \qquad \text{... eq. 2.20}$$

The first term, $\hat{J}_j(x_i)$, in equation 2.20 represents the classical interaction of one i^{th} electron with the remaining electron cloud, i.e. $N^{el} - 1$ electrons,

$$\hat{J}_j(x_i)|\chi_i(x_i)\rangle = \left[\int dx_j \chi_j^*(x_j) \frac{1}{|\vec{r_i} - \vec{r_j}|} \chi_j(x_j) \right] |\chi_i(x_i)\rangle. \qquad \text{... eq. 2.21}$$

The second term of the eq. 2.20 has no classical analogue. Unlike the Coulomb operator, the exchange operator is a non-local operator, since the energy contribution comes from a delocalized interaction between electron i and electron j, and it is defined as:

$$\hat{\mathcal{K}}_j(x_i)|\chi_i(x_i)\rangle = \left[\int dx_j \chi_j^*(x_j)\frac{1}{|\vec{r}_i - \vec{r}_j|}\chi_i(x_j)\right]|\chi_j(x_i)\rangle. \qquad \text{... eq. 2.22}$$

In general, the Coulomb operator represents Coulomb interactions between electrons that occupy orbitals χ_i and χ_j, whereas the Exchange operator deals with electrons with opposite spins.

The solution of the HF equations, eq. 2.17, will depend on the type of spin orbitals, $|\chi_i(x_i)\rangle$ used to describe an N^{el} system. Consecutively, if the spin orbitals are constrained to have the same spatial function for $|\alpha(\omega_i)\rangle$ and $|\beta(\omega_i)\rangle$ they lead to the: **a)** *Restricted Hartree-Fock* (RHF) equations; on the contrary, if the spin orbitals have different spatial functions for $|\alpha(\omega_i)\rangle$ and $|\beta(\omega_i)\rangle$ they lead to the: **b)** *Unrestricted Hartree-Fock* (UHF) equations, see Figure 2.2.

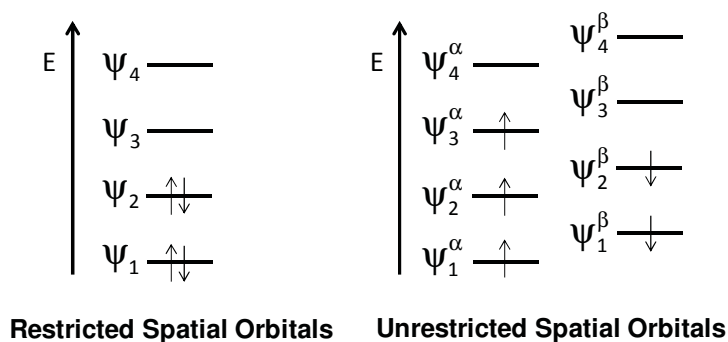**Restricted Spatial Orbitals   Unrestricted Spatial Orbitals**

Figure 2.2. Spin orbital representation of restricted (RHF) and unrestricted (UHF) spatial orbitals.

Since the solution of the HF equations, eq. 2.17, depends whether the orbitals of the system are *double* or *single* occupied, it is important to gain an expression given exclusively in terms of the spatial orbitals $|\psi_i(\vec{r}_i)\rangle$. Henceforth, the $\hat{f}$ operator is presented in the following sections in terms of spatial orbitals in the RHF and UHF procedures.

Restricted Hartree-Fock

In the case of an *even* number of N-electrons, i.e. RHF, all the spatial orbitals $|\psi_i(\vec{r}_i)\rangle$ are double occupied, and electrons having the same spatial orbital will differ only in their spin function $|\alpha(\omega_i)\rangle$ and $|\beta(\omega_i)\rangle$,

$$\hat{f}(x_i)|\psi_i(\vec{r}_i)\alpha(\omega_i)\rangle = \varepsilon_i|\psi_i(\vec{r}_i)\alpha(\omega_i)\rangle \qquad \text{... eq. 2.23}$$

and

$$\hat{f}(x_i)|\psi_i(\vec{r}_i)\beta(\omega_i)\rangle = \varepsilon_i|\psi_i(\vec{r}_i)\beta(\omega_i)\rangle. \qquad \text{... eq. 2.24}$$

This means that for a Slater-determinant with N^{el} spin functions, only $N^{el}/2$ spatial orbitals are needed, thus the results on eq. 2.23 are identical to those from eq. 2.24. Then, the *restricted* Fock operator has the then form of:

$$\hat{f}(r_i)|\psi_i(\vec{r}_i)\rangle = \varepsilon_i|\psi_i(\vec{r}_i)\rangle, \qquad \text{... eq. 2.25}$$

where $\hat{f}$ depends on the spatial orbitals $|\psi_i(\vec{r}_i)\rangle$. Consequently, the Coulomb $\hat{J}_j(x_i)$ and Exchange $\hat{K}_j(x_i)$ operators are now defined with respect to the spatial orbitals $|\psi_i(\vec{r}_i)\rangle$, and are analogous to equations 2.21 and 2.22.

The RHF equation, eq. 2.25, can be solved by introducing a set of known spatial *basis functions* $|\varphi_k(\vec{r}_i)\rangle$ instead of each *molecular orbital* (MO) $|\psi_i(\vec{r}_i)\rangle$. This method, devised in 1951 by Clemens C. J. Roothaan[51] and George G. Hall,[52] gives a set of algebraic equations that could be solved by standard matrix techniques. Therefore the MO can be expanded as a *linear combination* of k *basis functions* (*atomic orbitals*), giving the so-called *Linear Combination of Atomic Orbitals* (LCAO),

$$|\psi_i(\vec{r}_i)\rangle = \sum_{k=1}^{k} c_{ik}|\varphi_k(\vec{r}_i)\rangle, \qquad \text{... eq. 2.26}$$

where c_{ik} are the weights of the contributions of the k atomic orbitals $|\varphi_k\rangle$. In the praxis, the sum in equation 2.26 is truncated at a finite value k, for computational purposes.

Substituting the basis functions from equation 2.26 into the HF equations, eq. 2.17, will give:

$$\hat{f}(\vec{r}_i) \sum_{k=1}^{k} c_{ik}|\varphi_k(\vec{r}_i)\rangle = \varepsilon_i \sum_{k=1}^{k} c_{ik}|\varphi_k(\vec{r}_i)\rangle. \qquad \text{... eq. 2.27}$$

The coefficients c_{ik} in the equation 2.27 are derived variationally, therefore, the obtained ε_i energies, tend to a limiting value called the *HF limit*, i.e. the limit is reached when $k \rightarrow \infty$, according to the size of the basis functions used.

If the eq. 2.27 is multiplied from the left with φ_i^* and integrated with respect to $\vec{r}_i$, it gives the *Roothaan-Hall equations*:[51,52]

$$\sum_{k=1}^{k} c_{ik}\langle\varphi_i(\vec{r}_i)|\hat{f}_{ik}|\varphi_k(\vec{r}_i)\rangle = \varepsilon_i \sum_{k=1}^{k} c_{ik}\langle\varphi_i(\vec{r}_i)|\varphi_k(\vec{r}_i)\rangle. \qquad \text{… eq. 2.28}$$

The equation 2.28, can be then rewritten in a compact matricial way as:

$$\boldsymbol{FC} = \boldsymbol{SC}\boldsymbol{\epsilon}, \qquad \text{… eq. 2.29}$$

where the *Fock matrix* $\boldsymbol{F}$, with $k \, x \, k$ dimension, is formed from the matrix elements $\langle\varphi_i(\vec{r}_i)|\hat{f}_{ik}|\varphi_k(\vec{r}_i)\rangle$. The $\boldsymbol{S}$ matrix, also with $k \, x \, k$ elements, describes the overlap between two functions k and i. Both matrices are Hermitian, i.e. for real orbitals they are real and symmetric. The $\boldsymbol{C}$ matrix contains the coefficients for the molecular orbitals χ_i in columns, i.e. the first column gives the coefficients for χ_1, the second column those for χ_2 and k^{th} column those for χ_k. The energies of each $|\psi_i(\vec{r}_i)\rangle$ are found in the diagonalized matrix $\boldsymbol{\epsilon}$.

The solution of equation 2.28 is given by an initial guess of c_{ik} which defines the spatial orbitals $|\psi_i(\vec{r}_i)\rangle$ in equation 2.27 giving the matrix $\boldsymbol{C}^0$ in equation 2.29, thus, calculating the first Fock-matrix $\boldsymbol{F}^0$. Then, the eigenvalue problem is solved by diagonalization of $\boldsymbol{F}^0$. As a solution, a new coefficient matrix $\boldsymbol{C}^1$ is obtained which is again used to construct a new Fock matrix $\boldsymbol{F}^1$ which is diagonalized. The process of generating a new $\boldsymbol{C}$ with new c_{ik} values is called *iteration*. After each iteration, the c_{ik} are compared to the previous values obtained, and if they have not changed, i.e. the values are negligible; within a specified criterion (also known as *convergency parameter*) then the procedure has reached a *self-consistency*, making the iterative process to stop. Hence the name of the latter iterative procedure is *Self-Consistent Field* (SCF), and was introduced by Hartree in 1928.

Since the goal is to minimize the ε_i, eq. 2.27, an appropriate set of c_{ik} must be determined as an initial guess, i.e. the accuracy of the HF energy lies in the size and quality of the basis set expansion used in the equation 2.27.

Unrestricted Open-Shell Hartree-Fock

In order to obtain the UHF energies, John Pople and R. K. Nesbet[53] devised some suitable equations where the spatial orbitals $|\psi_i^\alpha(\vec{r}_i)\rangle$ and $|\psi_i^\beta(\vec{r}_i)\rangle$ are different for opposite spin functions $|\alpha(\omega_i)\rangle$ and $|\beta(\omega_i)\rangle$:

$$\hat{f}(x_i)|\psi_i^\alpha(\vec{r}_i)\alpha(\omega_i)\rangle = \varepsilon_i^\alpha|\psi_i^\alpha(\vec{r}_i)\alpha(\omega_i)\rangle \qquad \text{... eq. 2.30}$$

and

$$\hat{f}(x_i)\left|\psi_i^\beta(\vec{r}_i)\beta(\omega_i)\rangle = \varepsilon_i^\beta\right|\psi_i^\beta(\vec{r}_i)\beta(\omega_i)\rangle. \qquad \text{... eq. 2.31}$$

Therefore the obtained energy ε_i depends on their spin functions, $|\alpha(\omega_i)\rangle$ and $|\beta(\omega_i)\rangle$. Hence, equations 2.30 and 2.31 must be handled individually. The $\hat{f}$ operator is obtained by following the same steps that were used for the RHF; the only difference present is that the sum runs over an unequal number of α and β spins, where the Coulomb and Exchange operators maintain their form in equations 2.21 and 2.22, only now the spatial functions are differentiated according to the spin type. Thus, the Roothaan-Hall equations split into two sets of equations for α- and β-orbitals. These expressions are called *Pople-Nesbet* equations:[53]

$$\boldsymbol{F}^\alpha \boldsymbol{C}^\alpha = \boldsymbol{S}\boldsymbol{C}^\alpha \boldsymbol{\epsilon}^\alpha \qquad \text{... eq. 2.32}$$

$$\boldsymbol{F}^\beta \boldsymbol{C}^\beta = \boldsymbol{S}\boldsymbol{C}^\beta \boldsymbol{\epsilon}^\beta \qquad \text{... eq. 2.33}$$

where matrices $\boldsymbol{C}^\alpha$ and $\boldsymbol{C}^\beta$ contain the coefficients for the molecular orbitals $|\psi_i^\alpha(\vec{r}_i)\rangle$ and $|\psi_i^\beta(\vec{r}_i)\rangle$ respectively. The orbital energies are found along the diagonal of the matrices $\boldsymbol{\epsilon}^\alpha$ and $\boldsymbol{\epsilon}^\beta$. The two sets of equations 2.32 and 2.33 are coupled over the appropriate Coulomb and Exchange operators, eq. 2.21 and 2.22, hence giving the solution of the HF equation. The Pople-Nesbet equations 2.32 and 2.34, are also solved iteratively until the minimum total energy is reached.

B. Electronic States higher in energy than the ground state, i.e. Excited States

Through the framework of the HF approximation, where the basis functions aid to depict better the MOs, thus improving the portray of the wave-like behavior of the electrons in a molecule, a rather rigid physical picture is obtained because the one-to-one interaction between electrons is

not taken into account. This is especially important when molecules around their global minimum, i.e. in most stable electron configuration, lose their stability when an external energy is applied on them.

An example of external energy is electromagnetic radiation applied on a molecule, i.e. a molecule *absorbs* energy (*photon*) from electromagnetic radiation. The absorption of a photon can cause three types of *transitions* in a molecule accordingly to the type of energy, absorbed by the molecule. These transitions, which are studied by the Spectroscopy, are: *rotational*, *vibrational* and *electronic*.

An electromagnetic radiation that emits low energy, i.e. energy at short *wavelength*, is the *microwave* radiation. It cannot excite electrons in molecules nor can excite vibrations, therefore, it can only cause a *rotational transition* in molecules, i.e. an abrupt change in the angular momentum in the molecule. Thus, if a molecule gains angular momentum, a positive rotational transition is said to have occurred, on the contrary, if molecule loses angular momentum, it is said to have transitioned to a lower rotational energy state.

Photons more energetic than microwave radiation are those ones from the *infrared* (IR) region of the *electromagnetic spectrum*. Nevertheless, they have much less energy than photons in the *visible* or *Ultraviolet* (UV) regions of the electromagnetic spectrum. Photons from the IR region can excite vibrations in molecules. Therefore, when a particle gains vibrational energy, a positive vibrational transition is said to have occurred. On the contrary, when a particle loses a unit of vibrational energy, it is said to have transitioned to a lower *vibrational energy state*, see Figure 2.3 index b).

More energetic photons (such as UV-light) induce molecular electronic transitions, e.g. valence electrons in a molecule are excited from one energy level to a higher energy level (e*xcited state*). The change in energy associated with this transition provides information on the structure of a molecule and is associated with many molecular properties, such as valence energy levels and chemical bonding; especially the bonding character of molecular orbitals. After a molecule is excited, the lifetime of it in an excited state is usually short; consecutively, the system reverts either to the ground state or to a less excited state *emitting* photons. This giving of energy is often loosely described as *decay*.

The energies of the emitted photoelectrons are characteristic of their original electronic states, and depend also on vibrational state and rotational level. With the aim of describing the absorption and emission of light from a system, Alexander Jablonski proposed in 1935 a diagram which illustrates schematically the absorption/emission activity of a quantum system. This scheme

has been called the *Jablonski diagram* in honor to its developer. In Figure 2.3 the main quantum transitions, which are significant in this thesis are shown.
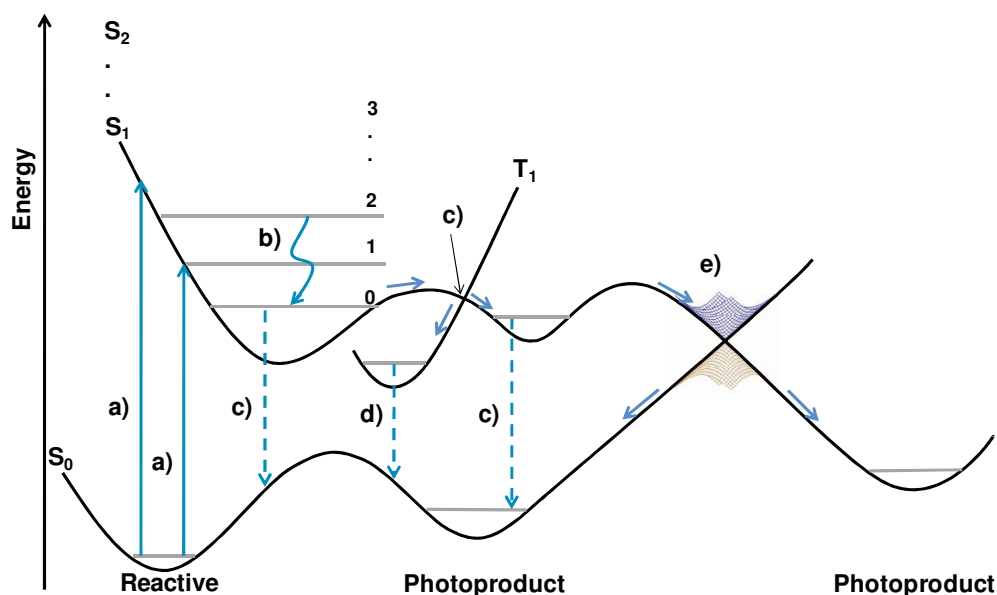

Figure 2.3. **a)** A chromophore absorbs light energy, and it is excited to a higher vibrational energy level, at a higher energy state: S_1. **b)** At each energy level, chromophores can exist in a number of vibrational energy levels (here represented by grey lines the relaxation along the vibrational energy levels is called *Vibrational Relaxation*. **c)** *Fluorescence*: occurs when a chromophore after being excited is rapidly relaxed to the lowest vibrational energy level. **d)** *Phosphorescence*: is similar to fluorescence, except the electron undergoes a spin conversion into a "forbidden" triplet state (here T_1) instead of the lowest singlet excited state, here S_1, and occurs with lower energy relative to fluorescence. **e)** *Intersystem crossing* is a radiationless process involving a transition between two electronic states with different spin multiplicity,[54] here from the S_1 to the T_1. **f)** *Conical Intersection* (CI), occurs when two adiabatic potential energy surfaces cross. The interstate coupling facilitates fast radiationless transitions between the crossing surfaces.

In order to obtain reliable physical information on excited state phenomena, i.e. suitable wave functions for excited states, electron-electron interaction (*electron correlation*) must be considered. Therefore, post-HF will be shortly introduced in the following sections.

Two types of electron correlation effects can be distinguished: (*dynamical* and *static*).[55] **(a)** The dynamical (*intra-orbital*) correlation describes the interaction between two electrons belonging to the same $|\psi_i(\vec{r}_i)\rangle$. **(b)** The static (*near-degeneracy*) correlation is caused by the inter-orbital correlation where two MOs are spatially close, i.e. having almost the same energy. The negligence of the static correlation can lead to a wrong ground state wave function, since it is associated with

electrons avoiding each other which occupy different spatial orbitals[48] $|\psi_i(\vec{r}_i)\rangle$. Statical effects, which are featured in chemical systems with excited states or in description of bond-dissociation, can be covered with the use of more than one Slater determinant to describe the wave function. In order to account for the absent electron correlation on HF method, post-HF will be discussed in the following sections.

The correlation energy, ε^{corr}, is defined as the difference between the HF energy E^{HF} and the lowest possible (exact) energy ε^{el} for a given basis set, and is given by,

$$\varepsilon^{corr} = \varepsilon^{el} - E^{HF}. \qquad \qquad \text{... eq. 2.34}$$

Post Hartree-Fock methods

In order to add the correlation energy in the solution of the electronic Schrödinger equation, eq. 2.9, different *ab initio* methods have been applied in this thesis: **(a)** Approaches which expand the *wave reference*, i.e. the one-determinant HF eq. 2.15, as *multi-electron* wave functions. This expansion can be solved variationally, eq. 2.14, like *Configuration Interaction* ($\mathbb{CI}$) or not variationally, like *Coupled Cluster* (CC). **(b)** Methods that add "*perturbations*", such as Møller-Plesset[56] (MPn) theory, start with a known wave reference and add a "perturbing" Hamiltonian which will represent a weak disturbance to the system. If the disturbance is not too large, the various physical quantities associated with the perturbed system (e.g. its energy levels and eigenstates) can be expressed as '*corrections*' to those of the simple system. Another type of electron correlation treatment which does not belong to *ab initio* calculations is the *Density Function Theory* (DFT) which will be treated in this thesis in the section 2.2.2.

A brief explanation of the post-HF methods used in this thesis will be done in the following sections.

Configuration Interaction

The $\mathbb{CI}$ method[57] is conceptually the simplest approach to include electron correlation energy in the HF method. In the $\mathbb{CI}$ approximation, a trial wave function $|\psi_0^{el}\rangle$ (from now on, the $|\phi^{el}\rangle$ from eq. 2.15 will be denoted as $|\psi_0^{el}\rangle$) is expanded as a linear combination of appropriate N^{el}-particle Slater determinants. Each linear combination of Slater determinants that represent an eigenstate will generate a *configuration state function* CSF. Therefore, the solution of the $\mathbb{CI}$ procedure accomplishes some eigenvalues, which are the energies of the ground and some electronically excited states, i.e. energies of the corresponding CSFs.

The determinants that build the CSFs are constructed by *exciting* an electron (or more) from occupied, $\frac{N^{el}}{2}$, MOs to unoccupied, $K - \frac{N^{el}}{2}$, virtual MOs in the $|\psi_0^{el}\rangle$; each of these substitutions gives a different *electronic configuration*. Electronic configurations representing single excitations consist of promoting one electron from the spatial orbital a to the spatial orbital r and is written as $|\psi_a^r\rangle$. Similarly, a double excitation involves exciting two electrons, one from a to r and another from b to s, $|\psi_{ab}^{rs}\rangle$. Applying the same notation for all other multiple excitations, then a trial wave function $|\phi^{el}\rangle$ can be written as a linear combination of all possible excited determinants, relative to the reference determinant $|\psi_0^{el}\rangle$:

$$|\phi^{el}\rangle = C_0|\psi_0^{el}\rangle + \sum_{\substack{a,r}} C_a^r |\psi_a^r\rangle + \sum_{\substack{a<b \\ r<s}} C_{ab}^{rs} |\psi_{ab}^{rs}\rangle + \sum_{\substack{a<b<c \\ r<s<t}} C_{abc}^{rst} |\psi_{abc}^{rst}\rangle + \cdots \qquad \text{... eq. 2.35}$$

The coefficients C in eq. 2.35 are determined by the variational principle, recall eq. 2.14. The restrictions such as: $...a < b < c$ and $r < s < t <...$ are present to avoid repetition, leading to a sum of the unique possible electronic configurations. These configurations are termed according to the number of promoted electrons: HF ground state: $|\psi_0^{el}\rangle$, singlet: $|\psi_a^r\rangle$, doublet: $|\psi_{ab}^{rs}\rangle$, triplet: $|\psi_{abc}^{rst}\rangle$, ..., N^{el}-tuple excitations.[41] A way of rewriting eq. 2.36 in a compressed way is:

$$|\phi^{el}\rangle = C_0|\psi_0^{el}\rangle + C_S|S\rangle + C_D|D\rangle + C_T T\rangle + \cdots \qquad \text{... eq. 2.36}$$

where $|S\rangle$ represents all the single excitations, $|D\rangle$ the doubles, $|T\rangle$ the triples and so on. Using the notation of the equation 2.36 the CI matrix can be expressed as a matrix representation:

$$\begin{array}{cccccc}
 & |\psi_0^{el}\rangle & |S\rangle & |D\rangle & |T\rangle & \cdots \\
|\psi_0^{el}\rangle & \langle\psi_0^{el}|\hat{H}^{el}|\psi_0^{el}\rangle & 0 & \langle\psi_0^{el}|\hat{H}^{el}|D\rangle & 0 & \cdots \\
|S\rangle & 0 & \langle S|\hat{H}^{el}|S\rangle & \langle S|\hat{H}^{el}|D\rangle & \langle S|\hat{H}^{el}|T\rangle & \cdots \\
|D\rangle & \langle D|\hat{H}^{el}|\psi_0^{el}\rangle & \langle D|\hat{H}^{el}|S\rangle & \langle T|\hat{H}^{el}|T\rangle & \langle D|\hat{H}^{el}|T\rangle & \cdots \\
|T\rangle & 0 & \langle T|\hat{H}^{el}|S\rangle & \langle T|\hat{H}^{el}|D\rangle & \langle T|\hat{H}^{el}|T\rangle & \cdots \\
\vdots & \vdots & \vdots & \vdots & \vdots & \cdots
\end{array} \qquad \text{... eq. 2.37}$$

where all matrix elements in eq. 2.37 that differ by more than two spin orbitals are strictly zero, e.g. there are no coupling between $|\psi_0^{el}\rangle$ and triples or quadruples. This is a consequence of applying the Slater-Condon rules[41] to the matrix elements , eq. 2.37, to the Hamiltonian operator. As well, there is no coupling between the $|\psi_0^{el}\rangle$ and any single excited determinant, by the virtue of the Brillouin theorem,[41] therefore all matrix elements of the form $\langle\psi_0^{el}|H^{el}|S\rangle$ are zero.

In the $\mathbb{CI}$, the number of determinants act as the limiting factor of the electron correlation, which is defined by the binomial coefficient $\binom{2K}{N^{el}}$.[41] Henceforth the larger the number of determinants in the $\mathbb{CI}$ expansion, the more exact the total final wave function can be, getting a well-define, size consisted and variational method. As a result, if all of the configurations are taken into account, the generated wave function is referred as *full configuration interaction* (FCI). Nevertheless, the larger the expansion is, the harder its solution will be completed, leading to high computational costs, even if the $\mathbb{CI}$ wave function is represented by symmetry adapted to the CSFs. For this reason, the $\mathbb{CI}$ method is just practical and limited to relatively small systems. Hence, *truncating* the $\mathbb{CI}$ expansion, eq. 2.36, in fewer matrix elements can be an option to avoid this limitation.

The most trivial and easiest truncation is to neglect all excitations, i.e. no correlation is considered, hence $|\phi^{el}\rangle = |\psi_0^{el}\rangle$. Another possibility is reducing the expansion considering only single excitations, i.e. CIS. Because of the Brillouin theorem, they can be expected to not largely contribute on the HF results, but influence on the charge distribution within the molecule, when mixing with $|D\rangle$ matrix elements in eq. 2.37. The inclusion of the doubly excited determinants, CID, is fundamental in the calculation of accurate energies, since double excitations mix directly with the HF reference function $|\psi_0^{el}\rangle$, eq. 2.37. Therefore, including single and double excitations can cover most of the correlation energy.[41] Thus, the lowest $\mathbb{CI}$ level which gives the best improvement over the HF result is the CISD method.

The truncation of the $\mathbb{CI}$ expansion results in the *size consistency* error. This means that the total error in the energy of a truncated CI calculation for an ensemble of molecules is not the sum of the errors in energy of the individual and isolated molecules. Fortunately, the truncated-CI energies can be corrected a posteriori with the *Davidson correction*,[58] or with further inclusion of excited determinants, like triple $|T\rangle$ and quadruple $|Q\rangle$ determinants.

Another way to simplify the calculation of the $\mathbb{CI}$ is not to take into account all electrons for all possible excitations e.g. to consider an approximation of *frozen* electrons in the energetically very low (core) orbitals. Consequently, the excited determinants only arise by promoting electrons from the *valence shell* (electrons that can participate in the formation of chemical bonds) orbitals, to the external (vacant virtual) orbitals. A pictorial view of the partitioning scheme in a $\mathbb{CI}$ calculation is shown in Figure 2.4.
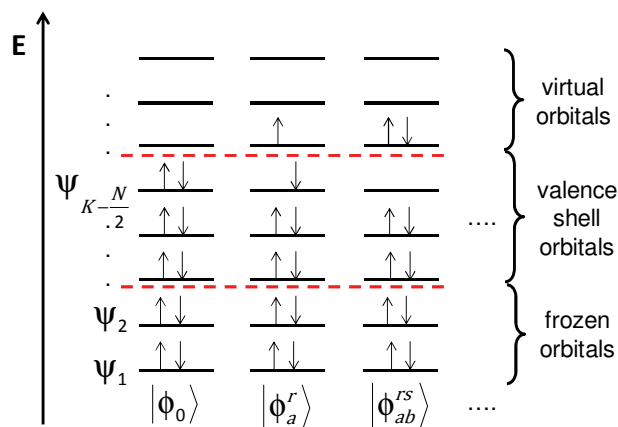
Figure2.4. Partition of the ψ-basis of spatial orbitals into the different sub-spaces for N-electrons in K spatial orbitals. As an example, two spatial orbitals have been considered frozen and some single and double excitations from the valence shell orbitals to the external orbitals have been shown.

An extra flexibility when high excitation energies are considered in the $\mathbb{CI}$ method can be obtained by allowing more than one reference determinant $|\psi_0^{el}\rangle$, this approach is called: *Multi-reference Configuration Interaction* (MRCI).

The MRCI method starts with a wave function reference that includes more than one determinant, the so called *reference determinants*,[47], from which all $|S\rangle$, $D\rangle$ … etc. are then applied. With the purpose of simplifying the MRCI method, as it has been seen in the CI method, eq. 2.36, truncated to into single or double excitations resulting in MRCIS or MRCISD, typically the expansion is.

The reference determinants CSFs are selected either by perturbation theoretical ansatz,[48] or by taking all CSFs that have been shown to be important in a previous CI calculation. The selection of adequate determinant references is reflected on the excitation energies, so that if one is not careful enough, the excitation energies obtained are not sufficiently *correlated* (lower).

Multiconfigurational Self-Consistence Field

Another possible improvement to the HF method relies on optimizing simultaneously the coefficients C of the FCI expansion eq. 2.36 with the coefficients c from equation 2.26 with the variational principle. This means that not just the expansion of the wave function is varied, but also the MOs are varied in order to obtain the total electronic wave function $|\phi^{el}\rangle$ with the lowest possible energy, thus giving rise the Multiconfigurational Self-Consisted Field (MCSCF) method.

A shortage in the MCSCF framework is that the number of iterations required for achieving convergence tends to increase with the number of CSF included. Because of this, the amounts of MCSCF wave functions that can be treated are somewhat smaller that for the $\mathbb{CI}$ method, otherwise it will be at the expense of a computationally very demanding wave function. Therefore, it is important to select the adequate CSFs that can accomplish the right flexibility of the MCSCF wave function, i.e. to include those CSFs that are needed to describe properly the chemical property of interest.

A an extension of the MCSCF approach, the so-called *Complete Active Space Self-Consistent Field* (CASSCF)[59,60] method, developed by Roos et al. diminishes the amount of CSFs included to describe the MCSCF wave function. This means that the linear combination of CSFs used for CASSCF method includes just the CSFs where a particular number of electrons arise in a particular number of orbitals. This can be achieved by partitioning orbitals into subsets according on how they are intended to be used in the wave function: *inactive*, *active* and *external* or virtual orbitals, see Figure 2.5. The set of active MOs, hence the name *active space* (AS), will typically include some of the *Highest Occupied Molecular Orbital* (HOMO) and some of the *Lowest Unoccupied Molecular Orbital* (LUMO) from an RHF calculation, as it is shown in Figure 2.5. The inactive MOs are always fixed doubly occupied. The last set of MOs is the virtual orbitals, which are unoccupied and span the rest of the orbital space. Therefore, the AS in the CASSCF method is set up considering all possible distributions of the N-electrons in the n chosen orbitals[48] taking into account spin and symmetry restrictions. This is conventionally written as CASSCF(N^{el},n). After the MOs have been divided, a FCI calculation is performed on those MOs belonging to the AS, thereby overcoming the size inconsistency of the truncated $\mathbb{CI}$.
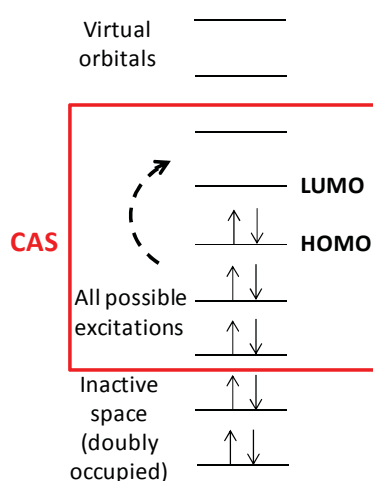

Figure 2.5. Representation of the active, inactive and virtual orbitals.

A possible disadvantage of the CASSCF method is that for any $\mathbb{CI}$ expansion, the CASSCF wave function becomes very large even for small active spaces. Therefore, the MOs included in the AS must be decided manually by considering the problem at hand and the computational expense.[48] If several points on the PES are desired, the AS should include all those orbitals that change along the PES considerably, or for which the electron correlation is likely to change, for which is necessary to carry out several test calculations. For this reason, some features that can be considered when selecting an appropriate set of orbitals in the AS are:[48] **a)** For each occupied orbital, there will be usually one corresponding virtual orbital. **b)** Including all the valence orbitals leads to a wave function that can enhance the description of the chemical phenomena of interest. Knowing that, a full valence CASSCF wave function rapidly becomes unmanageably large for realistic sized systems. **c)** The orbital energies from an RHF calculation may be used for selecting the important orbitals. Mainly, orbitals belonging or being close to the HOMO-LUMO, since the smaller the orbital energy difference, the larger contribution to the correlation energy. **d)** Orbitals with occupation numbers significantly different from 0 or 2 (in a RHF done with natural orbitals) are usually those that are the most important to include in the active space.

When dealing with excited states, the MOs can be simultaneously optimized for every electronic state or for an appropriate average of desired states, i.e. performing a *state-averaged* CASSCF (SA-CASSCF). The method then will be indicated as SAm-CASSCF with m being equal to the number of included *roots* (electronic states). A virtue of a SA-CASSCF is that all states are expressed using the same MOs, thereby ensuring orthogonality and differ only in the variationally optimized $\mathbb{CI}$-coefficients. Though, a drawback to the SA-CASSCF method is that the quality of any state's wave function, CSF, is lower than it will be if only one state is considered.

Since the number of CSFs in the CASSCF method quickly increases with the number of active orbitals, even for quite small active spaces, it may be desirable to use a smaller set of CSFs. One way to make this selection is to restrict the number of electrons in certain subspaces of the total active MOs. Henceforth, a variation of the CASSCF procedure is the *Restricted Active Space Self-Consistent Field* (RASSCF) method.[61] Where the active MOs are divided into three sections: RAS1, RAS2 and RAS3, each having restrictions on the occupation numbers (excitations) allowed. The model most used consists on applying a FCI on the configurations present in the RAS2 section (analogously to the CASSCF method). The RAS1 section consists of MOs that are doubly occupied in the HF reference determinant $|\psi_0^{el}\rangle$. The RAS3 section consists of MOs that are empty in the HF reference determinant. Extra configurations from those of the RAS2 section are generated by allowing, with the maximum of two electrons, excitations from the RAS1 to RAS2 and excitations from RAS2 to the RAS3 section, see Figure 2.6. In this way, a much larger number of CSFs (i.e. larger active space) can be considered.
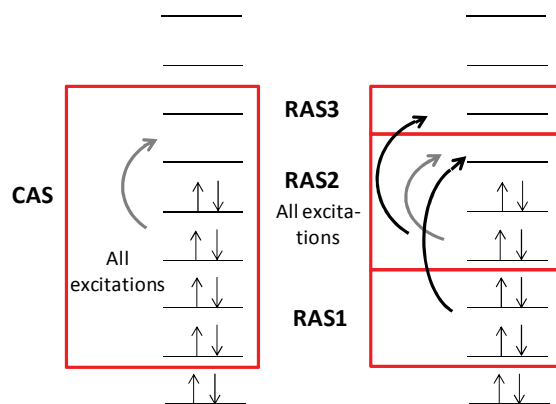
Figure 2.6. Representation of the CASSCF and the RASSCF orbital partitions.

Since the CASSCF method covers mainly static correlation, the dynamical correlation can be added either variationally with MRCI, or perturbationally, *via* Complete Active Space Second-Order Perturbation theory.[62] Then, a multi-configurational CASSCF wave function can be use as a reference wave function for a MRCI calculation or for CASPT2[59] calculation. In this thesis, CASPT2 calculations with a reference CASSCF wave function have been accomplished to account for dynamical correlation. For this reason, a brief explanation first of perturbation theory and then of the CASPT2 method is given.

The premise idea in perturbation methods is to start with a simple system for which a mathematical solution is known (exactly or approximately), and add a *weak disturbance* to the system. If the disturbance is not too large, the eigenvalues and eigenstates associated with the perturbed system can be expressed as small *corrections* to those of the reference system. In order to do so, from the eigenvalue problem eq. 2.9, the perturbation methods split the Hamiltonian operator $\hat{H}^{el}$ into two parts: the reference Hamiltonian operator $\hat{H}_0^{el}$ and the perturbation Hamiltonian operator $\hat{H}'$, i.e. a small perturbation $\hat{H}'$ is added to the *unperturbed* Hamiltonian operator $\hat{H}_0^{el}$:

$$\hat{H}^{el} = \hat{H}_0^{el} + \lambda \hat{H}', \qquad \text{eq. 2.38}$$

where λ is an arbitrary real parameter determining the strength of the perturbation. As the perturbation is increased, the new eigenenergies and eigenfunctions from eq. 2.9 must also change continuously, thus they can be written as a Taylor expansion in powers of the perturbation parameter λ:

$$|\phi_i^{el}\rangle = \lambda^0 \psi_i^0 + \lambda^1 \psi_i^1 + \cdots \ell, \qquad\qquad \text{eq. 2.39}$$

and

$$\varepsilon_i^{el} = \lambda^0 \varepsilon_i^0 + \lambda^1 \varepsilon_i^1 + \cdots \ell. \qquad\qquad \text{eq. 2.40}$$

For $\lambda = 0$, then $\phi^{el} = \psi_i^{(0)}$ and $\varepsilon^{el} = \varepsilon_i^{(0)}$; and these are known as the *zeroth-order* wave function and *zeroth-order* energy. The $\psi_i^{(1)}, \psi_i^{(2)}, \dots \ell$ and $\varepsilon_i^{(1)}, \varepsilon_i^{(2)}, \dots \ell$ are the first-order, second-order, ℓ^{th}-order corrections, where the ℓth-order energy or wave function becomes a sum of all terms up to order ℓ^{th}. Once the equations 2.39 and 2.40 are inserted into the eigenvalue equation 2.9, the second-order correction to the energy can be retrieved.

If the unperturbed Hamiltonian, $\widehat{H}_0^{el}$, is replaced by a sum of one-electron Fock operators, here from a RHF, as suggested by Moller and Plesset[56] for the *Moller-Plesset second-order* (MP2) method, it can be shown that the zeroth-order wave function is the HF determinant, and the zeroth-order energy is just a sum of MO energies. Henceforth, the first-order energy correction yields a correction for the overcounting of the electron-electron repulsion at zeroth-order, i.e. the first-order energy (sum of $\varepsilon_i^{(0)}$ and $\varepsilon_i^{(1)}$) is exactly the HF energy. Therefore, it is the 2nd order energy term, eq. 2.42, that accounts for the dynamical correlation that is missing from the HF, as it is seen for CI, eq. 2.37.

$$\varepsilon_i^2 = \sum_{i<j}^{Occ} \sum_{a<b}^{Vir} \frac{\langle\psi_0|\widehat{H}'|\psi_{ij}^{ab}\rangle\langle\psi_{ij}^{ab}|\widehat{H}'|\psi_0\rangle}{\varepsilon_0 - \varepsilon_{ij}^{ab}} \qquad\qquad \text{eq. 2.42}$$

Analogously, the dynamical correlation energy that is missing from a CASSCF calculation can be recovered within a MP2 type perturbation approach in the frame of CASPT2 method, which computes the first order wave function and the second order energy in the full CI space on the reference CASSCF wave and the Fock type one-electron operator.

For situations in which electronic wave functions are mixed with one another at SA-CASSCF level, such as avoided crossings or Rydberg-valence orbitals and valence-valence orbitals, the multistate CASPT2 (MS-CASPT2),[63] which is an extension of the CASPT2 method is strongly recommended. Where on the multi-configurational CASSCF wave function a multidimensional reference space, so to say, treats several states simultaneously. Hence includes the coupling of several electronic states through the diagonalization of the *effective Hamiltonian* $\widehat{H}^{eff}$. Where the diagonal elements are the single-state CASPT2 (SS-CASPT2) energies and the off-diagonal elements

represent the couplings between (SA)-CASSCF electronic states at second order. This allows for the simultaneous treatment of all the electronic states being calculated and for which accounts for a substantial amount of dynamic correlation energy. The diagonalization of the $\widehat{H}^{eff}$ produces a set of new wave functions and energies i.e. the MS-CASPT2-corrected energy values, for a detail explanation see Ref. 63.

It has to be considered, that the CASPT2 method can yield enough accurate eigenenergies only when a given AS and basis set is optimal for the phenomena to be describe. This means, where the AS is not complete on higher excited states, in combination with large diffuse basis sets. Since in this cases *intruder states* usually arise.

With the purpose of avoiding intruder states, i.e. to obtain continuous potential energy functions, the inclusion of sufficiently orbitals in the AS can be performed. Nevertheless, a huge number of active orbitals can make this calculation unworkable. In order to remove the intruder states, two remedies can be accomplished, the first one is to delete orbitals, nevertheless is not so accurate. The second procedure, which consists on adding a penalty parameter (*shift*) on the $\widehat{H}_0^{el}$ Hamiltonian, can eliminate weak intruder states in a small treatable AS. The latter shift procedure is called *level-shift technique*[64,65] LS-CASPT2. Mainly in the LS-CASPT2 a constant parameter is added to the external part of the $\widehat{H}_0^{el}$, from there any denominator close to zero, recall eq 2.42, is shifted away, thus avoiding the intruder states. Afterwards in the LS-CASPT2 procedure, the level shift effect is eliminated. With the LS-CASPT2, the second-order correlation energy $\varepsilon_i^{(2)}$ and the first-order wave function $\psi_i^{(1)}$ will depend on the level shift used. A detailed explanation of how to use the level-shift technique has been published in Refs. 64,65.

In this thesis the same level shift (0.3 a.u.) has been used for all states and geometries in order to minimize the effect on relative energies.

Coupled Cluster

Coupled cluster (CC) method is a numerical technique used to provide an approximate solution to the TISE, recall eq. 2.2. It essentially takes the basic HF determinant and adds back multi-electron wavefunctions to account for electron correlation. The wavefunction of the CC theory is written as:

$$|\phi^{el}\rangle = e^{\widehat{T}}|\psi_0^{el}\rangle,$$ ... eq. 2.43

where $|\psi_0^{el}\rangle$ is the HF determinant. $\hat{T}$ is an excitation operator which, when acting on $|\psi_0^{el}\rangle$, produces a linear combination of excited Slater determinants, and is determined by,

$$\hat{T} = \hat{T}_1 + \hat{T}_2 + \hat{T}_3 + \cdots + \hat{T}_{N^{el}}, \qquad \text{... eq. 2.44}$$

where $\hat{T}_1$ is the operator that accounts for all single excitations, $\hat{T}_2$ for all double excitations and so forth. Through the choice of $\hat{T}$ operator, the CC method guarantees the size extensivity in the solution. All truncated forms of CC are size consistent.

Therefore, the CC energy ε^{el} is obtained by solving the following Schrödinger equation:

$$\hat{H}e^{\hat{T}}|\psi_0^{el}\rangle = \varepsilon^{el}e^{\hat{T}}|\psi_0^{el}\rangle. \qquad \text{... eq. 2.45}$$

The size of the CC equations set, eq. 2.45, is given by the type of excitations accounted for, and are solved iteratively. A drawback of the CC method is that it is not variational.

An approximation of the CC method, which includes singles $\hat{T}_1$ and doubles $\hat{T}_2$ in a preservative way is the CC2 method,[66] which is used in this thesis. This method was proposed, in 1996 by Christiansen, Jørgensen and Koch, for response calculations on molecules which are out of reach for CCSD (coupled cluster for singlets and doubles) and higher correlated methods. It is one of the computationally cheapest methods for excited states and yields energies for singly-excited states which are corrected through second-order in the electron-electron interaction, i.e. dynamical correlation. CC2 can be implemented very efficiently with a so-called resolution of the identity (RI) approximation[67,68] for the integrals which describe the electron-electron interaction and thereby made applicable to relatively large molecules. The RI approximation leads again to a dramatic reduction in the computational requirements, and allows us to perform CC2 calculations on much larger molecules or with much larger basis sets than can be done with conventional (integral-direct) implementations. The error introduced by the RI approximation has been shown to be very small for selected examples[66].

2.2.2 Density Functional Theory

Up to now, we discussed the HF method which calculates the electronic wave functions and their corresponding energies. Though, the HF wave functions lack of electronic correlation, which can

be recovered by the use of CI or CC method. Nevertheless, a drawback of the latter methods is its enormous computational demand, i.e. more computational time. Thus, an economical method, *Density Functional Theory* (DFT) based on the electronic density and not in the refinement of the wave function obtained *via* HF, is introduced.

Density Functional Theory

DFT is another quantum mechanical method used to calculate the electronic energy of a molecular system, where the central focus is the *electron density*[iii] $\rho(\vec{r})$ which depends only on the three Cartesian coordinates $\vec{r} = x, y, z$, rather than the wave function ϕ which depends on $4\mathcal{N}$ coordinates. The theoretical foundations of DFT are based on two theorems postulated by Hohenberg and Kohn[69] in 1964. The first theorem states that the ground state density $\rho_0(\vec{r})$ exclusively determines the ground state energy and the ground state wave function; this implies that all molecular electronic properties of a *static* many-particle system are in function of its ground state electron density $\rho_0(\vec{r})$. Therefore, instead of using a Slater determinant of spin orbitals as HF method, the total energy is calculated in DFT *via* the minimization of the charge density functional $\varepsilon^{el}[\rho^{el}]$ which depends on the electron density,

$$\rho^{el}(\vec{r}) = \sum_i |\phi_i(\vec{r})|^2,$$

… eq. 2.46

where ϕ_i correspond to the orbitals. Thus the eq. 2.46 provides an implementation to the DFT conceptually and computationally very similar to the HF-procedure. The second theorem proves that the exact ground state density minimizes the total electronic energy of the molecular system. However, because the exact charge density is typically not known it is approximated by the sum of the squared one-electron wave functions. The minimization of the energy, stated in the second theorem, which states that the ground state electronic energy calculated from the trial charge density ρ^{TR} represents an upper-bound to the true ground electronic state energy, which would be obtained if the exact electron density was known $\rho_0(\vec{r})$,

$$\varepsilon^{DFT}[\rho^{TR}] \geq \varepsilon_0,$$

… eq. 2.47

where ε_0 is the true ground state energy.

The energy in the DFT approach is not given as the expectation value of an operator like in the HF method, but as a sum of several energy functionals which in turn depend on the electron density,

---

[iii] The term density means the number of electrons per unit volume in a give electronic state.

$$\varepsilon^{DFT}[\rho] = T[\rho] + V[\rho] + U[\rho] + \varepsilon^{xc}[\rho], \qquad \text{... eq. 2.48}$$

where $T[\rho]$ denotes the kinetic energy of the electrons, $V[\rho]$ represents the attraction between the nuclei and the electrons, $U[\rho]$ represents the Coulomb repulsion between electrons, and $\varepsilon^{xc}[\rho]$, known as the exchange-correlation energy, denotes the effects generated by the electron correlation and which has no classical counterpart. Accordingly, if the exact ground state density is inserted in the equation 2.48, then by the virtue of the second Hohenberg-Kohn theorem, eq. 2.47, the total energy ε^{DFT} can be minimized with respect to the density, thus yielding the Kohn-Sham equations.[70]

Analogous to the HF equations, recall eq. 2.18, the Kohn-Sham approach leads to a set of one-electron equations that are solved iteratively. The difference with the HF equations lies in the form of the effective potential, eq. 2.20, which now is no longer given by V^{HF}, but by an effective DFT potential V^{DFT} defined as.

$$V^{DFT}(\vec{r}) = \int \frac{\rho(\vec{r}')}{|\vec{r} - \vec{r}'|} d\vec{r}' + V^{xc}(\vec{r}), \qquad \text{... eq. 2.49}$$

where the first term is equivalent to the Coulomb-term of the HF equations, while the V^{xc} is the potential due to the non-classical exchange-correlation energy ε^{xc}, and is defined *via* the partial derivative of ε^{xc},

$$V^{XC}(\vec{r}) = \frac{\delta \varepsilon^{xc}}{\delta \rho(\vec{r})}. \qquad \text{... eq. 2.50}$$

If the exact form of the exchange-correlation energy ε^{xc} were well-known, then the DFT method would solve for the exact total energy of the system, i.e. the solution of the Kohn-Sham equation would generate the correct energy eigenvalue of the total Hamiltonian of the Schrödinger equation.

The Kohn-Sham approach is in principal exact. Nevertheless, a drawback of the Kohn-Sham approach is that the correct form of ε^{xc} is not known, so the ability of DFT calculations is to find a *functional* that describes ε^{xc} adequately. Hence, the properties of a many-electron system can be determined within DFT by using adequate *functionals*. Some of the approximations to construct the exchange correlation functionals are: The Local-density approximation (LDA) and local spin density approximation (LSDA), [69-71] the generalized gradient approximations (GGA), [72,73] and the hybrid functionals.[74] The hybrid functionals, used in the present thesis, were introduced by Axel Becke[72] in 1993. They include a part of exact correlation (calculated from the Slater-determinant

set up by the KS-orbitals), and the rest fitted to experimental data. Their main advantage is the possibility to include correlation effects in a calculation that costs roughly as much as a HF-calculation. Among the hybrid functionals, one of the most widely used is the three parameter functional B3LYP introduced by A. Becke[75], which mixes the exact HF-exchange part with other DFT exchange-correlation parts arising from the Lee-Yang-Parr (LYP)[76] and Vosko-Wilk-Nusair (VWN) functionals[77]. And this B3LYP functional was used in this thesis.

Time-dependent Density Functional Theory

Time-dependent functional theory (TDDFT) is an extension of DFT, and is used to investigate the properties and dynamics of molecules in the presence of time-dependent potentials, such as electric or magnetic fields, where TDDFT can extract features like excitation energies, frequency-dependent response properties, and photoabsorption spectra. The conceptual and computational foundations between DFT and TDDFT are analogous, but for the second case, the energy is not only dependent of the density (Hohgenberg-Kohn theorem), but also of time, which arises for the Runge-Gross theorem.[78] Then the electron density is calculated through,

$$\rho^{el}(\vec{r},t) = \sum_i |\phi_i(\vec{r},t)|^2.$$

… eq. 2.51

Where the electronic density is built from the Kohn-Sham $\phi_i(\vec{r},t)$ orbitals. The electrostatic interaction is calculated as,

$$V^{TDDFT}(\vec{r},t) = \int \frac{\rho(\vec{r}',t)}{|\vec{r}-\vec{r}'|}d\vec{r}' + V^{xc}(\vec{r},t),$$

… eq. 2.52

which is similar to the equation 2.49, therefore, equation 2.53 can be solved when the V^{xc} is known:

$$V^{XC}(\vec{r},t) = \frac{\delta A^{xc}}{\delta\rho(\vec{r},t)}.$$

… eq. 2.53

A^{xc} represents the Action operator. In time-dependent systems there can be no variational principle based on the total energy, simply because the total energy is not a conserved quantity, thus, the A^{xc} operator is a quantity analogous to the energy. And is given by the time-dependent Kohn-Sham equation,

$$A^{xc}[\rho] = \int_{t_0}^{t_1} dt \, \langle \Psi(t) | i\frac{\partial}{\partial t} - \hat{H}(t) | \Psi(t) \rangle.$$

If calculations of photoabsorption spectra are intended to be run then Linear-response TDDFT can be used. For a more detailed description of the linear response theory, see the Ref. 79.

A detailed monograph on performance and applicability of DFT can be found in Ref. 80 and for TDDFT the reader is referred to.[79,81]

2. 3 Solution to the Time-dependent Schrödinger Equation

With the purpose of knowing how a molecular system evolves in time, Reaction Molecular Dynamics simulations must be employed. However, since molecular systems generally consist of a vast number of particles, solving the TDSE, recall eq. 2.1, is only possible when the dynamics can be reduced to few degrees of freedom. In bigger systems, alternative approaches have been suggested in order to circumvent the dimensionality. One possibility is to use mixed quantum-classical dynamics (MQCD) simulations. In the MQCD, the electrons are treated quantum mechanically solving the TDSE for several electronic states, while the nuclei are treated classically. A number of trajectories are defined by the position $\vec{R}(t)$ and velocity $\vec{v}(t)$ of the nuclei at every time, in contrast to quantum mechanics (QM), where the position and velocity of the nuclei cannot be known simultaneously. In order to imitate an initial nuclear quantum probability, a set of initial conditions is taken into account creating an ensemble of trajectories, i.e. a swarm of geometries and velocities is described with a Wigner distribution.

In order to simulate the evolution of the trajectories the Velocity-Verlet algorithm[82,83] is considered. The Velocity-Verlet algorithm is a numerical method used to solve Newton's equations of motion and is commonly used to calculate trajectories in molecular dynamics. Consequently, if for a given set of initial coordinates $\vec{R}(t = 0)$, the initial velocity $\vec{v}(t = 0)$ are known, then a new position is calculated assuming a constant acceleration during the time step:

$$\vec{R}(t + \Delta t) = \vec{R}(t) + \vec{v}(t)\Delta t + \frac{1}{2\boldsymbol{\mathcal{M}}_I} \nabla E^{pot}\left(\vec{R}(t)\right)\Delta t^2.$$

In eq. 2.55 $\nabla E^{pot}(\bar{R})$ is the gradient of the potential that describes the acceleration of the system and $\boldsymbol{\mathcal{M}}_I$ is the mass of nuclei. The new velocity at the end of the time step $(t + \Delta t)$ is given by,

$$\vec{v}(t + \Delta t) = \vec{v}(t) + \frac{1}{2\mathcal{M}_I} \nabla E^{pot}\left(\vec{R}(t)\right) \Delta t + \frac{1}{2\mathcal{M}_I} \nabla E^{pot}\left(\vec{R}(t + \Delta t)\right) \Delta t. \qquad \text{... eq. 2.56}$$

Since classical trajectories are defined locally, they can only follow one gradient, i.e. the trajectory is attached to one electronic superposition state at every time. This represents quite a disadvantage for classical trajectories, especially when simulating systems near avoided crossings or during excitations, when population transfer between two states can be present. One possibility to solve this problem is the Surface Hopping (SH) method.[84,85] In this methodology, the trajectories are simulated in a single electronic eigenfunction but they are able to switch from one electronic state to another during the dynamics. Moreover, statistical evaluation of the complete set of propagated trajectories should recover the character of the splitting wave packet over different states. Nevertheless, a drawback of the SH method is to find a proper algorithm to calculate the SH probabilities, which are obtained through the coefficients c that represent the probability of finding the single trajectory in a specific PES. These coefficients represent the population of a wave packet.

The criterion of fewest switches of Tully[86] is often considered to obtain the c in the SH approach. This criterion minimizes the number of surface hops per trajectory whilst guaranteeing the correct ensemble averaged state populations at all times. To calculate the evolution of the coefficients in time, one has to solve the TDSE for the electrons, recall 2.1. In order to do so, the wave packet $\left|\Psi\left(\vec{R}(t); \vec{r}, t\right)\right\rangle$ is expanded as a linear combination of basis functions, normally the BO solutions of the electronic TISE:

$$\left|\Psi\left(\vec{R}(t); \vec{r}, t\right)\right\rangle = \sum_k c_k(t) \left|\varphi_k\left(\vec{R}(t); \vec{r}\right)\right\rangle, \qquad \text{... eq. 2.57}$$

similar to the adiabatic picture, where the electronic wave function is a linear combination, recall eq. 2.26, of all adiabatic states wave functions $\left|\varphi_k(\vec{r})\right\rangle$. To obtain the hopping probabilities by means of the fewest switches criterion, the derivative of the coefficients with respect to time has to be obtained. This is given by,

$$\frac{\partial c_l(t)}{\partial t} = \sum_k c_k(t) \left\{ \frac{i}{\hbar} H_{kl}\left(\vec{R}(t)\right) + K_{kl}\left(\vec{R}(t)\right) \right\}, \qquad \text{... eq. 2.58}$$

where $H_{kl}\left(\vec{R}(t)\right) = \left\langle \varphi_l\left(\vec{R}(t); \vec{r}\right) \middle| \hat{H}\left(\vec{R}(t); \vec{r}\right) \middle| \varphi_k\left(\vec{R}(t); \vec{r}\right) \right\rangle$ represents the diabatic Hamiltonian. The $K_{kl}\left(\vec{R}(t)\right)$ term evaluates the change of the electronic basis functions $\left|\varphi(\vec{r})\right\rangle$ with time. This term is equivalent to the variation of the basis functions with the nuclear coordinate $\vec{R}(t)$ times the velocity $\vec{v}(t)$,

$$K_{kl}\left(\vec{R}(t)\right) = \langle\varphi_l(\vec{R}(t);\vec{r})\left|\frac{d}{d\vec{R}(t)}\right|\varphi_k(\vec{R}(t);\vec{r})\rangle\vec{v}(t).$$

<div align="right">... eq. 2.59</div>

The equation 2.59 is solved using the fifth order Butcher algorithm.[87] Moreover, the time dependent coefficients are corrected for decoherence effects.[88] This factor corrects the excess of coherence by weighting the different eigenstates depending of the velocity of the trajectory. The hopping probability, within the SH approach, from a state l to a specific state k, through the time-dependent c of the electronic wave function is then calculated as,

$$P_{lk} = \frac{2\mathcal{R}\left\{\frac{i}{\hbar}H_{kl}\left(\vec{R}(t)\right) + \langle\varphi_l(\vec{R}(t);\vec{r})\left|\frac{d}{d\vec{R}(t)}\right|\varphi_k(\vec{R}(t);\vec{r})\rangle\vec{v}(t)\right\}}{c_l^*(t)c_k^*(t)},$$

<div align="right">... eq. 2.60</div>

with $\mathcal{R}$ being the real part of a complex term, and the $\langle\varphi_l(\vec{R}(t);\vec{r})\left|\frac{d}{d\vec{R}(t)}\right|\varphi_k(\vec{R}(t);\vec{r})\rangle$ term describing the non-adiabatic couplings. A detailed monograph on performance and applicability of SH method can be found in Ref. 89.

2.4 Other Computational Issues

a) Basis sets and Natural Atomic Orbitals

The two most common ways to describe atomic orbitals are: *Slater-type*[90] orbitals (STOs), named after John C. Slater who introduced them in 1930, and *Gaussian-type* orbitals (GTOs). Although STOs offer a better description of the electronic behavior, GTOs are numerically easier to deal with. For this reason, in 1950, Frank Boys proposed to use a linear combination (*contraction*) of several GTOs, to represent a single STO,[91] see Figure 2.7.
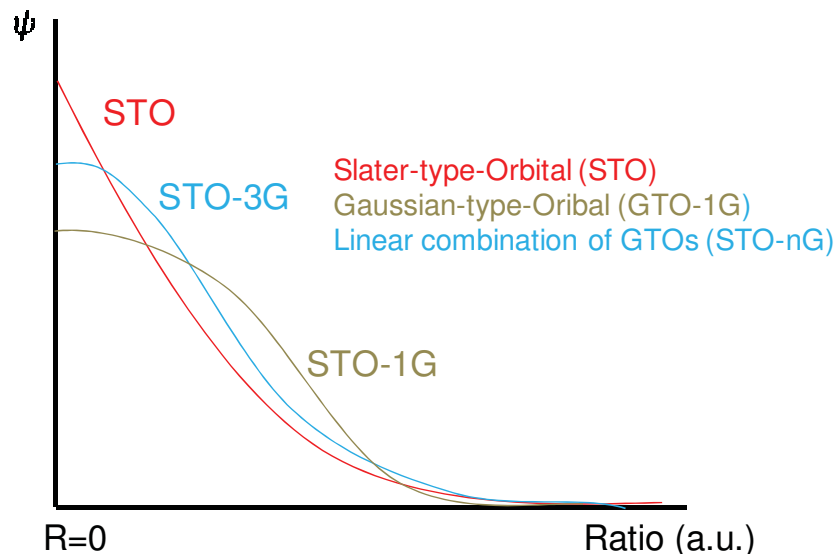
Figure 2.7. The representation of an STO (the curve in red) through a linear combination of *primitive* gaussians. Three GTOs (brown) can describe better a STO than one GTO (in blue).

Nowadays, many different sets of contractions, which refer to various ways of how orbitals are combined in order to make an approximation to a wave function, have been conceived. These sets of contractions are commonly called *basis sets*.[48]

Amongst the most popular basis sets are: **a)** The *Pople-type* (see Ref. 55 for more information), in which the accuracy lies in a partition of the electrons in core (a selected first set of basis functions) and valence (a second different set of basis functions, also selected by hand). These basis sets are called *split-valence* basis set. **b)** The *Dunning-type* (see Ref. 92 for more information) which owe its accuracy to the so called *polarization functions*, where an electron-electron interaction is included. Some of the calculations done in this thesis were performed using Pople-type and Dunning-type of basis sets as implemented in Gaussian package[93] and TURBOMOLE package.[94,95] Other basis sets used in this thesis are those ones disposed in the MOLCAS package.[96] They have been used since they involve the *Atomic Natural Orbitals* concept,[97] reducing the computational time[98] and therefore computational costs.

b) Reaction paths

A reaction path connects the several chemical species that evolve during a reaction process, i.e. an ensemble of molecular entities which travel through the PES, recall Figure 2.1, at a given

temperature along the reaction.[99] A way to study the reaction path is through optimization methods. [100,101]

Optimization methods provide very valuable information and may give a chemical insight of the molecular entities participating throughout the reaction path. The optimization methods concentrate on locating stationary points, i.e. conical intersections (CI), transition states (TS) and minima, on the PES. Therefore, the continuous line connecting reactants and products, without the effect of temperature, through the lowest energy region of the valley in the PES is called the *minimum energy path* (MEP). If the MEP is calculated in mass-weighted coordinates is called *Intrinsic Reaction Coordinate* (IRC),[102] which can be used to obtain physical properties of the intermediate molecules between reactants and products. There are several methods to determine the IRC from a saddle point down to the reactants or products, all of them trying to solve the steepest descent reaction path. For more detail see Ref. 101.

An alternative strategy to the IRC method is to interpolate between reactants and products; this is called *linear interpolation coordinates* (LIC) method. In this case, the search takes as reference points either the reactants or the products. The LIC methods are specially used to look for a saddle point by going gradually uphill or to progressively refine the interpolation between reactants and products.

Examples of other more sophisticated strategies to obtain reaction path can be seen in the review written by Schlegel and the references therein.[100]

c) Atoms in Molecules Theory

The atoms in molecules (AIM) theory,[103,104] developed by Prof. R. Bader in the early 1960s, is a quantum chemical model that characterizes the chemical bonding of a system based on the topology of the quantum charge density. In addition to bonding, AIM allows the calculation of certain physical properties on a per-atom basis, by dividing space up into atomic volumes containing exactly one nucleus. In AIM, an atom is defined as a proper open system, i.e. a system that can share energy and electron density, which is localized in the 3D space. Each atom acts as a local attractor of the electron density, and therefore it can be defined in terms of the local curvatures of the electron density. A detailed monograph on the performance and applicability of AIM can be found in the Ref. 104.

d) The Kasha rule

Kasha's rule states[23,24] that vibrational relaxation takes place between excited levels towards the lowest-lying excited level, from where emission of a photon takes place, allowing the system to go back to its fundamental state, see Figure 2.8. Therefore, the photo-emission of the Kasha's rule, termed as *fluorescence* in the case of a singlet state and *phosphorescence* from a triplet state, is expected in appreciable yield only from the low-lying excited state, i.e. the emission wavelength is independent of the excitation wavelength.
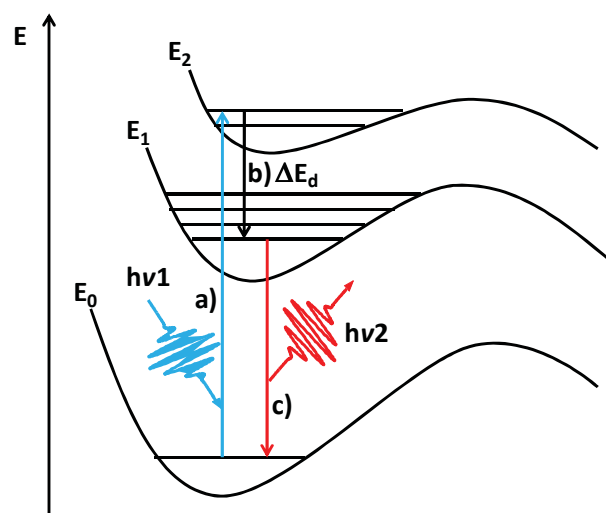
Figure 2.8. Kasha's rule[23,24]: **a)** A photon with energy hν1 excites an electron from the fundamental level E_0 up to an excited energy level E_n, here E_2. **b)** Vibrational relaxation takes place between excited levels, here from E_2 to E_1, and part of the energy is dissipated ΔE_d. **c)** The energy is totally dissipated by emission of a photon of energy hν2, and allows the system to go back to its fundamental ground state E_0.

e) Solvation Effects

An essential subject of study in the field of computational chemistry field is the effect of solvents. Solvation can be modelled in two ways: [47]

- Implicit (also known as continuum solvation). The implicit model is a method of representing solvent as a continuous medium. To determine how to define an implicit model, one must consider the solvation process itself.

- Explicit. The explicit model is suitable for achieving the knowledge of the explicit behaviour of the surroundings. This includes the shape and ability to form H-bonds or solvent shell structures. Moreover, in this way, it is possible to analyze the van der Waals interactions, the dynamics of the solvent-solute models, charge transfer effects and the hydrophobic effects.

For a thorough description of the explicit as well as the implicit solvation and their applicability, see Ref. 47.

In this thesis, only explicit solvation was employed in order to know how one molecule of water affects the spectroscopy properties of *o*-NBA.

CHAPTER 3

Results

With the aim of gaining some insight into the mechanism of the intramolecular H-transfer in *o*-NBA, we have modeled through quantum chemical (QC) calculations the deactivation of excited *o*-NBA and performed mixed quantum-classical dynamics (MQCD) simulations to obtain a time-resolved picture of the mechanism. In order to achieve these goals, we started by calculating the UV-absorption spectrum of *o*-NBA. These calculations have helped to characterize the singlet excited states of *o*-NBA populated upon UV-irradiation. Once the main spectroscopic states have been characterized, two photoreaction deactivation pathways connecting these states at the Franck-Condon region with the main intermediate ketene are presented and discussed. The relaxation pathways to the ground state have been obtained with the help of IRC calculations. These calculations allow locating and connecting the main critical points, namely, conical intersection (CI), local minima and transition states (TS).

The characterization of the UV-absorption spectrum and the relaxation mechanism from the excited *o*-NBA has been performed using different QC approaches. Both monoreferential (TD-DFT, RI-CC2) and multiconfigurational (MS-CASPT2/CASSCF) methods have been combined to provide a global static mechanistic picture on this H-transfer reaction.

Finally, the static QC picture has been completed with semi-classical dynamics simulations that provide important information about the time scales of the H-transfer process and the product distributions. More precisely, two types of MQCD simulations will be described. First, we will discuss in detail MQCD simulations aiming to reproduce *o*-NBA deactivation upon experimental irradiation wavelengths at ca. 260 nm. Then, the time-resolved H-transfer starting from the S_1 potential will be described.

3.1 UV-absorption spectrum

The goal of this section is to assign the experimental UV-absorption spectrum of *o*-NBA. These experiments have been performed by the group of Prof. Dr. P. Gilch (Ludwig-Maximilians Universität). First, we will describe the assignment of the experimental UV-spectrum of *o*-NBA based on gas phase calculations. Then, the influence of solvent will be modeled considering the complex of *o*-NBA with one water molecule. Finally, a comparison of the *o*-NBA UV/Vis absorption

spectrum with that of its two non-reactive isomers, i.e. *m*-NBA and *p*-NBA, is given. Further details on the theoretical UV-spectra of *o*-NBA in gas phase, 1:1 *o*-NBA-water complex and *o*-NBA non-reactive isomers, *m*-NBA and *p*-NBA can be found in references, J. Phys. Chem. A. **2008**, *112*, 5046-5053, Z. Phys. Chem, 2008, 222, 1263-1278, and Phys. Chem. Phys. Chem. **2011**, *13*, 4269-4278, respectively.

3.1.1 Computational details

The *o*-NBA experimental geometries reported by Coppens et al.[105] in an X-ray analysis were used to calculate the vertical spectrum of *o*-NBA. This molecule is characterized by a C_1 symmetry because the two substituents, CHO and NO_2, that are in *ortho-* position, form a dihedral angle of 30° with respect to the aromatic ring, see Figure 3.1. Additionally, both substituents form a H-bond which has been characterized in this thesis through the Atoms in Molecues theory, developed by Bader.[104]
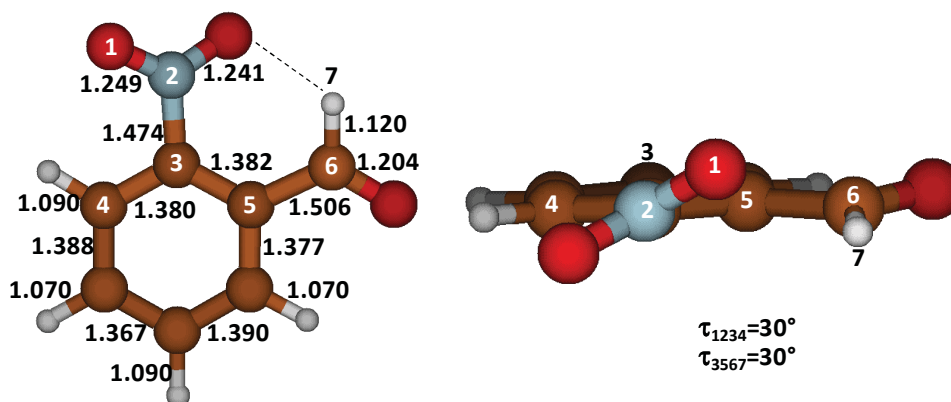

Figure 3.1. *o*-NBA X-ray geometrical parameters, reported by Coppens et al.,[105] used to calculate the vertical excited spectrum at TD-DFT, RI-CC2 and MS-CASPT2//CASSCF levels of theory.

a) Gas phase

The vertical excited energies were calculated using the state-of-the-art MS-CASPT2/CASSCF/ANO-L approach. To carry out a CASSCF calculation an adequate active space (AS) has to be selected. Hints on the orbitals that need to be included in the AS were obtained from monoreferential, TD-DFT and CC2, calculations. For supplementary information on the computational details of two last methods see article 3.4.1.
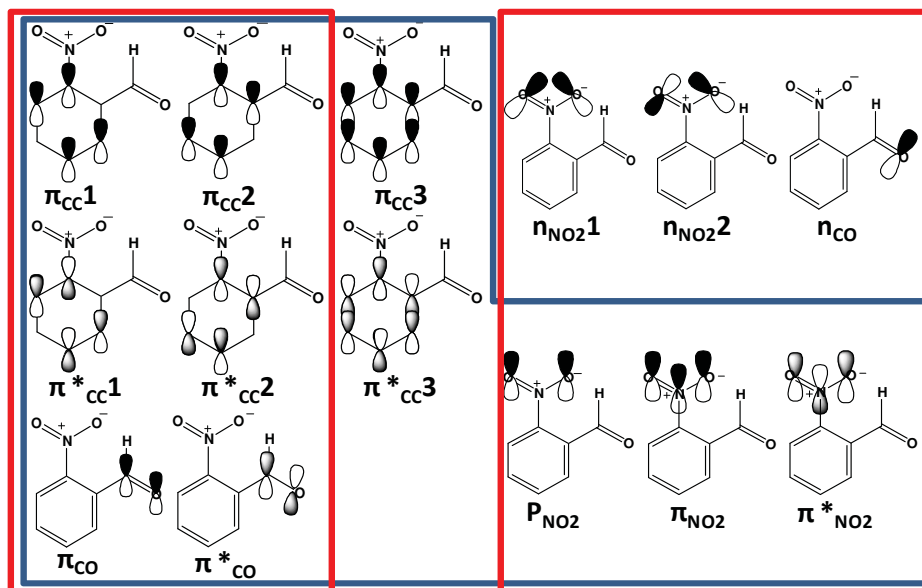
Figure 3.2. For the CASSCF vertical spectrum, the two following AS were used: (16,12)AS, orbitals inside the red squares; and the (12,11)AS, orbitals inside the blue square.

Among all the AS examined, the two more suitable were (16,12), and (12,11), described in Figure 3.2.The larger (16,12) AS contains the lone pairs from the two functional groups, NO_2 and CHO, and therefore is suitable in describing the $n\pi^*$ transitions. This AS does not contain all $\pi\pi^*$ orbitals and thus is unable to describe the higher in energy $\pi \rightarrow \pi^*$ band. This particular state can be described with the (12,11) AS, which in turn, excludes the lone pairs, and thus cannot describe adequately the low-energy part of the *o*-NBA spectrum.

b) 1:1 *o*-NBA-H₂O complexes

The most favored coordinate position for a water molecule within the 1:1 *o*-NBA-H_2O complex is within the benzene plane. Other complexes with water molecules located either over or under the benzene moiety were also calculated and were proven to be less stable. This can be explained by the fact that in these positions, the molecules of water cannot establish H-bonds with CHO and NO_2 functional groups and can only interact weakly with *o*-NBA, see Figure 3.3.
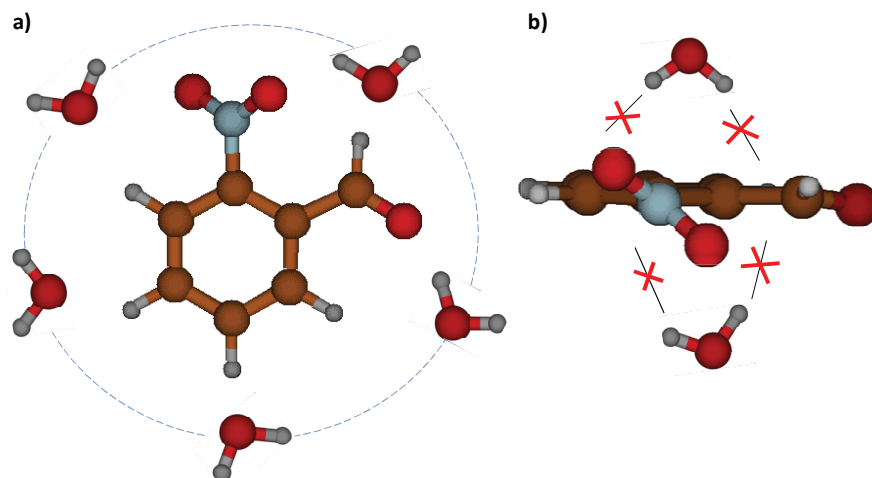
Figure 3.3. **a)** The most favorable position of the water molecule around the *o*-NBA. **b)** Less favorable positions.

The 1:1 *o*-NBA-water complexes have been optimized with DFT using the B3LYP functional and the Dunning aug-cc-pVDZ basis set. The large size of this complex prevented the use of multiconfigurational methods. Therefore, the UV-absorption spectra of the two most stable *o*-NBA-water complexes were calculated using the monoconfigurational RI-CC2 method and the TZVP basis set, which have been proven to deliver reliable results in gas phase. Further computational details can be found in the article 3.4.2.

c) Non-reactive NBA isomers: *meta*-Nitrobenzaldehyde (*m*-NBA) and *para*-Nitrobenzaldehyde (*p*-NBA)

The two non-reactive isomers of *o*-NBA: *m*-NBA and *p*-NBA, see Figure 3.4, have Cs symmetry. The planarity in the *m*-NBA isomer allows the rotation of the CHO functional group leading to two possible stereoisomers: one with the hydrogen looking towards the NO_2 group, called *m*-NBA1, and one with the oxygen looking towards the nitro group, called *m*-NBA2. Both stereoisomers are interconnected through the rotation of a C-C single bond, passing *via* a transition state *m*-NBA(TS) at an intermediate angle. On the contrary, the *p*-NBA molecule presents only one stereoisomer.
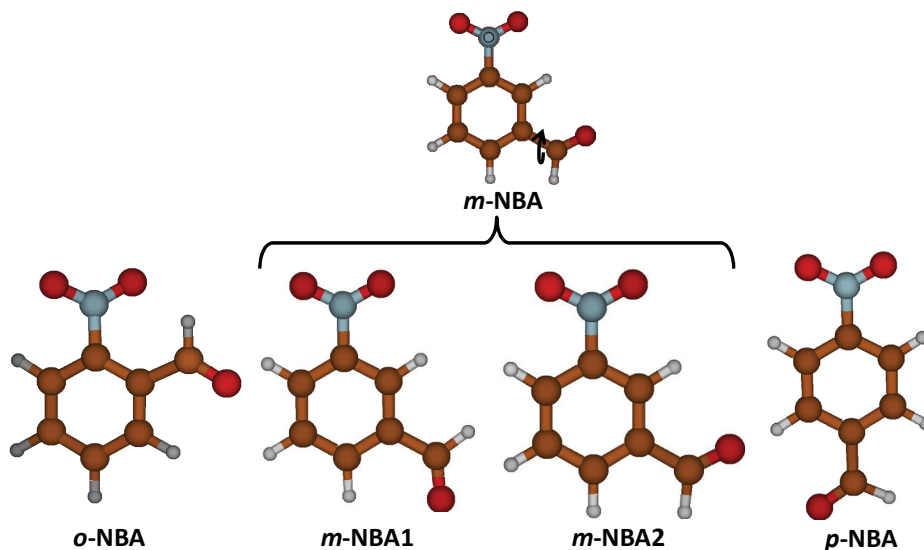
Figure 3.4. The three isomers of the NBA, *o*-NBA, *m*-NBA and *p*-NBA. The isomer *m*-NBA due the rotation of the CHO group can present two stereoisomers, *m*-NBA1 and *m*-NBA2.

The three *o*-NBA isomers, *p*-NBA, *m*-NBA1 and *m*-NBA2, were fully optimized with the B3LYP/6-311G(*d,p*) method. These optimized geometries were used for the calculation of their vertical excited spectrum by means of RI-CC2/TZVP and compared with the results obtained with the MS-CASPT2/CASSCF level of theory. The reference CASSCF wave functions were obtained with two active spaces, the (16,12)AS and the (12,11)AS. For more details concerning the computational methods as well the AS see article 3.4.3 and Appendix A.

3.1.2 Results on the NBA UV-absorption spectra

a) Gas phase: *o*-NBA UV/Vis absorption spectrum

The experimental absorption spectrum of *o*-NBA has been recorded in cyclohexane (a non-polar aprotic solvent) to minimize solute-solvent interactions and allow for a better comparison with the gas phase calculations, see Figure 3.5. The experimental absorption spectrum shows three main bands (black line): a very intense band centered at 220 nm, a less intense shoulder peaking at 250 nm and a very weak absorption at 300nm. For the quantitative analysis of the band positions, solvent shifts, and oscillator strengths, the experimental spectrum was subject of a fitting procedure using a sum of Gaussians as trial functions. It has to be stressed that a Gaussian is only an approximation for the true vibronic envelope of an electronic transition. It may well be that

more than one Gaussian is required for the description of the envelope or that two transitions are described by one Gaussian. Thus, a one to one association between a deconvoluted Gaussian and an electronic transition is sometimes not possible, but the deconvolution facilitates the assignment of the experimental spectrum. In this way, the experimental absorption spectrum was deconvoluted into 6 Gaussians. The lowest in energy band is fitted with two Gaussians, one at 292 and the other at 337 nm, the central band is also fitted with two Gaussians, at 248 and 261 nm, and the third band is decomposed with two Gaussians, at 204 and 225 nm.
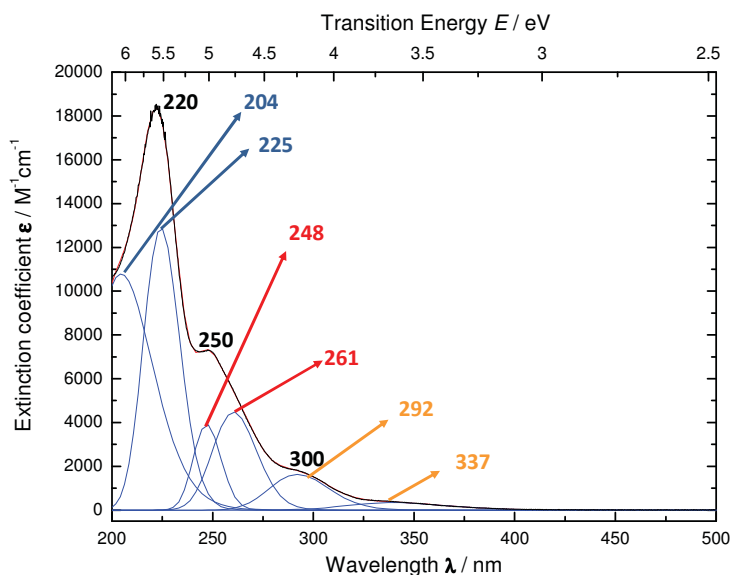

Figure 3.5. Gaussian deconvolution of the experimental absorption spectrum[106] of *o*-NBA. The values in black refer to the center main bands of the spectrum of the *o*-NBA in cyclohexane. Different colors are given to the six Gaussians which deconvolute the experimental absorption spectrum.

A summary of the energies, oscillator strengths (*f*) and main configurations contributing to the lowest-lying excited states calculated at MS-CASPT2/CASSCF/ANO-L level of theory is presented in Table 3.1. In addition, it is presented in this table the spectroscopic state (S_5 in blue), i.e. the state that is experimentally populated upon irradiation at 260 nm, whereby the photoreaction is initiated.

State	Configuration	ΔE (nm)	f
S_1	n → π*	372	0.0026
S_2	n → π*	324	0.0000
S_3	n → π*	319	0.0006
S_4	π → π*	278	0.0147
S_5	P_{NO2} → π* / π → π*	251	0.2269
S_6	P_{NO2} → π*	223	0.0469

n → π*

CT π (benzene) → π* (nitro)

Local
π (NO_2) → π* (NO_2)

▦ (12,11) AS, spectroscopic state

☐ (16,12) AS

Table 3.1. MS-CASPT2//CASSCF/ANO-L transition energies ΔE (nm), configurations and oscillator strength f of the states contributing to the vertical absorption spectrum of o-NBA. CASSCF wave functions were constructed from a (16,12) AS. The reduced (12,11) AS was employed for the description of the S_5 spectroscopic state.

The calculated gas phase absorption spectrum of o-NBA could be mainly divided in two regions. The low-energy region of the spectrum comprised between 372 - 319 nm is characterized by nπ* transitions involving lone pair orbitals of the nitro and CHO group and π* orbitals from the benzene moiety. These states are weakly absorbing. Beyond ~280 nm the gas phase calculated UV-spectrum is characterized by ππ* transitions. In this region charge transfer (CT) π → π* excitations from the benzene moiety towards the NO_2 and CHO groups are present. At higher energies, ca. 250 nm, we find ππ* transitions occurring within the NO_2 group, which attending to Laimgruber et al. oscillator strength[33] correspond to the spectroscopic state.

In view of the above theoretical results the experimental absorption spectrum is assigned as follows, see Figure 3.6. The two first Gaussians peaking at 292 and 337 nm, are assigned to the nπ* excitations and are depicted in orange. The following two Gaussians, at 248 and 261 nm, are assigned to a CT ππ* transition and a local ππ* excitation within the nitro group. This local ππ* excitation corresponds to the spectroscopic state. The last two Gaussians in blue centered at 225 and 204 nm, belong to the high-energy region, and were assigned to local ππ* excitations within the nitro group.
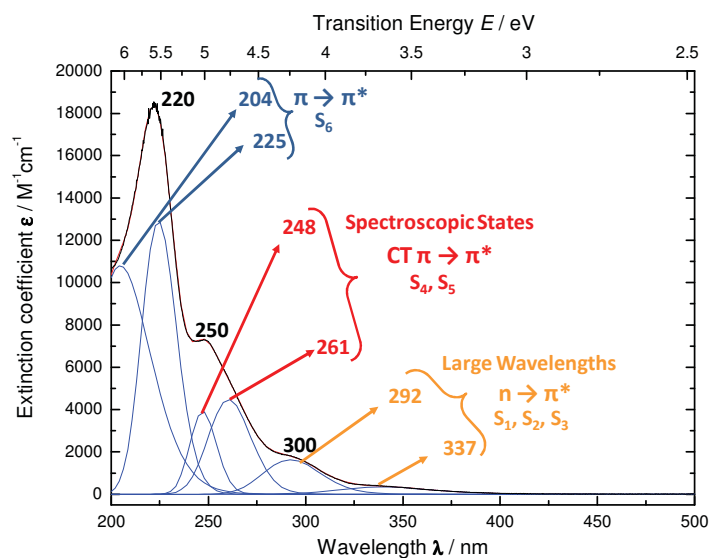
Figure 3.6. Theoretical assignment of *o*-NBA experimental absorption spectrum[106].

From this assignment it can be concluded that at short wavelengths the S_5 state is excited, while large wavelengths populate the S_1 state. Therefore, the mechanism of the H-transfer from both states, i.e. S_5 and S_1, has been investigated, as explained in Section 3.4.

b) Solvent influence on the UV-absorption spectrum of *o*-NBA: UV-absorption spectrum of the 1:1 *o*-NBA-water complex

In this section, we investigate the effect of solvation on the vertical excitation energies of the *o*-NBA. For this, we have taken as a solvatable model the complex formed by the *o*-NBA and one molecule of water. A full description of the results can be found in the publication Z. Phys. Chem. **2008**, *222*, 1263-1278, see article in the section 3.4.2.

As already mentioned, the most stable 1:1 *o*-NBA-H_2O complexes correspond to structures where the water molecule is located around the *o*-NBA. All optimized structures lie within few Kcal/mol above the most stable complex, which we denote as molecule **1**, see Figure 3.7. Thus, all of them are expected to be experimentally accessible. Structural changes and the effect of the water molecule on the intramolecular H-bond of *o*-NBA have been carefully analyzed by means of the topological analysis of the charge density. In general it is found that the strength of the intramolecular H-bond is not much affected upon water complexation, except for two complexes. In the first complex, **6,** H_2O is simultaneously interacting with the hydrogen of the CHO group and the oxygen of the NO_2 group, consequently weakening the intramolecular H-bond. The second complex, **11**, presents the NO_2 group twisted and thus the H-bond is totally broken. For more details see article 3.4.2.

Figure 3.7 shows all the optimized 1:1 *o*-NBA-H$_2$O complexes and their relative energies with respect to complex **1**. Two complexes were chosen for evaluating the effects of solvation on the vertical absorption spectrum. The first is complex **1**, which corresponds to the most stable complex. Complex **4** was selected, even if the molecules **2** and **3** are energetically more stable, since in this complex the water molecule interacts with *o*-NBA through two H-bonds and probably represents a good model for incorporating solvation effects. This effect is not observed in complexes **2** and **3**.
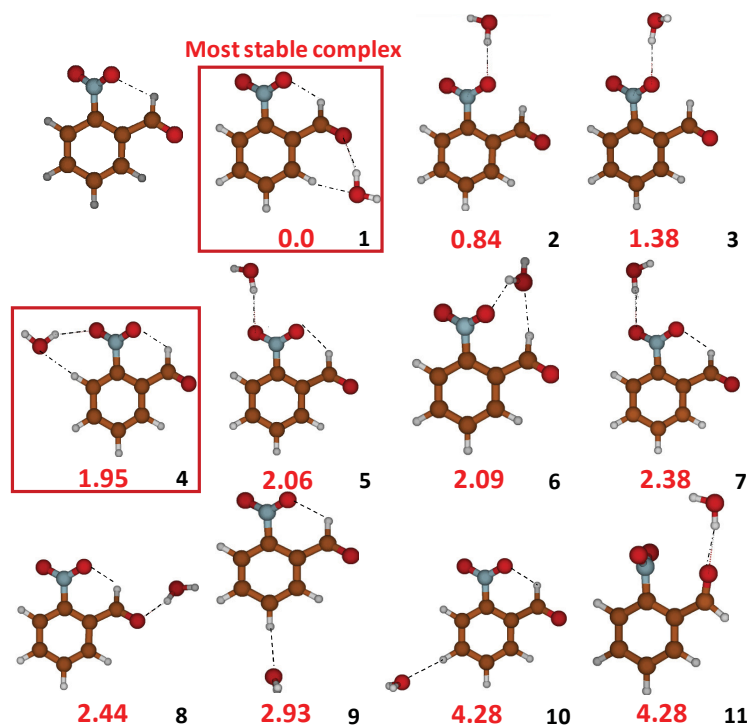

Figure 3.7. B3LYP/aug-cc-pVDZ optimized geometries of the most stable *o*-NBA-H$_2$O complexes. The ΔE (in red) are in Kcal/mol. The molecules inside the red squares are those selected to calculate the vertical excited spectra. The intramolecular H-bond is conserved in all the complexes but **11**.

The influence of a water molecule in the UV-absorption spectrum of *o*-NBA has been examined by comparing the vertical excitation energies and oscillator strengths *f* of the system in gas phase with those of the two complexes, i.e. **1** and **4**, see Table 3.2.

	o-NBA gas phase			Complex1			Complex4			
	Configuration	ΔE (eV)	f	Configuration	ΔE (eV)	f	Configuration	ΔE (eV)	f	
S_1	$n \rightarrow \pi^*$	3.62	0.0117	$n \rightarrow \pi^*$	3.86	0.0067	$n \rightarrow \pi^*$	3.91	0.0078	**n → π***
S_2	$n \rightarrow \pi^*$	4.09	0.0014	$n \rightarrow \pi^*$	4.50	0.0021	$n \rightarrow \pi^*$	4.53	0.0029	
S_3	$n \rightarrow \pi^*$	4.11	0.0038	$n \rightarrow \pi^*$	3.98	0.0018	$n \rightarrow \pi^*$	3.81	0.0025	
S_4	$\pi \rightarrow \pi^*$	4.57	0.0072	$\pi \rightarrow \pi^*$	4.75	0.0184	$\pi \rightarrow \pi^*$	4.75	0.0174	**CTπ(benzene)→π*(nitro,aldehyde)**
S_5	$n \rightarrow \pi^*$	4.95	0.0145	$n \rightarrow \pi^*$	5.64	0.0270	$n \rightarrow \pi^*$	5.29	0.0080	**n → π***
S_6	$\pi \rightarrow \pi^*$	5.30	0.1335	$\pi \rightarrow \pi^*$	5.45	0.1114	$\pi \rightarrow \pi^*$	5.50	0.1355	
S_7	$\pi \rightarrow \pi^*$	5.82	0.0872	$\pi \rightarrow \pi^*$	5.95	0.1575	$\pi \rightarrow \pi^*$	5.96	0.1809	**CTπ(benzene)→π*(nitro,aldehyde)**
S_8	$\pi \rightarrow \pi^*$	6.20	0.1421	$\pi \rightarrow \pi^*$	6.22	0.2609	$\pi \rightarrow \pi^*$	6.21	0.2151	
S_9	$P_{NO2} \rightarrow \pi^*$	6.21	0.2038	$P_{NO2} \rightarrow \pi^*$	6.53	0.1535	$P_{NO2} \rightarrow \pi^*$	6.54	0.2023	**Local π (NO$_2$) → π* (NO$_2$)**

Table 3.2. RI-CC2/TZVP excitation energies ΔE (nm) for **1** and **4** 1:1 *o*-NBA-H$_2$O complexes and the *o*-NBA in gas phase[106]. For all structures, the main configurations composing the wave function and the corresponding oscillator strength *f* are given.

Although shifted to the blue, the CC2 absorption spectra of the two considered complexes is very similar to that calculated for *o*-NBA in the gas phase,[106] see Table 3.2. The spectrum of *o*-NBA in gas phase at MS-CASPT2 level of theory consists of three bands, recall Figure 3.5 and article 3.4.2, which can also be distinguished in the 1:1 *o*-NBA-water complexes. The major changes on going from gas to condensed phase refer to the order in which the excited states appear within each band but not to the band composition. In particular the states S_4 and S_5, see Table 3.2, are switched in comparison with the MS-CASPT2 assignment, recall Figure 3.5. Besides the blue-shift, a change in the intensities of the three bands is observed upon the inclusion of solvent-solute effect. According to the CC2 calculations, the first and third bands maintain their respective intensities with respect to the gas phase spectrum, while the central one increases the intensity in water solution.

c) *o*-NBA Non-reactive isomers UV-absorption spectra in the gas phase

In addition to the previous studies, we have considered also interesting to study the influence of the relative position of the two substituents of the aromatic ring in the absorption spectrum of nitrobenzaldehyde. For this, we have compared the absorption spectrum of *o*-NBA with that of its two positional isomers, *p*-NBA and *m*-NBA. The gas-phase UV-spectra of these molecules have been also recorded by Gilch and co-workers.[38] The results in full detail are contained in the publication Phys. Chem. Chem. Phys. **2011**, *13*, 4269-4278.

At the B3LYP/6-311G(*d*,*p*) level of theory, the two stereoisomers of *m*-NBA are almost energetically degenerated, see Figure 3.8, being *m*-NBA1 just 0.53 Kcal/mol more stable than *m*-NBA2. The size of the energetic barrier separating the two isomers, i.e. 8.84 Kcal/mol, see Figure 3.8, reveals that at room temperature both isomers are accessible and will contribute to the absorption spectrum.
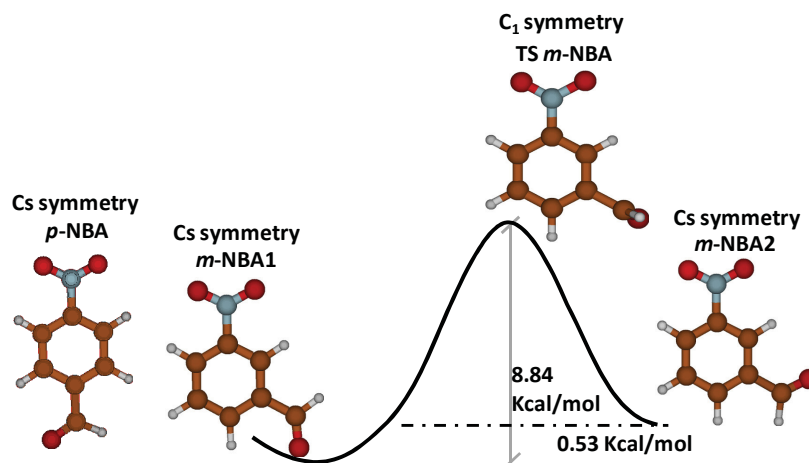
Figure 3.8. B3LYP/6-311G(*d*,*p*) fully optimized geometries of the NBA isomers, *p*-NBA, *m*-NBA1, *m*-NBA2 and the TS between the two *m*-NBA stereoisomers. The TS of the *m*-NBA lies 8.84 Kcal/mol above *m*-NBA1.

As for *o*-NBA experimental absorption spectrum, the spectra of *m*-NBA and *p*-NBA isomers was deconvoluted in 6 Gaussians to simplify the assignment of the most important bands. Further deconvolutions, with a larger number of Gaussians have also been performed in order to assign the experiment. These deconvolutions are provided in the article 3.4.3 which is part of this thesis. Nevertheless, for the sake of simplicity only 6 Gaussians were considered for the theoretical assignment of the spectrum.

The assignment of *m*-NBA and *p*-NBA experimental absorption spectra recorded by Prof. Gilch et al. is shown in Figure 3.9. The vertical absorption spectra of both *o*-NBA isomers, *m*-NBA and *p*-NBA, also present three main bands, see Figure 3.9. In the case of the *m*-NBA spectrum, in which the two stereoisomers contribute to its characterization, the highest energy band was fitted to Gaussians at 225 and 248 nm. Al lower energies, the shoulder, also seen in the *o*-NBA spectrum, and was decomposed to Gaussians at 248 and 257 nm. Finally, the weak band at low-energies was fitted to two Gaussians: at 286 and 334 nm. For the *p*-NBA absorption spectrum, the three main bands were fitted to six Gaussians, as in the *o*-NBA and *m*-NBA isomers. Namely, the first band was fitted into Gaussians at 299 and 334 nm, the second band into Gaussians at 261 and 243 nm, and the third, most intense, band into Gaussians at 194 and 214 nm.

Similarly to the case of *o*-NBA, the two ASs (16,12) and (12,11) were considered for the theoretical prediction of *m*-NBA and *p*-NBA spectra.
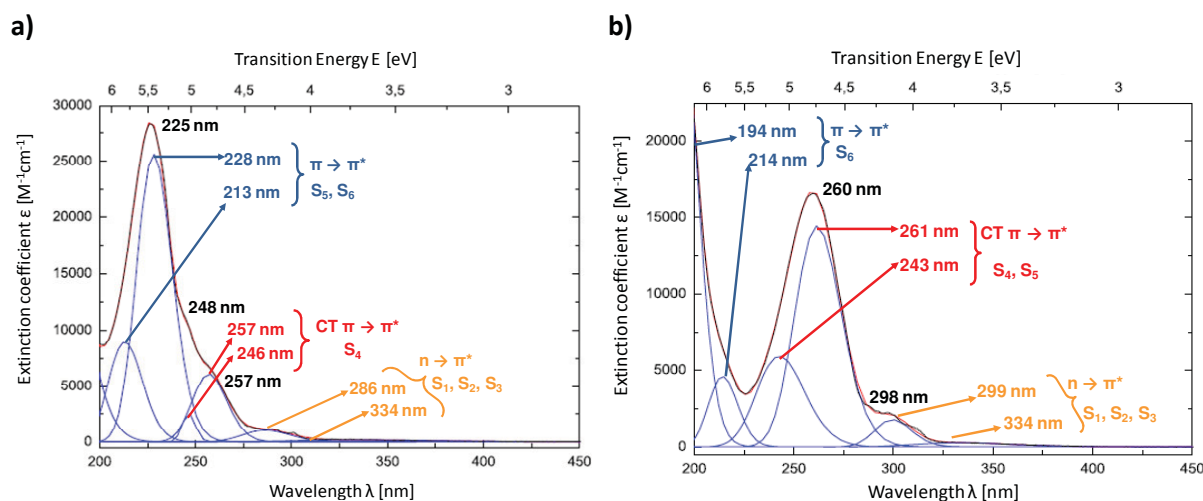
Figure 3.9. Gaussian deconvolution of the experimental absorption spectra of a) *m*-NBA and b) *p*-NBA. The values in black refer to the center of the main band of the experimental absorption spectrum and different colors are given to the six deconvoluted Gaussians.

From the performed calculations it can be deduced that the three isomers, *m*-NBA1, *m*-NBA2 and *p*-NBA, show analogous spectra. In all the cases the region around 300 nm is composed of n → π* transitions from the lone pairs of the nitro and the aldehyde group, to the π* orbitals of the nitro and aldehyde group. In the region ca. 250 nm local π → π* excitations within the arene and the nitro group are present. Finally, in the region at ~220 nm, π → π* transitions from the nitro group occur. Charge transfer π → π* excitations from the benzene to the nitro group, also take place in this region of the spectrum.

The spectra of the three isomers exhibit many commonalities, such as three main bands, in which transitions around 350 nm arise from nπ* absorptions. These are followed by a band of intermediate intensity peaking around 300 nm, that is dominated by ππ* excitations and finally, strong absorptions, at ca. 250 nm, ascribed as local ππ* excitations within the nitro group occur. Nevertheless, a comparison with the *o*-NBA spectrum in gas phase reveals that in the case of the *m*-NBA the band highest in energy is slightly shifted to red. Yet the two bands that follow this band, i.e. the shoulder and the lowest in energy band, are shifted to blue. For the *p*-NBA the high energy band and the low energy band experience a shift to the blue, the center band, on the contrary to the *m*-NBA has a shift to the red. These shifts in the spectra have been attributed to possible solvatochromic effects, i.e. the *p*-NBA isomer interacts more with the solvent, and thereby shifts to higher energies are present in the most intense band; for more details see article 3.4.3.

Despite these similarities, the three systems cannot undergo the same photoreaction, i.e. H-transfer, since *p*-NBA and *m*-NBA do not possess a H-bond. Interestingly, the three isomers show similar transient times in the experiment performed by Gilch and coworkers.[107] In the following section, we are concerned in describing the reaction path that connects the FC geometry to the nitrosobenzoic acid photoproduct, a process that takes place through a ketene intermediate.[33] To this aim, a two-step procedure has been undertaken: **a)** We have performed QC calculations, using the MS-CASPT2/CASSCF approach, with the purpose of scanning relevant regions of the global Potential Energy Surface (PES); results are given in the section 3.2. **b)** We have carried out MQCD calculations to obtain time-resolved mechanistic information, and this is shown in the section 3.3.

3.2 QC Static picture of the reaction path from the excited *o*-NBA to the main ketene intermediate in gas phase

Recent femtosecond UV/Vis experiments[33,35,36] have provided important clues on the H-transfer mechanism of *o*-NBA. Transient UV/Vis spectra recorded at low 388 nm and high 258 nm excitation energies are plotted in Figure 3.10. Upon 388 nm excitation (black line Figure 3.10) the low-lying excited states of nπ* character should be populated. The transient spectrum reveals the formation of the ketene in few hundreds of femtoseconds. The absorption decays in ca. 1 ns since it evolves to the nitroso product. Upon 258 nm excitation, the state populated should be the S_5. The transient spectrum at this wavelength shows an additional peak at time zero which decays at 100 fs. This peak can be ascribed to the absorption of an intermediate minimum. Also, in this case the ketene absorption decays in 1 ns which indicates the formation of the nitroso product.
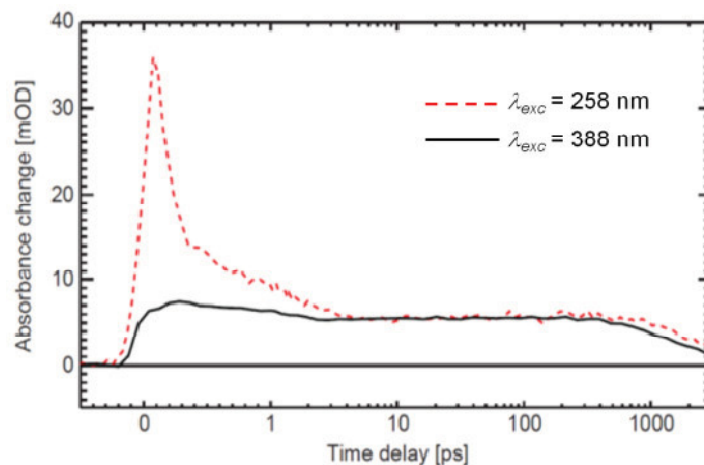
Figure 3.10. Femtosecond UV/Vis absorption spectra of *o*-NBA. The ketene is detected after irradiation at 388 nm (black solid line) and ∼260 nm (red dotted line) excitation wavelengths. The time axis is linear until 1 ps and logarithmic thereafter.

The quantum yield at both wavelengths is of 0.5, this suggests that the same H-transfer mechanism takes place at 388 and 260 nm excitations. Moreover, this is confirmed with the similarity between the transient spectra at both wavelengths.

From the QC point of view, different photoreactive mechanisms have been considered: The first one, a non-Kasha path, considers the relaxation of the S_5 spectroscopic state to the S_0 through a series of CI along which the hydrogen is progressively transferred. In the second path, the Kasha path, the excited *o*-NBA relaxes non-radiatively to the S_1 potential from where the H-transfer takes place. A detailed explanation of both pathways is given below.

3.2.1 Computational details

The energy paths connecting the S_5 spectroscopic state and the ketene transient were traced with the help of intrinsic reaction coordinates (IRC) and linear interpolation internal coordinates (LIIC) calculations, which allow the location of the critical points along the H-transfer mechanism.[iv] Stationary points in both paths, non-Kasha and Kasha, were subsequently optimized making use of different AS and roots by means of the CASSCF/6-31G* protocol. For a detail description see Appendix A and article 3.4.4. Final relative electronic energies, used to construct the energy profiles, were calculated at MS-CASPT2/CASSCF(16,13) with 14 roots for the non-Kasha path and

---

[iv] A description of the IRC and LIIC calculations can been found in the chapter of methods, section 2.4.9.

MS-CASPT2//CASSCF(16,13) with 5 roots for the Kasha path. Further details are in article 3.4.4 and Appendix A.

3.2.2 Results of the statical picture

a) Deactivation from the S_5 excited state

As already mentioned, the S_5 excited state at the FC involves local $\pi\pi^*$ transitions within the nitro group. From this state, at 4.5 eV at MS-CASPT2 level of theory, the molecule relaxes through the $(S_5/S_4)_X$ CI (at 4.0 eV), see Figure 3.11. This CI corresponds to the crossing of the $\pi\pi^*$ spectroscopic state and the FC S_4 state, also of $\pi\pi^*$ character. At this CI, *o*-NBA is characterized by stretched N-O distances and smaller C-N and C-O bonds. Also importantly, the NO_2 group folds perpendicular to the aromatic ring compared to the FC structure. From this point of the PES the system reaches the $(S_4/S_3)_X$ CI (at 3.9 eV). This crossing point is the result of the intersection between the $\pi\pi^*$ FC spectroscopic state and the $n\pi^*$ FC S_3 state. The proximity in the PES of these two CIs explains the very similar geometries of the two structures. The minimum relaxation pathway from this CI leads to a planar minimum on S_3, named $(\pi\pi^*)_{Min}$ (at 3.8 eV), see Figure 3.11. This minimum conserves the character of the spectroscopic state, i.e. $\pi\pi^*$ excitations within the nitro group. We assume that trapping at this minimum leads to the peak observed in the experimental transient absorption spectrum upon 260 nm irradiation, recall Figure 3.10.
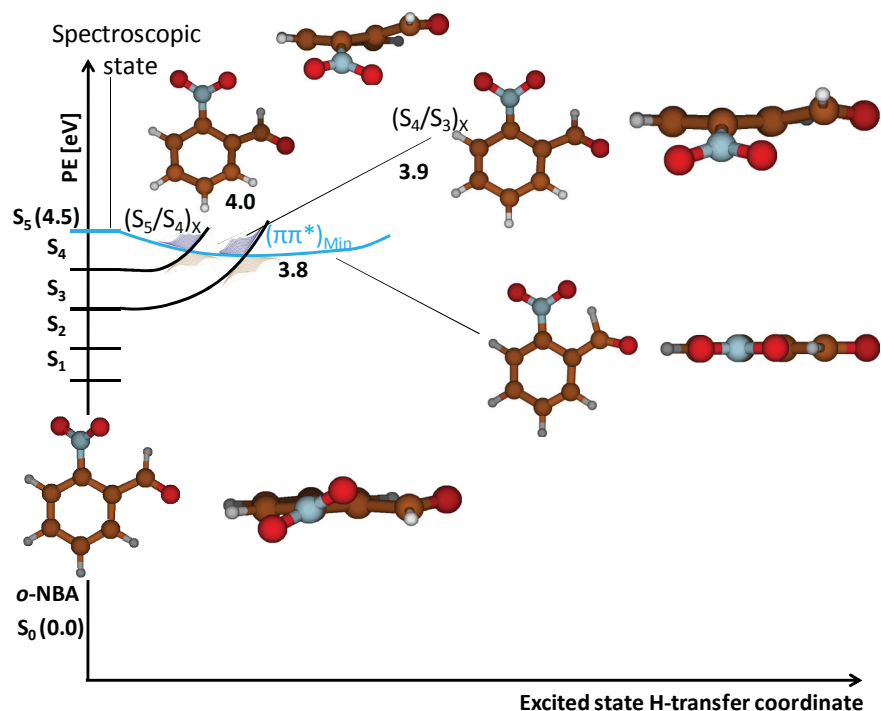
Figure 3.11. Potential energy profile for the deactivation from the spectroscopic S_5 state to the S_3 $\pi\pi^*$ minimum upon high-energy excitations, i.e. 260 nm[33,36,38], calculated at MS-CASPT2/CASSCF(16,13) level of theory. The blue line represents the minimum relaxation pathway.

From the minimum at S_3 potential, two possibilities of complete relaxation to the GS of the system have been explored: In the first one, from the S_3 minimum the system relaxes and simultaneously transfers the hydrogen from the CHO to the NO_2 group. This occurs through a cascade of CIs until the ketene intermediate is reached, see subsection **b**. The second path, involves an internal conversion to the S_1 minimum, $(n\pi^*)_{Min}$, followed by H-transfer, see subsections **c** and **d**.

b) The non-Kasha reactive path from the S_3

From the geometry of the different stationary points located along this path we can infer that the H-transfer is initiated after deactivation from the S_3 minimum. Before deactivation, the system needs to overcome an energy barrier of 0.8 eV to access the ketene state which corresponds to the crossing of the former state and the $\pi\pi^*$ spectroscopic state, see Figure 3.12. The minimum energy path from this point leads to the $(S_3/S_2)_X$ CI (at 3.6 eV). At the $(S_3/S_2)_X$ CI the hydrogen that is going to be transferred, lies already halfway between the CHO and the NO_2 groups. In order for the latter conformational changes occur the NO_2 and CHO groups must approach the aromatic plane of the *o*-NBA. The system further relaxes to the GS *via* the $(S_2/S_1)_X$ CI (at 3.4 eV) in which the hydrogen is completely transferred to the NO_2 group. This intersection point corresponds to the

crossing of the ketene state and the ground state. When the H-O bond is consolidated at the $(S_2/S_1)_X$ CI, the C=C=O angle of the aldehyde group will evolve towards 180° gaining the ketene form. Therefore, the three consecutive CIs, $(S_3/S_2)_X$, $(S_2/S_1)_X$ and $(S_1/S_0)_{X-Ket}$, lie along the H-transfer coordinate, red line Figure 3.12, which allows the decay to the GS and the formation to the ketene. The down-hill shape of the potential at these points favors the transformation of the *syn*-ketene (at 1.7 eV) which evolves to the more stable *anti*-ketene (at 1.0 eV), where simultaneous rotation of the OH group and the linearization of the OCC fragment take place.
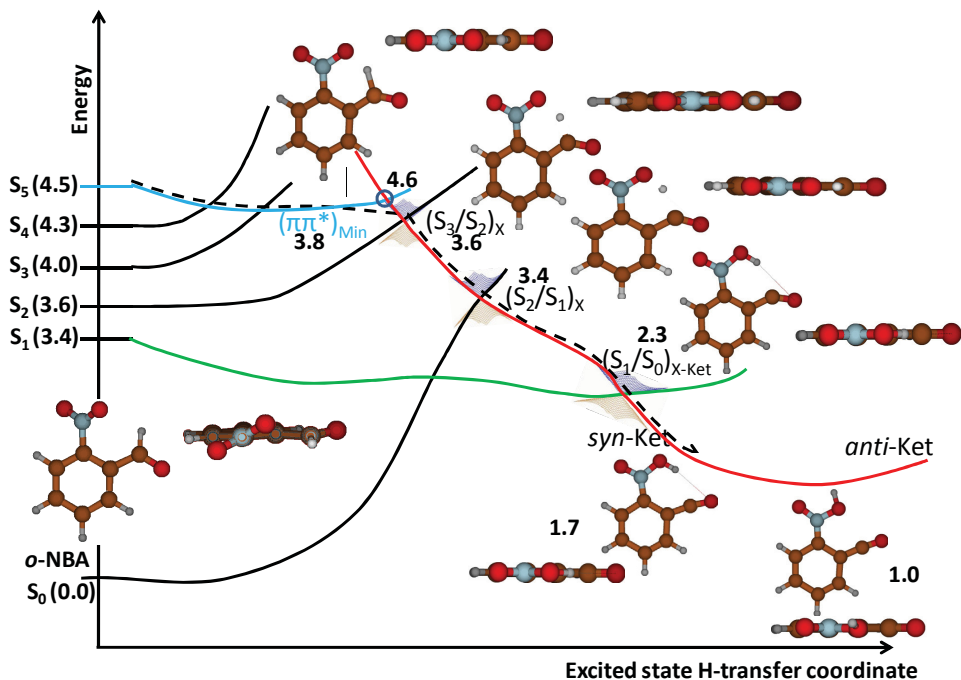

Figure 3.12. Non-Kasha potential energy profile, at MS-CASPT2/CASSCF(16,13) level of theory, for the relaxation from the minimum at the S_3 potential populated after high excitation energies.

c) Internal conversion from the S_3 minimum to the S_1 excited state, the Kasha path

Within this section only CASSCF energies are presented. This is because to obtain MS-CASPT2 energies turned out to be especially computational demanding due to the large number of excited states and the big AS.

Starting from the S_3 minimum, of 5.0 eV at CASSCF(16,13), a barrier of 0.43 eV level of theory has to be overcome in order to access the non-radiative deactivation funnel $(S_3/S_2)_{X-K}$ CI (at 5.4 eV), see Figure 3.13. Similarly to $(S_5/S_4)_X$ CI this intersection point involves the crossing of the $\pi\pi^*$ spectroscopic state with the S_2 FC state, of $n\pi^*$ character. For accessing this CI, the system needs

to undergo a planarization of its two functional groups, which form dihedrals of 171° (NO_2) and 5° (CHO) with respect to the aromatic moiety. Along the MEP, the system reaches a second CI, also with $n\pi^*/\pi\pi^*$ character, the $(S_2/S_1)_{X-K}$ CI. Curiously, this CI requires the folding of the NO_2 group, which is now located almost perpendicularly to the arene. The steepest descent reaction pathway from this intersection point leads directly to the minimum characterized by a $n\pi^*$ character in the S_1 potential $(n\pi^*)_{Min}$, in which the H-transfer takes place. An examination of the structure of these CIs reveals that the H-transfer does not yet take place, since the hydrogen remains attached to the carbonyl group in all cases. It is important to stress that the $(S_3/S_2)_{X-K}$ and $(S_2/S_1)_{X-K}$ CIs, belonging to the Kasha path, differ from the $(S_3/S_2)_X$ and $(S_2/S_1)_X$ CIs at the non-Kasha path, see subsection **b**, in the configuration of the wave function. While in the non-Kasha path a configuration $n\pi^*$ involving the ketene is present, in the Kasha path the $\pi\pi^*$ spectroscopic character is maintained.
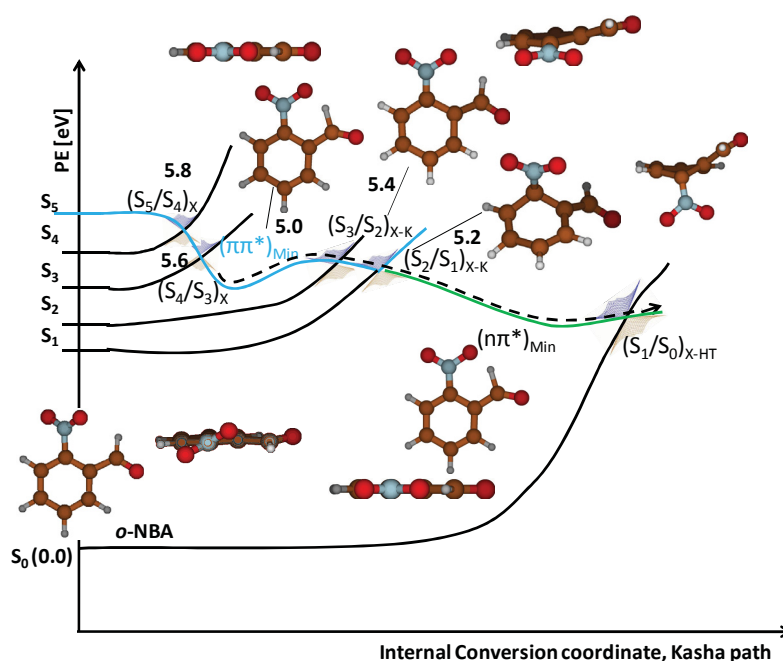

Figure 3.13. Kasha potential energy profile, at CASSCF(16,13) level of theory, for high-energy excitations, i.e. 260 nm[33,36,38].

For either pathway, the non-Kasha or the Kasha, the molecule requires planarization in order to transfer the hydrogen. This planarization can be completed either at high-energy, i.e. at the non-Kasha path, or at low-energy, i.e. at the Kasha path.

d) H-transfer from the S₁ excited state

Once the population has been transferred to the S_1 minimum, H-transfer takes place. This is the mechanism operating upon irradiation at 388 nm, where a low-lying $n\pi^*$ S_1 state is populated. QC calculations predict a swallow minimum in the S_1 potential. An energy barrier of less than 0.1 eV separates this minimum from the $(S_1/S_0)_{X-HT}$ crossing, at 1.8 eV at MS-CASPT2/CASSCF(16,13), see Figure 3.14. Similarly to the $(S_3/S_2)_X$ CI in the non-Kasha path, the $(S_1/S_0)_{X-HT}$ presents a geometry with the H-atom lying halfway between the carbon of the CHO group and the oxygen of the NO_2 group. The $(S_1/S_0)_{X-HT}$ crossing, bifurcates the population between the FC ground state minimum and the biradical (BIR) transient, consistent with a backward and a forward reaction giving an specific quantum yield. The BIR, which has a bent C=C=O group, is separated from the final product, the *anti*-ketene, by an almost barrierless path of less than 0.5 eV. This low-energy barrier in the S_0, that the system needs to surmounts to reach the *anti*-ketene, leads to the $(S_1/S_0)_{X-Ket}$ CI of the non-Kasha path. The *anti*-ketene tautomer, which corresponds to the most stable product along the path, is characterized by the newly formed O-H bond pointing away from the C=C=O group. These changes in the conformation of the molecule give stability, and thus the *anti*-ketene is the final product.
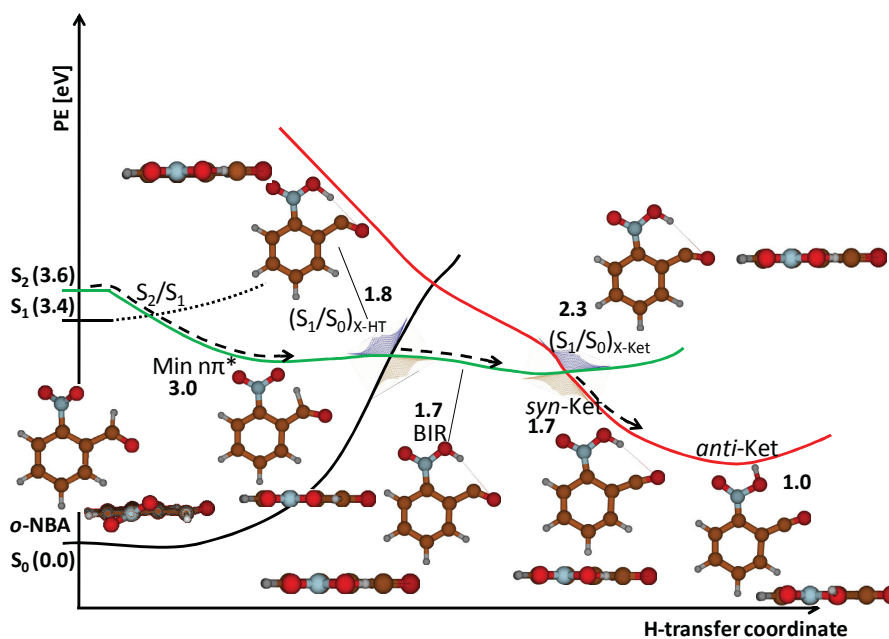

Figure 3.14. Potential energy profile, at MS-CASPT2/CASSCF(16,13) level of theory, for the deactivation from the S_1 minimum accessed after irradiation at 388 nm[38] or from a cascade of CIs along the Kasha deactivation pathway. The green line represents the H-transfer path at the low-energy region of the excited *o*-NBA relaxation mechanism.

From a thermodynamic point of view, considering the QC calculation and the experimental transient absorption spectra, the most probable mechanism for the H-transfer is the Kasha path. This is because a weakly fluorescent $n\pi^*$ state after the decay of the $\pi\pi^*$ state has been found.[38] In order to have a decisive understanding of the chemical process at molecular level, however, it is imperative to gain some information about the natural dynamics of the system. With this aim, an MQCD study of the deactivation from the spectroscopic S_5 state and from the low-energy S_1 state has been performed and is described in the following section. The results of the non-Kasha path and concomitant H-transfer on the S_1 potential are contained in the publication Chem. Comm. **2011**, *47*, 6383-6385, see article 3.4.4.

3.3   A time-resolved MQCD picture

As a final step, in order to obtain a complete description of the H-transfer mechanism in the *o*-NBA, non-adiabatic dynamic simulations using the TD-DFT method, from the S_5 (see sections 3.3.1a and 3.3.2a), and CASSCF method, from the S_1 (see sections 3.3.1b and 3.3.2b), are presented.

3.3.1 Computational details

MQCD simulations were employed to simulate the electronic deactivation of *o*-NBA from higher lying excited states and S_1 electronic excited states, populated by experimental irradiation at 260 and 388 nm, respectively. Within this approach, nuclei motion is treated classically following the Newton's equations which are solved numerically using the Velocity Verlet algorithm with a time step of 0.5 fs. The electrons are followed quantum mechanically solving the TDSE. The electronic energy gradients, required to describe nuclear motion, and non adiabatic couplings were obtained using the TD-DFT or the *ab initio* CASSCF(10,8)/6-31G* method, depending whether the simulation were started from the S_5 or S_1 excited state, respectively.

Due to the presence of non-adiabatic couplings between the electronic states, the surface hopping method according to Tully`s fewest switches algorithm was used. The experimental deactivation time upon excitation at 260 nm is of ca. 100fs,[33,35,38] hence the dynamics simulations were propagated for a maximum of 500 fs. The deactivation upon excitation at 388 nm was also found to be ultrafast and therefore dynamics simulations were run for about ca. 60 fs. For a thorough comprehension of the methods used in this section, see Ref. 89.

a) MQCD simulations upon 260 nm wavelength

Here, the TD-DFT method was employed for the on-the-fly electronic structure calculations due to **b)** the large number of excited states that need to be simultaneously described, **a)** the limitations connected to the current sizes employed in this type of MQCD simulations, and the impossibility to employ a small AS which can describe all the states and critical points simultaneously; and **c)** the huge computational cost that would imply the use of multireference methods, such as CASSCF, in this particular situation.

Initial conditions for 200 trajectories were generated, considering a Wigner distribution for the ground state harmonic oscillator at 0K, calculated at the B3LYP/def-TZVP level of theory. Excitation energies and oscillator strengths were computed for each initial condition. The absorption spectrum of *o*-NBA in the 4.47 – 5.07 eV energy range was simulated from the superposition of all the transitions, convoluted with Lorentzian line shape functions. In order to ensure a realistic simulation of the experiment, a 0.5 eV wide "excitation energy window" centered at the experimental irradiation energy of 260 eV was considered. Within this window, a total of 129 trajectories were selected according to their probability in the spectrum. The choice of these initial conditions was performed according to a stochastic algorithm.

b) MQCD simulations from the S$_1$ state

Multireference methods, such as MR-CI or CASPT2/CASSCF, are ideally preferred for excited state calculations, since they are able to deal with near degeneracy situations including dynamical correlation. Unfortunately, analytic gradients for the above methods are not always available in standard *ab initio* packages. For this reason, we have chosen the CASSCF level of theory for this dynamic simulation. Nevertheless, a previous assessment of the quality of the CASSCF potential energy profile has been performed taking as benchmark MS-CASPT2 calculations.

Initial conditions of the geometries and velocities for 200 trajectories were generated with a Wigner distribution of the ground state. The harmonic frequencies were obtained at the B3LYP/TZVP level of theory.

3.3.2 Results of the dynamics simulations

In this section, we aim at providing a time-dependent picture of the deactivation mechanism for *o*-NBA molecules excited at 60 nm (subsection **a**) and for those molecules excited with 388 nm

wavelengths or reaching the S_1 potential after deactivation from higher lying excited states populated with 260 nm wavelengths following the Kasha path (subsection **b**).

a) MQCD simulations for excited *o*-NBA at 260 nm

The MQCD simulated vertical excited spectrum of *o*-NBA at B3LYP/def-TZVP level of theory is presented in Figure 3.15. The spectrum of *o*-NBA, red line, is generated by the convolution of the nine lowest-lying excited states. Similarly to the experimental absorption spectrum, recall Figure 3.6, three bands can be distinguished. The most intense band, **A**, centered at ca. 5.25 eV, arises from the TD-DFT, S_9, S_8 and S_7 excited states. The S_7, S_6 and S_5 states contribute to the less intense central shoulder, **B**, centered at ca. 4.75 eV. Finally, the first four TD-DFT excited states contribute to the lowest in energy weak absorption tail, **C**, located at 3.5 eV.
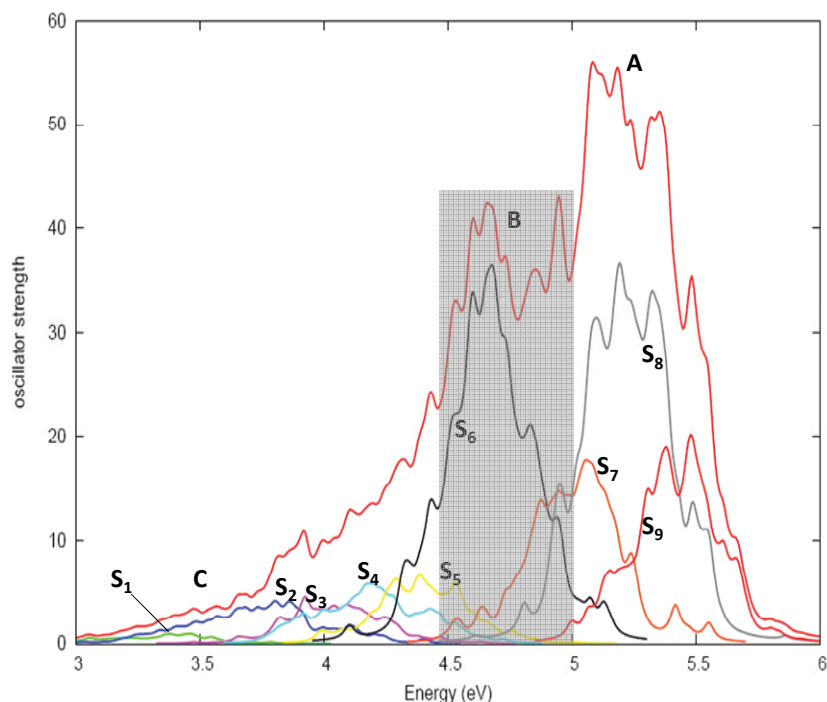

Figure 3.15. Simulated UV-vertical spectrum at TD-B3LYP level of theory. The red line denotes the global spectrum convoluted from nine lowest lying excited states. The grey square marks the energy window chosen to simulate the experiments.

In order to theoretically simulate the natural dynamics of *o*-NBA upon excitations at ~260 nm, the set of 129 trajectories comprised in the energy window, from 4.47 to 5.07 eV (grey square in Figure 3.15), were launched. According to Figure 3.15, the excited states contributing to a larger extent to this region of the spectrum are the S_6 (black line), followed by S_7 (orange line) and S_5 (yellow line) states. At this point it is worth noting that at the FC structure and below 5 eV, TD-DFT

65

predicts one additional transition not present in MS-CASPT2 spectrum, which corresponds to a $n\pi^*$ excitation. Assuming a similar state ordering as in FC, we can assign the TD-DFT S_6 state to the $\pi\pi^*$ spectroscopic state, S_5 at MS-CASPT2 level of theory, allowing a direct comparison with the quantum chemical results, reported in the previous section.

In order to facilitate the time evolution analysis of the o-NBA deactivation from the S_9 to the S_3 state, the total population of the S_0-S_9 states for the 129 trajectories considered was normalized to 1. A careful examination of Figure 3.16 allows the clear identification of hopping time intervals. For instance, in the time range comprised from 5 to 20 fs, square **A** in Figure 3.16, we observe a decrease in the population of the S_6 state coupled to an increase of the population of the S_5 that can be directly ascribed to the system exploring regions of the PES close to the S_6/S_5 CI (S_5/S_4 CI at MS-CASPT2/CASSCF level of theory). After 20 fs the population of the S_5 begins to diminish while that of the S_4 state (pink line) increases, **C** in Figure 3.16. This change of the relative populations is indicative of the $S_5 \rightarrow S_4$ ($S_4 \rightarrow S_3$ at MS-CASPT2/CASSCF) non-radiative decay.
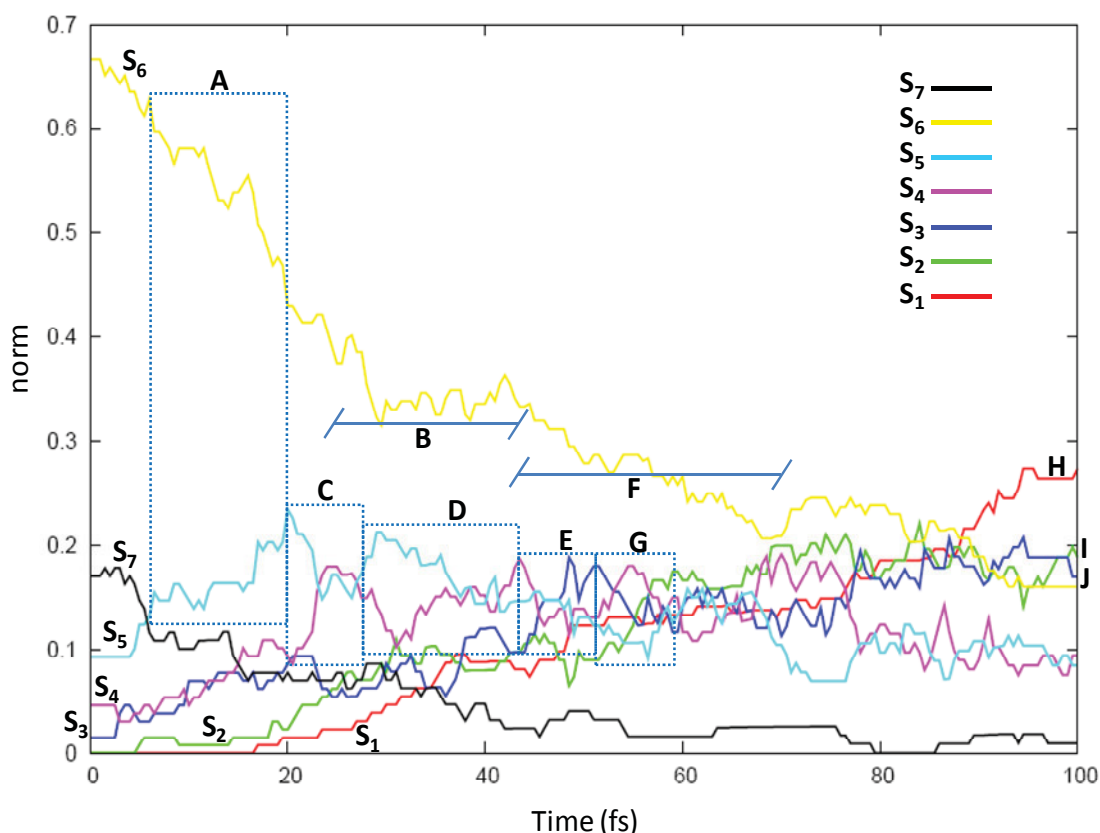

Figure 3.16. Time evolution of the average population of the S_1-S_9 states for the 129 trajectories selected from the energy window comprised between 4.47 to 5.07 eV. Because internal conversion to S_0 was not computed, the population of S_1 can be considered as the sum of S_1 and S_0 states.

Then, an inversion of the population between the S_5 and S_4 states takes place, square **D** in Figure 3.16, which is in perfect agreement with the picture provided by quantum chemical methods which predict the presence of a minimum in the S_4 potential (S_3 at MS-CASPT2/CASSCF) and a very flat potential profile along the minimum energy path, recall Figure 3.11. Around 43 fs, the population of the S_3 starts to increase while the population of S_4 and S_5 states shows a slight decrease. This can be attributed to the deactivation *via* the S_4/S_3 funnel, square **E**.

Besides the small swaps in the population of the S_5–S_1 states, from 40 to 70 fs, see **F** in Figure 3.16, the average population of these states remains almost constant in this time interval. Beyond 70 fs the population of the S_3, S_2 and S_1 states starts to increase, reaching at 100 fs a population of ~18, ~20 and ~27% respectively, see **H**, **I** and **J** in Figure 3.16.

In order to characterize the geometry of the deactivation funnels and compare it to that of the quantum chemically predicted CI at CASSCF/6-31G* level of theory, the geometries at the time of the hop were averaged for all the trajectories, see Figure 3.17. For doing this comparison, two important issues need to be taken into account: **a)** the hopping does not necessarily take place at the minimum energy crossing geometry, and **b)** once the system planarizes in the first steps to the deactivation, the distortion of the dihedral angel of the NO_2 group relative to the aromatic ring can take place in both directions, i.e. above or below the ring plane, this results in an average dihedral angle of ca. 180° which is not comparable with the value obtained with QC calculations. For this reason, a direct comparison of average geometries from MQCD simulations and the QC CI geometries is not possible, and only general features will be compared in the following. Similar to the QC description of the Kasha path, the two consecutive TD-DFT S_6/S_5 and S_5/S_4 CIs (S_5/S_4 and S_4/S_3 CI at MS-CASPT2/CASSCF level) conical intersections present very similar distortions of the system, involving the stretching of the N-O bond *cis* to the aldehyde and the reinforcement of the C-N and C-C(HO) bonds (C-N= 1.482 Å and C-C(HO)=1.504 Å at B3LYP/6-311G** level of theory). From the superposition of the geometries at the time of the hop, it is possible to observe that certain trajectories show a slightly bent NO_2 moiety at the time of the hop in agreement with QC predicted structures. Also in agreement with CASSCF CIs, TD-DFT S_4/S_3 and S_2/S_1 (S_3/S_2 and S_2/S_1 at MS-CASPT2/CASSCF level of theory) hopping geometries show a reinforcement of the two N-O bond lengths. In the case of TD-DFT S_3/S_2 CI, the percentage of molecules visiting regions of the PES where the NO_2 folds is also significant, in perfect agreement with the CASSCF picture.

Besides the difference of distances in the intramolecular H-bond between MQCD average geometry and the QC CASSCF optimized geometry, it is observed that the H-bond is never transferred along these CIs. This indicates the preference of the Kasha path in the deactivation mechanism of the *o*-NBA.
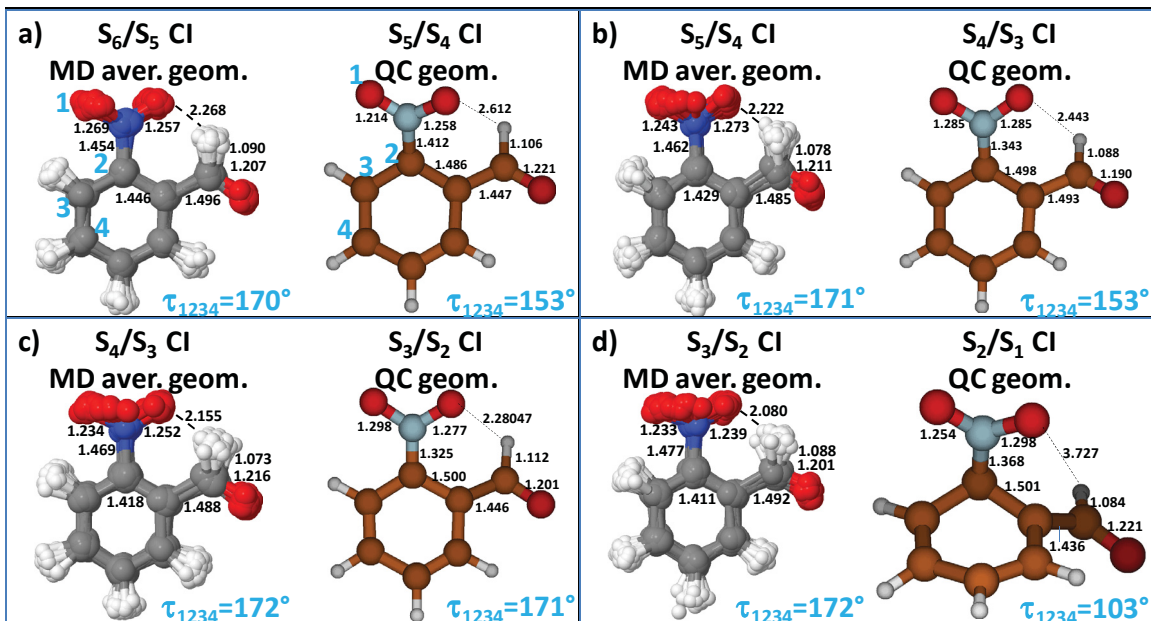
Figure 3.17. Average geometry at the time of the hop for all non radiative funnels involved in the deactivation from the S6 to the S_1 state. The average geometries are compared with the optimized structures at CASSCF/6-31G* level of theory.

In the following, two exemplary trajectories started from the S_7 and S_6 excited states, contributing in the largest extent to the energy window selected to simulate the experiment, are discussed in more detail. Both trajectories end in the S_1 state, see Figure 3.18, where QC methods predict the H-transfer to occur. Due to the method employed to compute derivative coupling terms (TD-DFT), it is not possible to describe $S_1 \rightarrow S_0$ deactivation. Deactivation from the S_1 potential, has been instead theoretically described using MQCD simulations and the CASSCF method for electronic structure calculations, see section 3.3.2b. The examination of Figure 3.18 **a)** and **b)** reveals that both trajectories share some features along their deactivation pathways.

A common signature to both trajectories is the presence of recrossings between the TD-DFT S_6 (light pink), S_5 (orange) and S_4 (blue-green) states, which point out the flatness of the potential energy surface in this region in perfect agreement with QC calculations. Worth to note is also the time spent by the system (ca. 30 fs) in both trajectories in the potential S_4, which is in consistent with the prediction of a minimum in this potential by multiconfigurational methods (S_3 at MS-CASPT2/CASSCF). Once in the S_3 potential, the system deactivates very quickly to the S_2 and from there to the S_1 indicating the proximity of both deactivation funnels also in agreement with quantum chemical predictions. Deactivation to the S_1 excited state is achieved in about 100 fs.
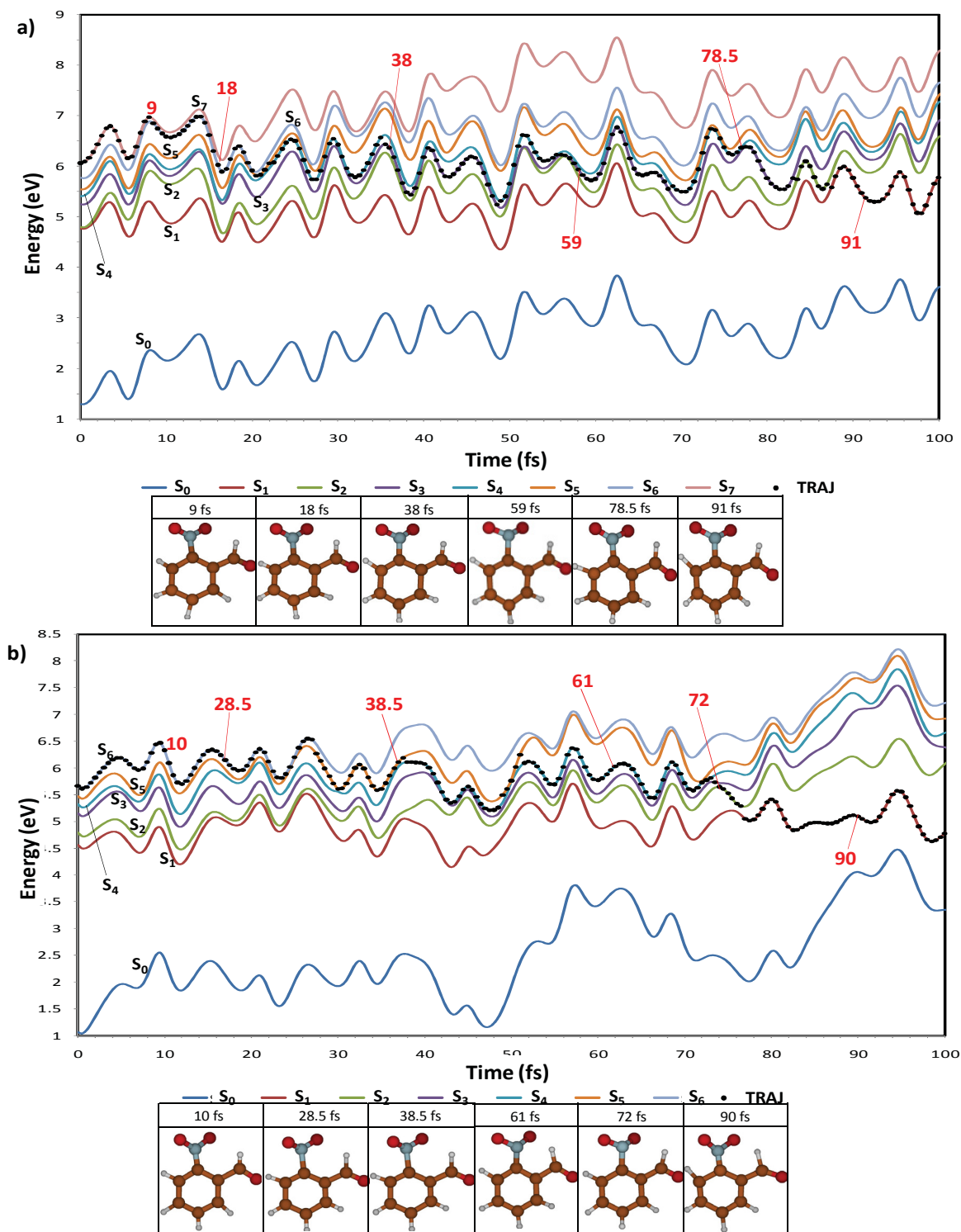
Figure 3.18. Time evolution of the S_7-S_0 potential energies and corresponding snapshots at selected times, as indicated. **a)** Trajectory corresponding to the deactivation of *o*-NBA from the S_7 to the S_1 potential. **b)** Trajectory corresponding to the deactivation of *o*-NBA from the S_6 to the S_1 potential. Points along the potential energy curves symbolize at which potential the system is at the specific time.

The geometry snapshots along the mechanism, either from the S_7 or the S_6, leading to o-NBA in the S_1 excited state, point to minor distortions of the ring, changes in the position of the NO_2 group relative to the aromatic moiety and stretching motion of the C-H bonds from both the CHO group and the aromatic ring, and C-N bond.

b) MQCD simulations from the S_1 nπ* excited state

The nπ* band of the o-NBA vertical absorption spectrum[106] (recall Figure 3.6), is composed of three states (S_1-S_3). All three states are weakly absorbing according to MS-CASPT2//CASSCF(16,12) calculations, but the lowest S_1 state is the one with the highest oscillator strength. Therefore, and for the sake of simplicity, we have performed MQCD simulations starting only from the electronically S_1 excited state. Thus, the goal of this section is to investigate the $S_1 \rightarrow S_0$ relaxation mechanism through surface-hopping dynamic simulations in gas phase. The results can be also found in the publication Phys. Chem. Chem. Phys. DOI: 10.1039/C0CP01372B, article accepted and in press.

The main drawback of the level of theory employed for the electronic calculations is that predicts a qualitatively different energy profile before the H-transfer takes place in comparison with the more accurate MS-CASPT2 theory. In fact, CASSCF predicts a TS between the nπ* minimum in the S_1 potential and the $(S_1/S_0)_{X-HT}$ CI. This $(S_1)_{TS}$ is not present at MS-CASPT2 level of theory, which on the contrary, predicts an almost barrierless H-transfer. Along the rest of the S_1 path, there is a good agreement between the CASSCF and the MS-CASPT2 results. However, due to this artificial barrier, the CASSCF-based dynamic simulations launched from the FC geometry remain trapped in the $(nπ*)_{Min}$. Therefore, in order to provide a more realistic picture we have investigated the formation of the ketene intermediate from 200 trajectories starting from the $(S_1)_{TS}$, avoiding, thus the artificial bottleneck of population trapped in the $(nπ*)_{Min}$.

From the trajectories launched at the TS, about 35% of them hop to the ground state, through the $(S_1/S_0)_{X-HT}$ CI, while the remaining 65% do not reach the CI and evolve to the $(nπ*)_{Min}$, see Figure 3.18. All the molecules that pass through the $(S_1/S_0)_{X-HT}$ CI are branched into two different minima of the ground state: 69% return to the starting material, o-NBA, while 31% of the trajectories complete the H-transfer, leading to the ketene intermediate, see Figure 3.18. This estimated branching ratio at $(S_1/S_0)_{X-HT}$ is not completely consistent with the experimental yield of ca. 50% that has been recorded in various solvents.[30,33,35,36] This can be attributed to the fact that our calculations are performed in gas phase and not in solution, and additionally, to the fact that the kinetic energy gained by the system is underestimated when arriving at the $(S_1/S_0)_{X-HT}$ CI from the TS geometry. This is because we started our trajectories from the TS, and therefore, many molecules do not possess enough energy to keep the momentum towards the ketene.

In order to characterize the geometry of the $(S_1/S_0)_{X-HT}$ CI, the geometries were averaged at the time of the $S_1 \rightarrow S_0$ hop for all trajectories. This geometry was found to be in good agreement with the $(S_1/S_0)_{X-HT}$ CI optimized at MS-CASPT2/CASSCF level of theory, where a partial H-transfer is promoted by the planarity of the two substituents of *o*-NBA.
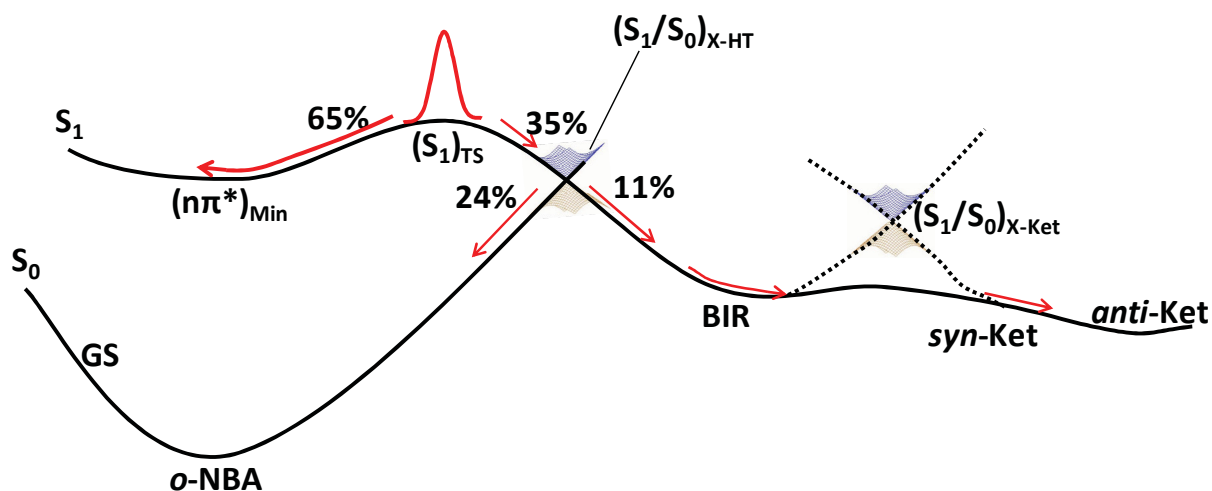

Figure 3.18. Potential energy profile of the S_0 and the S_1 states along the H-transfer reaction coordinate. The arrows and percentages show the distribution of products obtained from MQCD simulations starting from the TS of the S_1 potential, preceding the $(S_1/S_0)_{X-HT}$ CI.

The analysis of the trajectories that reach the ketene reveals that its formation takes place *via* a biradical structure. This biradical is formed in about 10 to 20 fs. The conversion of the biradical to the Ketene involves surmounting an energy barrier corresponding to a second CI region centered on the $(S_1/S_0)_{X-Ket}$ CI, recall Figure 3.14. In fact, we have identified trajectories showing several hops between the ground and first excited state on that region of the PES, which confirm the presence of the quantum chemically predicted $(S_1/S_0)_{X-Ket}$. Additionally, none of the trajectories that reach the biradical on the S_0 potential presents a back H-transfer, i.e. the H-transfer is irreversible. Therefore, it can be deduced that the complete yield of the reaction is determined by the $(S_1/S_0)_{X-HT}$ CI, where the creation of the ketene and the regeneration of the starting material compete.

Overall, the tautomerization is completed in the femtosecond time scale, in agreement with the experimental results which show that the phototautomerization is ultrafast after excitation at 388 and 260 nm.

Finally, two exemplary trajectories started from the $(TS)_{S1}$ are discussed in more detail in order to get better insight into the deactivation of *o*-NBA beginning from the S_1 state. The first trajectory

leads to the FC geometry, while the second trajectory exemplifies the formation of the ketene intermediate.

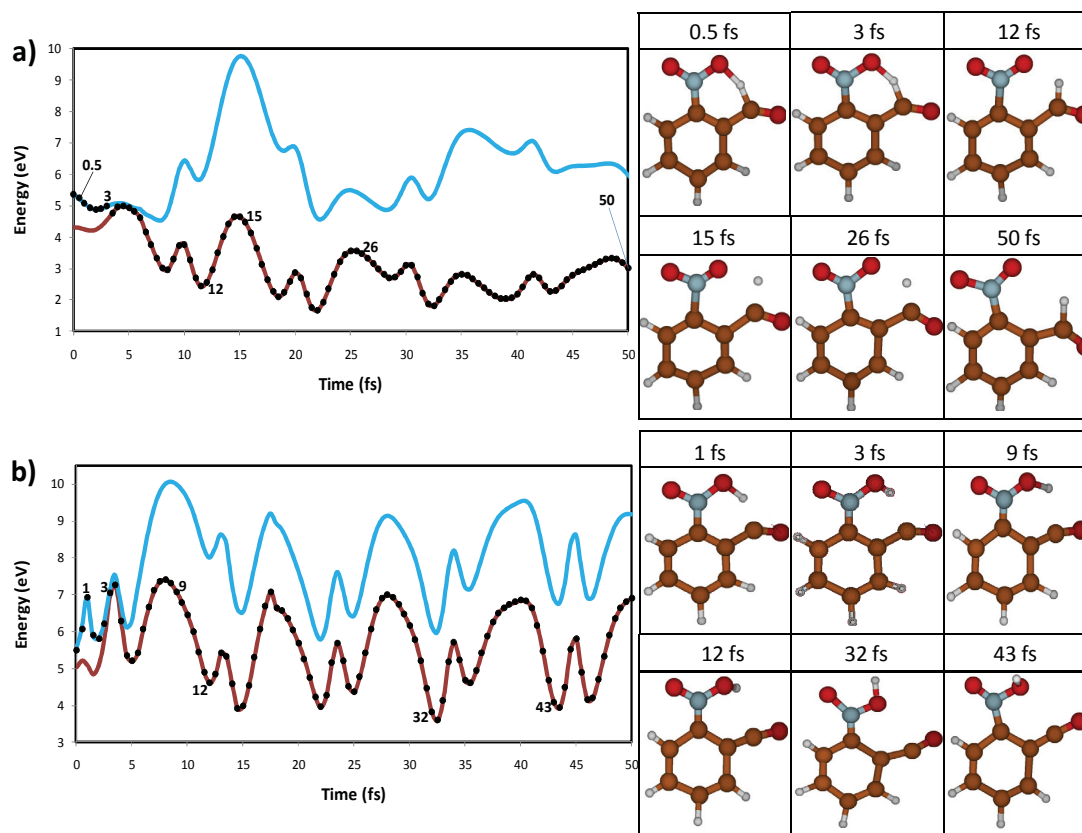Figure 3.19. a) Exemplary trajectory launched from the $(S_1)_{TS}$ that regenerates the FC o-NBA ground state. b) Trajectory launched from the $(S_1)_{TS}$ evolving to the ketene intermediate.

The geometry snapshots along the mechanism returning to the o-NBA ground state point to minor distortions of the ring and stretching motion of the C-H located at the CHO group. The o-NBA at the ground state is recovered in about 50 fs. Regarding the trajectory evolving to the ketene, the energy excess is employed in the rotation of the H-atom around the N-O bond and the linearization of the C-C-O moiety. The H-atom continues rotating around the N-O bond, which corresponds to an oscillation between the *syn-* and *anti-* ketene tautomers. The formation of the ketene is completed in less than 50 fs. As it can be inferred from the decay lifetimes in both trajectories, the relaxation to the ground state occurs extremely fast because the $(TS)_{S1}$ lies very close to the $(S_1/S_0)_{X-HT}$ CI, and thus making the passage through the CI very efficient.

3.4 Articles

In the following section, the articles that have arisen during this thesis are collected.

Article 3.4.1. Electronic States of *o*-Nitrobenzaldehyde: A combined Experimental and Theoretical Study

Verónica Leyva, Inés Corral,Thomas Schmierer, Björn Heinz, Ferran Feixas, Annapaola Migani, Lluís Blancafort, Peter Gilch, and Leticia González

Electronic States of *o*-Nitrobenzaldehyde: A Combined Experimental and Theoretical Study

Verónica Leyva,[†,‡] **Inés Corral,**[*,‡] **Thomas Schmierer,**[§] **Björn Heinz,**[§] **Ferran Feixas,**[∥]
Annapaola Migani,[∥] **Lluís Blancafort,**[∥] **Peter Gilch,**[§] **and Leticia González**[*,†,‡]

*Institut für Chemie und Biochemie, Freie Universität Berlin, Takustr. 3, 14195 Berlin, Germany, Institut für
Physikalische Chemie, Friedrich-Schiller-Universität Jena, Helmholtzweg 4, 07743 Jena, Germany, Fakultät für
Physik, Ludwig-Maximilians-Universität München, Oettingenstr. 67, 80538 Munich, Germany, and Institut de
Química Computacional, Universitat de Girona, Campus de Montilivi, 17071 Girona, Spain*

The experimental UV/vis absorption spectrum of *ortho*-nitrobenzaldehyde (*o*-NBA) has been assigned by means of MS-CASPT2/CASSCF, TD-DFT, and RI-CC2 theoretical computations. Additional information on the nature of the absorbing bands was obtained by comparing the *o*-NBA spectrum with that of related compounds, as, e.g., nitrobenzene and benzaldehyde. For wavelengths larger than ∼280 nm, the absorption spectrum of *o*-NBA is dominated by a series of weak nπ* absorptions from the NO$_2$ and CHO groups. These weak transitions are followed in energy by a more intense band, peaking at 250 nm and arising from charge transfer $\pi\pi$* excitations involving mainly benzene and nitro orbitals. Finally, the most intense band centered at 220 nm has its origin in the overlap of two different absorptions: the first one localized in the NO$_2$ substituent and the second one arising from a charge transfer excitation involving the NO$_2$ and the CHO fragments, respectively.

1. Introduction

More than 100 years ago, Ciamician and Silber reported the photo-induced transformation of *ortho*-nitrobenzaldehyde (*o*-NBA) into *ortho*-nitrosobenzoic acid.[1] Their report is regarded as the advent of modern organic photochemistry.[2] However, the elucidation of the mechanism of the "oldest" organic photore-action had to await the emergence of (highly) time-resolved spectroscopy. In 1980, George and Scaiano[3] observed solvent-dependent transients on the nanosecond time scale and below. Later experiments with higher time resolution led Yip and Sharma[4] to the conclusion that the species with the solvent-dependent lifetime is a ketene. This ketene intermediate would result from a photo-induced hydrogen transfer from the aldehyde substituent to the nitro group. It was then postulated to constitute the first ground-state intermediate in a cascade of reactions yielding the nitroso product. Recently, by means of femtosecond IR spectroscopy some of us have proven the existence of the ketene as an intermediate.[5] This experiment has also revealed that the ketene is formed on an ultrashort time scale of ∼400 fs and it is formed in the electronic ground state. This short formation time scale points to an excited singlet state as the precursor of the ketene and strong non-adiabatic effects mediating the decay of the excited state.

From the theoretical point of view, nothing is known about either the assignment of the excited states of *o*-NBA or the mechanism of its photoreaction. Simpler systems, like nitroben-zene and benzaldehyde, have been investigated with multicon-figurational methods in refs 6 and 7, respectively. These calculations are a useful reference point for this work, since they have been carried out at a level of theory comparable to the one used here.

In a joint experimental and theoretical effort, we aim at unravelling the dynamics of the hydrogen transfer reaction in *o*-NBA by means of steady-state as well as time-resolved spectroscopy and quantum mechanical methods. Since hydrogen transfer is assumed to initiate the transformation of most photoreactive nitroarenes[8] our investigation strives for under-standing the mechanistic patterns of a very general reaction. As a starting point, we characterize here the adiabatic excited singlet states of *o*-NBA. A tentative assignment based on the experimental absorption spectrum of *o*-NBA and related com-pounds is first given. The assignment is then supported by computing *o*-NBA with different state of the art quantum chemical methods. Specifically, we have performed multistate second-order perturbation theory on complete active space self-consistent field wavefunctions (MS-CASPT2/CASSCF), time-dependent density functional theory (TD-DFT), and second-order approximate coupled cluster (CC2) calculations.

2. Experimental Methods

UV/vis absorption spectra were recorded using a Lambda 19 spectrometer from Perkin-Elmer. The cyclohexane solvent was of spectroscopic grade (Sigma-Aldrich, Chromasolv). The aromatic compounds (*o*-NBA (Merck, for synthesis), *o*-nitro-toluene (Aldrich, 99+%), *o*-ethylnitrobenzene (Aldrich, 96%), toluene (Merck, Uvasol), and benzaldehyde (Merck, for syn-thesis)) were used as received. Sample solutions had concentra-tions of approximately 1 mM. Fused silica cells with a path length of 1–10 mm depending on the sample absorbance were used to record the spectra. The solvent contribution was corrected for by recording solvent blanks. To obtain the gas-phase spectrum of *o*-ethylnitrobenzene, a small drop of the substance was placed in a 50 mm fused silica sample cell. After equilibration between liquid and gas phase, the spectrum was recorded using the empty cell as a blank.

[†] Freie Universität Berlin.
[‡] Friedrich-Schiller-Universität Jena.
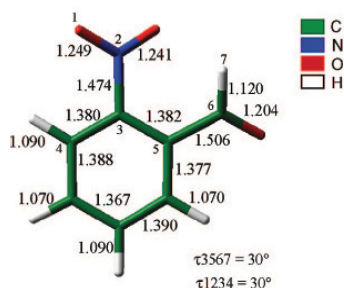[§] Ludwig-Maximilians-Universität München.
[∥] Universitat de Girona.

75

Electronic States of *o*-Nitrobenzaldehyde

J. Phys. Chem. A, Vol. 112, No. 23, 2008 **5047**

Figure 1. Most relevant geometrical parameters of the experimental structure of *o*-nitrobenzaldehyde.[9] The distances are in angstroms and the angles in degrees.

3. Computational Methods

The electronic calculations for *o*-NBA were performed on the X-ray experimental structure reported by Coppens et al.[9] The relevant geometrical parameters are summarized in Figure 1. In this structure of C_1 symmetry, the NO_2 and CHO substituents are non-coplanar with the aromatic skeleton, lying in planes forming a 30° dihedral angle with respect to the benzene ring.

The theoretical absorption spectrum was calculated at MS-CASPT2/CASSCF[10] level of theory and compared with those obtained using TD-DFT[11] and CC2[12] methods. The TD-DFT calculations were performed using the B3LYP functional combined with the triple zeta quality basis set 6-311G(d,p). Other functionals, namely, PBE and BLYP, were also tested and showed negligible differences in their vertical excited spectra; therefore, results are only reported for the B3LYP functional. The CC2 Franck-Condon excitation energies were calculated using the TZVP basis set and the resolution of the identity (RI) approximation.[13]

The MS-CASPT2/CASSCF calculations have been performed with the atomic natural orbital large basis set, ANO-L,[14] designed for the accurate description of the ionization potentials, electron affinities, and polarizabilities. The following contraction schemes were used: a set of (14s9p4d3f) was contracted to [4s3p2d] for C, O, and N and (8s4p3d)/[3s2p] for H. The initial wavefunctions of the MS-CASPT2/CASSCF protocol were obtained through state average SA-CASSCF calculations performed on six roots with equal weights of A_1 symmetry and were subsequently used as reference in the MS-CASPT2 calculation,[15] which accounts for dynamical correlation effects. In cases where the active space is not complete, intruder states usually arise. To remove intruder states, the level-shift technique[16] with a parameter of 0.3 a.u. was considered. This parameter was chosen after a careful examination of the stability of the excitation energies and the comparison of the excited states reference weight with that of the ground state. Moreover, the reliability of the MS-CASPT2 calculations has been assessed on the basis of the off-diagonal elements of the asymmetric, effective multistate Hamiltonian. These elements should be small, and complementary H_{ij} and H_{ji} elements should have similar values. In the MS-CASPT2/CASSCF(16,12) calculations of Table 2, the off-diagonal elements are smaller than 5 mHartree, and the largest difference between off-diagonal element pairs is 2.5 mHartree. In turn, the multistate correction on the CASPT2 energies is small, less than 1.5 mHartrees for the six states. Thus, the MS-CASPT2 procedure can be safely used here.

In the CASSCF method, the selection of the active orbitals and electrons is the key step to obtain reliable eigenfunctions

and eigenenergies. Despite the medium size of *o*-NBA, the choice of the relevant orbitals/electrons is nontrivial and deserves some comment. The complete active space in *o*-NBA should include 24 electrons in 17 orbitals, which comprises the 3 π,π^* orbital pairs of the benzene ring, 1 π,π^* pair of the CO group, 2 π,π^* pairs in the NO_2 group plus a nonbonding P_{NO_2} orbital, and the 6 lone pairs (n) on the oxygen atoms of the nitro and carbonyl groups. Such an active space (24,17) is beyond the current computer capabilities, and therefore, several restricted active spaces have been investigated. The tested reduced active spaces include (12,11), (16,12), (16,13), and (18,14). The smallest active space (12,11) excludes all lone pairs, while the biggest active space employed (18,14) includes only one lone pair per oxygen atom. The intermediate active spaces include several lone pairs at the expense of some π,π^* pairs. A detailed composition of the active spaces can be found in Table 1. As will be shown in the next section, TD-DFT and CC2 calculations predict $n\pi^*$ transitions in the low-lying spectral energy region, confirming the key role of the n orbitals. Obviously, the active space (12,11), excluding lone pairs, cannot describe adequately the low-energy part of the *o*-NBA spectrum. On the contrary, the (18,14) active space should be the best affordable choice to describe both $\pi\pi^*$ and $n\pi^*$ transitions simultaneously. Because of the enormous computational effort involved in the calculation of electronic excited states with this active space, the more practicable (16,12) active space was chosen to describe the markedly multiconfigurational character of *o*-NBA (see also next section). This active space is shown in Figure 2a and comprises 16 electrons distributed into 2 pairs of π_{CC} and π^*_{CC} orbitals localized on the benzene moiety, the π_{CO}, π^*_{CO} orbitals, the lone pair n_{CO} from the aldehyde group, 2 nitro lone pair orbitals n_{NO_2}, and the bonding, antibonding, and nonbonding π_{NO_2}, $\pi^*_{NO_2}$, and P_{NO_2} orbitals from the nitro group. It should be noted, however, that this active space with a small number of roots (vide infra) fails to describe one of the low-lying $\pi\pi^*$ excitations, and thus, this missing state has been calculated with the (12,11) active space that in turn excludes lone pairs (see Figure 2b).

All the MS-CASPT2/CASSCF calculations were performed using the *MOLCAS 6.0* quantum chemistry software,[17] while TD-DFT and RI-CC2 calculations were carried out with the *Gaussian03*[18] and *TURBOMOLE* (v 5.7)[19] suite of programs, respectively.

4. Results and Discussion

4.1. Active Space Dependence. Before assigning the experimental absorption spectrum of *o*-NBA with the help of the theoretical results, we shall shortly comment on the dependence of the vertical excitation energies and order of the states when using different active spaces in the MS-CASPT2 methodology. Also, we will justify the use of different active spaces when rationalizing the complete low-energy part of the absorption spectrum. Figure 3 is a summary of the results obtained with the different active spaces embodied in Table 1. As anticipated, the vertical spectrum calculated with the (12,11) active space is exclusively dominated by $\pi\pi^*$ excitations localized in the aromatic ring, CT excitations, or a mixture of both. The inclusion of two (i.e., (16,13) active space) or more (i.e., (16,12) active space) lone pairs from the NO_2 or the carbonyl group orbitals introduces $n\pi^*$ excitations in the low-energy region of the spectrum. Note that the active space (16,12) includes three lone pairs at the expense of removing a $\pi\pi^*$ pair, with respect to the (12,11) and (16,13) active spaces; see Table 1. As can be seen from Figure 3, the excitation energies for the $n\pi^*$ tran-

76

TABLE 1: Composition of the CASSCF Active Spaces Employed in This Work

	π_{CC}	π_{CC}	π_{CC}	π_{CO}	π_{NO_2}	P_{NO_2}	n_{NO_2}	n_{NO_2}	n_{NO_2}	n_{NO_2}	n_{CO}	n_{CO}	$\pi^*_{NO_2}$	π^*_{CO}	π^*_{CC}	π^*_{CC}	π^*_{CC}
(12,11)	X	X	X	X	X	X							X	X	X	X	X
(16,12)		X	X	X	X	X	X	X			X		X	X	X	X	
(16,13)	X	X	X	X	X	X	X	X					X	X	X	X	X
(18,14)	X	X	X	X	X	X	X	X			X		X	X	X	X	X

TABLE 2: CASSCF and MS-CASPT2 Vertical Excited Spectra and Single Components of the Gaussian Decomposition of the Experimental Spectrum of *o*-Nitrobenzaldehyde in Cyclohexane[a]

	CASSCF/ANO-L					MS-CASPT2/ANO-L					exp. abs. spectrum		
state	configuration	CI coeff	ΔE (eV)	ΔE (nm)	f	configuration	CI coeff	ΔE (eV)	ΔE (nm)	f	abs.band (nm)	Gauss. center (nm)	Gauss.f
S_1	$n_{NO_2} \rightarrow \pi^*_{NO_2}$	−0.43	3.77	329	0.0027	$\pi_{CC1} \rightarrow \pi^*_{NO_2}$	−0.41	3.33	372	0.0026	300	337	0.008
	$\pi_{CC1} \rightarrow \pi^*_{NO_2}$	−0.40				$n_{NO_2} \rightarrow \pi^*_{NO_2}$	−0.40						
S_2	$n_{CO} + n_{NO_2} \rightarrow \pi^*_{NO_2}$	0.61	4.65	267	0.0005	$n_{CO} + n_{NO_2} \rightarrow \pi^*_{CC} + \pi^*_{CO}$	0.43	3.82	324	0.0000		292	0.030
	$n_{CO} - n_{NO_2} \rightarrow \pi^*_{NO_2}$	0.37				$n_{CO} - n_{NO_2} \rightarrow \pi^*_{NO_2}$	0.42						
S_3	$n_{NO_2} \rightarrow \pi^*_{NO_2}$	0.61	4.29	289	0.0001	$n_{NO_2} \rightarrow \pi^*_{NO_2}$	0.52	3.88	319	0.0006			
	$n_{CO} + n_{NO_2} \rightarrow \pi^*_{NO_2}$	−0.45				$n_{CO} + n_{NO_2} \rightarrow \pi^*_{CC} - \pi^*_{CC}$	0.42						
S_4	$\pi_{CC2} \rightarrow \pi^*_{NO_2}$	−0.37	6.01			$\pi_{CC2} \rightarrow \pi^*_{NO_2}$	−0.36	4.45	278	0.0147	250	261	0.078
	$\pi_{CC2} \rightarrow \pi^*_{CC} - \pi^*_{NO_2}$	0.36				$\pi_{CC2} \rightarrow \pi^*_{CC} - \pi^*_{NO_2}$	0.36						
	$\pi_{CC1} \rightarrow \pi^*_{CC} + \pi^*_{CO}$	−0.35				$\pi_{CC1} \rightarrow \pi^*_{CC} + \pi^*_{CO}$	−0.34						
S_5	$P_{NO_2} \rightarrow \pi^*_{CC} + \pi^*_{NO_2}$	−0.58	7.07	175	0.2447	$P_{NO_2} \rightarrow \pi^*_{CC} + \pi^*_{NO_2}$	−0.52	4.94	251	0.2269		248	0.047
	$\pi_{CC1} \rightarrow \pi^*_{CC} + \pi^*_{NO_2}$	0.45				$\pi_{CC1} \rightarrow \pi^*_{CC} + \pi^*_{NO_2}$	0.54						
S_6	$P_{NO_2} \rightarrow \pi^*_{NO_2}$	0.54	6.59	188	0.0550	$P_{NO_2} \rightarrow \pi^*_{NO_2}$	0.53	5.55	223	0.0469	220	225	0.250
S_7												204	0.420

[a] All bands are obtained with a (16,12) reference active space, except S_3, which is obtained with a (12,11) active space (see Table 1 for details). Corresponding orbitals in Figure 2.

sitions provided by the (16,12) and (16,13) active spaces agree with each other satisfactorily. Because of the prohibitive cost of the (18,14) active space, our calculation is restricted to the estimation of the CASSCF transition energy for the first singlet excited state (not included in Figure 3). It is worth mentioning that this energy compares reasonably well with that obtained with CAS (16,12) and CAS (16,13), which are underestimated by 0.3 and 0.2 eV, respectively. The lack of n_{CO} lone pairs of the (16,13) active space, however, prevents it from predicting the existence of a third $n\pi^*$ excited state calculated at 3.82 eV by the (16,12) active space. This state consists of the following one electron excitations: $n_{CO} + n_{NO_2} \rightarrow \pi^*_{CC} + \pi^*_{CO}$ and $n_{CO} + n_{NO_2} \rightarrow \pi^*_{NO_2}$. In the region from 4 to 6 eV, the smaller active space, namely, (12,11), predicts the existence of three $\pi\pi^*$ states at 4.48, 4.94, and 5.73 eV. Only the first and third of them are described in this region with the SA calculations over 6 and 5 roots performed with the active spaces (16,12) and (16,13), respectively. The second low-lying $\pi\pi^*$ state does not appear with these active spaces and the chosen number of roots. This state can only be described when using 10 roots; however, the inclusion of such a high number of states introduces several double excitations that lead to a worsening of the SA orbitals and remaining excitation energies. Therefore, henceforth we restrict ourselves to the results obtained with the (16,12) active space and 6 roots.

4.2. Absorption Spectrum of *o*-NBA. Experimental spectra were recorded in a nonpolar aprotic solvent (cyclohexane) to minimize solute−solvent interactions and allow for a better comparison with the gas-phase calculations discussed below. To roughly quantify the residual solvent effect, the gas-phase spectrum of *o*-Ethylnitrobenzene (*o*-ENB) was compared to the one in solution (Figure 4). *o*-ENB was chosen since its vapor pressure is appreciable at room temperature. Gas- and solution-phase spectra resemble each other in shape. Weak absorption bands at longer wavelengths are followed by stronger ones in the deeper UV region. In general, the solution-phase spectrum is shifted towards longer wavelengths. The magnitude of this shift depends on the nature of the considered band. In the case

of *o*-ENB, the maximal shift observed is around 15 nm (~0.3 eV) for the band at ~250 nm. Solvent-induced shifts of this magnitude must be allowed for when comparing condensed-phase experimental and gas-phase computed spectra.

The experimental absorption spectrum of *o*-NBA recorded in cyclohexane (see Figure 5a) shows several overlapping bands. Maxima of three distinct bands centered at 220, 250, and 300 nm can be directly discerned. Further bands and exact band positions were extracted by a Gaussian decomposition. A Gaussian decomposition is justified as follows: For a *single* vibronic transition, one expects a Lorentzian line shape for purely homogeneous broadening, a Gaussian one for purely inhomogeneous, and a Voigt profile for an intermediate case.[20] In the present case, broadenings—either homogeneous or inhomogeneous—completely smear out the vibrational progression, i.e., single vibronic transitions are not resolved. Under these circumstances, the line shape function has to represent a vibrational envelope. As an approximation for this (complex) envelope, Gaussian and Lorentzian trial functions have been suggested (for a recent review, see ref 21). Here, in line with ref 21, Gaussian functions are better suited than Lorentzian ones. Such a procedure requires at least five Gaussian components. A very good agreement is obtained when using six components (Figure 6). For each Gaussian component i, the oscillator strength f_i was calculated according to[22]

$$f_i = 4.32 \cdot 10^{-9} \int \varepsilon_i(\tilde{\nu}) \, d\tilde{\nu}$$

Hereby, ϵ_i is the extinction coefficient measured in units M^{-1} cm^{-1} as a function of wavenumber $\tilde{\nu}$. The center frequencies and the oscillator strengths are compiled in Figure 6 and Table 2. Information about the origin of these bands can be obtained from the comparison of the absorption spectrum of *o*-NBA with that of related compounds, namely, *o*-nitrotoluene (*o*-NT), *o*-ethylnitrobenzene (*o*-ENB), benzaldehyde, and toluene (Figure 5). For wavelengths larger than ~230 nm, the spectrum of *o*-NBA bears strong similarities to those of *o*-NT and *o*-ENB. Considerable differences are observed when comparing the
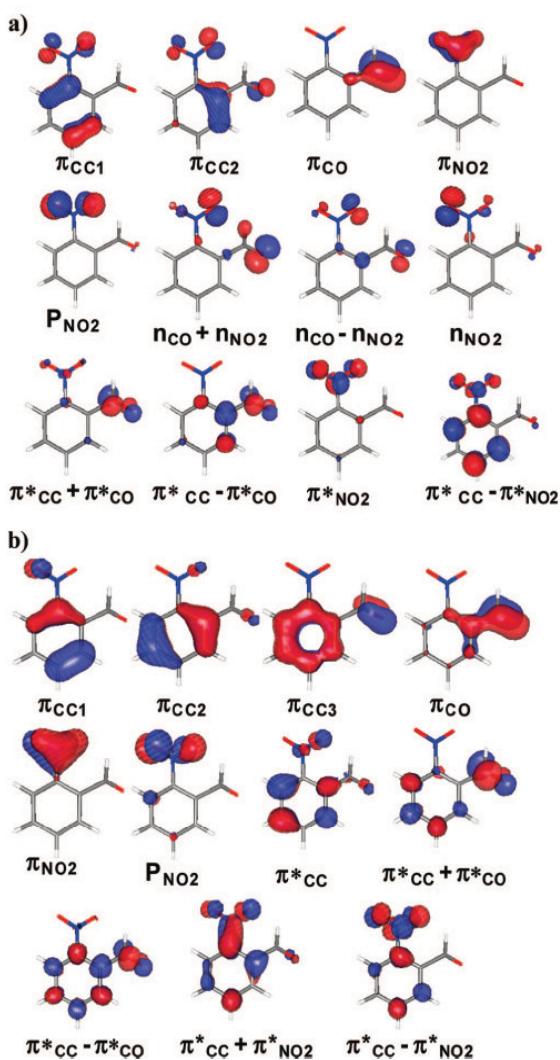
Electronic States of *o*-Nitrobenzaldehyde

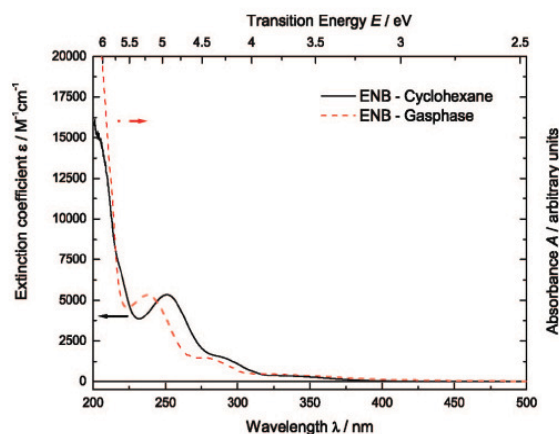*J. Phys. Chem. A, Vol. 112, No. 23, 2008* **5049**

Figure 4. Experimental absorption spectrum of *o*-Ethylnitrobenzene (ENB) in the gas phase and in cyclohexane solution. For ENB in solution, the ordinate gives the extinction coefficient ϵ as a function of the wavelength λ. The gas-phase spectrum has been arbitrarily scaled for an easy comparison.

Figure 2. Molecular orbitals included in the (16,12) (a) and the (12,11) (b) active spaces of the SA-CASSCF/ANO-L calculations over six (a) and five (b) roots, respectively.
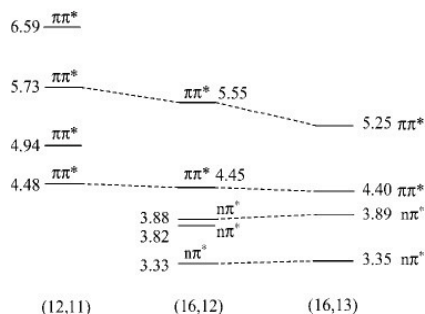
Figure 3. Relative MS-CASPT2 excitation energies (in eV) and state ordering employing different active spaces.
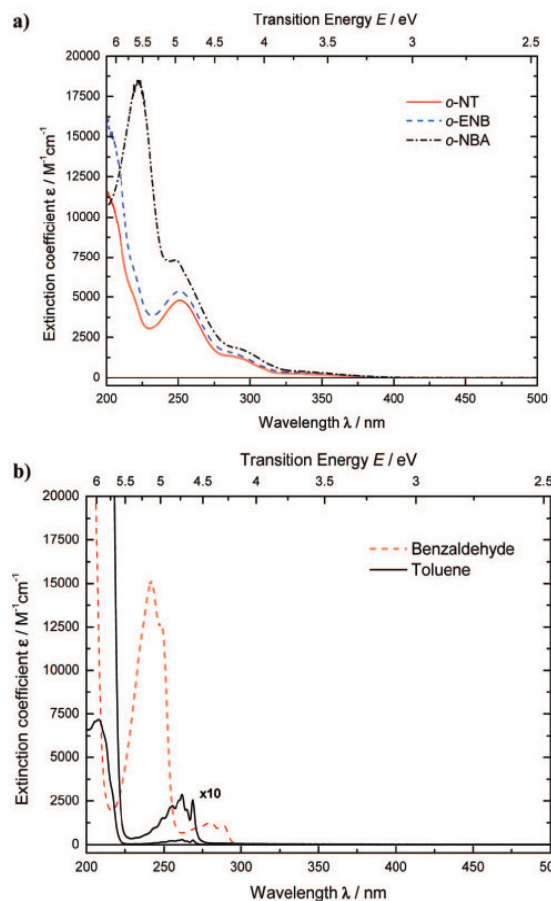

Figure 5. Absorption spectra of some nitroarenes (*o*-NBA, *o*-NT, *o*-ENB, part a) and toluene and benzaldehyde (part b) all dissolved in cyclohexane. In all spectra, the extinction coefficient ϵ is plotted as a function of the wavelength λ.

spectrum of *o*-NBA with that of toluene. Generally, the extinction coefficients of toluene are much smaller than those of all other compounds throughout the spectral range covered. Furthermore, vibrational progressions in toluene are recorded, whereas they are not resolved in the nitroarenes. From that, one

can deduce that the benzene ring alone is not responsible for the absorption properties of *o*-NBA. Benzaldehyde features an intense absorption band around 230 nm and a weak absorption
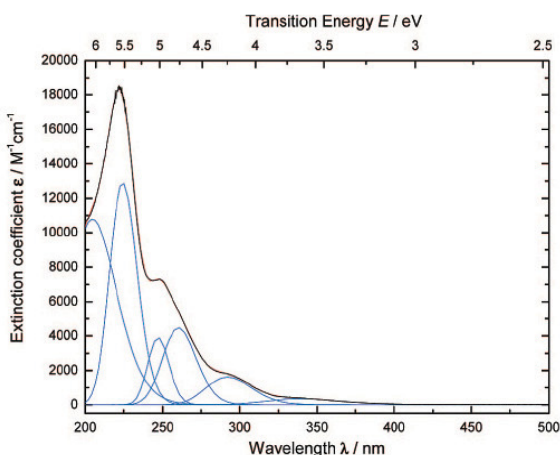
78

5050 *J. Phys. Chem. A, Vol. 112, No. 23, 2008*

Leyva et al.

Transition Energy E / eV

Figure 6. Experimental absorption spectrum (in black) and its Gaussian decomposition (single components in blue and their sum in red) of *o*-NBA in cyclohexane. The spectrum is represented with a linear wavelength scale. Gaussian fitting was done employing a linear frequency (or energy) scale.

that spreads from 275 to 300 nm; see Figure 5b. By allowing for small shifts, these bands might be related—at least partially—to the intense band at 220 nm and to the broad band peaking at 300 nm of *o*-NBA, respectively.

Hence, the low-energy part of the *o*-NBA spectrum (250–350 nm) could in principle be related to the excited states of benzaldehyde and nitrobenzene or to excitations that involve the nitro and carbonyl group chromophores simultaneously. Other spectral properties of *o*-NBA should be attributable to the nitrobenzene moiety. Indeed, the gas-phase spectrum of nitrobenzene[23] strongly resembles those of the nitroarenes investigated here. It shows a couple of weak transitions at long wavelengths above 270 nm and a rather strong ($\epsilon = 8500$ M^{-1} cm^{-1}) one at 240 nm.[23]

To further assign the experimental bands of *o*-NBA, theoretical calculations in the gas phase have been performed. The Frank-Condon excitation energies and their associated oscillator strengths calculated at MS-CASPT2/CASSCF(16,12), TD-DFT, and CC2 levels of theory are reported in Tables 2, 3, and 4, respectively. In Table 2, the experimental Gaussian centered at 248 nm is assigned on the basis of a MS-CASPT2/CAS SCF(12,11) calculation (see section 4.1).

For an easier comparison among the different methods, the computed spectral data are summarized as stick spectra in Figure 7. The results of the Gaussian decomposition (cf. Figure 6) of the experimental spectrum of *o*-NBA are also included. When comparing the experimental and computed spectra, two facts should be kept in mind. First, the Gaussian decomposition relies on the fact that every absorbing transition leads to a band that can be approximated by a Gaussian-shaped function. The overlap of these Gaussians results in the experimental absorption bands. Deviation of the real band shape from the Gaussian one can result in systematic errors. Secondly, the experimental spectrum was obtained in solution, and thus, spectral shifts of up to 0.3 eV are possible. With these facts in mind, we now proceed to assign the experimental Gaussian decomposition to the excited states of *o*-NBA theoretically calculated.

Comparing the position and oscillator strengths of the six fitted Gaussians with our more reliable MS-CASPT2/CASSCF vertical excitation energies and oscillator strengths, we can relate the Gaussians peaking at 261, 248, and 225 nm to the theoretical

TABLE 3: TD-B3LYP/6-311G(d,p) Transition Energies ΔE (eV, nm), Main One Electron Excitations, Weights, and Oscillator Strengths f of the Lower-Lying Electronic States of *o*-Nitrobenzaldehyde[a]

		TD-B3LYP/6-311G(d,p)			
state	weight	configuration	ΔE (eV)	E (nm)	f
S_1	0.635	$n_{CO} \rightarrow \pi^*_{CC} + \pi^*_{NO2}$	3.31	374	0.0006
S_2	−0.397	$n_{NO2}2 \rightarrow \pi^*_{CC} + \pi^*_{NO2}$	3.77	329	0.0124
	0.465	$\pi_{CC1} \rightarrow \pi^*_{CC} + \pi^*_{NO2}$			
S_3	0.346	$n_{NO2}1 \rightarrow \pi^*_{CC} + \pi^*_{NO2}$	4.15	299	0.0044
	0.449	$n_{CO} \rightarrow \pi^*_{CC} + \pi^*_{CO}$			
S_4	0.494	$\pi_{CC2} \rightarrow \pi^*_{CC} + \pi^*_{NO2}$	4.28	289	0.0149
	0.331	$n_{CO} \rightarrow \pi^*_{CC} + \pi^*_{CO}$			
S_5	0.491	$n_{NO2}1 \rightarrow \pi^*_{CC} + \pi^*_{NO2}$	4.46	278	0.0126
	0.307	$\pi_{CC2} \rightarrow \pi^*_{CC} + \pi^*_{NO2}$			
S_6	0.451	$n_{NO2}2 \rightarrow \pi^*_{CC} + \pi^*_{NO2}$	4.82	257	0.1021
	0.400	$\pi_{CC1} \rightarrow \pi^*_{CC} + \pi^*_{NO2}$			
S_7	0.531	$\pi_{CC1} \rightarrow \pi^*_{CC} + \pi^*_{CO}$	5.15	241	0.0267
S_8	0.512	$\pi_{CC2} \rightarrow \pi^*_{CC} + \pi^*_{CO}$	5.43	229	0.1106
S_9	0.512	$P_{NO2} \rightarrow \pi^*_{CC} + \pi^*_{NO2}$	5.65	219	0.0143
	0.348	$P_{NO2} \rightarrow \pi^*_{CC} + \pi^*_{CO}$			
S_{10}	0.589	$n_{CO} \rightarrow \pi^*_{CC} - \pi^*_{NO2}$	5.75	216	0.0066
S_{11}	0.446	$n_{NO2}1 \rightarrow \pi^*_{CC} + \pi^*_{CO}$	5.78	215	0.0409
	0.429	$n_{NO2}2 \rightarrow \pi^*_{CC} + \pi^*_{CO}$			
S_{12}	0.438	$n_{NO2}1 \rightarrow \pi^*_{CC} + \pi^*_{CO}$	5.80	214	0.1110

[a] Corresponding orbitals in Figure 8a.

TABLE 4: RI-CC2/TZV(P) Transition Energies ΔE(eV, nm), Main One-Electron Excitations, CI Coefficients, And Oscillator Strengths, f, of the Low-Lying Electronic States of *o*-Nitrobenzaldehyde[a]

		RI-CC2/TZV(P)			
state	configuration	coeff	ΔE (eV)	ΔE (nm)	f
S_1	$n_{NO2}2 \rightarrow \pi^*_{CC} + \pi^*_{NO2}$	0.5870	3.62	343	0.0117
	$n_{NO2}1 \rightarrow \pi^*_{CC} + \pi^*_{NO2}$	−0.5151			
S_2	$n_{NO2}1 \rightarrow \pi^*_{CC} + \pi^*_{NO2}$	0.5734	4.09	303	0.0014
	$n_{NO2}2 \rightarrow \pi^*_{CC} + \pi^*_{NO2}$	0.5182			
S_3	$n_{CO} \rightarrow \pi^*_{CC} + \pi^*_{NO2}$	0.5545	4.11	301	0.0038
	$n_{CO} \rightarrow \pi^*_{CC} + \pi^*_{CO}$	0.5379			
S_4	$\pi_{CC2} \rightarrow \pi^*_{CC} + \pi^*_{NO2}$	0.7093	4.57	271	0.0072
	$\pi_{CC1} \rightarrow \pi^*_{CC} + \pi^*_{CO}$	0.4634			
S_5	$n_{CO} \rightarrow \pi^*_{CC} + \pi^*_{NO2}$	−0.6777	4.95	250	0.0145
	$n_{CO} \rightarrow \pi^*_{CC} + \pi^*_{CO}$	0.4940			
S_6	$\pi_{CC1} \rightarrow \pi^*_{CC} + \pi^*_{NO2}$	0.8428	5.30	234	0.1335
S_7	$\pi_{CC1} \rightarrow \pi^*_{CC} + \pi^*_{CO}$	0.6331	5.82	213	0.0872
	$\pi_{CC2} \rightarrow \pi^*_{CC} + \pi^*_{CO}$	−0.4863			
S_8	$P_{NO2} \rightarrow \pi^*_{CC} + \pi^*_{NO2}$	0.6157	6.20	200	0.1421
	$\pi_{CC2} \rightarrow \pi^*_{CC} + \pi^*_{CO}$	−0.5575			
S_9	$\pi_{CC2} \rightarrow \pi^*_{CC} + \pi^*_{CO}$	−0.5810	6.21	200	0.2038
	$P_{NO2} \rightarrow \pi^*_{CC} + \pi^*_{NO2}$	−0.5585			
S_{10}	$n_{CO} \rightarrow \pi^*_{CC} - \pi^*_{NO2}$	0.5835	6.31	197	0.0050
S_{11}	$\pi_{CC2} \rightarrow \pi^*_{CC} + \pi^*_{CO}$	0.3996	6.55	189	0.1556
	$n_{NO2}1 \rightarrow \pi^*_{CC} + \pi^*_{CO}$	−0.3719			
S_{12}	$n_{NO2}2 \rightarrow \pi^*_{CC} + \pi^*_{CO}$	0.6714	6.73	184	0.0233
S_{13}	$n_{NO2}1 \rightarrow \pi^*_{CC} + \pi^*_{CO}$	0.5237	6.88	180	0.0781

[a] Corresponding orbitals in Figure 8b.

absorptions at 278, 251, and 223 nm, respectively (see Table 2 and Figure 7). In general, the corresponding states have $\pi\pi^*$ character. The transition calculated at 278 nm, which is the lowest $\pi\pi^*$ state, is a mixture of a $\pi_{CC2} \rightarrow \pi^*_{CC} - \pi^*_{NO2}$ excitation inside the benzene ring and two charge transfer (CT) excited states, namely, $\pi_{CC2} \rightarrow \pi^*_{NO2}$ and $\pi_{CC1} \rightarrow \pi_{CC} + \pi^*_{CO}$ (see Figure 2a). The considerable mixing of the orbitals involved in the excited states and the marked multiconfigurational character of the wavefunctions, previously observed in other
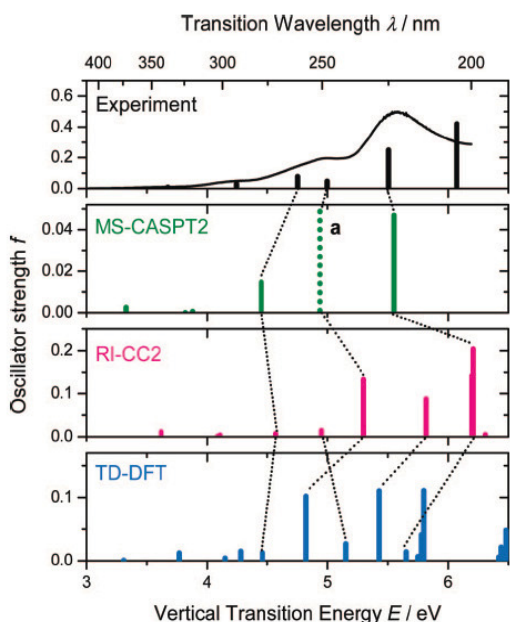
Electronic States of *o*-Nitrobenzaldehyde

J. Phys. Chem. A, Vol. 112, No. 23, 2008 **5051**

Figure 7. Comparison of the experimental and computed spectra of *o*-NBA. The upper panel shows the experimental spectrum and its Gaussian decomposition in stick representation (the height of a stick represents the oscillator strength *f*). The lower panels show the stick spectra obtained by the computational methods indicated. (a) Indicates band calculated with the (12,11) active space. See text for details.

theoretical nitroarene studies,[6] makes it difficult to assign a predominant one-electron excitation to these transitions. This state calculated at 278 nm can also be interpreted as a combination of the excited states of benzaldehyde and nitrobenzene, which have their lowest calculated $\pi\pi^*$ transitions at 286 and 282 nm, respectively.[6,7] Indeed, the orbitals involved in the $\pi_{CC1} \rightarrow \pi^*_{CC} + \pi^*_{CO}$ configuration of *o*-NBA compare with the ones calculated for the $2^1A'$ state in benzaldehyde.[7]

The experimental Gaussian at 248 nm is not described within the six roots MS-CASPT2/CASSCF(16,12) calculation, but it is present in the vertical excited spectrum calculated with the smaller active space (12,11); recall Figure 3. Our calculations performed with the (12,11) active space predict this state to appear at 251 nm—in good agreement with the experiment. It is a mixture of two main $\pi\pi^*$ transitions, the first localized within the benzene ring and the second of CT involving the nitro group and the antibonding orbitals of benzene. The relevant orbitals for this state are shown in Figure 2b. Accordingly, the difference dipole moment vector with respect to the ground state is parallel to the C_3-N_2 axis and amounts to 3.7 Debye. This transition can be related to the band calculated at 248 nm for nitrobenzene, which shows a similar change in the dipole moment.[6]

Finally, the band calculated at 223 nm involves mainly two orbitals localized in the nitro group. Its counterpart in nitrobenzene should be the 2^1B_2 state,[6] which is calculated at 222 nm; nevertheless, the different shapes of the orbitals in *o*-NBA and nitrobenzene make it difficult to establish a clear-cut correspondence. Note that the highest Gaussian resolved experimentally at 204 nm cannot be predicted by MS-CASPT2 due to the limitations associated with the calculated number of roots and the size of the active spaces employed. This peak will be discussed later with the help of linear response calculations.

According to MS-CASPT2 calculations, the lowest-energy experimental tail with Gaussians resolved at 292 and 337 nm

TABLE 5: Leading Configurations for the Low-Lying Excited States of NBA at the TD-B3LYP/6-311G(d,p), RI-CC2/TZV(P), and MS-CASPT2/ANO-L Levels of Theory, Respectively

configuration	TD-DFT	RI-CC2	MS-CASPT2
$n_{CO} \rightarrow \pi^*_{CC} + \pi^*_{NO2}$	S_1	S_3, S_5	S_2
$n_{NO2}2 \rightarrow \pi^*_{CC} + \pi^*_{NO2}$	S_2, S_6	S_1, S_2	S_2
$n_{NO2}1 \rightarrow \pi^*_{CC} + \pi^*_{NO2}$	S_3, S_5	S_1, S_2	S_1, S_3
$n_{CO} \rightarrow \pi^*_{CC} + \pi^*_{CO}$	S_4	S_3, S_5	S_2, S_3
$\pi_{CC1} \rightarrow \pi^*_{CC} + \pi^*_{NO2}$	S_2, S_6	S_6	S_1, S_5
$\pi_{CC2} \rightarrow \pi^*_{CC} + \pi^*_{NO2}$	S_4, S_5	S_4	S_4
$\pi_{CC1} \rightarrow \pi^*_{CC} + \pi^*_{CO}$	S_7	S_7	S_4
$\pi_{CC2} \rightarrow \pi^*_{CC} + \pi^*_{CO}$	S_8	S_8, S_9	$-$
$P_{NO2} \rightarrow \pi^*_{CC} + \pi^*_{NO2}$	S_9	S_8, S_9	S_5

can be interpreted as the overlap of three weakly absorbing transitions of predominant $n\pi^*$ character localized either in the NO_2 or the CHO moiety, that appear at 372, 324, and 319 nm, respectively. Similar to the S_4 state, the three $n\pi^*$ states stem from the combination of transitions occurring in nitrobenzene and benzaldehyde. Specifically, these states are mixtures of the two lowest $n\pi^*$ transitions of nitrobenzene and the $1A''$ state of benzaldehyde, which have been calculated between 347 and 299 nm.[6,7] However, the loss of planarity of the substituents in *o*-NBA induces a significant mixing with a $\pi\pi^*$ state, especially in S_1 (see the configurations in Table 2), which results in an increase of the calculated oscillator strength.

Hereafter, we present the results obtained with the two response methods CC2 and TD-DFT and their comparison with the previous MS-CASPT2 results. To facilitate the interpretation and comparison of CC2 and TD-DFT spectra, the leading configurations of the lowest excited states for the three methods have been summarized in Table 5. It is worth noting that the low-lying states predicted by the three methods involve the same molecular orbitals (compare Figures 2 and 8). From the examination of Tables 3, 4, and 5, we can learn that for wavelengths larger than 200 nm the TD-DFT and RI-CC2 spectra are composed of nine states that in turn appear as linear combinations of nine different configurations: four of $n\pi^*$ type and five showing a $\pi\pi^*$ character (see first column Table 5). The four $n\pi^*$ configurations are responsible for the lowest-absorbing electronic states. Among these configurations, one exhibits a clear CT character between the two substituents ($n_{CO} \rightarrow \pi^*_{CC} + \pi^*_{NO2}$), whereas the other three configurations show a CT character from one of the lone pairs into a π^*_{CC} orbital of the benzene ring. At the RI-CC2 level, these configurations generate four $n\pi^*$ states (S_1-S_3 and S_5), which span from 343 to 250 nm (see Table 4). In the case of TD-DFT, the $n\pi^*$ configurations mix with several $\pi\pi^*$ configurations and therefore are present in six electronic states (see Table 3). As already discussed above, only three low-lying $n\pi^*$ states were found at the MS-CASPT2 level. Inspection of the CASSCF virtual orbitals (recall Figure 2a) shows that the $\pi^*_{CC} + \pi^*_{CO}$ orbital is probably not well-described at this level, due to the absence of one of the π^* orbitals of the benzene ring in the active space (compare the shape of this orbital from the three methods in Figures 2a and 8a,b). This would be the reason why CASSCF and CASPT2 calculations fail to predict the existence of the fourth low-lying $n\pi^*$ state.

The remaining five configurations are of the $\pi\pi^*$ type. Four of them correspond to a partial CT from the benzene ring (π_{CC1} and π_{CC2} orbitals) to the nitro ($\pi^*_{CC} + \pi^*_{NO2}$) and aldehyde ($\pi^*_{CC} + \pi^*_{CO}$) orbitals. The fifth $\pi\pi^*$ configuration corresponds approximately to a local excitation within the nitro group. In all methods employed, the two lowest $\pi\pi^*$ states (S_4 and S_5 in
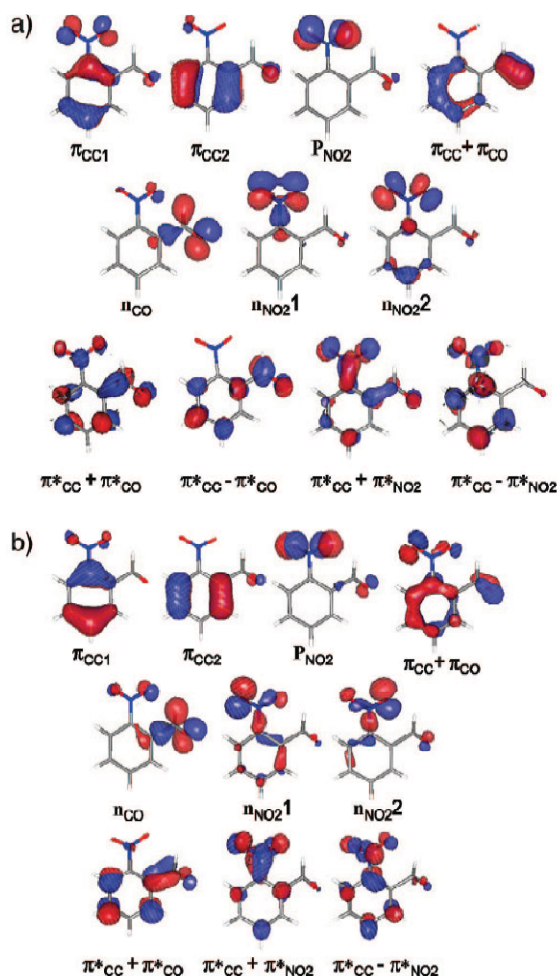
5052 *J. Phys. Chem. A, Vol. 112, No. 23, 2008*

Leyva et al.

a)

π_{CC1} π_{CC2} P_{NO2} $\pi_{CC} + \pi_{CO}$

n_{CO} $n_{NO2}1$ $n_{NO2}2$

$\pi^*_{CC} + \pi^*_{CO}$ $\pi^*_{CC} - \pi^*_{CO}$ $\pi^*_{CC} + \pi^*_{NO2}$ $\pi^*_{CC} - \pi^*_{NO2}$

b)

π_{CC1} π_{CC2} P_{NO2} $\pi_{CC} + \pi_{CO}$

n_{CO} $n_{NO2}1$ $n_{NO2}2$

$\pi^*_{CC} + \pi^*_{CO}$ $\pi^*_{CC} + \pi^*_{NO2}$ $\pi^*_{CC} - \pi^*_{NO2}$

Figure 8. Relevant TD-B3LYP (a) and CC2 (b) molecular orbitals for the interpretation of NBA's vertical excited spectrum.

MS-CASPT2, S_4 and S_6 in CC2, and S_5 and S_6 in TD-DFT) are mainly composed of the two benzene → nitro transitions, although at the TD-DFT and MS-CASPT2 levels, these states are mixed with other configurations. The next $\pi\pi^*$ states are benzene → aldehyde transitions at the RI-CC2 (S_7, S_8, and S_9) and TD-DFT (S_7 and S_8) levels of theory with certain mixings. Specifically, at RI-CC2 the S_8 and S_9 states are mixed with the $P_{NO2} → \pi^*_{CC} + \pi^*_{NO2}$ configuration.

These configurations are poorly represented with MS-CASPT2, once more, because of the lack of flexibility of the active space to properly describe the $\pi^*_{CC} + \pi^*_{CO}$ orbital. This is why these two electronic states have no counterpart in MS-CASPT2 theory. The difficulty in describing the benzene → aldehyde transitions may also explain the loss of quality of the wave function when more roots are included. Finally, the local nitro group transition (S_6 at MS-CASPT2, $S_8 + S_9$ CC2, and S_9 TD-DFT) is predicted by the three methods to give rise to states higher in energy than the benzene → nitro and benzene → aldehyde transitions.

Beyond the S_9 excited state, CC2 and TD-DFT methods predict a weakly absorbing CT state involving the aldehyde lone pair and the benzene molecular orbital $\pi^*_{CC} - \pi^*_{NO2}$ at 197 and 216 nm, respectively. More intense is, however, the state that follows in energy, which presents a $n_{NO2} → \pi^*_{CC} + \pi^*_{CO}$

character. None of these two states is, however, present in the MS-CASPT2 spectrum due to, on one hand, the limitation of the number of roots calculated and, on the other hand, the poor description of the $\pi^*_{CC} + \pi^*_{CO}$ orbital by this method. In view of the oscillator strength predicted by CC2 theory for this electronic state peaking at 189 nm (CC2), we assign the Gaussian band calculated at 204 nm from the experimental spectrum to a $n_{NO2} → \pi^*_{CC} + \pi^*_{CO}$ transition (see Table 4).

From the former analysis, we can conclude that the composition of the low-lying excited states predicted by the three methods employed here is based on the same nine configurations, although important differences are found in the way the different configurations combine to yield the respective electronic states. It is also worth highlighting that the three methods considered report the same state ordering for the calculated electronic states, even if positions and oscillator strengths of the excited states change in some cases from method to method. An interpretation of the experimental spectrum of *o*-NBA has to take these facts into account. In general, the non-negligible multireference character of the ground-state wavefunction imposes the use of CASSCF-based methods, with their inherent limitation on the size and choice of the active space. The response methods can complement the information missed by the MS-CASPT2/CASSCF theory, but caution must be exercised in the interpretation of TD-DFT, which lacks accuracy, especially when treating CT states. Still, on the basis of our complementary findings an assignment seems possible and reads as follows: The weak experimental absorption band ranging from 400 to 280 nm stems from the overlap of four different $n\pi^*$ excitations from the lone pairs of the nitro and aldehyde groups into benzene π^*_{CC}, π^*_{CO}, and π^*_{NO2} orbitals. The experimental absorption band centered at 250 nm arises from the joint absorption of two CT π (benzene) → π^* (nitro) transitions. Finally, the intense experimental band at 220 nm is the result of an overlap of two $\pi\pi^*$ excitations located in the same frequency range, one within the NO_2 moiety and a second one involving a CT $n_{NO2} → \pi^*_{CC} + \pi^*_{CO}$ transition. According to our calculations, contributions from π (benzene) → π^* (aldehyde) to the experimental bands at 250 and 220 nm are also expected.

5. Conclusions

This paper reports on the analysis of the electronic absorption spectrum of *o*-NBA, based on highly correlated quantum chemical calculations and the comparison of the experimental *o*-NBA spectrum with those of other nitroarenes, toluene, and benzaldehyde.

In general, the three theoretical methods considered in this work, namely, MS-CASPT2/CASSCF, CC2, and TD-DFT, lead to a consistent assignment of the experimental absorption spectrum of *o*-NBA. They predict the lowest-lying electronic excited states as linear combinations of the same nine electronic configurations. Still, the weight of the configurations inside each electronic state differs in some cases from one method to the other, and some discrepancies are found concerning the positions and oscillator strengths of the absorbing states. Nevertheless, the state ordering provided by the three methods is maintained. Taking into account the markedly multiconfigurational character of the ground-state wavefunction and the importance of the CT transitions in the low-energy region of the *o*-NBA spectrum, we propose the following assignment of the experimental spectrum. The very broad tail in the *o*-NBA spectrum peaking at 300 nm is assigned to the absorption of several $n\pi^*$ excitations involving π^* orbitals localized either in the benzene

Electronic States of *o*-Nitrobenzaldehyde

J. Phys. Chem. A, Vol. 112, No. 23, 2008 **5053**

ring or in the NO_2 and the CHO moieties. In the range between 270 and 240 nm, two CT π (benzene) $\rightarrow \pi^*$ (nitro) absorptions were calculated. The experimentally observed intense band around 220 nm corresponds to the superposition of two intense states, the first one being a $\pi\pi^*$ state localized within the NO_2 group and the second one being an $n\pi^*$ state involving a CT excitation from the nitro to the aldehyde group. Finally, our calculations predict π (benzene) $\rightarrow \pi^*$ (aldehyde) contributions for the two most intense bands of the spectrum.

In view of the ultrafast hydrogen transfer measured for *o*-NBA after excitation at 260 nm,[5] one might expect a reactive state around this wavelength. Relaxation on such a state would lead to the hydrogen transfer. According to our calculations, such a reactive state could be any of the CT states involving the benzene and the nitro moieties. As a response to neutralize the generated charges induced by the CT state, the hydrogen transfer is the result of a proton which follows the electron. A possible reactive state is the $\pi\pi^*$ state that appears at 251 nm in the MS-CASPT2 calculation, since it has a significant charge transfer to the nitro group. In this state, the virtual orbital that acts as electron "acceptor" has the signature of the bonding pattern of the primary ketene photoproduct (double bond between the nitrogen and the adjacent carbon; see orbital $\pi^*_{CC} + \pi^*_{NO2}$ of Figure 2b). Alternatively, and following Kasha's rule and in accordance with the hints provided by, e.g., ref 3, the reaction could take place after an initial rapid internal conversion relaxation on the lowest excited state surface. This would lead to population of an $n\pi^*$ state located at the nitro group. Such a state features a hole in a lone pair of this group, which might attract the hydrogen located at the aldehyde function of *o*-NBA, triggering the photoreaction. Calculations to obtain minimum-energy paths and relaxation pathways in *o*-NBA are in progress to elucidate the different proposed mechanisms.

References and Notes

(1) Ciamician, G.; Silber, P. *Ber. Dtsch. Chem. Ges.* **1901**, *34*, 2040.
(2) Roth, H. D. *Pure Appl. Chem.* **2001**, *73*, 395.
(3) George, M. V.; Scaiano, J. C. *J. Phys. Chem.* **1980**, *84*, 492.
(4) Yip, R. W.; Sharma, D. K. *Res. Chem. Intermed.* **1989**, *11*, 109.
(5) Laimgruber, S.; Schreier, W. J.; Schrader, T.; Koller, F.; Zinth, W.; Gilch, P. *Angew. Chem. Int. Ed.* **2005**, *44*, 7901.
(6) Kröhl, O.; Malsch, K.; Swiderek, P. *Phys. Chem. Chem. Phys.* **2000**, *2*, 947.
(7) Molina, V.; Merchán, M. *J. Phys. Chem. A* **2001**, *105*, 3745.
(8) Pelliccioli, A. P.; Wirz, J. *Photochem. Photobiol. Sci.* **2002**, *1*, 441.
(9) Coppens, P.; Schmidt, G. M. J. *Acta Crystallogr.* **1964**, *17*, 222.
(10) Roos, B. O. In *Ab Initio Methods in Quantum Chemistry II*, Lawley, K. P., Ed.; Wiley: Chichester, 1987.
(11) Gross, E. K. U.; Kohn, W. *Adv. Quantum Chem.* **1990**, *21*, 255.
(12) Christiansen, O.; Koch, H.; Jorgensen, P. *Chem. Phys. Lett.* **1995**, *243*, 409.
(13) Hättig, C.; Weigend, F. *J. Chem. Phys.* **2000**, *113*, 5154.
(14) Widmark, P.-O.; Malmqvist, P.-A.; Roos, B. O. *Theor. Chim. Acta* **1990**, *77*, 291.
(15) Finley, J.; Malmqvist, P.-A.; Roos, B. O.; Serrano-Andrés, L. *Chem. Phys. Lett.* **1998**, *288*, 299.
(16) Roos, B. O.; Anderson, K. *Chem. Phys. Lett.* **1995**, *245*, 215.
(17) Karlström, G.; Lindh, R.; Malmqvist, P. A.; Roos, B. O.; Ryde, U.; Veryazov, V.; Widmark, P.-O.; Cossi, M.; Schimmelpfennig, B.; Neogrady, P.; Seijo, L. *Comput. Mater. Sci.* **2003**, *28*, 222.
(18) Frisch, M. J.; Trucks, G. W.; Schlegel, H. B.; Scuseria, G. E.; Robb, M. A.; Cheeseman, J. R.; Montgomery, J. J. A.; Vreven, T.; Kudin, K. N.; Burant, J. C.; Millam, J. M.; Iyengar, S. S.; Tomasi, J.; Barone, V.; Mennucci, B.; Cossi, M.; Scalmani, G.; Rega, N.; Petersson, G. A.; Nakatsuji, H.; Hada, M.; Ehara, M.; Toyota, K.; Fukuda, R.; Hasegawa, J.; Ishida, M.; Nakajima, T.; Honda, Y.; Kitao, O.; Nakai, H.; Klene, M.; Li, X.; Knox, J. E.; Hratchian, H. P.; Cross, J. B.; Bakken, V.; Adamo, C.; Jaramillo, J.; Gomperts, R.; Stratmann, R. E.; Yazyev, O.; Austin, A. J.; Cammi, R.; Pomelli, C.; Ochterski, J. W.; Ayala, P. Y.; Morokuma, K.; Voth, G. A.; Salvador, P.; Dannenberg, J. J.; Zakrzewski, V. G.; Dapprich, S.; Daniels, A. D.; Strain, M. C.; Farkas, O.; Malick, D. K.; Rabuck, A. D.; Raghavachari, K.; Foresman, J. B.; Ortiz, J. V.; Cui, Q.; Baboul, A. G.; Clifford, S.; Cioslowski, J.; Stefanov, B. B.; Liu, G.; Liashenko, A.; Piskorz, P.; Komaromi, I.; Martin, R. L.; Fox, D. J.; Keith, T.; Al-Laham, M. A.; Peng, C. Y.; Nanayakkara, A.; Challacombe, M.; Gill, P. M. W.; Johnson, B.; Chen, W.; Wong, M. W.; Gonzalez, C.; Pople, J. A. *Gaussian 03*, revision C.02; Gaussian, Inc.: Wallingford, CT, 2004.
(19) Ahlrichs, R.; Bär, M.; Häser, M.; Horn, H.; Kölmel, C. *Chem. Phys. Lett.* **1989**, *162*, 165.
(20) Demtröder, W. *Laser Spectroscopy: Basic Concepts and Instrumentation*; Springer Verlag: Berlin, 2002.
(21) Antonov, L.; Nedeltcheva, D. *Chem. Soc. Rev.* **2000**, *29*, 217.
(22) Berlman, I. B. *Handbook of Fluorescence Spectra of Aromatic Molecules*, 2nd edition; Academic Press: New York, 1971.
(23) Galloway, D. B.; Barth, J. A.; Huey, L. G.; Crim, F. F. *J. Chem. Phys.* **1993**, *98*, 2107.

JP711949J

Article 3.4.2. *Ortho*-Nitrobenzaldehyde 1:1 Water Complexes. The Influence of Solute Water Interactions in the Vertical Excited Spectrum

Verónica Leyva, Inés Corral and Leticia González

Ortho-Nitrobenzaldehyde 1:1 Water Complexes. The Influence of Solute Water Interactions in the Vertical Excited Spectrum

By Verónica Leyva[1,2], Inés Corral[2], and Leticia González[2,*]

[1] Institut für Chemie und Biochemie, Freie Universität Berlin, Takustr. 3, 14195 Berlin, Germany.
[2] Institut für Physikalische Chemie, Friedrich-Schiller-Universität Jena, Helmholtzweg 4, 07743 Jena, Germany

Dedicated to Prof. Dr. Hans-Heinrich Limbach on the occasion of his 65th birthday

Ortho-Nitrobenzaldehyde / Water Complexes / Hydrogen Bonding Interaction

The intermolecular hydrogen bonding interaction of a water molecule with the caging group *ortho*-nitrobenzaldehyde (*o*-NBA) has been studied by means of quantum mechanical methods. The *o*-NBA chromophore presents two functional groups, NO_2 and CHO, interconnected by an intramolecular hydrogen bond. Both groups compete for the interaction with the solvent molecule, leading to eleven possible stable isomers that are very close in energy. The effect of the binding water on the electronic properties of *o*-NBA has been analyzed in structural terms as well as using the atoms-in-molecules theory of Bader. Binding energies for all complexes are reported, and in general they range from 5 to 13 kJ/mol. Special attention has been paid to the effect of the water molecule on the vertical excitation energies of *o*-NBA. Upon water complexation the absorption spectrum of *o*-NBA shifts to higher energies and it is characterized by three bands of comparable intensities as those recently measured for *o*-NBA in gas phase.

1. Introduction

Cage compounds are molecules whose biological activity can be controlled by light, switching from an inactive ("closed cage") to an active ("open cage") form. The inactive form of the cage compound is obtained by functionalizing the active moiety with a suitable photoremovable protecting group or caging group [1,2]. 2-Nitrobenzyl substituents are the most prevalent groups present in caged com-

---

* Corresponding author. E-mail: leticia.gonzalez@uni-jena.de

2-Nitrobenzyl   2-Nitrosobenzaldehyde

Scheme 1.

ortho-nitrosoester   *ortho*-nitrosobenzoic acid
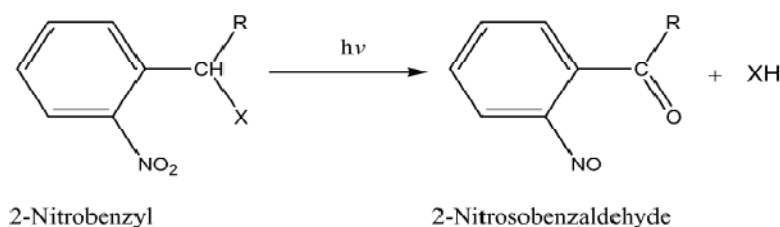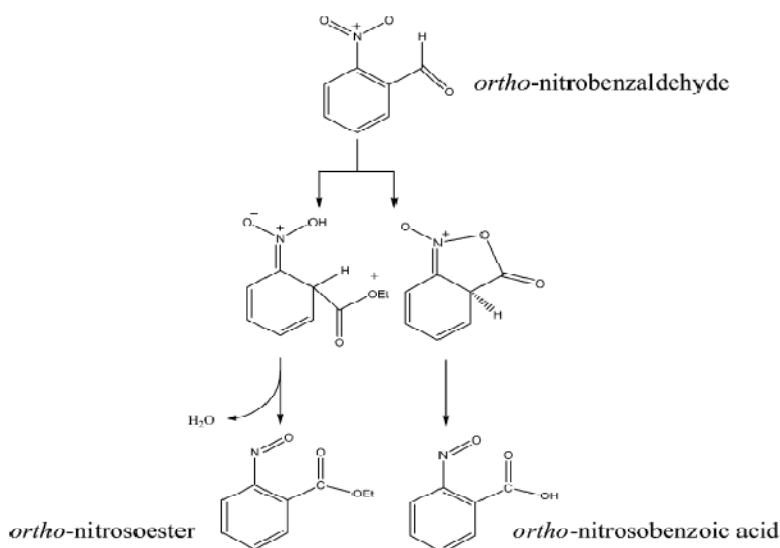
Scheme 2.

pounds, due to their compatibility with a wide variety of functional groups, their easy synthesis and their reasonable light sensitivity [1]. The utility of these systems relies on their ability of undergoing an internal redox reaction upon irradiation which leads to the 2-nitrosobenzaldehyde related by-product and the active biomolecule, see Scheme 1. An interesting caging group is the *ortho*-nitrobenzaldehyde (*o*-NBA). Its transformation to give *o*-nitrosobenzoic acid (see Scheme 2) has been experimentally investigated by a number of authors since the early times of photochemistry [3–6]. This photo-conversion was first proposed to proceed via the hydrolysis of an enol molecule obtained from an intermediate triplet diradical [4]. Later pump-probe [6] and femtosecond vibrational [5] experiments, however, suggest that the primary step in this reaction, an intermolecular hydrogen transfer, takes place through a ketene closed-shell intermediate.

As a first step towards understanding the photolysis mechanism of *o*-NBA leading to *o*-nitrosobenzoic acid we have recently characterized its experimental absorption spectrum and assigned it with the help of response and multiconfigurational methods [7]. In particular, we have used and compared the performance of second order approximated Coupled-Cluster (CC2) [8] and complete active

space self consistent field, CASSCF, corrected with second order perturbation theory in its multistate version, MS-CASPT2 method [9]. In that paper we show that both methods predict the same ordering of the states. Additionally, CC2 is able to describe a number of states which due to the restrictions on the active space and the number of roots the CASSCF method cannot take into account. In Ref. 7 we concluded that, when comparing it with MS-CASPT2/CASSCF, CC2 performs reasonably well in the low energy region of *o*-NBA absorption spectrum, although CC2 excitation energies are non-negligibly blue-shifted and the intensities of the bands are different.

Since the photoinduced hydrogen transfer reaction in the *o*-NBA has been always investigated in condensed media [3–6], we find interesting to explore the explicit effects of a solvent molecule in the system. Specifically, we have analyzed the changes in the vertical excitation energies and oscillator strengths upon the explicit inclusion of solvent-solute interactions using CC2 response theory. Within the accuracy of the employed method, we expect that the results reported here can show the main trends which should be observed experimentally. In particular, we have considered the 1:1 complex between the *o*-NBA and one water molecule. *o*-NBA presents two active sites for water solvation. Hence, *o*-NBA in aqueous solution can act simultaneously as a H donor through the CHO group and the benzene moieties or as a H acceptor through the O atoms of the NO_2 and CHO groups. The first part of this paper concentrates on i) the characterization of the most stable geometrical arrangements between the water molecule and the chromophore, paying attention to the influence of the polar solvent molecule on the intramolecular hydrogen bond of *o*-NBA, and ii) the analysis of the stability ordering of the resulting complexes. In the second part of this work, the electronic absorption spectrum in the gas phase is compared with that of two of the most stable solvated complexes. In the two selected complexes the water attaches the NO_2 and the CHO functional groups, respectively.

2. Computational details

The *o*-NBA water complexes have been optimized using the B3LYP functional and the Dunning double zeta core-correlation polarized valence basis set augmented with diffuse functions, aug-cc-pVDZ [10,11]. The B3LYP functional includes the Becke's three parameter nonlocal hybrid exchange potential [12] and the non-local correlation functional of Lee, Yang and Parr [13]. This basis set is flexible enough to properly describe hydrogen bonds formed between the *o*-NBA and the water molecule and combined with the hybrid functional B3LYP provides reliable geometrical structures and binding energies [14–18]. The nature of the optimized stationary points is confirmed by the calculation of the vibrational frequencies at the same level of theory. Zero point vibrational energy (*ZPVE*) corrections are also considered at this level of theory.

Relative energies (ΔE_0) of the different isomers are obtained using the refined B3LYP/aug-cc-pVTZ energies and *ZPVE* corrections. Binding energies, with (D_0) and without (D_e) *ZPVE* corrections are calculated as

$$D_e = E_{\text{NBA-water}} - (E_{\text{NBA}} + E_{\text{water}}),\tag{1}$$

$$D_0 = E_{\text{NBA-water}} + ZPVE_{\text{NBA-water}} - (E_{\text{NBA}} + ZPVE_{\text{NBA}} + E_{\text{water}} + ZPVE_{\text{water}}),\tag{2}$$

where $E_{\text{NBA-water}}$, E_{NBA} and E_{water} are the *ZPVE* uncorrected B3LYP/aug-cc-pVTZ energies of the complex, *o*-NBA and water, respectively, in their most stable conformations. The binding energies can also be corrected with the basis set superposition error (*BSSE*), which is evaluated using the counterpoise method of Boys and Bernardi [19]. Within this method the energies of the *o*-NBA and water fragments are calculated separately using the basis functions of the whole complex and their own basis functions in the geometry of the supermolecular complex. Then the *BSSE* is calculated as

$$BSSE = (E'_{\text{NBA}} + E'_{\text{water}}) - (E_{\text{NBA}} + E_{\text{water}}),\tag{3}$$

where E_{NBA} and E_{water} are the energies of the respective fragments using their own basis functions, and E'_{NBA} and E'_{water} are the energies of the species using the basis functions of the whole complex. As defined in Eq. (3) the *BSSE* is a positive quantity. Accordingly, the corrected binding energy D'_0 is obtained as

$$D'_0 = D_0 - BSSE.\tag{4}$$

All optimizations and single point calculations have been performed using the GAUSSIAN03 suite of programs [20].

The nature of the bonding properties of the different complexes has been further investigated using the quantum theory of atoms-in-molecules (QTAIM) proposed by Bader [21], based on the topological analysis of the charge density. The charge density at the bond critical points (bcp) and ring critical points (rcp) provides information on the relative strength of intra- and intermolecular hydrogen bonds. The value of the charge density at the critical points was evaluated at B3LYP/6-311+G(d,p) level of theory.

The vertical electronic excited states of the two most stable *o*-NBA-water complexes, with water sitting on the NO_2 and CHO substituents, have been calculated using the second order approximated Coupled-Cluster method [8] (CC2) and the resolution of the identity approximation [22], RI, which transforms four-center-two-electron integrals into three-center ones, leading to important computational savings. The RI-CC2 method is combined with the TZVP basis set [23].

3. Results

3.1 Ground state properties of the 1:1 o-NBA-water complexes

The gas-phase optimized *o*-NBA molecule presents C_1 symmetry with the NO_2 and CHO substituents forming ca. 30° dihedral angle with respect to the benzene
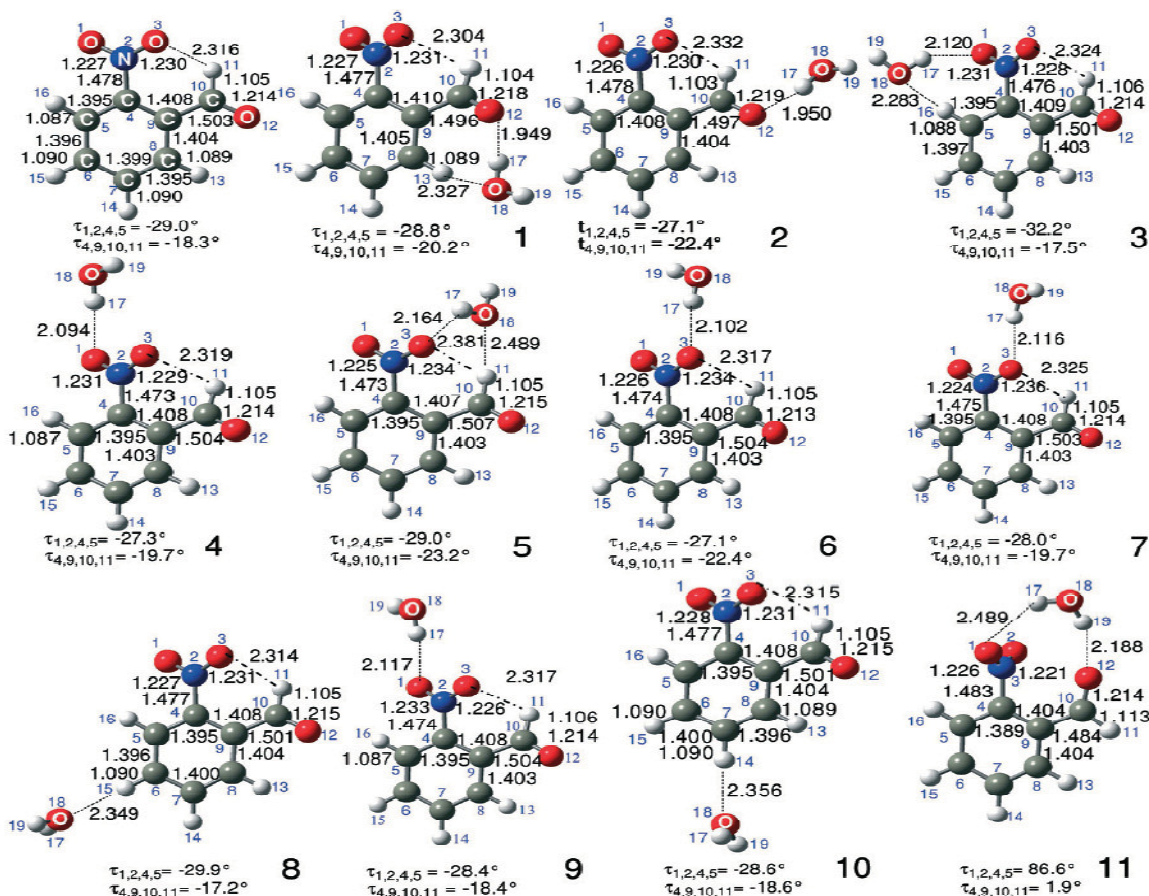
Fig. 1. B3LYP/aug-cc-pVDZ optimized geometries of *o*-NBA and 1:1 water complexes. Bond lengths in Å and dihedral angles in degrees.

ring [7]. This non-coplanar arrangement minimizes on one hand the steric constraint between NO_2 and CHO and on the other favours the formation of an intramolecular H-bond bridging the H of the aldehyde and one of the O from the nitro. When adding a single water molecule, eleven ground state 1:1 complexes have been found, in which the water is peripherically H-bonded to the *o*-NBA. Complexes with the H_2O molecule facing the π-system of the benzene ring have not been considered as they are less stable in energy [24–26]. The *o*-NBA and the optimized water complexes (structures **1–11**) with their most important geometrical parameters are collected in Fig. 1. The charge density at the bcp of the intra- and intermolecular H-bonds formed between the *o*-NBA and the water are summarized in Table 1.

The optimized eleven complexes can be divided in three different groups, one where the water acts as a proton donor (**2, 4, 6, 7, 9** and **11**), another where it is a proton acceptor (**8** and **10**) and a third one where water interacts as a proton donor-acceptor simultaneously (**1, 3** and **5**).

Table 1. Charge density (eau^{-3}) at the bond critical points at the inter- and intramolecular H-bonds of the *o*-NBA and 1:1 water complexes calculated with B3LYP/6-311+G(d,p)// B3LYP/aug-cc-pVDZ. The numbering of the atoms is provided in Fig. 1.

Structure		Electron density (eau^{-3})
o-NBA	$O_3 \cdots H_{11}$	0.0163
1	$O_{18} \cdots H_{13}$	0.0101
	$O_{12} \cdots H_{17}$	0.0228
	$O_3 \cdots H_{11}$	0.0169
2	$O_{12} \cdots H_{17}$	0.0243
	$O_3 \cdots H_{11}$	0.0163
3	$O_1 \cdots H_{17}$	0.0147
	$O_{18} \cdots H_{16}$	0.0110
	$O_3 \cdots H_{11}$	0.0159
4	$O_1 \cdots H_{17}$	0.0169
	$O_3 \cdots H_{11}$	0.0162
5	$O_3 \cdots H_{17}$	0.0149
	$O_{11} \cdots H_{18}$	0.0151
	$O_3 \cdots H_{11}$	0.0077
6	$O_3 \cdots H_{17}$	0.0168
	$O_3 \cdots H_{11}$	0.0162
7	$O_3 \cdots H_{17}$	0.0162
	$O_3 \cdots H_{11}$	0.0161
8	$O_{18} \cdots H_{15}$	0.0107
	$O_3 \cdots H_{11}$	0.0159
9	$O_1 \cdots H_{17}$	0.0162
	$O_3 \cdots H_{11}$	0.0161
10	$O_{18} \cdots H_{14}$	0.0106
	$O_3 \cdots H_{11}$	0.0163
11	$O_1 \cdots H_{17}$	0.0078
	$O_{11} \cdots H_{19}$	0.0122

In the case where the water is a proton donor, four complexes have been found with the water molecule attached to the nitro group (**4, 6, 7, 9**), one where the water interacts with the aldehyde group (**2**), and one where the water molecule is attached to both the nitro and the aldehyde groups (**11**).

In general, the N—O bond participating in the intermolecular H-bond with water in complexes **4, 6, 7** and **9** is weakened in a small extent (ca. 0.005 Å) while the counter N—O is reinforced in a similar amount. The changes in the distances of the NO_2 group are less noticeable in structures **4** and **6** compared to complexes **9** and **7**, respectively. This is due to the weak electrostatic interaction between the H_{19} and the O_1 not involved in the intermolecular H-bond, which counteracts the electronic effects derived from the intermolecular H-bond. Ac-

cordingly, the intermolecular H-bond in the complexes **4** and **6** is shorter than that of complexes **9** and **7**, respectively. The strength of the intermolecular H-bond is also correlated with the binding energies (vide infra) and charge density at this bond. Indeed, the electron density at the bcp between O_1H_{17} and O_3H_{17} at complexes **4** and **6** is slightly bigger than at **9** and **7**, respectively (see Table 1). The rest of the geometrical parameters are hardly unaffected by the complex formation, including the intramolecular H-bond.

In complex **2**, the water is attached to the aldehyde group forming a very strong H-bond. This is reflected in the H-bond distance and the charge density at this bond (0.0243 eau^{-3}). Except for bonds surrounding the intermolecular H-bond, the geometry of *o*-NBA remains undistorted upon water complexation. In complex **11** the water molecule can only act as a donor towards both nitro and aldehyde groups since the aldehyde group is rotated in a *cis* conformation with respect to the NO_2 group, which in turn lies perpendicular to the benzene ring plane. These deformations result in a very planar benzaldehyde moiety, compare the dihedral angle $\tau_{4,9,10,11}$ in **11** and the rest of the complexes. As a consequence of the gained planarity, the π conjugation of the benzene ring with the CHO group is enhanced, leading to strong changes in the structure, especially in the C-CHO bond that is reinforced by ca. 0.02 Å and in the aromatic scaffolding. The two intermolecular H-bonds with the NO_2 and CHO groups strongly differ in their strength, as indicated by the O-H bond distances (see Fig. 1) and charge densities at the bcp's (see Table 1).

The H-bond formed by the water molecule acting as an acceptor is similar in complexes **8** and **10**. In both complexes the water molecule was found to be oriented perpendicularly to the benzene plane in order to minimize the interaction with the benzene π cloud. It is noticeable that these intermolecular H-bonds are much longer and thus weaker, than those found in the other *o*-NBA-water structures.

In structures **1**, **3** and **5**, the water is forming ring-like structures with different parts of *o*-NBA. Similarly to structure **11**, in complex **5** water bridges the nitro and aldehyde groups. Contrary to complex **11**, in the case of **5** water acts at the same time as donor and acceptor and forms a four-membered ring which shares as a side the intramolecular H bond with the six member structure present in *o*-NBA. Accordingly, two rcp's are found. Small changes can be appreciated in the geometries of the nitro and aldehyde groups, while the rest of the molecule remains unperturbed. Notice that the intramolecular H-bond in **5** increases by 0.07 Å, and the charge density at the bcp decreases concomitantly (0.0077 eau^{-3} against 0.0163 eau^{-3} in *o*-NBA). The weakening of this bond can be understood in terms of the perturbations that the two new intermolecular H-bonds cause to both atoms involved in the intramolecular H-bond, namely the O of the nitro group and the H of the aldehyde group. Structures **1** and **3** also form two H-bonds, but this time involving one H from the benzene and either the nitro (**3**) or the aldehyde group (**1**). As it will be discussed later, structure **1** was found to be the most stable among all studied complexes. It presents two very strong

Table 2. B3LYP/aug-cc-pVTZ//B3LYP/aug-cc-pVDZ total (Hartrees), zero point vibrational correction (*ZPVE*, Hartrees), relative energies without and with *ZPVE* (kJ/mol), basis set super-position errors (*BSSE*, kJ/mol), binding energies without and with *BSSE* (kJ/mol) and perma-nent dipole moments (Debye) of *o*-NBA, water and the corresponding 1:1 complexes.

	Total Energy (Hartrees)	ZPVE (Hartrees)	ΔE_e (kJ/mol)	ΔE_o (kJ/mol)	BSSE (kJ/mol)	D_o (kJ/mol)	D_o' (kJ/mol)	μ Total (Debye)
o-NBA	−550.27268	0.1117	–	–	–	–	–	–
H$_2$O	−76.46618	0.0212	–	–	–	–	–	–
1	−626.74689	0.1358	0.0	0.0	0.4	−13.7	−13.3	3.4
2	−626.74555	0.1356	3.5	3.0	0.3	−10.7	−10.4	8.8
3	−626.74469	0.1350	5.8	3.8	0.4	−9.9	−9.5	3.6
4	−626.74378	0.1350	8.2	6.3	0.6	−7.5	−6.8	8.1
5	−626.74361	0.1350	8.6	6.7	0.8	−7.0	−6.3	3.2
6	−626.74356	0.1350	8.8	6.8	0.3	−6.9	−6.6	7.4
7	−626.74310	0.1348	9.9	7.5	0.9	−6.2	−5.3	5.5
8	−626.74234	0.1342	12.0	7.8	0.6	−5.9	−5.3	8.8
9	−626.74300	0.1349	10.2	7.9	0.6	−5.8	−5.2	8.5
10	−626.74222	0.1342	12.3	8.2	0.7	−5.5	−4.8	8.7
11	−626.74007	0.1349	17.9	15.7	0.3	2.0	1.6	9.5

intermolecular H-bonds and the sum of their charge densities is larger than that observed for the strong intermolecular H-bond in complex **2** (see Table 1). In both complexes, the N—O or C—O bond is weakened, while the C—N or C—C distances connecting the functional group to the benzene are reinforced. As with the rest of the complexes, the benzene scaffolding is not much affected.

Total, relative and binding energies of all complexes together with their cor-responding dipole moments are collected in Table 2.

As mentioned above, the most stable *o*-NBA-water complex is the one la-beled as **1** and showing two H-bonds besides the one present in *o*-NBA alone. It should be noted though, that energy differences between all studied complexes are very small so that experimentally other complexes beyond **1** should be present. Taking into account the error of the employed method (more than 2 kcal/mol), it is difficult to establish a preferential order of stability; however, we believe that the present level of accuracy allows us to establish which are the most favored complexes. In general, compounds forming several intermolecular H-bonds are more stable than those with a single one. Exceptionally, structure **11** is disfavored despite the multiple intermolecular interactions, due to the con-strained *cis* disposition of the two electron rich groups which generate strong repulsion between the nitro and aldehyde electron clouds. Also the geometrical constraints arising from the three H-bonds in which H$_{11}$ and O$_3$ participate, jus-tify the relative low stability of complex **5** with respect to the other complexes. Complexes **2** and **3** are almost degenerated and their energy difference lies within 3 kJ/mol with respect to the most stable complex **1**. From structure **4** to **10** the

energy difference increases to ca. 8 kJ/mol. The stability order is maintained upon inclusion of *ZPVE* corrections except in the case of the complexes **8** and **9** which are exchanged due to the different value of *ZPVE* correction. The difference between ΔE_e and ΔE_0 (relative energies without and with considering *ZPVE* corrections) amounts to ca. 2 kJ/mol, see Table 2. It is interesting to note that complexes **8** and **10** have slightly smaller *ZPVE*s than the rest of complexes due to their weaker intermolecular interaction with water. The small *ZPVE* of complex **8** is responsible of its destabilization with respect to complex **9**.

The binding energies D'_0 of all complexes are tabulated in Table 2. In the most stable complex, D'_0 amounts to –13 kJ/mol. The binding energies of the rest of complexes decrease according to their reverse stability order. In the case of the complex **11**, the binding energy is positive because it has been calculated using the energy of *o*-NBA with the nitro and aldehyde groups in *trans* position while in complex **11** both groups lie in a *cis* conformation.

As observed in other studies [27,28], the *BSSE* at the here employed level of theory amounts to less than 1 kJ/mol and thus they do not lead to any drastic effect in the binding energies.

3.2 Electronic excited states of most stable 1:1 o-NBA-water complexes

The gas phase experimental absorption spectrum of NBA is characterized by three main bands [7]. The lowest energy part of the spectrum corresponds to a tail which has been assigned to weak nπ* absorptions starting from the lone pairs of the NO_2 and the CHO group. At higher energy, this weak shoulder is followed by a more intense band that peaks at 250 nm and arises from aromatic ππ* excitations localized inside the benzene ring as well as from some charge transfer (CT) excited states. Finally, the most intense band is centred on 220 nm and it involves the overlap of two different absorptions involving the NO_2 and the CHO fragments, respectively [7].

To study the influence of water complexation in the absorption spectrum of *o*-NBA, the vertical excited states of two different *o*-NBA-water isomers have been calculated. We have chosen the structure **1**, which is the most stable 1:1 complex at the B3LYP/aug-cc-pVTZ level of theory, where the water molecule interacts with the aldehyde group, and the complex **3**, the most stable complex with the water molecule sitting on the nitro group. Vertical excitation energies with their main configurations and corresponding oscillator strengths are compiled in Table 3. For the sake of comparison, gas phase excitation energies of *o*-NBA are also included. A correlation of the excitation energies for the three species is presented in Fig. 2. The orbitals involved in the transitions are shown in Fig. 3 and their energies are correlated in Fig. 4.

As it can be seen in Table 3, the first two excited states of *o*-NBA in gas phase correspond to nπ* excitations from the lone pairs of the NO_2 group to the virtual orbital π*$_{CC}$+π*$_{NO2}$, mainly localized in the benzene ring and the NO_2 group, see Fig. 3. The third and fifth excited states, also of nπ* character, corre-

Table 3. RI-CC2/TZVP excitation energies for *o*-NBA, and 1:1 water complexes **1** and **3** (cf. Fig. 1). For the three structures the main configurations composing the wavefunction with the corresponding coefficients and the oscillator strengths are tabulated.

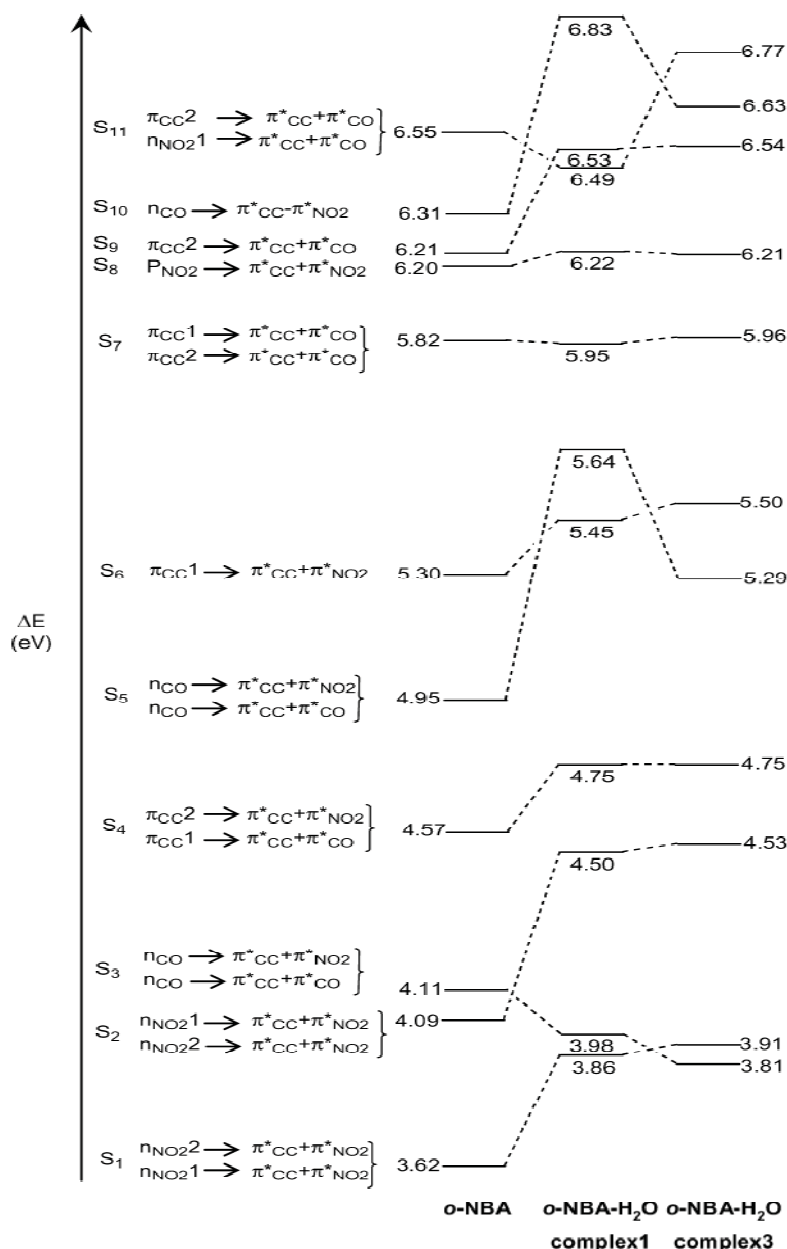|	*o*-NBA				Complex1				Complex3			
	Configuration	Coeff.	ΔE (eV)	f	Configuration	Coeff.	ΔE (eV)	f	Configuration	Coeff.	ΔE (eV)	f
S_1	$n_{NO2}2 \rightarrow \pi^*_{CC} + \pi^*_{NO2}$	0.587	3.62	0.0117	$n_{NO2}2 \rightarrow \pi^*_{CC} + \pi^*_{NO2}$	0.609	3.86	0.0067	$n_{NO2}2 \rightarrow \pi^*_{CC} + \pi^*_{NO2}$	−0.662	3.91	0.0078
	$n_{NO2}1 \rightarrow \pi^*_{CC} + \pi^*_{NO2}$	−0.515										
S_2	$n_{NO2}1 \rightarrow \pi^*_{CC} + \pi^*_{NO2}$	0.573	4.09	0.0014	$n_{NO2}1 \rightarrow \pi^*_{CC} + \pi^*_{NO2}$	0.683	4.50	0.0021	$n_{NO2}1 \rightarrow \pi^*_{CC} + \pi^*_{NO2}$	0.641	4.53	0.0029
	$n_{NO2}2 \rightarrow \pi^*_{CC} + \pi^*_{NO2}$	0.518										
S_3	$n_{CO} \rightarrow \pi^*_{CC} + \pi^*_{CO}$	0.538	4.11	0.0038	$n_{CO} \rightarrow \pi^*_{CC} + \pi^*_{CO}$	0.459	3.98	0.0018	$n_{CO} \rightarrow \pi^*_{CC} + \pi^*_{CO}$	0.483	3.81	0.0025
S_4	$\pi_{CC}2 \rightarrow \pi^*_{CC} + \pi^*_{NO2}$	0.709	4.57	0.0072	$\pi_{CC}2 \rightarrow \pi^*_{CC} + \pi^*_{NO2}$	0.693	4.75	0.0184	$\pi_{CC}2 \rightarrow \pi^*_{CC} + \pi^*_{NO2}$	0.676	4.75	0.0174
	$\pi_{CC}1 \rightarrow \pi^*_{CC} + \pi^*_{CO}$	0.463			$\pi_{CC}1 \rightarrow \pi^*_{CC} + \pi^*_{CO}$	−0.506			$\pi_{CC}1 \rightarrow \pi^*_{CC} + \pi^*_{CO}$	−0.483		
S_5	$n_{CO} \rightarrow \pi^*_{CC} + \pi^*_{NO2}$	−0.678	4.95	0.0145	$n_{CO} \rightarrow \pi^*_{CC} + \pi^*_{NO2}$	−0.551	5.64	0.0270	$n_{CO} \rightarrow \pi^*_{CC} + \pi^*_{NO2}$	−0.637	5.29	0.0080
	$n_{CO} \rightarrow \pi^*_{CC} + \pi^*_{CO}$	0.494							$n_{CO} \rightarrow \pi^*_{CC} + \pi^*_{CO}$	0.608		
S_6	$\pi_{CC}1 \rightarrow \pi^*_{CC} + \pi^*_{NO2}$	0.843	5.30	0.1335	$\pi_{CC}1 \rightarrow \pi^*_{CC} + \pi^*_{NO2}$	0.759	5.45	0.1114	$\pi_{CC}1 \rightarrow \pi^*_{CC} + \pi^*_{NO2}$	0.783	5.50	0.1355
S_7	$\pi_{CC}1 \rightarrow \pi^*_{CC} + \pi^*_{CO}$	0.633	5.82	0.0872	$\pi_{CC}1 \rightarrow \pi^*_{CC} + \pi^*_{CO}$	−0.556	5.95	0.1575	$\pi_{CC}1 \rightarrow \pi^*_{CC} + \pi^*_{CO}$	0.667	5.96	0.1809
S_8	$\pi_{CC}2 \rightarrow \pi^*_{CC} + \pi^*_{CO}$	−0.558	6.20	0.1421	$\pi_{CC}2 \rightarrow \pi^*_{CC} + \pi^*_{CO}$	0.768	6.22	0.2609	$\pi_{CC}2 \rightarrow \pi^*_{CC} + \pi^*_{CO}$	0.899	6.21	0.2151
S_9	$P_{NO2} \rightarrow \pi^*_{CC} + \pi^*_{NO2}$	−0.559	6.21	0.2038	$P_{NO2} \rightarrow \pi^*_{CC} + \pi^*_{NO2}$	0.648	6.53	0.1535	$P_{NO2} \rightarrow \pi^*_{CC} + \pi^*_{NO2}$	0.719	6.54	0.2023
S_{10}	$n_{CO} \rightarrow \pi^*_{CC} - \pi^*_{NO2}$	0.584	6.31	0.0050	$n_{CO} \rightarrow \pi^*_{CC} - \pi^*_{NO2}$	0.570	6.83	0.0186	$n_{CO} \rightarrow \pi^*_{CC} - \pi^*_{NO2}$	0.665	6.63	0.0103
S_{11}	$n_{NO2}1 \rightarrow \pi^*_{CC} + \pi^*_{CO}$	−0.372	6.55	0.1556	$n_{NO2}1 \rightarrow \pi^*_{CC} + \pi^*_{CO}$	0.543	6.49	0.0761	$n_{NO2}1 \rightarrow \pi^*_{CC} + \pi^*_{CO}$	0.682	6.77	0.0259

Fig. 2. Correlation diagram showing the excitation energies of complex **1** and **3** (see Fig. 1) relative to the *o*-NBA. Energies in eV calculated with RI-CC2/TZVP.

spond to electronic excitations from the lone pair of the CHO group into the $\pi^*_{CC}+\pi^*_{NO2}$ and the $\pi^*_{CC}+\pi^*_{CO}$ orbitals, both being positive linear combination of π^*_{CC} from the benzene and the π^*_{NO2} and π^*_{CO} orbitals, respectively, (see Fig. 3). Upon coordination of a single water molecule to the CHO, complex **1**, or to the NO_2 group, complex **3**, the three $n\pi^*$ excited states with big contribu-

Orbitals	*o*-NBA	*o*-NBA-H₂O 1	*o*-NBA-H₂O 3
$\pi_{CC} + \pi_{CO}$			
$n_{NO2}1$			
$n_{NO2}2$			
P_{NO2}			
n_{CO}			
$\pi_{CC}1$			
$\pi_{CC}2$			
$\pi^*_{CC} + \pi^*_{NO2}$			
$\pi^*_{CC} + \pi^*_{CO}$			
$\pi^*_{CC} - \pi^*_{NO2}$			
$\pi^*_{CC} - \pi^*_{CO}$	—		

Fig. 3. RI-CC2 optimized orbitals participating in the electronic excited states of *o*-NBA and 1:1 water complexes.

tions of excitations into the $\pi^*_{CC}+\pi^*_{NO2}$ orbital (S_1, S_2 and S_5) shift to higher energies, while the excited state with the large contribution of the n_{CO} $\rightarrow \pi^*_{CC}+\pi^*_{CO}$ transition (S_3) stabilizes, see Table 3 and Figure 2. This stabilization is likely due to the fact that the $\pi^*_{CC}+\pi^*_{CO}$ orbital is stabilized when going
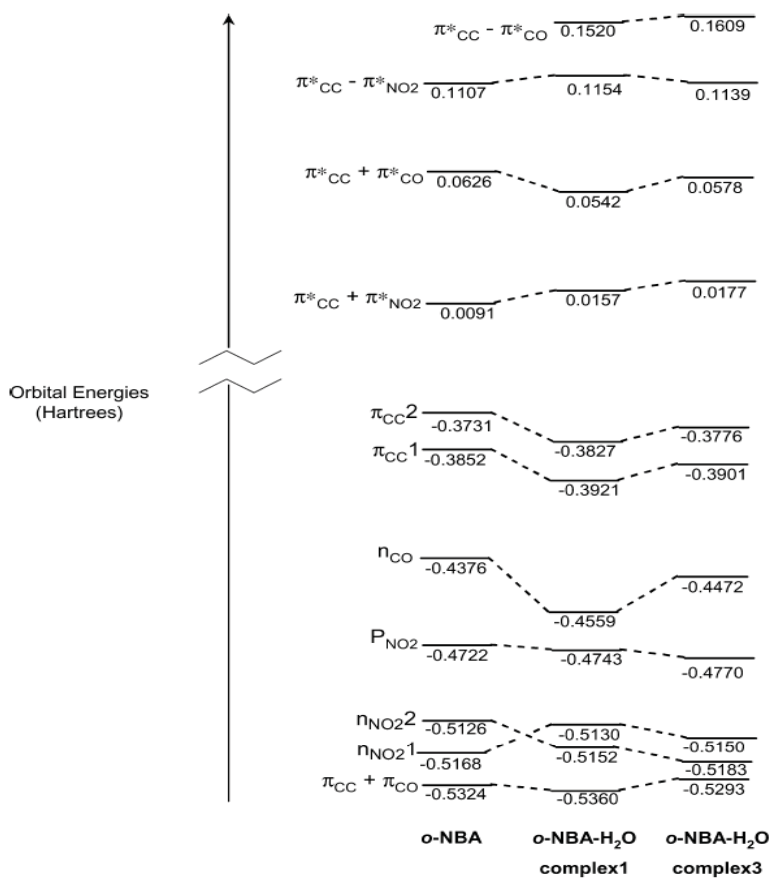
Fig. 4. Correlation diagram showing the orbital energies of *o*-NBA and complexes **1** and **3**. Energies in Hartrees.

from the isolated *o*-NBA to complex **1** or complex **3** (see Fig. 4). The simultaneous red-shift of the $n_{CO} \rightarrow \pi^*_{CC}+\pi^*_{CO}$ excited state and the blue-shift of the other $n \rightarrow \pi^*_{CC}+\pi^*_{NO2}$ transition leads to the inversion of the excitations contributing to the weak broad tail of the experimental absorption spectrum in the gas phase. Thus, the $n_{CO} \rightarrow \pi^*_{CC}+\pi^*_{CO}$ transition becomes the first excited state in complex **3** and the second in complex **1**. The magnitude of the oscillator strengths of these $n\pi^*$ states (cf. Table 3) is similar to the one calculated for the system in gas phase. Therefore, no changes concerning this weak band should be expected in the experimental spectrum.

The effect of water on the π(benzene) $\rightarrow \pi^*$(nitro) excitations (S_4 and S_6), which contribute to the first intense absorption band at 250 nm in gas phase are less significant than those found in the $n\pi^*$ excitations. Water complexation leads to the stabilization of the π_{CC1} and π_{CC2} orbitals of the benzene moiety, see Fig. 4. This, together with the destabilization of the $\pi^*_{CC}+\pi^*_{NO2}$ orbital, accounts for a blue-shift associated to the $\pi_{CC1} \rightarrow \pi^*_{CC}+\pi^*_{NO2}$ transition and the $\pi_{CC2} \rightarrow \pi^*_{CC}+\pi^*_{NO2}$ excited states. Moreover, the large stabilization observed in

the n_{CO} orbital in complex **1** justifies the inversion among the $n_{CO} \rightarrow \pi^*_{CC}+\pi^*_{NO2}$ and the $\pi_{CC1} \rightarrow \pi^*_{CC}+\pi^*_{NO2}$ excitations. Even if the addition of a water molecule does not affect the ordering of the states contributing to this band, important changes occur in the calculated oscillator strengths. While the intense $\pi_{CC1} \rightarrow \pi^*_{CC}+\pi^*_{NO2}$ excitation in the *o*-NBA keeps its strength in the two complexes, the $\pi_{CC2} \rightarrow \pi^*_{CC}+\pi^*_{NO2}$ transition trebles its intensity in the *o*-NBA-water clusters.

From the comparison of the energies collected in Table 3 and the examination of Fig. 2, it is possible to conclude that excitations from the benzene moiety into the aldehyde group, contributing to the first and second intense bands peaking at 250 and 220 nm in gas phase, remain almost unaffected upon water complexation (see S_7 and S_8 excited states in Table 3). In this case, both pairs of orbitals involved in the excitations, namely the π_{CC1}, π_{CC2} and $\pi^*_{CC}+\pi^*_{CO}$, stabilize in the water complexes, hence leading to excitation energies very similar to the ones calculated for isolated *o*-NBA.

Finally, let us discuss the changes in the calculated transitions contributing to the experimental band at 220 nm. The $P_{NO2} \rightarrow \pi^*_{CC}+\pi^*_{NO2}$ excitation (S_9) is shifted to higher energies in the complexes **1** and **3** while the S_{11} excited state, $n_{NO2} \rightarrow \pi^*_{CC}+\pi^*_{CO}$, is red-shifted in complex **1** but blue-shifted in **3**. As a consequence, the $P_{NO2} \rightarrow \pi^*_{CC}+\pi^*_{NO2}$ and $n_{NO2} \rightarrow \pi^*_{CC}+\pi^*_{CO}$ transitions are swapped in complex **1** with respect to the gas phase. The large stabilization of the $n_{NO2}1 \rightarrow \pi^*_{CC}+\pi^*_{CO}$ state can also be explained in terms of the changes experienced by the orbital energies upon complexation. The $n_{NO2}1$ orbital in complex **1** lies higher in energy with respect to *o*-NBA; as mentioned above, the virtual orbital $\pi^*_{CC}+\pi^*_{CO}$ is stabilized. The net effect is then a decrease in the excitation energy of the state S_{11} in the complex **1**. In what the intensity is concerned, this band should not show dramatic changes with respect to the one in gas phase. As it can be seen in Table 3, the increase of oscillator strength of the state S_8 is compensated by the decrease in S_{11}.

4. Conclusion

In the present study the effect of a water molecule on the electronic properties of a nitrobenzyl-based caging group has been investigated. All possible configurations of the 1:1 *o*-NBA-water complex, except the one with water interacting with the electronic π system have been optimized. All the isomers lie within few kJ/mol above the most stable one; thus, all of them are expected to be experimentally accessible. The structural changes and effects on the intramolecular H-Bond of *o*-NBA have been carefully analyzed, also by means of the topological analysis of the charge density. In general, the strength of this intramolecular H-Bond is not much affected except for the complex where the water molecule is simultaneously interacting with the H of the CHO and the O of the NO_2 group.

The influence of a water molecule in the UV absorption spectrum of *o*-NBA has been examined by comparing the vertical excitation energies and oscillator strengths of the system in gas phase with that of two of the most stable isomers in which water is attached to the aldehyde and nitro group, respectively. The absorption spectrum of the two complexes considered is very similar and shifted to the blue with respect to the spectrum in gas phase. The spectrum of *o*-NBA is gas phase consists of three bands [7], which can also be distinguished in the 1:1 water complexes. The major changes on going from gas to condensed phase refer to the order in which the excited states appear within each band but not to the band composition. Experimentally, besides the blue-shift, a change in the intensities of the three bands should be observed. According to the CC2 calculations, the first and third bands should maintain their respective intensities with respect to the gas phase spectrum, while the central one should be much more intense in water solution.

Acknowledgement

References

1. J. A. McCray, D. R. Trentham, Annu. Rev. Biophys. Biophys. Chem. **18** (1989) 239.
2. S. R. Adams, R. Y. Tsien, Annu. Rev. Physiol. **55** (1993) 755.
3. G. Ciamician, P. Silber, Ber. Dtsch. Chem. Ges. **34** (1901) 2040.
4. M. V. George, J. C. Scaiano, J. Phys. Chem. **84** (1980) 492.
5. S. Laimgruber, W. J. Schreier, T. Schrader, F. Koller, W. Zinth, P. Gilch, Angew. Chem. Int. Ed. **44** (2005) 7901.
6. R. W. D. K. Sharma, Res. Chem. Intermed. **11** (1989) 109.
7. V. Leyva, I. Corral, T. Schmierer, B. Heinz, F. Feixas, A. Migani, L. Blancafort, P. Gilch, L. González, J. Phys. Chem. A **112** (2008) 5046.
8. O. Christiansen, H. Koch, P. Jorgensen, Chem. Phys. Lett. **243** (1995) 409.
9. B. O. Roos, *in K.P. Lawley (Ed.), Ab initio Methods in Quantum Chemistry II, Wiley.* Chichester (1987).
10. T. H. Dunning Jr., J. Chem. Phys. **90** (1989) 1007.
11. R. A. Kendall, T. H. Dunning Jr., R. J. Harrison, J. Chem. Phys. **96** (1992) 6796.
12. A. D. Becke, J. Chem. Phys. **98** (1993) 1372.
13. C. Lee, W. Yang, R. G. Parr, Phys. Rev. B: Condens. Matter **37** (1988) 785.
14. L. González, O. Mó, M. Yáñez, J. Comp. Chem. **18** (1997) 1124.
15. L. González, O. Mó, M. Yáñez, J. Chem. Phys. **109** (1998) 139.

16. L. González, O. Mó, M. Yáñez, J. Elguero, J. Molec. Struct. (Theochem) **371** (1996) 1.
17. K. Müller-Dethlefs, P. Hobza, Chem. Rev. **100** (2000) 143.
18. A. K. Rappé, E. R. Bernstein, J. Phys. Chem. A **104** (2000) 6117.
19. S. F. Boys, F. Bernardi, Mol. Phys. **19** (1970) 553.
20. M. J. Frisch, G. W. Trucks, H. B. Schlegel, G. E. Scuseria, M. A. Robb, J. R. Cheeseman, J. Montgomery, T. Vreven, K. N. Kudin, J. C. Burant, J. M. Millam, S. S. Iyengar, J. Tomasi, V. Barone, B. Mennucci, M. Cossi, G. Scalmani, N. Rega, G. A. Petersson, H. Nakatsuji, M. Hada, M. Ehara, K. Toyota, R. Fukuda, J. Hasegawa, M. Ishida, T. Nakajima, Y. Honda, O. Kitao, H. Nakai, M. Klene, X. Li, J. E. Knox, H. P. Hratchian, J. B. Cross, V. Bakken, C. Adamo, J. Jaramillo, R. Gomperts, R. E. Stratmann, O. Yazyev, A. J. Austin, R. Cammi, C. Pomelli, J. W. Ochterski, P. Y. Ayala, K. Morokuma, G. A. Voth, P. Salvador, J. J. Dannenberg, V. G. Zakrzewski, S. Dapprich, A. D. Daniels, M. C. Strain, O. Farkas, D. K. Malick, A. D. Rabuck, K. Raghavachari, J. B. Foresman, J. V. Ortiz, Q. Cui, A. G. Baboul, S. Clifford, J. Cioslowski, B. B. Stefanov, G. Liu, A. Liashenko, P. Piskorz, I. Komaromi, R. L. Martin, D. J. Fox, T. Keith, M. A. Al-Laham, C. Y. Peng, A. Nanayakkara, M. Challacombe, P. M. W. Gill, B. Johnson, W. Chen, M. W. Wong, C. Gonzalez, J. A. Pople, Gaussian 03, Revision C.02 Gaussian, Inc., Wallingford CT (2004).
21. R. F. W. Bader, *Atoms in Molecules: A Quantum Theory*. Clarendon Press, Oxford, England (1990).
22. C. Hättig, F. Weigend, J. Chem. Phys. **113** (2000) 5154.
23. A. Schäfer, C. Huber, R. Ahlrichs, J. Chem. Phys. **100** (1994) 5829.
24. K. Sakotaa, N. Yamamotob, K. Ohashia, M. Saekic, S. Ishiuchic, M. Sakaic, M. Fujiic, H. Sekiya, Chem. Phys. **283** (2002) 209.
25. K. R. F. Somers, A. Ceulemans, Chem. Phys. **301** (2004) 61.
26. R. B. Zhang, K. R. F. Somers, E. S. Kryachko, M. T. Minh Tho Nguyen, T. Zeegers-Huyskens, A. Ceulemans, J. Phys. Chem. A **109** (2005) 8028.
27. R. Crespo-Otero, L. A. Montero, W.-D. Stohrer, J. M. García de la Vega, J. Chem. Phys. **123** (2005) 134107.
28. J. Moc, J. Panek, Chem. Phys. Lett. **419** (2006) 362.

Article 3.4.3. A comparative analysis of the UV/Vis absorption spectra of nitrobenzaldehydes

Verónica Leyva, Inés Corral, Thomas Schmierer, Peter Gilch and Leticia González

PCCP

PAPER

A comparative analysis of the UV/Vis absorption spectra of nitrobenzaldehydes†

Verónica Leyva,[a] Inés Corral,*[b] Thomas Schmierer,[cd] Peter Gilch[cd] and Leticia González*[a]

In a joint experimental and theoretical study, the UV/Vis absorption spectra of the three isomers (*ortho, meta, para*) of nitrobenzaldehyde (NBA) were analyzed. Absorption spectra are reported for NBA vapors, cyclohexane and acetonitrile solutions. All spectra are poor in vibronic structure and hardly affected in shape by the surroundings (vapor or solution). Moderate solvatochromic shifts of ~ -0.2 eV are measured. For all isomers vertical transition energies, oscillator strengths, and excited state dipole moments were computed using the MS-CASPT2/CASSCF and CC2 methods. Based on these calculations the experimental transitions were assigned. The spectra of all isomers are characterized by weak ($\varepsilon_{max} \approx 100$ M^{-1} cm^{-1}) transitions around 350 nm (3.6 eV), arising from $n\pi^*$ absorptions starting from the lone pairs of the nitro and aldehyde moieties. The next band of intermediate intensity peaking around 300 nm (4.2 eV, $\varepsilon_{max} \approx 1000$ M^{-1} cm^{-1}) is dominated by $\pi\pi^*$ excitations within the arene function. Finally, strong absorptions ($\varepsilon_{max} \approx 10\,000$ M^{-1} cm^{-1}) were observed around 250 nm (5.0 eV) which we ascribe to $\pi\pi^*$ excitations involving the nitro and benzene groups.

1. Introduction

The substitution pattern of nitrobenzenes strongly affects their photoreactivity. While *meta*(*m*)- and *para*(*p*)-substituted nitrobenzenes are usually photochemically inert, the *ortho*(*o*)-derivatives commonly photoreact with high quantum yields provided that the substituent contains hydrogen atom(s).[1] The obvious rationale for this observation is that photoexcitation triggers a transfer of a hydrogen atom from the *ortho*-substituent to the nitro group. The transfer is ensued by further reactions which eventually result in the formation of the photoproduct. For *o*-nitrobenzaldehyde (*o*-NBA) femtosecond spectroscopy showed that this transfer involves excited singlet and triplet states.[2–5] The transfer *via* the singlet channel is dominant and occurs on the time scale of some 100 fs.[4] In a comparative study[3] on all three isomers of nitrobenzaldehyde it has been shown that the reactive isomer (*o*-NBA) does not differ substantially from the non-reactive isomers in terms of

fluorescence decay patterns. For all isomers photoexcitation to an upper singlet state results in an ultrafast (<100 fs) decay of the fluorescence emission. A slower component (~ 0.5–1 ps) of the decay carries only a very small amplitude (0.01 of the initial signal). The tentative interpretation of this observation has been that an initially excited (bright) $\pi\pi^*$ state decays *via* internal conversion and populates a "darker" $n\pi^*$ state.[3] Hydrogen transfer (*o*-NBA) and/or intersystem crossing (*o,m,p*-NBA) in turn depopulate this state.

We are presently working on a firmer interpretation based on high-level quantum chemistry and quantum dynamics. As a part of this effort, we here present a joint experimental and theoretical study on the vertical excitation energies and oscillator strengths of nitrobenzaldehydes. This work is an extension of an earlier investigation[6] focusing on *o*-NBA only. For the sake of completeness these results will be briefly reviewed below. The paper is organized as follows. Absorption spectra of the three isomers as vapors and in cyclohexane and acetonitrile solutions will be presented. These environments were chosen for two reasons. Vapor spectra were recorded to facilitate the comparison with the quantum chemical computations which were conducted for vacuum conditions. Further measured solvatochromic shifts should show trends on the changes of dipole moments upon excitation. Then the electronic ground state of the three isomers will be characterized in terms of equilibrium geometries by means of quantum chemical computations. Thereby, also the issue of conformational variety and aromaticity will be addressed. Based on the computed

[a] *Institut für Physikalische Chemie, Friedrich-Schiller-Universität Jena, Helmholtzweg 4, 07743 Jena, Germany*
[b] *Departamento de Química C-9, Universidad Autónoma de Madrid, Cantoblanco, 28049 Madrid, Spain*
[c] *Fakultät für Physik, Ludwig-Maximilians-Universität München, Oettingenstr. 67, 80538 München, Germany*
[d] *Institut für Physikalische Chemie, Heinrich-Heine-Universität Düsseldorf, Universitätsstr. 1, 40225 Düsseldorf, Germany*
† Electronic supplementary information (ESI) available: Full assignment (including molecular orbitals) of the MS-CASPT2/CASSCF and CC2 vertical spectra. See DOI: 10.1039/c0cp01372b

This journal is © the Owner Societies 2011

Phys. Chem. Chem. Phys., 2011, **13**, 4269–4278 | 4269

geometries, vertical excitation energies, oscillator strengths, and permanent dipole moments in the excited state will be evaluated. These computational results will then be compared with the experimental spectra to arrive at a consistent assignment of the transitions responsible for the UV/Vis spectra.

2. Experimental methods

All experimental spectra presented were measured with a commercial dual beam spectrograph (Perkin Elmer, Lambda 19). Cyclohexane (Merck, Uvasol) and acetonitrile (Sigma Aldrich, spectrophotometric grade, ≥ 99.5 %) were used as solvents. o-Nitrobenzaldehyde was purchased from Merck, m- and p-NBA from Sigma-Aldrich. All of them were used as received. For the solution spectra the samples were held in 1 mm fused silica cells. Typical concentrations were in the range of 0.3–1 mM. To obtain gas phase spectra a heatable home-built cell was used. This cell was of cylindrical shape and featured a path length of 10.4 cm. Front and back of the cylinder consisted of a double layer of optical windows (fused silica) with a spacing of ~1 mm in between. The cylindrical body of the cell was encircled by a brazen pipe. Water with a temperature of 90 °C was flown through the pipe to heat up the nitrobenzaldehyde sample and generate a vapor pressure sufficient to obtain spectra. The hot water also flowed through the spacing of the front and back windows. Thereby crystallization of the sample on the windows was prevented. Typical optical densities at absorption maxima were of the order of 0.1–0.5.

3. Computational details

Ground state structures for the isomers were optimized before computing the UV spectra. The optimization in the electronic ground state relied on density functional calculations using the B3LYP functional and the 6-311G(d,p) basis set. This level of theory demonstrated for o-NBA[6] a good agreement with the available X-ray geometry.[7] The B3LYP approach includes Becke's three parameter hybrid exchange potential[8] and the Lee Yang Parr correlation functional.[9] The optimizations were performed with GAUSSIAN-03 suite programs.[10]

An energy decomposition analysis (EDA) has been performed to estimate the effect of the substituents on the aromaticity of the system in the ground state. A detailed description of this method can be found e.g. in ref. 11–14. EDA can provide useful information on the π conjugation and the nature of the bonds[15] or even explain the way the position of the substituents can influence a reaction site through resonance and field/inductive effects.[16] EDA calculations have been performed at the BP86/TZ2P level of theory[17–19] and the ADF code[12,20,21] fragmenting the system into three parts: the benzene ring, the aldehyde and the nitro group.

The vertical UV absorption spectra have been calculated on the optimized geometries by means of the second order coupled cluster (CC2) method[22] and the multi-state second order perturbation theory[23] on complete active space self consistent field wave functions[24] (MS-CASPT2/CASSCF). MS-CASPT2/CASSCF prescription has been shown to be one of the most accurate ones to calculate excitation energies,

with errors ranging from 0.1 to 0.3 eV.[25] Errors in the calculation of the oscillator strengths are much more difficult to quantify. Guided by the results obtained in our earlier study on o-NBA[6] the CAS reference wave functions have been built with two different active spaces, namely 16 electrons in 12 orbitals (16,12) and 12 electrons in 11 orbitals (12,11). The (16,12) active space aims to describe the nπ* transitions starting from the lone pairs of the nitro and aldehyde groups. Therefore, it includes three lone pairs, two from the nitro group and one from the aldehyde group, and additionally two pairs of π_{CC}/π^*_{CC} orbitals from the benzene ring, one pair of π_{CO}/π^*_{CO} from the aldehyde group, one pair of π_{NO2}/π^*_{NO2}, and a non-bonding π orbital P_{NO2} from the nitro group (see Fig. S1 and S2, ESI†). Since it is not possible to include the whole π system and the lone pairs in the same active space, we designed the smaller (12,11) active space to account for the high energy ππ* transitions at the expense of excluding the lone pairs. Specifically, this active space includes three π_{CC}/π^*_{CC} pairs from the aromatic moiety, one pair of π_{CO}/π_{CO}^* from the aldehyde group, the pair of π_{NO2}/π^*_{NO2}, and the non-bonding π orbital P_{NO2} from the nitro group. The calculations for the p- and m-NBA isomers are done within C_s symmetry, while the earlier calculation for o-NBA was performed without symmetry.[6] Accordingly, the (16,12) active space calculations were performed as one root for the ground state of A′ symmetry and as state-average (SA) over three roots for the electronic excited states of A″ symmetry (nπ* excitations). The (12,11) calculations were done with state averaging over 4 roots of A′ symmetry, which includes the ground state and three ππ* excited states. The weight is the same for all the states considered.

The dynamical correlation has been introduced by means of the second order perturbation theory on the SA-CASSCF wave functions. To remedy the appearance of intruder states, the level-shift technique[26] with a parameter of 0.3 a.u. has been used. Oscillator strengths have been obtained with the RAS state interaction method (RASSI)[27] using MS-CASPT2 energies and perturbation modified CAS (PM-CAS) transition dipole moments. The large atomic natural orbital basis set ANO-L,[28] contracted as C,O,N[4s3p2d]/H[3s2p], has been employed in all the multiconfigurational calculations. MS-CASPT2/CASSCF and CC2 vertical excited spectra have been computed using MOLCAS 6.0 software[29] and the Turbomole package,[30] respectively.

4. Experimental results

The spectra of the three isomers exhibit many commonalities so their properties will be described jointly; differences among them are mentioned on the way. The nitrobenzaldehydes start absorbing at wavelengths smaller than 400 nm (3.1 eV), see Fig. 1. In the spectral range of 200–400 nm (6.20–3.10 eV) four bands are directly discernible (by the band shape analysis described below more bands will be resolved). Their peak extinction increases with decreasing wavelength. The bands of lowest transition energy are centered at ~350 nm (3.6 eV). Their extinction coefficients at the peak are of the order of 100 M^{-1} cm^{-1}. These lowest energy bands do not exhibit any vibronic structure. The bands second lowest in energy peak

102

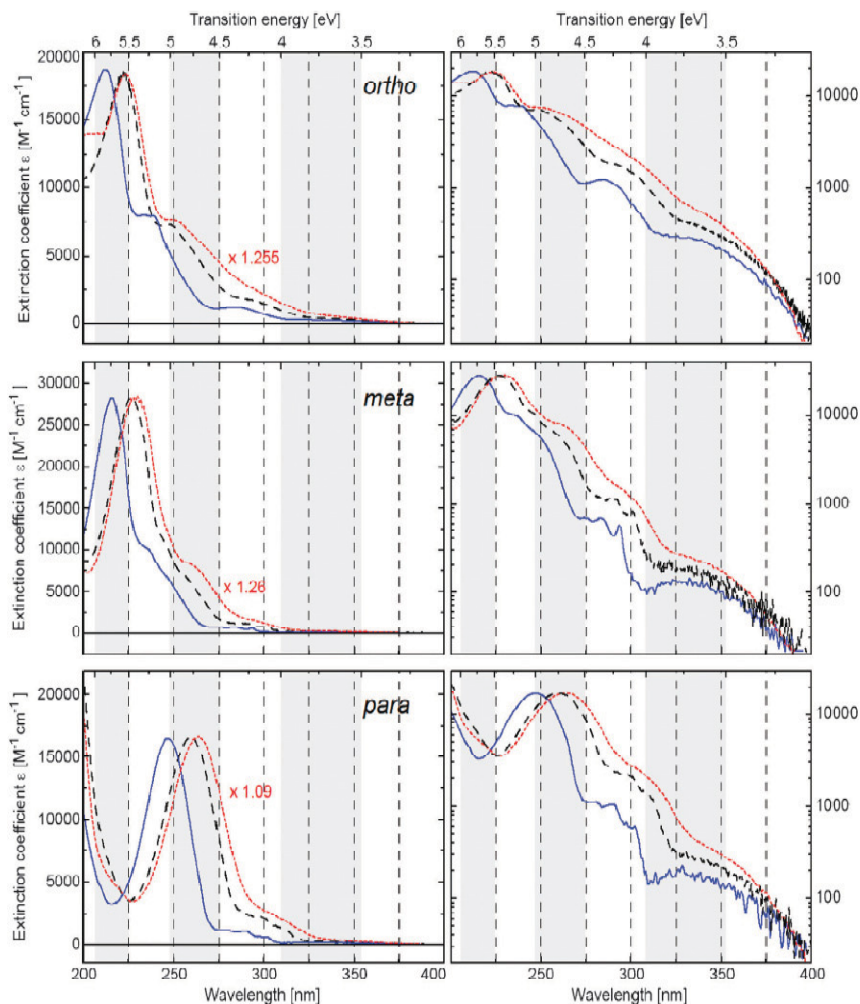**Fig. 1** UV/Vis absorption spectra of the three isomers of nitrobenzaldehyde in different surroundings. The extinction coefficients in M^{-1} cm^{-1} are plotted *versus* a linear wavelength axis (lower *x*-axis). An energy scale is given by the upper *x*-axis. In the spectra on the left the extinction axis is linear, on the right it is logarithmic to highlight weaker transition. For the sake of comparison all spectra were normalized to the peak value of NBA dissolved in cyclohexane (black dashed line). The necessary scaling factor for NBA in acetonitrile (red dotted line) is given in the graph. For the NBA vapour (blue solid line) the scaling factor in terms of extinction coefficient could not be evaluated.

around 300 nm (4.2 eV) and exhibit extinction coefficients of around 1000 M^{-1} cm^{-1}. For the *meta*- and *para*-isomers a vibronic progression is observed in non-polar surroundings. Around 250 nm (5.0 eV) bands with extinction coefficients of ~10 000 M^{-1} cm^{-1} are located. These bands lack a vibronic structure. The bands highest in energy in the spectral range covered are centered at ~225 nm (5.6 eV)—except for the *para*-isomer, for which it is located at wavelengths smaller than 200 nm (6.2 eV). The extinction coefficients exceed 10 000 M^{-1} cm^{-1} and the bands are structureless. Gas phase and solution spectra are very similar in shape. The same observation has been made for nitrobenzene[31] and *o*-ethylnitrobenzene.[6] This suggests that intramolecular mechanisms mostly hold responsible for broad spectral features. With increasing

polarity (gas phase, cyclohexane, and acetonitrile) all bands move to longer wavelengths, *i.e.* the bands exhibit positive solvatochromism.

For a more quantitative assessment of band positions, solvent shifts, and oscillator strengths, the experimental spectra were subjected to a fitting procedure using a sum of Gaussians as trial functions (for the justification of this approach see ref. 6). It has to be stressed that a Gaussian is only an approximation for the true vibronic envelope of an electronic transition. It may well be that more than one Gaussian is required for the description of the envelope or that two transitions are described by one Gaussian. Thus, the statement "one Gaussian stands for one transition" must not be made. Fitting of the spectra required 7–8 Gaussians. In our

This journal is © the Owner Societies 2011

Phys. Chem. Chem. Phys., 2011, **13**, 4269–4278 | **4271**
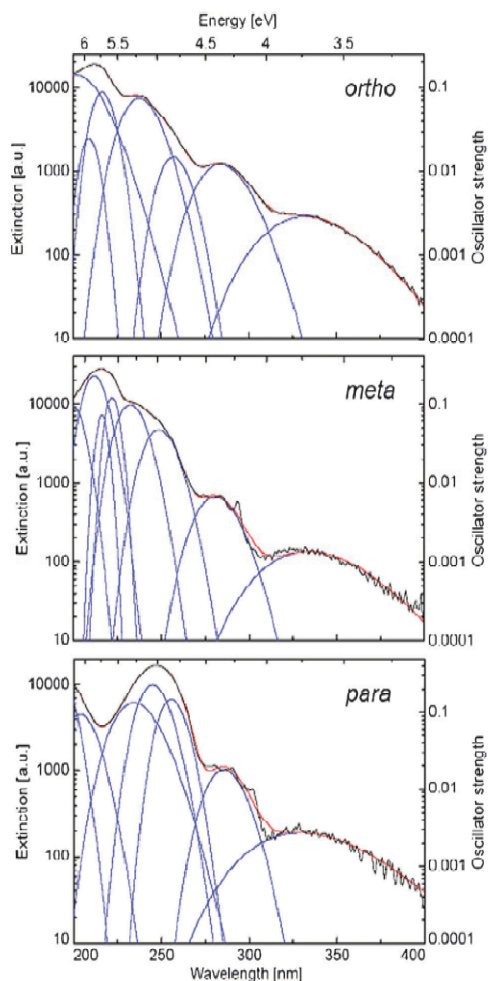
103

Fig. 2 Gaussian decomposition of the UV/Vis absorption spectra (black lines) of the three NBA isomers as vapours. The extinction coefficients were obtained by scaling the measured absorption spectra so that the highest vapour extinction equals the highest value in cyclohexane solution (cf. Fig. 1). The Gaussian components are represented by blue lines, their sum by the red lines. Note that the y-axis is logarithmic.

previous analysis[6] on o-NBA in solution (acetonitrile) 6 Gaussians sufficed to describe the spectrum. For the present vapor spectrum, which exhibits more structure, a better description is obtained using 7 Gaussians. The quality of the fits for vapor data can be assessed from Fig. 2 and the numerical results for all environments are compiled in Table 1. The oscillator strength f_i for each Gaussian is based on the following equation:[32]

$$f_i = 4.32 \times 10^{-9} \int \varepsilon_i(\tilde{v}) \mathrm{d}\tilde{v} \qquad (1)$$

Hereby, ε_i is the extinction coefficient of the Gaussian component measured in units $M^{-1} cm^{-1}$ as a function of the wavenumber $\tilde{v}$ in cm^{-1}. The values refer to one Gaussian, i.e. not necessarily to one electronic transition. Since for the NBA vapors concentrations were not determined, extinction coefficients and thereby oscillator strengths f_i could not be calculated. The oscillator strengths f_i given in Table 1 were determined for cyclohexane solutions.

For all three isomers one determines Gaussians centered around 3.8 eV (vapour value) featuring oscillator strengths of ~0.01. A second Gaussian with a comparable strength is located at 4.3 eV. The third Gaussian at ~4.8 eV exceeds these strengths by roughly one order of magnitude. Whereas for the first three Gaussians all isomers resemble each other, stronger differences are observed for those located at higher energies. The fourth Gaussians of o-NBA and m-NBA are centered on 5.3 eV, the o-NBA Gaussian being by a factor of three higher in oscillator strength. For p-NBA the fourth Gaussian is lower in energy (5.06 eV) and carries substantial oscillator strength. Differences are more pronounced for the fifth Gaussian being located at 5.73 eV ($f_5 = 0.098$, o-NBA), 5.59 eV (0.009, m-NBA), and 5.29 eV (0.100, p-NBA). The sixth Gaussian represents a rather strong transition ($f \approx 0.15$) and peaks around ~5.9 eV. Values for the seventh Gaussian are subject to a substantial error for o-NBA and p-NBA since their maxima are located outside the spectral range covered. For m-NBA a Gaussian with a larger oscillator strength of 0.420 peaks at 5.86 eV.

The positions of all Gaussians experience solvatochromic shifts. Except for the first Gaussians and the Gaussians at the high energy edge of the spectrum the following trend is observed. Going from gas phase to cyclohexane solution causes a peak shift of ~ −0.2 eV (i.e. to lower energies). Going to the more polar solvent, acetonitrile, induces an additional

Table 1 Compilation of the results from the Gaussian decomposition of the spectra of the three isomers depicted in Fig. 1. The centres of the Gaussians are given in eV. The respective oscillator strengths for the NBA isomers dissolved in cyclohexane were computed using eqn (1)

	ortho				meta				para			
No.	Vapour (eV)	Cyclohexane (eV)	Oscillator strength	Acetonitrile (eV)	Vapour (eV)	Cyclohexane (eV)	Oscillator strength	Acetonitrile (eV)	Vapour (eV)	Cyclohexane (eV)	Oscillator strength	Acetonitrile (eV)
1	3.73	3.74	0.011	3.61	3.72	3.88	0.008	3.67	3.76	3.63	0.006	3.61
2	4.37	4.21	0.022	4.21	4.42	4.27	0.011	4.26	4.34	4.17	0.028	4.11
3	4.82	4.76	0.083	4.70	4.99	4.86	0.110	4.68	4.85	4.61	0.090	4.55
4	5.22	5.03	0.047	4.96	5.34	5.06	0.016	5.06	5.06	4.84	0.190	4.79
5	5.73	5.48	0.098	5.48	5.59	5.31	0.009	5.28	5.29	5.14	0.100	5.05
6	5.93	5.65	0.170	5.66	5.74	5.42	0.230	5.42	6.08	5.84	0.110	6.03
7	6.14	6.28	—	6.09	5.86	5.61	0.420	5.74	6.48	6.40	—	6.31
8					6.21	6.91	—	6.32				

104

shift of 0.05 eV. The observation that a larger shift is caused for the change of gas phase to unpolar solvent as compared to the change of unpolar to polar solution is in line with predictions of a Lippert–Mataga treatment.[33] In principle such a treatment can afford dipole moments of excited states. Yet, to deduce dipole moments from the experimental data they need to be parallel for ground and excited states—otherwise the problem is under-determined. For none of the isomers symmetry fixes the direction of the dipole moment and therefore the moments of different states do not need to be parallel. Indeed, the quantum chemical calculations described below show that the directions of the dipole moments differ. A treatment based on *the assumption* that the dipole moments are parallel predicts dipole moments of the excited states which are by 2–3 D larger than that of the ground state.

5. Computational results

5.1 Ground state equilibrium structures

Transition energies were computed on the ground state geometries obtained at the B3LYP/6-311G(d,p) level of theory. The optimized structures will be compared with diffraction data when available. X-ray structures have been reported for the *ortho*-[7] and *para*-[34] isomers. To our knowledge, there are no diffraction data on *m*-NBA. A detailed description of

the *o*-NBA structure can be found in ref. 6. Briefly, DFT calculations and diffraction data[7,35] agree that the hydrogen atom of the aldehyde substituent points to the nitro group (see Fig. 3). *o*-NBA adopts a non-planar structure. The angle which the nitro group and the benzene plane span amounts to 30° and the angle between the aldehyde function and the ring equals 30°. This distortion is the result of a balance between minimizing the steric hindrance of the NO_2 and CHO groups while forming a hydrogen bond between both fragments. Note that although the existence of this hydrogen bond has been questioned in the literature,[35,36] a topographic analysis of the charge density in *o*-NBA reveals a clear interaction between the O atom of the nitro group and the aldehyde hydrogen in the gas phase structure.[37] Also as a consequence of these two effects, the C_4–C_5 bond distance in *o*-NBA stretches by almost 0.02 Å, as compared to the other isomers.

For the *meta*-isomer one expects two conformers which differ in the orientation of the aldehyde group. The two conformers, labelled *m*-NBA(1) and *m*-NBA(2), are inter-connected through the rotation of the C_3–C_7 single bond, passing *via* a transition state, *m*-NBA(TS), at an intermediate angle. Both conformers are planar. In line with an earlier investigation[38] the two conformers are energetically almost degenerate (see Fig. 3), *m*-NBA(2) being just 0.02 eV less stable than *m*-NBA(1). Assuming a negligible difference in
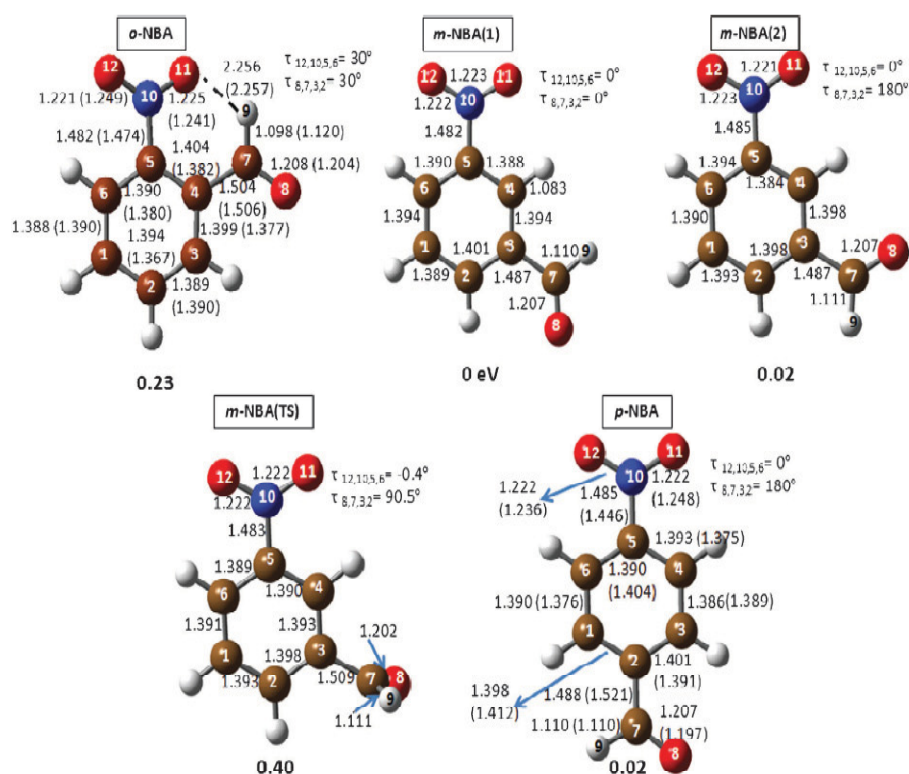

Fig. 3 Ground state equilibrium geometry and relative energies in eV of the three isomers of nitrobenzaldehyde and that of the transition state connecting the two *meta*-conformers as obtained from B3LYP/6-311G(d,p) optimisations. Values in parentheses correspond to experimental values when available.[7,34] Bond distances are in angstroms and bond angles in degrees.

105

entropy this indicates that at room temperature both conformers co-exist. Consequently, both will contribute to the same extent to the UV absorption spectrum. The height of the energy barrier associated with the TS (170i cm^{-1}) amounts to 0.40 eV with respect to the most stable conformer, m-NBA(1). The interconversion between the two conformers should thus be slow on spectroscopic time scales. The slightly higher stability of the m-NBA(1) isomer compared to m-NBA(2) could be explained in terms of the electrostatic interactions between the oxygen atoms of the NO$_2$ or carbonyl groups and their adjacent hydrogens. The m-NBA(1) and m-NBA(2) are structurally very similar. The out-of-plane distortion of the aldehyde fragment in the TS leads to a slightly stretched C$_3$–C$_7$ distance by 0.022 Å compared to the planar molecules.

As in the two $meta$-isomers, the nitro and aldehyde groups of the $para$-isomer are coplanar with the plane of the arene ring, in agreement with the X-ray structure.[34] The $para$-isomer lies at $ca.$ 0.02 eV above the most stable m-NBA(1) isomer. Its geometry is very similar to that of the m-NBA isomers. In comparison to the $ortho$-isomer, the most significant differences are found in the C–C bond that connects the aldehyde group with the arene ring. This bond is shorter in p- and m-NBA, and therefore stronger, due to the lack of the hydrogen bond present in o-NBA.[37]

Quite interesting is the comparison of the structure of the aldehyde group for all the isomers. While one would expect the $ortho$-isomer to have the largest C$_7$–H$_9$ distance, since it participates in the hydrogen bond with the NO$_2$ group, m-NBA(1), m-NBA(2) and p-NBA exhibit C–H bonds longer by 0.015 Å with respect to o-NBA. Once more, it is the balance between the strength of the intramolecular hydrogen bond and the steric constraints between the two substituents that conditions the geometry of the aldehyde group.

After discussing the relative energies and geometrical differences of the three isomers, it is useful to compare them in terms of aromaticity. Below we summarize the results of the EDA on the $ortho$-, $meta$-, and $para$-substituted NBA, see Table 2. The total interaction energy ΔE_{int} corresponds to the sum of the electrostatic, Pauli repulsion and orbital terms, ΔE_{elstat}, ΔE_{Pauli} and ΔE_{orb}. The ΔE_{orb} energy can be partitioned into the σ and π bonding contributions, ΔE_σ and ΔE_π. Since o-NBA is not planar, the partition of ΔE_{orb} into its

π- and σ-components was not possible for this isomer. From the examination of the obtained energies it appears that σ contributions are much larger than π, indicating that the σ-bonding is stronger than π-bonding in all isomers. Moreover, we observe that the ΔE_π energies for the $para$- and $meta$-isomers are very similar. Therefore, no significant differences due to conjugation effects are expected in the spectra of the three isomers ($vide\ infra$).

5.2 Computed vertical transition energies and spectral assignment

In order to assign the experimental bands, gas phase vertical excitation energies with their corresponding oscillator strengths have been computed at the CC2 and MS-CASPT2 levels of theory. The results from the Gaussian decomposition of the experimental spectra for the three NBA isomers are compiled in Table 1. Tables 3, 4 and 5 collect the results obtained with CC2 and MS-CASPT2 theories. The involved orbitals of the $meta$- and $para$-isomers are shown in Fig. S1 and S2, ESI.†

For completeness, we briefly review here the absorption spectrum of o-NBA,[6] see Table 3. Although the values obtained with CC2 and MS-CASPT2 are not identical, general statements regarding the interpretation of the spectrum of the three isomers can be made. The lowest part of the spectrum is characterized by nπ* absorptions from the NO$_2$ and CHO groups, appearing at energies below $ca.$ 4.2 eV. (Energies referring to theoretical values are denoted as eV$_t$, experimental values eV$_e$.) In the following experimental values are vapour phase transition energies and oscillators strengths based on fitting the cyclohexane spectra ($cf.$ Table 1). Both types of computations assign the weak and broad low energy band to the S$_1$–S$_3$ transitions. The S$_4$ and S$_5$ are $\pi\pi$* excitations at the MS-CASPT2 level of theory, responsible for the band at 4.96 eV$_e$. CC2 intercalates one additional state, which allows to associate one-to-one the three experimental Gaussians at 4.37, 4.82 and 5.22 eV$_e$ with S$_4$, S$_5$ and S$_6$. The most intense band is centred at 5.93 eV$_e$ and it is characterized by an excitation within the NO$_2$ group and calculated at 5.55 eV$_t$ by MS-CASPT2 and at 6.20 eV$_t$ by CC2.

Similar to o-NBA, the lowest energy region of the spectra of m-NBA and p-NBA is composed of one weak band peaking in the experiment at 3.72 eV$_e$ and 3.76 eV$_e$ which we ascribe to nπ* transitions (see Tables 4 and 5). These bands are assigned to the S$_1$, S$_2$, and S$_3$ states of the two conformers, m-NBA(1) and m-NBA(2), as well as to the same states for p-NBA. In m- and p-NBA, our calculations, at both levels of theory, yield transitions of nπ* character whereby n orbitals, located at the nitro as well as the carbonyl function, are involved. The electron accepting π* orbitals are situated at the nitro and carbonyl functions as well as at the benzene ring ($cf.$ Tables S1 and S2 and Fig. S1 and S2 in the ESI†). Since vibronic couplings are not incorporated in the theoretical calculations, negligible oscillator strengths for the nπ* states of the planar $meta$- and $para$-isomers are obtained.

We assign the band at 4.42 eV$_e$ to the sum of the S$_4$ states of the two conformers of m-NBA, which are theoretically predicted to absorb around 4.30 eV$_t$ or 4.83 eV$_t$ at MS-CASPT2 and

Table 2 Energy decomposition analysis for o-, m- and p-NBA at the BP86/TZ2P//B3LYP/6-311G(d,p) level of theory. Energies are in eV

	o-NBA	m-NBA(1)	m-NBA(2)	p-NBA
ΔE_{Int}/eV	−6.77	−7.55	−7.50	−8.04
ΔE_{Pauli}/eV	31.30	32.18	31.99	34.31
ΔE_{elstat}[a]/eV	−13.63	−14.45	−14.38	−15.54
%	35.8	36.4	36.4	36.7
ΔE_{orb}[a]/eV	−24.43	−25.28	−25.12	−26.81
%	64.2	63.6	63.6	63.3
ΔE_σ[b]/eV	—	−23.75	−23.68	−25.31
%	—	93.9	94.0	94.4
ΔE_π[b]/eV	—	−1.53	−1.50	−1.50
%	—	6.1	6.0	5.6

[a] The percentages give the contribution to the total attractive ΔE_{elstat} + ΔE_{orb}. [b] The percentages give the contribution to the orbital interactions ΔE_{orb}.

4274 | *Phys. Chem. Chem. Phys.*, 2011, **13**, 4269–4278

This journal is © the Owner Societies 2011

106

Table 3 MS-CASPT2/CASSCF and CC2 excitation energies ΔE (in eV and nm), oscillator strengths f, and results of the Gaussian decomposition of the experimental spectrum of o-NBA

o-NBA

MS-CASPT2/CASSCF			RI-CC2				Experiment		
States	ΔE (eV, nm)	f	States	ΔE (eV, nm)	f	Assignment	Gauss center (eV, nm)		f
S_1	3.33	372	0.00	S_1	3.62	343	0.012	$n \to \pi^*$	3.73	332	0.011

MS-CASPT2/CASSCF			RI-CC2				Experiment		
States	ΔE (eV, nm)	f	States	ΔE (eV, nm)	f	Assignment	Gauss center (eV, nm)	f	
S_1 3.33 372 0.00			S_1 3.62 343 0.012			$n \to \pi^*$	3.73 332	0.011	

States	ΔE (eV, nm)	f	States	ΔE (eV, nm)	f	Assignment	Gauss center (eV, nm)	f
S_1	3.33 372	0.00	S_1	3.62 343	0.012	$n \to \pi^*$	3.73 332	0.011
S_2	3.82 324	0.00	S_2	4.09 303	0.001	$n \to \pi^*$		
S_3	3.88 319	0.00	S_3	4.11 301	0.004	$n \to \pi^*$		
S_4	4.45 278	0.01	S_4	4.57 271	0.007	$\pi \to \pi^*$	4.37 284	0.022
—			S_5	4.95 250	0.015	$n \to \pi^*$	4.82 257	0.083
S_5	4.94 251	0.23	S_6	5.30 234	0.134	$\pi \to \pi^*$	5.22 238	0.047
—			S_7	5.82 213	0.087	$\pi \to \pi^*$	5.73 216	0.098
S_6	5.55 223	0.05	S_8	6.20 200	0.142	$P_{NO_2} \to \pi^*/\pi \to \pi^*$	5.93 209	0.170
			S_9	6.21 200	0.204	$P_{NO_2} \to \pi^*/\pi \to \pi^*$	6.14 202	—

Table 4 MS-CASPT2/CASSCF and CC2 excitation energies ΔE (in eV and nm), oscillator strengths f, and results of the Gaussian decomposition of the experimental spectrum of m-NBA

m-NBA(1)							m-NBA(2)							m-NBA		
MS-CASPT2/CASSCF			RI-CC2				MS-CASPT2/CASSCF			RI-CC2				Experiment		
States^a	ΔE (eV, nm)	f	States	ΔE (eV, nm)	f	Assignment	States^a	ΔE (eV, nm)	f	States	ΔE (eV, nm)	f	Assignment	Gauss center (eV, nm)		f
S_1	3.63 341	0.000	S_1	3.92 316	0.000	$n \to \pi^*$	S_1	3.60 344	0.000	S_1	3.93 315	0.000	$n \to \pi^*$	3.72 334	0.008	
S_2	3.74 331	0.000	S_2	4.00 310	0.000	$n \to \pi^*$	S_2	3.69 336	0.000	S_2	4.00 310	0.000	$n \to \pi^*$			
S_3	4.16 298	0.000	S_3	4.58 271	0.000	$n \to \pi^*$	S_3	4.13 300	0.000	S_3	4.57 271	0.000	$n \to \pi^*$			
S_4	4.29 289	0.002	S_4	4.83 257	0.010	$\pi \to \pi^*$	S_4	4.30 288	0.001	S_4	4.83 256	0.003	$\pi \to \pi^*$	4.42 281	0.011	
—			S_5	5.58 222	0.000	$n \to \pi^*$	—			S_5	5.54 224	0.000	$n \to \pi^*$	4.99 249	0.110	
S_5	5.02 247	0.159	S_6	5.63 220	0.106	$\pi \to \pi^*$	S_5	5.43 229	0.051	S_6	5.79 214	0.081	$\pi \to \pi^*$	5.34 232	0.016	
—			S_7	6.12 203	0.436	$\pi \to \pi^*$	—			S_7	6.09 204	0.591	$\pi \to \pi^*$	5.59 222	0.009	
—			S_8	6.33 196	0.000	$n \to \pi^*$	—			S_8	6.19 200	0.000	$n \to \pi^*$	5.74 216	0.230	
S_6	5.74 216	0.031	S_9	6.35 195	0.285	$P_{NO_2} \to \pi^*/\pi \to \pi^*$	S_6	5.79 214	0.013	S_9	6.22 199	0.050	$P_{NO_2} \to \pi^*/\pi \to \pi^*$	5.86 212	0.420	

^{a} The first three excited states (S_1–S_3) are computed with the active space CAS(16,12) and states S_4–S_6 are calculated with CAS(12,11).

Table 5 MS-CASPT2/CASSCF and CC2 excitation energies ΔE (in eV and nm), oscillator strengths f, and results of the Gaussian decomposition of the experimental spectrum of p-NBA

p-NBA

MS-CASPT2/CASSCF			RI-CC2				Experiment		
States^a	ΔE (eV, nm)	f	States	ΔE (eV, nm)	f	Assignment	Gauss center (eV, nm)		f
S_1	3.53 352	0.000	S_1	3.83 324	0.000	$n \to \pi^*$	3.76 330		0.006
S_2	3.60 344	0.000	S_2	3.94 315	0.000	$n \to \pi^*$			
S_3	4.04 307	0.000	S_3	4.51 275	0.000	$n \to \pi^*$			
S_4	4.19 296	0.008	S_4	4.74 262	0.018	$\pi \to \pi^*$	4.34 286		0.028
S_5	4.85 256	0.373	S_5	5.47 227	0.454	$\pi \to \pi^*$	4.85 256		0.090
—			S_6	6.24 199	0.000	$n \to \pi^*$	5.06 245		0.190
							5.29 234		0.100
S_6	5.57 223	0.024	S_7	6.29 197	0.023	$P_{NO_2} \to \pi^*$	6.08 204		0.110
			S_8	6.45 192	0.000	$n \to \pi^*$	6.48 191.3		—
			S_9	6.76 183	0.149	$\pi \to \pi^*$			
			S_{10}	6.89 180	0.063	$\pi \to \pi^*$			

^{a} The first three excited states (S_1–S_3) are computed with the active space CAS(16,12) and states S_4–S_6 are calculated with CAS(12,11).

CC2, respectively (see Table 4). For p-NBA the experimental value is 4.34 eV$_e$ and the calculations deliver an energy of 4.19 eV$_t$ (MS-CASPT2) or 4.74 eV$_t$ (CC2). This transition exhibits a (weak) vibronic progression. For all isomers the transitions involve promotions of electrons from benzene centred π orbitals to π^* orbitals located at the benzene ring and the nitro group.

Going to higher energies the absorption spectra of the isomers are substantially different, requiring separated discussions of the isomers. For m-NBA, the two experimental Gaussians that decompose the band at $ca.$ 5.3 eV$_e$ are due to the S_5 states of both $meta$-conformers, at 5.02 and 5.43 eV$_t$ (MS-CASPT2), or due to the S_6 states at 5.63 and 5.79 eV$_t$ (CC2). Note that the CC2 method intercalates one dark $n\pi^*$ state, which does

107

not contribute to the spectrum. The energies of the S_5 state of the two *meta*-conformers differ by about 0.4 eV (MS-CASPT2) or 0.2 eV (CC2). This energy gap is much larger than for any other transition (Table 4); this is due to the fact that the orbitals involved in these transitions are not of the same nature for both isomers. The most intense band centred at *ca.* 5.7 eV$_e$ is decomposed in terms of three Gaussians, which can be assigned with the help of CC2 to the $S_7(1)$, $S_7(2)$, $S_9(1)$ and $S_9(2)$ (S_8 is a dark nπ^* state), while with MS-CASPT2 only provides one transition with the number of states calculated. These are all $\pi\pi^*$ transitions with the participation of the nitro and carbonyl groups.

In the experimental *p*-NBA spectrum a very intense and broad absorption peaking around 4.96 eV$_e$ is recorded. The best experimental description of this band is done with three

Gaussians centred at 4.85, 5.06, and 5.29 eV$_e$. However, in this spectral range the computations predict only the S_5 state at 4.85 eV$_t$ (MS-CASPT2) or the combination of the S_5 state at 5.47 eV$_t$ and a weak nπ^* absorption at 6.24 eV$_t$ (CC2), see Table 5. The bright states correspond to $\pi\pi^*$ transitions that partially involve charge transfer from the benzene ring to the nitro group. The next absorbing states contribute to the band highest in energy, which is also characterized by aromatic transitions including the P_{NO2} non-bonding orbital.

In general, we observe that the excitation energies obtained with CC2 are blue-shifted with respect to MS-CASPT2 values by *ca.* 0.3 eV and 0.6 eV for the nπ^* and $\pi\pi^*$ excitations, respectively. Not surprisingly, the energy values obtained multiconfigurationally for the main peaks are in better agreement with the experiment, while the CC2 values are in many cases
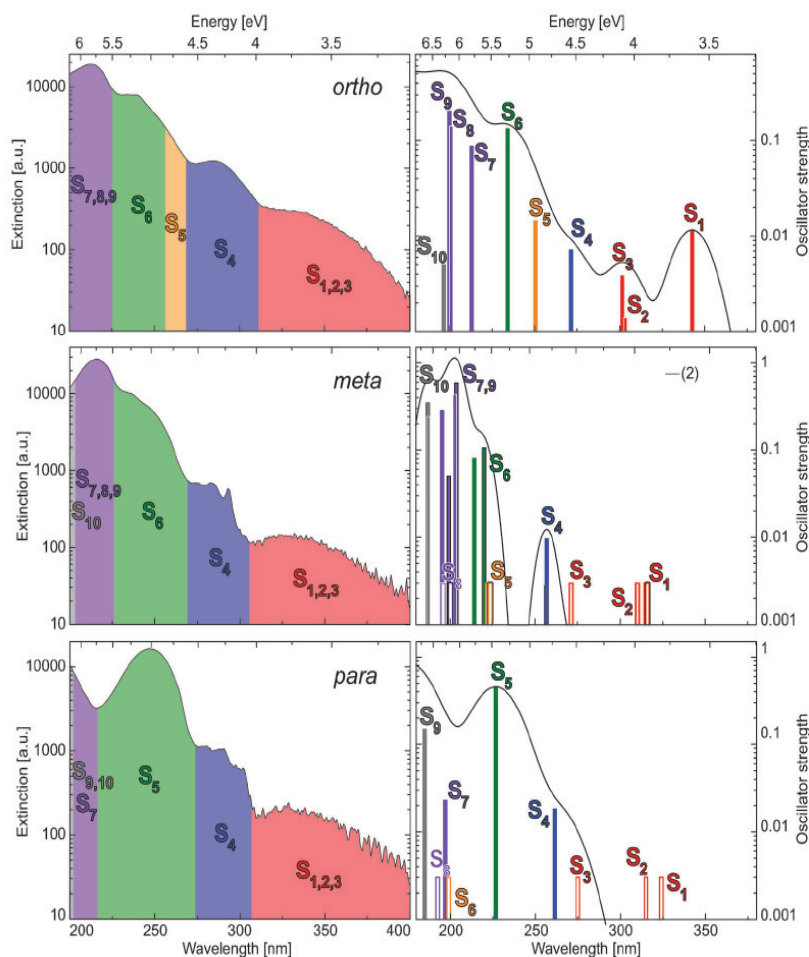
Fig. 4 Comparison of computed (CC2) spectra of the three isomers of NBA with experimental vapour spectra. In the right panels transition energies and oscillator strengths are represented by coloured bars. Since for the *m*- and *p*-NBA the calculations cannot reproduce the experimental intensity of the nπ^* transitions that is due to vibronic effects, the strengths of corresponding transitions (represented by open bars) have arbitrarily been set to 0.01. The *meta*(1)-conformer of the *meta*-isomer is distinguished from the *meta*(2)-conformer by the solid black lines surrounding the bars. For the sake of comparison with the experimental data, smooth *ortho*-, *meta*- and *para*-spectra were generated by convoluting each transition with a Gaussian of 12, 5.5 and 14 nm full width at half maximum (FWHM), respectively. For the *meta*-isomer spectra of the two conformers were averaged.

overestimated. However, the single reference CC2 method, which can describe a much large number of states in a single calculation, is better suited to assign individual Gaussians, as deconvoluted from the experimental spectrum. Interestingly, the oscillator strengths predicted by CC2 are in better agreement with the intensity of the experimental bands than those calculated by MS-CASPT2. Fig. 4 (right) shows the simulated *ab initio* spectrum using CC2 excitations and oscillator strengths. Disregarding the energetic shifts, the agreement of the CC2 spectra with the experimental ones is reasonable, in particular for intense bands located at high energies. As stated above, the computations cannot reproduce the experimental intensity of the band associated with $n\pi^*$ transitions of *m*- and *p*-NBA. Therefore, only the transition energies of the lowest energy band of these two isomers can be compared with the experiments. For the non-planar *o*-NBA the computations yield (relative) transition strengths for these states in reasonable agreement with the experiment.

Finally, we discuss the solvatochromic shifts and the dipole moments of the excited states. The discussion will be restricted to the *ortho*- and *para*-isomers. The two conformers of the *meta*-isomer differ already substantially (by ~3 D) in their ground state dipole moments.[38] Thus, the two conformers are expected to exhibit different solvatochromic effects. In the experiment only a "superposition" of these effects is measured. The MS-CASPT2/CASSCF computation yields a dipole moment of 4.22 D for the ground state of *o*-NBA (see Table 6) close to the experimental value of 4.6 D.[39] Except for the S_4 and S_5 states the computed excited state dipole moments are slightly smaller than that of the S_0 state. The dipole moments of the excited states span angles in between ~2° and 40° with the moment of the ground state. An analysis based on a Lippert–Mataga treatment[33] (data not shown) incorporating the vector character of the dipole moments shows that for all except the S_4 and S_5 states shifts to higher frequencies with increasing polarity should occur. This predication is not in line with the experiment.

Similarly, for *p*-NBA one computes a S_0 dipole moment of 2.78 D comparable to the experimental value of 2.39 D.[40] Except for the S_1 and S_5 states all moments are smaller than that of the ground state. The angles spanned by the moments cover a broader range (2°–90°) than the angles for *o*-NBA. A "vector" Lippert–Mataga treatment only predicts shifts to lower frequencies for the S_1 and S_5 states. In the experiment all transitions shift to lower frequencies. At present we cannot

state whether this discrepancy is due to flaws in the Lippert–Mataga treatment or to errors connected to the calculated dipole moments. In any case, one cannot rely on the solvatochromic shifts to corroborate the band assignment provided by the theoretical calculations.

6. Conclusions

The electronic absorption spectra of the three isomers *o*-, *m*-, and *p*-NBA have been analyzed, both experimentally and with the help of multiconfigurational MS-CASPT2/CASSCF and CC2 calculations. Their spectra are all characterized by weak transitions ($\varepsilon_{max} \approx 100$ M^{-1} cm^{-1}) centered around 3.5 eV. These transitions could be attributed to the promotions of electrons from n-orbitals, located at the nitro- as well as the carbonyl-function, to π^* orbitals. Stronger transitions ($\varepsilon_{max} \approx 1000$ M^{-1} cm^{-1}) at ~4 eV involve π- and π^*-orbitals of the benzene ring. For *m*- and *p*-NBA a faint vibronic structure is observed. At higher energies the spectra of *o*- and *m*-NBA are very similar exhibiting shoulders at ~5.3 eV and a peak at ~5.8 eV. Shoulders and peaks could be attributed to $\pi\pi^*$-transitions with a strong charge transfer (CT)-character. The *para*-isomer features a strong band at about 5 eV enclosing presumably two electronic transitions of CT-character.

The spectra of all isomers experience solvatochromic shifts of ~−0.20 eV (gas phase → cyclohexane) and ~−0.25 eV (gas phase → acetonitrile). The differences of the shifts induced by the various solvents are not very pronounced. Photoreactivity and stability do not show up in the UV/Vis spectra. The spectrum of the photoreactive *ortho*-isomer resembles that of the photostable *meta*-isomer. The two spectra in turn differ from the spectrum of the photostable *para*-isomer. In line with that, ultrafast fluorescence decays were recorded for all isomers.[3] In these experiments the excitation was tuned to 260 nm (4.77 eV) addressing $\pi\pi^*$ states with CT character for all isomers. These states decay within ≤100 fs resulting in a strong (two orders of magnitude) reduction of the fluorescence signal. This reduction is in line with the population of $n\pi^*$ states which—as this study shows—are one to two orders of magnitude weaker in oscillator strength.

Acknowledgements

Table 6 Dipole moments (in D) for *o*- and *p*-NBA of ground and excited states computed at the MS-CASPT2/CASSCF level of theory. Modulus of the moments as well as the angles (in degrees) spanned between ground and excited state moments are given

	$\|\mu_{ii}\|/D$ *o*-NBA	Θ_{0i}/degrees	$\|\mu_{ii}\|/D$ *p*-NBA	Θ_{0i}/degrees
S_0	4.223		2.784	
S_1	3.320	21.5	4.714	33.3
S_2	2.939	14.6	1.770	55.9
S_3	2.751	1.9	1.793	49.3
S_4	5.034	5.6	2.695	1.9
S_5	8.184	11.3	5.027	20.0
S_6	2.670	38.1	2.428	90.2

Notes and references

1 A. P. Pellicciolli and J. Wirz, *Photochem. Photobiol. Sci.*, 2002, 1, 441.
2 S. Laimgruber, W. J. Schreier, T. Schrader, F. Koller, W. Zinth and P. Gilch, *Angew. Chem., Int. Ed.*, 2005, 44, 7901.

3 B. Heinz, T. Schmierer, S. Laimgruber and P. Gilch, *J. Photochem. Photobiol., A*, 2008, **199**, 274.
4 S. Laimgruber, T. Schmierer, P. Gilch, K. Kiewisch and J. Neugebauer, *Phys. Chem. Chem. Phys.*, 2008, **10**, 3872.
5 T. Schmierer, W. J. Schreier, F. O. Koller, T. E. Schrader and P. Gilch, *Phys. Chem. Chem. Phys.*, 2009, **11**, 11596.
6 V. Leyva, I. Corral, T. Schmierer, B. Heinz, F. Feixas, A. Migani, L. Blancafort, P. Gilch and L. Gonzalez, *J. Phys. Chem. A*, 2008, **112**, 5046.
7 P. Coppens and G. M. J. Schmidt, *Acta Crystallogr.*, 1964, **17**, 222.
8 A. D. Becke, *J. Chem. Phys.*, 1993, **98**, 1372.
9 C. T. Lee, W. T. Yang and R. G. Parr, *Phys. Rev. B: Condens. Matter*, 1988, **37**, 785.
10 M. J. Frisch, G. W. Trucks, H. B. Schlegel, G. E. Scuseria, M. A. Robb, J. R. Cheeseman, J. A. Montgomery, T. Vreven, K. N. Kudin, J. C. Burant, J. M. Millam, S. S. Iyengar, J. Tomasi, V. Barone, B. Mennucci, M. Cossi, G. Scalmani, N. Rega, G. A. Petersson, H. Nakatsuji, M. Hada, M. Ehara, K. Toyota, R. Fukuda, J. Hasegawa, M. Ishida, T. Nakajima, Y. Honda, O. Kitao, H. Nakai, M. Klene, X. Li, J. E. Knox, H. P. Hratchian, J. B. Cross, V. Bakken, C. Adamo, J. Jaramillo, R. Gomperts, R. E. Stratmann, O. Yazyev, A. J. Austin, R. Cammi, C. Pomelli, J. W. Ochterski, P. Y. Ayala, K. Morokuma, G. A. Voth, P. Salvador, J. J. Dannenberg, V. G. Zakrzewski, S. Dapprich, A. D. Daniels, M. C. Strain, O. Farkas, D. K. Malick, A. D. Rabuck, K. Raghavachari, J. B. Foresman, J. V. Ortiz, Q. Cui, A. G. Baboul, S. Clifford, J. Cioslowski, B. B. Stefanov, G. Liu, A. Liashenko, P. Piskorz, I. Komaromi, R. L. Martin, D. J. Fox, T. Keith, A. Laham, C. Y. Peng, A. Nanayakkara, M. Challacombe, P. M. W. Gill, B. Johnson, W. Chen, M. W. Wong, C. Gonzalez and J. A. Pople, *Gaussian 03, Revision C.02*, Gaussian, Inc., Wallingford CT, 2004.
11 F. M. Bickelhaupt and E. J. Baerends, *Rev. Comput. Chem.*, 2000, **15**, 1.
12 G. te Velde, F. M. Bickelhaupt, E. J. Baerends, S. J. A. van Gisbergen, C. Fonseca Guerra, J. G. Snijders and T. Ziegler, *J. Comput. Chem.*, 2001, **22**, 931.
13 T. Ziegler and A. Rauk, *Theor. Chim. Acta*, 1977, **46**, 1.
14 K. Morokuma, *J. Chem. Phys.*, 1971, **55**, 1236.
15 A. Kovács, C. Esterhuysen and G. Frenking, *Chem.–Eur. J.*, 2005, **11**, 1813.
16 I. Fernández and G. Frenking, *J. Org. Chem.*, 2006, **71**, 2251.
17 A. D. Becke, *J. Phys. Chem. A*, 1988, **38**, 3098.
18 J. P. Perdew, *J. Phys. Chem. B*, 1986, **33**, 8822.
19 J. G. Snijders, E. J. Baerends and P. Vernooijs, *At. Data Nucl. Data Tables*, 1982, **26**, 483.
20 C. Fonseca Guerra, J. G. Snijders, G. te Velde and E. J. Baerends, *Theor. Chem. Acc.*, 1998, **99**, 391.
21 E. J. Baerends, J. Autschbach, D. Bashford, A. Bérces, F. M. Bickelhaupt, C. Bo, P. M. Boerrigter, L. Cavallo, D. P. Chong, L. Deng, R. M. Dickson, D. E. Ellis, M. van Faassen, L. Fan, T. H. Fischer, C. Fonseca Guerra, A. Ghysels, A. Giammona, S. J. A. van Gisbergen, A. W. Götz, J. A. Groeneveld, O. V. Gritsenko, M. Grüning, F. E. Harris, P. van den Hoek, C. R. Jacob, H. Jacobsen, L. Jensen, G. van Kessel, F. Kootstra, M. V. Krykunov, E. van Lenthe, D. A. McCormack, A. Michalak, M. Mitoraj, J. Neugebauer, V. P. Nicu, L. Noodleman, V. P. Osinga, S. Patchkovskii, P. H. T. Philipsen, D. Post, C. C. Pye, W. Ravenek, J. I. Rodríguez, P. Ros, P. R. T. Schipper, G. Schreckenbach, M. Seth, J. G. Snijders, M. Solà, M. Swart, D. Swerhone, G. te Velde, P. Vernooijs, L. Versluis, L. Visscher, O. Visser, F. Wang, T. A. Wesolowski, E. M. van Wezenbeek, G. Wiesenekker, S. K. Wolff, T. K. Woo, A. L. Yakovlev and T. Ziegler, ADF2009.01, SCM, Theoretical Chemistry, Vrije Universiteit, Amsterdam, The Netherlands, 2009, http://www.scm.com.
22 O. Christiansen, H. Koch and P. Jorgensen, *Chem. Phys. Lett.*, 1995, **243**, 409.
23 J. Finley, P. A. Malmqvist, B. O. Roos and L. Serrano-Andres, *Chem. Phys. Lett.*, 1998, **288**, 299.
24 B. O. Roos, *Ab initio Methods in Quantum Chemistry II*, ed. K. P. Lawley, Wiley, Chichester, 1987.
25 I. Corral and L. González, *J. Comput. Chem.*, 2008, **29**, 1982.
26 B. O. Roos and K. Andersson, *Chem. Phys. Lett.*, 1995, **245**, 215.
27 P. A. Malmqvist and B. O. Roos, *Chem. Phys. Lett.*, 1989, **155**, 189.
28 P. O. Widmark, P. A. Malmqvist and B. O. Roos, *Theoret. Chim. Acta*, 1990, **77**, 291.
29 G. Karlström, R. Lindh, P. Å. Malmqvist, B. O. Roos, U. Ryde, V. Veryazov, P. O. Widmark, M. Cossi, B. Schimmelpfennig and P. N. a. L. Seijo, *Comput. Mater. Sci.*, 2003, **28**, 222.
30 R. Ahlrichs, M. Bär, M. Häser, H. Horn and C. Kölmel, *Chem. Phys. Lett.*, 1989, **162**, 165.
31 D. B. Galloway, J. A. Bartz, L. G. Huey and F. F. Crim, *J. Chem. Phys.*, 1993, **98**, 2107.
32 N. J. Turro, V. Ramamurthy and J. C. Scaiano, *Principles of Molecular Photochemistry: An Introduction*, University Science Books, Sausalito, 2009.
33 J. R. Lakowicz, *Principles of Fluorescence Spectroscopy*, Springer, New York, 3rd edn, 2006.
34 J. A. King and G. L. Bryant, *Acta Crystallogr., Sect. C: Cryst. Struct. Commun.*, 1996, **52**, 1691.
35 P. Coppens, *Acta Crystallogr.*, 1964, **17**, 573.
36 S. Pinchas, *Anal. Chem.*, 1957, **29**, 334.
37 V. Leyva, I. Corral and L. Gonzalez, *Z. Phys. Chem.*, 2008, **222**, 1263.
38 A. Konopacka, J. Kalenik and Z. Pawelka, *J. Molec. Struct.*, 2004, **705**, 75.
39 R. J. Sengwa and K. Kaur, *Indian J. Phys., B*, 1999, **73**, 493.
40 C. T. Aw, E. L. K. Tan and H. H. Huang, *J. Chem. Soc., Perkin Trans. 2*, 1972, 1638.

110

Article 3.4.4. Ultrafast irreversible phototautomerization of *o*-nitrobenzaldehyde

Annapaola Migani, Verónica Leyva, Ferran Feixas, Thomas Schmierer, Peter Gilch, Inés Corral, Leticia González and Lluís Blancafort

ChemComm

COMMUNICATION

Ultrafast irreversible phototautomerization of *o*-nitrobenzaldehyde†

Annapaola Migani,‡[a] Verónica Leyva,[b] Ferran Feixas,[a] Thomas Schmierer,[c] Peter Gilch,[c] Inés Corral,§[b] Leticia González[b] and Lluís Blancafort*[a]

o-Nitrobenzaldehyde is photolabile because of an irreversible phototautomerization, whereas comparable aromatic compounds function as photoprotectors because the tautomerization is reversible. In this experimental and theoretical study we track down the cause of this difference to the electronic changes that occur during the tautomerization.

Excited state hydrogen transfer (ESHT) plays an essential role in the functionality of chemical and biological systems.[1] It is also one of the fastest chemical reactions, with time scales as short as 50 fs.[2] In *o*-nitrobenzaldehyde (*o*-NBA), one of the oldest photochemical compounds,[3,4] the intramolecular ESHT occurs within 400 fs after excitation.[5–8] The tautomerization is irreversible and yields a ketene/acid-nitro tautomer (Ket) (Scheme 1), which further reacts to *o*-nitroso benzoic acid. This transformation is on the basis of using *o*-NBA in pH jump experiments.[9] Related nitroarenes also undergo irreversible phototautomerization and are used as photolabile protecting groups.[10] This functionality is different from that found in other aromatic compounds, such as *o*-hydroxybenzaldehyde[11] or *o*-hydroxyphenyltriazole,[12] where ultrafast intramolecular ESHT is reversible, allowing their use as photoprotectors. Thus, the applications of ESHT depend crucially on the reversible or irreversible character of the phototautomerization. In the present

study we combine femtosecond UV/vis transient absorption spectroscopy with high-level *ab initio* calculations (see ESI† for experimental and computational details). For the first time, we have established the mechanism of the irreversible phototautomerization of *o*-NBA and clarified the difference with respect to the photostable compounds.

Recent spectroscopic studies on *o*-NBA detected the Ket intermediate within the first 400 fs after excitation at 258 nm or 268 nm.[5–8] The Ket tautomer is identified by characteristic absorptions at 450 nm (UV/Vis) and 2100 cm^{-1} (IR).[5,6] Here we use femtosecond UV/Vis transient absorption to monitor the Ket formation at low excitation energies (388 nm) and compare with high excitation energies.[6] The UV/Vis transient spectra after 388 nm and 258 nm excitation are plotted in Fig. 1. At 388 nm (black solid line), where a low lying (n,π^*) state is populated, the ketene transient appears within a few hundreds of femtoseconds. In addition, the transient time trace after 258 nm excitation (red dashed line) exhibits a pronounced peak around time zero that decays within the first 100 fs and is assigned to the (π,π^*) state. For either excitation wavelength the transient absorption decays in approximately 1 ns due to the transformation of the ketene to the final nitroso product. The quantum yield of this product is around 0.5 for both wavelengths[13] suggesting that the same mechanism underlies ESHT at both wavelengths. The femtosecond time scale indicates that one or more conical intersections (CIs) enable the fast access to the ground state.

The key mechanistic feature of the tautomerization in *o*-NBA is the relocation of two electrons from the in-plane to the out of plane conjugated orbital system (coded in red and
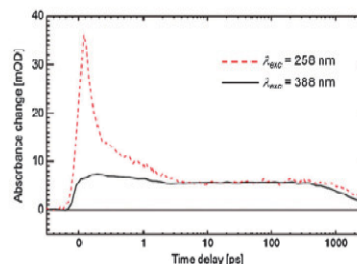

Scheme 1

[a] *Department of Chemistry and Institute of Computational Chemistry, University of Girona, Campus de Montilivi, 17071 Girona, Spain. E-mail: lluis.blancafort@udg.edu; Fax: +34 972418356*
[b] *Institut für Physikalische Chemie, Friedrich Schiller Universität Jena, Helmholtzweg 4, 07743 Jena, Germany*
[c] *Institut für Physikalische Chemie, Heinrich Heine Universität Düsseldorf, Universitätsstr. 1, 40225 Düsseldorf, Germany*

Fig. 1 Femtosecond UV/Vis absorption spectra of *o*-NBA at 450 nm detection wavelength (ketene absorption peak)[4,6] after 388 nm and 258 nm excitation. The time axis is linear until 1 ps and logarithmic thereafter.
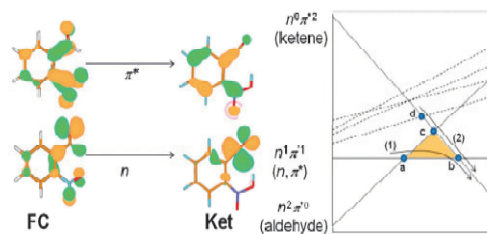
Fig. 2 Orbitals and state correlation diagram for *o*-NBA phototautomerization.

green in Scheme 1, respectively). This determines the correlation diagram for the tautomerization (Fig. 2). Thus, the reactant and product configurations differ in the occupations of an n and a π^* orbital of the reactant. Orbital n is the oxygen lone pair orbital of the aldehyde, which evolves to an anti-bonding orbital of the ketene (see Fig. 2). In the aldehyde ground state configuration, n is doubly occupied and π^* is empty (configuration $n^2\pi^{*0}$), while the ketene ground state has the opposite configuration ($n^0\pi^{*2}$). Consequently, the aldehyde ground state correlates with a high-lying excited state of the ketene, and the ketene ground state with a high-lying aldehyde excited state. There is a third relevant state with an intermediate $n^1\pi^{*1}$ configuration, which correlates with an (n,π^*) state of the aldehyde and a low lying excited state of the ketene. The remaining excited states are displayed with dotted lines. The diagram corresponds to a photochemically allowed, thermally forbidden reaction, and this determines the irreversibility of the phototautomerization. Moreover, it contains several crossings which translate into CIs on the potential energy surface. These CIs are associated with two product formation paths: one along the lower side of the triangle formed by the crossings a, b and c, and one along the cascade formed by d, c and b (paths 1 and 2 in Fig. 2).

The computational results are obtained with the MS CASPT2// CASSCF approach (MS-CASPT2 energies on the CASSCF optimized structures and minimum energy paths). According to our calculations, the state populated after excitation at 388 nm is the (n_{NO_2},π^*) state, which is S_2 at **FC** (calculated vertical excitation 340 nm, oscillator strength 0.02). This state relaxes through an S_2/S_1 crossing to a planar minimum on the S_1 surface, (n,π^*)$_{Min}$. The barrier for hydrogen transfer from this minimum is smaller than 0.1 eV. During the transfer, the path reaches $(S_1/S_0)_{X-HT}$, which corresponds to crossing a of Fig. 2. At this structure, the singly occupied n orbital is delocalized between the aldehyde and nitro moieties (see Fig. 3). After passage through $(S_1/S_0)_{X-HT}$, the reaction path leads to the ground state biradical **Bir** species, with ($n^1\pi^{*1}$) configuration (resonance structure in Fig. 3). The **Bir** transient, which has a bent ketene moiety, is separated from the final product by a barrier of less than 0.1 eV. Along the path, which involves a concerted OCC bend and OH bond rotation, the configuration changes from biradical ($n^1\pi^{*1}$) to ketene ($n^0\pi^{*2}$). This completes the electronic relocation from the in-plane to the out-of-plane orbital system. The change of configuration takes place in the vicinity of a CI between these two states that corresponds to b in Fig. 2 ($(S_1/S_0)_{X-Ket}$ in Fig. 5). The product is the more stable *anti*-**Ket** tautomer. The preference for this conformer contributes to the irreversibility of the tautomerization because the newly formed OH bond points away from the ketene, and the barrier for the reverse hydrogen transfer is 0.8 eV. Mixed classical quantum dynamics calculations consistently show that the formation of *anti*-**Ket** along path 1 takes place on the femtosecond scale.[14]

The state populated by excitation at 258 nm is a (π,π^*) state (calculated vertical excitation 4.5 eV, *i.e.* 279 nm, oscillator strength 0.05). This state relaxes from S_5 at **FC** to a planar minimum on S_3, (π,π^*)$_{Min}$ (Fig. 4), which corresponds to the transient peak observed in the first 100 fs after excitation at 258 nm (Fig. 1).[6] The fast decay of this peak implies that (π,π^*)$_{Min}$ continues to decay very quickly from S_3, and we have considered two possibilities: internal conversion to the S_1 minimum, (n,π^*)$_{Min}$ followed by hydrogen transfer along path 1, and access to path 2. The internal conversion must involve a series of crossings of the (π,π^*) state with other states such as the S_5/S_4 and S_4/S_3 crossings shown in Fig. 4. The complete
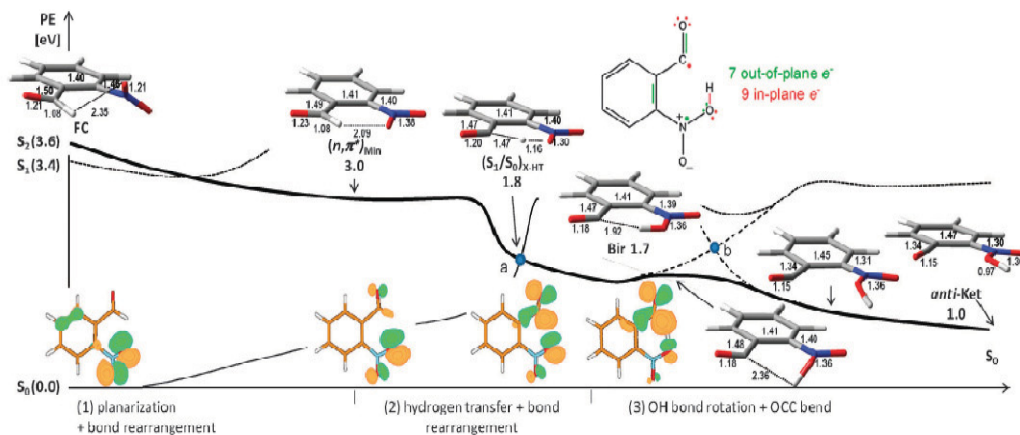

Fig. 3 Energy profiles along the ESHT coordinate on the (n,π^*) state (path 1, lower side of the CI triangle), and plots of the singly occupied n orbital.
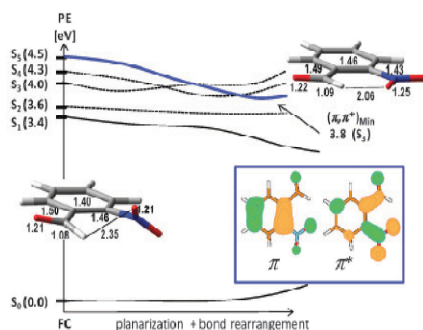
This journal is © The Royal Society of Chemistry 2011

113

Fig. 4 Energy profiles for decay of the (π,π*) state (blue line) after 258 nm excitation. Inset: orbitals involved in the excitation.
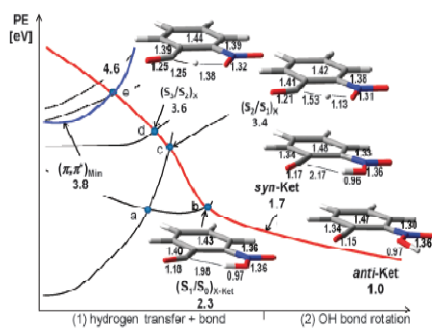

Fig. 5 Energy profiles along the CI cascade on the ketene state (red line, path 2) and access from the bright (π,π*) state (blue line).

decay path has not been optimized because of the high density of states (see ESI†), but internal conversion to S_1 is consistent with the detection of a weakly fluorescent (n,π*) state after the decay of the (π,π*) state.[6] The hydrogen transfer from **(n,π*)$_{Min}$** probably competes with population of the triplet manifold from this minimum.[7]

For the direct tautomerization mechanism along the CI cascade (path 2, see Fig. 5) we have optimized three CIs corresponding to points d, c, and b. They are crossings of the ketene state with a higher lying reactant state ((S$_3$/S$_2$)$_X$), the aldehyde state ((S$_2$/S$_1$)$_X$), and the intermediate (n,π*) ((S$_1$/S$_0$)$_{X-Ket}$). They lie along the hydrogen transfer coordinate, where the energy of the ketene state decreases steeply. This path goes through the *syn*-Ket conformer and continues to *anti*-Ket after rotation of the newly formed OH bond. The barrier to access the cascade from **(π,π*)$_{Min}$** has been estimated by locating the crossing between the (π,π*) and ketene states with a linear interpolation (e in Fig. 5). The resulting value of 0.8 eV is an upper limit to the actual value (see ESI†), but it suggests that internal conversion to S_1 and stepwise ESHT along path 1 will be dominant after excitation at 258 nm. Tunneling could contribute to path 2 because **(π,π*)$_{Min}$** is prearranged for the hydrogen transfer, but the cascade will be more relevant for higher excitation energies.

To conclude, the global mechanistic picture for the ultrafast, irreversible phototautomerization of *o*-NBA consists of a stepwise path involving the (n,π*) state and a direct path with early access to the ketene state. The relocation of two electrons

from the in-plane to the out-of-plane orbitals explains the differences between the intramolecular ESHT of photolabile and photoprotecting compounds. For *o*-NBA, the photo-tautomerization is photochemically allowed and thermally forbidden, similar to the [2+2] cycloaddition textbook example. The back hydrogen transfer is prevented by a barrier, and the new tautomer reacts further to yield the final product.[15] The electronic relocation also makes the reverse tautomerization of *o*-nitrotoluene slow[16] and the phototautomerization of *o*-acylbenzaldehyde irreversible.[17] In contrast, in the aromatic photoprotectors the number of in-plane and out-of-plane electrons remains constant during the tautomerization. As a consequence, the back hydrogen transfer is barrierless and exothermic, laying the ground for the photostability.

Notes and references

1 M. Rini, B. Z. Magnes, E. Pines and E. T. J. Nibbering, *Science*, 2003, **301**, 349; C. Tanner, C. Manca and S. Leutwyler, *Science*, 2003, **302**, 1736; T. Schultz, E. Samoylova, W. Radloff, I. V. Hertel, A. L. Sobolewski and W. Domcke, *Science*, 2004, **306**, 1765.
2 A. Douhal, F. Lahmani and A. H. Zewail, *Chem. Phys.*, 1996, **207**, 477.
3 G. Ciamician and P. Silber, *Ber. Dtsch. Chem. Ges.*, 1901, **34**, 2040; R. W. Yip and D. K. Sharma, *Res. Chem. Intermed.*, 1989, **11**, 109.
4 M. V. George and J. C. Scaiano, *J. Phys. Chem.*, 1980, **84**, 492; S. Kuberski and J. Gebicki, *J. Mol. Struct.*, 1992, **275**, 105.
5 S. Laimgruber, W. J. Schreier, T. Schrader, F. Koller, W. Zinth and P. Gilch, *Angew. Chem., Int. Ed.*, 2005, **44**, 7901.
6 B. Heinz, T. Schmierer, S. Laimgruber and P. Gilch, *J. Photochem. Photobiol., A*, 2008, **199**, 274.
7 S. Laimgruber, T. Schmierer, P. Gilch, K. Kiewisch and J. Neugebauer, *Phys. Chem. Chem. Phys.*, 2008, **10**, 3872.
8 V. Leyva, I. Corral, T. Schmierer, B. Heinz, F. Feixas, A. Migani, L. Blancafort, P. Gilch and L. González, *J. Phys. Chem. A*, 2008, **112**, 5046; T. Schmierer, W. J. Schreier, F. O. Koller, T. E. Schrader and P. Gilch, *Phys. Chem. Chem. Phys.*, 2009, **11**, 11596.
9 T. P. Causgrove and R. B. Dyer, *Chem. Phys.*, 2006, **323**, 2.
10 P. Klan, A. P. Pelliccioli, T. Pospisil and J. Wirz, *Photochem. Photobiol. Sci.*, 2002, **1**, 920.
11 S. Lochbrunner, T. Schultz, M. Schmitt, J. P. Shaffer, M. Z. Zgierski and A. Stolow, *J. Chem. Phys.*, 2001, **114**, 2519; J. D. Coe and T. J. Martinez, *Mol. Phys.*, 2008, **106**, 537; A. Migani, L. Blancafort, M. A. Robb and A. D. DeBellis, *J. Am. Chem. Soc.*, 2008, **130**, 6932.
12 M. Wiechmann, H. Port, F. Laermer, W. Frey and T. Elsaesser, *Chem. Phys. Lett.*, 1990, **165**, 28; M. J. Paterson, M. A. Robb, L. Blancafort and A. D. DeBellis, *J. Am. Chem. Soc.*, 2004, **126**, 2912; A. L. Sobolewski, W. Domcke and C. Hattig, *J. Phys. Chem. A*, 2006, **110**, 6301.
13 H. J. Kuhn, S. E. Braslavsky and R. Schmidt, *Pure Appl. Chem.*, 2004, **76**, 2105.
14 V. Leyva, I. Corral, F. Feixas, A. Migani, L. Blancafort, J. González-Vázquez and L. González, manuscript under revision.
15 M. L. Donten, P. Hamm and J. VandeVondele, *J. Phys. Chem. B*, 2011, **115**, 1073–1083.
16 T. Schmierer, S. Laimgruber, K. Haiser, K. Kiewisch, J. Neugebauer and P. Gilch, *Phys. Chem. Chem. Phys.*, 2010, **12**, 15653.
17 J. C. Netto-Ferreira and J. C. Scaiano, *Can. J. Chem.*, 1993, **71**, 1209.

114

Article 3.4.5. A non-adiabatic quantum-classical dynamical study of the intramolecular excited state hydrogen transfer in *ortho*-Nitrobenzaldehyde

Verónica Leyva, Inés Corral, Ferran Feixas, Annapaola Migani, Lluís Blancafort, Jesús González-Vázquezya and Leticia González

PAPER

A non-adiabatic quantum-classical dynamics study of the intramolecular excited state hydrogen transfer in *ortho*-nitrobenzaldehyde†

Veronica Leyva,[a] Inés Corral,‡[a] Ferran Feixas,[b] Annapaola Migani,[b] Lluís Blancafort,[b] Jesús González-Vázquez§[a] and Leticia González*[ac]

Ab initio surface-hopping dynamics calculations have been performed to simulate the intramolecular excited state hydrogen transfer dynamics of *ortho*-nitrobenzaldehyde (*o*-NBA) in the gas phase from the electronic S_1 excited state. Upon UV excitation, the hydrogen is transferred from the aldehyde substituent to the nitro group, generating *o*-nitrosobenzoic acid through a ketene intermediate. The semiclassical propagations show that the deactivation from the S_1 is ultrafast, in agreement with the experimental measurements, which detect the ketene in less than 400 fs. The trajectories show that the deactivation mechanism involves two different conical intersections. The first one, a planar configuration with the hydrogen partially transferred, is responsible for the branching between the formation of a biradical intermediate and the regeneration of the starting material. The conversion of the biradical to the ketene corresponds to the passage through a second intersection region in which the ketene group is formed.

1. Introduction

The exchange of a proton or a hydrogen atom (if proton transfer is coupled to electron transfer) between an acidic and a basic group lying at the same or different molecules in the electronic ground state might be regarded as one of the most elementary reactions in chemistry and biochemistry, governing primal processes such as acid–base equilibria,[1] water auto-ionization,[2] or enzyme catalytic reactions.[3–5]

Upon UV/vis irradiation, aromatic systems can experience an increase of the acidity and/or basicity of the H-donor and/or acceptor moieties,[6] allowing the transfer of the proton (hydrogen) to occur in the electronic excited state and resulting in what is known as excited state hydrogen transfer (ESHT)—or excited state intramolecular hydrogen transfer if the acidic and basic groups are located within the same molecule. This particular property, inherent to certain dyes, has been exploited for the design of *e.g.* (i) molecular laser materials able to efficiently invert the population between the S_0 of the initial molecule and the S_1 of its tautomer,[7–9] (ii) photostabilizers with

an enhanced rate of intersystem crossing[10,11] or internal conversion[12,13] from the lowest excited states to the ground state, or (iii) molecular information storage devices.[14] Photoinduced hydrogen transfer has also been claimed to be partially responsible for DNA's robustness with respect to UV photolesions.[15,16]

Regardless of inter- or intra-molecular, ESHT reactions take place in ultrafast timescales ($K_{ESHT} > 10^{12}$ s^{-1}),[17] and therefore, femtosecond (fs) spectroscopy is the ideal tool to monitor their dynamics, pointing to the existence of very efficient decay funnels governed by conical intersections (CI) that lead to the corresponding product.

Compared to the vast amount of quantum mechanical calculations providing a static description of the ESHT mechanisms at a molecular level, papers devoted to dynamics aspects of ESHT mechanisms are less common. Wavepacket propagations and mixed quantum-classical dynamics (MQCD) are certainly among the most suitable methods to investigate non-radiative ultrafast decay processes, such as ESHT, in molecules of medium size. Good examples are the quantum studies on models of reduced dimensionality investigating the photochemical dynamics of proton (hydrogen) transfer in Watson and Crick base pairs in DNA or similar, see the case of pyrrole pyridine complex[18] or cytosine guanine base pairs.[19] A similar approach is employed to study the ESHT in cationic and neutral water dimers: four[20] or $(2 + 1)$[21] subsets of coordinates, respectively, were used to construct EOM-IP-CCSD and MP2/CC2 potential energy surfaces (PES) on which wavepacket propagations are performed. A similar framework, but in combination with time-dependent

[a] *Institut für Physikalische Chemie, Friedrich Schiller Universität Jena, Helmholtzweg 4, 07743 Jena, Germany*
[b] *Institute of Computational Chemistry and Department of Chemistry, University of Girona, Campus de Montilivi, 17071 Girona, Spain*
[c] *Abbe Center of Photonics, Friedrich Schiller Universität Jena, Germany. E-mail: leticia.gonzalez@uni-jena.de*

116

density functional theory (DFT), is used to study excited state ultrafast proton dynamics of classic intramolecular hydrogen-bonded systems, such as salicylidene derivatives,[22] 1-hydroxy-2-acetonaphthone[23] or 10-hydroxybenzoquinoline.[24]

Full-dimensional surface hopping approaches[25,26] represent a very convenient alternative to investigate ESHT dynamics when a large number of nuclear coordinates are decisive in the deactivation mechanism and nuclear quantum effects such as tunnelling can be neglected. In the MQCD approach a wavepacket is simulated by running a swarm of classical trajectories and the passage through the CI region is treated with a trajectory surface hopping algorithm that decides on which surface the trajectory is propagated. One of the main advantages of this approach is that electronic structure calculations can be implemented on-the-fly, i.e. the PESs do not have to be constructed in advance. Instead, the gradients, and eventually the Hessian, are calculated at every step of the propagation. This approach allows including all degrees of freedom in the dynamics, but it is only practical if combined with quantum chemical methods where the gradients and nonadiabatic couplings are available analytically. Ideally, one would use a multi-reference method that accounts for dynamic electronic correlation, such as complete active space second order perturbation (CASPT2), multistate CASPT2 (MS-CASPT2), or multi-reference configuration interaction. However, analytic gradients are generally not available for these methods and the ab initio molecular dynamics calculations are often carried out at the complete active space self-consistent field (CASSCF) level of theory, which can treat the regions of energy degeneracy but does not account for dynamic electronic correlation. Therefore, to assess the dynamics and identify possible artefacts due to the level of theory used for the trajectories, it is mandatory to prospect in advance the possible critical points which will be explored in the dynamics and compare the reaction paths at the level of theory used for the trajectories and at a higher level of theory. The intrinsic validity of the MQCD approach has been already assessed in the literature by comparing with exact quantum dynamics simulations in simple models, see for example ref. 26 and 27. In particular, reliability of the computed rates depends very much on the amount of trajectories. As stated by Barbatti et al. in the case of ab initio dynamics, the simulation of a photochemical process with ca. 100 trajectories is expected to be statistically representative.[28] In cases where the on-the-fly calculations (which are the bottleneck of the MQCD approach) are too computationally demanding statistics might serve only for qualitative purposes.

The trajectory surface hopping protocol has been used, for instance, to investigate the HT from the carboxyl to the amino group in the biologically relevant tryptophan cation[29] or intramolecular ESHT in the two H-chelating compounds 2-(2'-hydroxyphenyl)benzothiazole[24,30] and 10-hydroxybenzo-quinoline.[24] Additionally, the ab initio multiple spawning (AIMS) method of Martínez and co-workers,[31,32] which expands the wavepacket on the basis of a time-dependent set of frozen Gaussian functions and considers at the same time all molecular degrees of freedom explicitly, can be used. Exemplary AIMS simulations have been performed on malonaldehyde,[33,34] o-hydroxybenzaldehyde[35] or methyl salicylate[36] systems.

Scheme 1
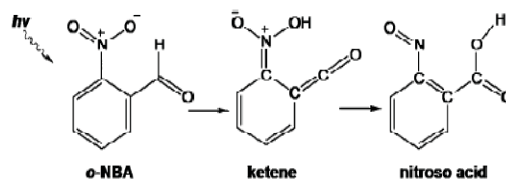
The goal of this paper is to simulate the intramolecular ESHT dynamics of ortho-nitrobenzaldehyde (o-NBA), where a hydrogen is transferred from the aldehyde substituent to the nitro group upon UV excitation, generating o-nitrosobenzoic acid through a ketene intermediate[37-41] (see Scheme 1). This reaction is the key process responsible for the wide applicability of o-NBA as a caging or photoremovable protecting group in organic synthesis[42] or in the production of oligonucleotides microarrays used in DNA chips.[43] Time-resolved experiments[38-41] where the ketene transient was characterized by femtosecond stimulated Raman[44] UV and IR spectroscopy[45] have revealed that the formation of the ketene takes place through two predominant channels: a rapid pathway on the singlet excited state, which leads to the ketene in several hundreds of femtoseconds, and a slower channel of approximately 220 ps, presumably on the triplet manifold. These experiments have been carried out exciting both in the low (388 nm)[46] and high (258 nm)[45] energy regions of the spectrum. According to our previous MS-CASPT2 calculations,[47,48] these regions are dominated by states of $n\pi^*$ and $\pi\pi^*$ character, respectively. However, the experimental and theoretical results suggest that the same mechanism dominates at both excitation wave lengths, and therefore we focus on deactivation after excitation of the $n\pi^*$ band. This band is composed of three weakly absorbing states, but for the sake of simplicity we have started the molecular dynamics simulations on S_1.

A schematic representation of the deactivation mechanism from the S_1 state, obtained in a recent MS-CASPT2 study of the PES,[46] is shown in Fig. 1. After excitation at the red edge of the spectrum, there is a direct, almost barrierless path from the minimum of the $n\pi^*$ state, $(n\pi^*)_{Min}$, to a S_1/S_0 CI where the hydrogen is being transferred from the aldehyde to the
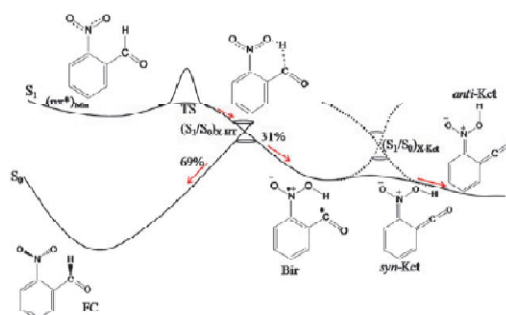

Fig. 1 Potential energy profile of the ground (S_0) state and first electronic excited state (S_1) along the reaction coordinate which promotes ESHT based on MS-CASPT2//CASSCF calculations.[46] The arrows and percentages show the amount of products as obtained from MQCD simulations starting from the TS of the S_1 potential.

2 | Phys. Chem. Chem. Phys., 2011, **III**, 1–9

This journal is © the Owner Societies 2011

nitro group, labeled $(S_1/S_0)_{X-HT}$. The ground state pathway from the $(S_1/S_0)_{X-HT}$ crossing point to the ketene corresponds to a very flat potential and goes through a biradical minimum (Bir) and a saddle point (syn-Ket). It leads to the more stable ketene product (anti-Ket), which has the hydroxy group rotated with respect to the syn-Ket isomer. The passage through the $(S_1/S_0)_{X-HT}$ crossing explains the formation of the product in the ground state on the femtosecond scale, in agreement with the experiment. In contrast to this, recent DFT based calculations by Cheng et al.[49] propose that the hydrogen transfer takes place only on the S_1 surface and leads to the excited-state ketene. The latter mechanism was obtained by optimizing the hydrogen transfer coordinate in the ground state and calculating the excited-state energy profile with single point calculations on the ground state structures. Instead, the mechanism presented in Fig. 1 has been obtained using a much more reliable approach, where the excited state reaction coordinate is optimized directly. The comparison of the two mechanisms shows that the ground-state based approach gives the wrong mechanistic picture.

The reaction path displayed in Fig. 1 involves several degrees of freedom, and the PES is too complex to be described with a reduced number of dimensions. Therefore, to simulate the dynamics, we have carried out CASSCF on-the-fly surface hopping calculations involving all degrees of freedom. One of our main points of interest is to simulate the consecutive passage through the two regions of CIs, going beyond the static picture given by our recent PES study:[46] in the first region of intersection, we center on the competition between ESHT and the recovery of the initial molecule in the ground state, and in the second region we focus on the efficiency of the transformation of the biradical transient to the ketene and the role of non-adiabatic effects. As we discuss in detail below, the barrier to access $(S_1/S_0)_{X-HT}$ from $(n\pi^*)_{Min}$ is overestimated at the CASSCF level used for the dynamics, and the main part of our trajectories are started from the TS on the CASSCF surface to sample the intersection regions efficiently. Moreover, since the starting energy exceeds the height of the barrier for hydrogen transfer, quantum nuclear effects, such as tunnelling, are not expected to be important in this case.

2. Computational details

MQCD simulations at the CASSCF level of theory were employed to simulate the electronic deactivation of o-NBA from the first electronic excited state, S_1. The MQCD methodology treats the nuclei classically with trajectories that follow the Newton equations while the electrons are followed quantum mechanically with the time-dependent Schrödinger equation. For the nuclear motion, the Velocity Verlet[50,51] algorithm was employed with a time step of 0.5 fs. The energy gradients required in the classical motion were performed in the electronic part.[52–55] In this methodology, the electronic wavefunction is expanded as a linear combination of the time-independent Schrödinger equation eigenfunctions for the particular nuclear configuration, in the frame of the Born–Oppenheimer approximation. The coefficients of this expansion are followed using the 5th order Butcher algorithm.[56] As these coefficients are followed in a single trajectory there is an excess of coherence

between the different electronic states, therefore time-dependent populations were corrected as suggested by Granucci and Persico[57] with a decoherence parameter of $\alpha = 0.1$ hartree. As demonstrated by Zhu et al.[58] dynamics results are insensitive to this parameter.

Two different initial conditions were generated, depending on whether the trajectories are started from the electronic ground state equilibrium geometry and projected vertically onto the S_1 (results discussed in the ESI†) or started from the transition state (TS) of the S_1. In the former case, the initial geometries and velocities were generated with a Wigner distribution of 179 geometries, where each nuclear coordinate is treated with a harmonic oscillator in the ground state. This distribution accounts for the quantum vibrational ground state probability of the electronic ground state potential and was obtained using harmonic frequencies for the optimized geometry at the B3LYP/TZVP level of theory[59,60] calculated with the TURBOMOLE[61,62] package. In the case of starting at the TS, an uncorrelated Wigner distribution for the vibrational ground state is also employed, but it is spawned for all the normal modes at the CASSCF level of theory (vide infra) except the imaginary one. In this imaginary mode, the trajectories were generated with no momentum and at the TS equilibrium position. The anharmonicity of the system, not considered in the Wigner distribution, is enough to escape very fast from the TS geometry. A total of 200 trajectories were generated in this way.

Due to the presence of non-adiabatic couplings between the ground and the first excited state,[63,64] the surface hopping method according to the Tully's fewest switches algorithm[65] is used. After a hop, the total energy is conserved by adjusting the velocity with the potential energy difference between the S_0 and S_1 states. This excess of potential energy is put in the direction of the velocity vector (i.e. in the kinetic energy of the nuclei), avoiding frustrated hops, as in ref. 66. The deactivation from the dynamics simulations is ultrafast and therefore the dynamics simulations were run for about 60 fs with the NEWTON-X package.[67,68] In this time, all the trajectories show deactivation to the ground state for a time long enough as to consider them complete.

The on-the-fly CASSCF calculations and the initial conditions at the TS were carried out with the COLUMBUS program system[69] and the 6-31G(d) basis set.[70] Two states were averaged with equal weights. The active space comprises ten electrons in eight orbitals (see Fig. 2). The orbitals are obtained using the B3LYP/TZVP equilibrium geometry of o-NBA with a two-
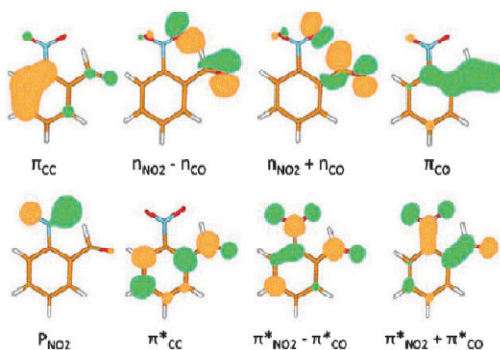

Fig. 2 Active space of CASSCF(10,8) calculations.

This journal is © the Owner Societies 2011

Phys. Chem. Chem. Phys., 2011, **111**, 1–9 | 3

118

state calculation. They correspond to two lone pairs located in the nitro and carbonyl groups, the π_{CO}, π_{CO}^* pair located in the carbonyl group, the non-bonding P_{NO2} and an antibonding n_{NO2}^* orbital located in the nitro group, and the most important π_{CC}, π_{CC}^* orbital pair located in the benzene ring. As seen in Fig. 2, some of these orbitals form linear combinations between them. With this active space, the wavefunction of the electronic ground state can be mainly described by the electronic configuration: $(\pi_{CC})^2(n_{NO2} - n_{CO})^2(n_{NO2} + n_{CO})^2 (\pi_{CO})^2(P_{NO2})^2 (\pi_{CC}^*)^0(\pi_{NO2}^* - \pi_{CO}^*)^0(\pi_{NO2}^* + \pi_{CO}^*)^0$.

3. Results

Because of the general difficulty of using analytical gradients at the CASPT2 or MS-CASPT2 level of theory combined with the trajectory surface hopping algorithm, our MQCD trajectories are carried out at the CASSCF level of theory, which is capable of treating the passage through the CI although it lacks dynamic correlation. To estimate the reliability of CASSCF trajectories, in Table 1 we compare the energies of the critical points optimized at the CASSCF(10,8)/6-31G* level of theory used for our dynamics with the MS-CASPT2 energies obtained in ref. 46. The main difference between the energy profiles at the two levels of theory is found in the initial part of the path. MS-CASPT2 predicts an almost barrierless hydrogen transfer, but at the CASSCF level there is a TS between the $n\pi^*$ minimum and the $(S_1/S_0)_{x-HT}$ CI, with an associated barrier of 1.4 eV (see Fig. 1). Along the rest of the path there is good agreement between the CASSCF and MS-CASPT2 results; however, due to the artificial barrier, CASSCF-based dynamics simulations launched at the Franck Condon (FC) geometry remain trapped in the $(n\pi^*)$ minimum for a long time (see ESI†). To avoid the artificial bottleneck of population trapped in the $(n\pi^*)_{Min}$ due to the lack of dynamical correlation, we have adopted a protocol followed in comparable problems:[71–73] the formation of the ketene intermediate is investigated starting the trajectories from the TS—similar to running fleeting trajectories in transition path sampling.[74] These calculations should better describe the formation of the ketene along the reaction path sketched in Fig. 1. Fig. 3 shows the obtained distribution of C_6-H_8 and O_9-H_8 distances involved in the ESIHT of o-NBA at the end of propagation. About 35% of the trajectories hop to the ground state (circles), while the remaining 65% of trajectories do not reach the CI and evolve to the $(n\pi^*)_{Min}$ (crosses). Similarly to the results of

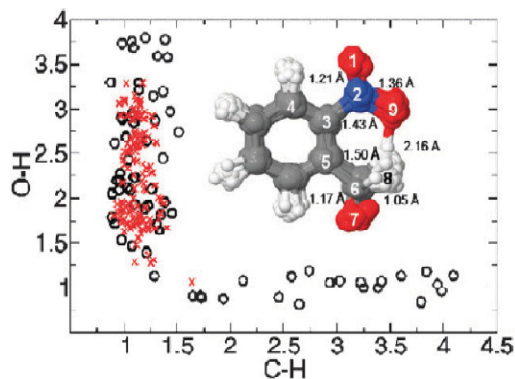**Fig. 3** O_9-H_8 and C_6-H_8 bond distances at the final time of the simulation for the set of trajectories propagated from the TS in the S_1 state. The crosses and circles indicate trajectories ending in the S_1 and S_0, respectively. The inset shows a superposition of the corresponding geometries at the end of the propagation, indicating the average bond distances.

the simulations launched from the FC equilibrium geometry (see discussion in the ESI†), the molecules trapped in the S_1 potential show C_6-H_8 distances around 1.1 Å. The O_9-H_8 distances show a large variation (from 1.2 Å to 3.4 Å) because of the larger amount of gained kinetic energy corresponding to the TS. The average geometry of the trajectories (inset of Fig. 3) staying in the S_1 state does not surprisingly resemble the one found for the trajectories starting from the FC equilibrium geometry and the $(n\pi^*)_{Min}$ optimized structure at the CASSCF(14,12) level of theory.

The molecules that pass through the $(S_1/S_0)_{x-HT}$ CI are branched into two different minima of the ground state—consistent with the back and forward reactions. The back reaction corresponds to the recovery of o-NBA at the FC geometry and the forward reaction to the formation of the ketene (recall Fig. 1). Fig. 4 shows the time evolution of the relevant bond distances and angles of all the trajectories in the S_0 and S_1 states. As we see in Fig. 4a, there are two different sets of trajectories that show a different behavior in the ground state. On the one side, those trajectories evolving to the ketene intermediate transfer the hydrogen to the nitro group, converging to a short O_9-H_8 distance ($ca.$ 1.0 Å), characteristic of Bir or Ket structures. On the other side, the molecules reacting back to the o-NBA equilibrium geometry result in $O_9\cdots H_8$ distances between 2.5 and 3.5 Å. The C_6-H_8 distances (Fig. 4b) show the opposite behavior: they oscillate weakly around 1.1 Å in the S_1 (at the $(n\pi^*)_{Min}$), a bit more in the S_0 (FC), and strongly after the ESIHT has taken place. Fig. 4b also illustrates the completely different behavior in the C_6-H_8 distances between trajectories ending in the reactant or in the product. While trajectories coming back to the reactant are vibrating around 1.0 Å, there is not a unique value of this vibration on the product side. In order to evaluate the torsion movement of the aldehyde group with respect to the benzene ring and the appearance of the ketene group, the $O_7-C_6-C_5$ angle is resolved in time for all the trajectories (panel 4c) as well as for those with C_6-H_8 distances larger than 2.0 Å the latter corresponding to the exclusive formation of the biradical and ketene species (panel 4d).

4 | *Phys. Chem. Chem. Phys.*, 2011, **III**, 1–9

This journal is © the Owner Societies 2011

119
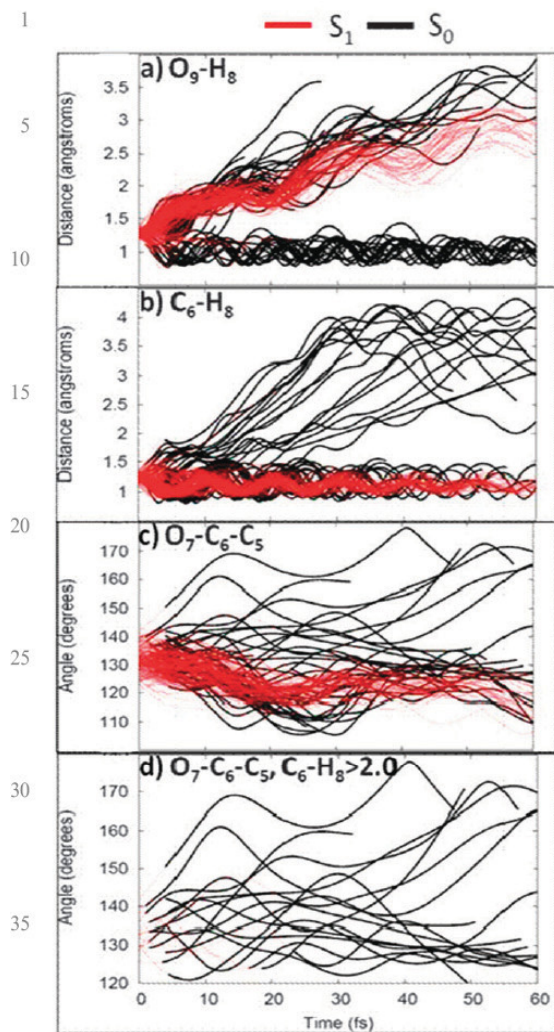
Fig. 4 Time evolution of the O_9–H_8 bond distance (a), C_6–H_8 bond distance (b), O_7–C_6–C_5 bond angle (c), and O_7–C_6–C_5 bond angle for C_6–H_8 distances larger than 2.0 Å (d), in the S_1 and S_0 electronic states. Distances in Å and angles in degrees.

Initially, at the TS geometry, the O_7–C_6–C_5 value is *ca.* 130°. In less than 50 fs the system evolves in the S_1 to smaller values ($\sim$120°), characteristic of the $(n\pi^*)_{Min}$ (4c). The molecules hopping to the ground state show large oscillations of the O_7–C_6–C_5 bending vibration, indicating a high vibrational excitation, as detected experimentally.[40] Bent structures can be assigned to the biradical intermediate, while angles of *ca.* 180° correspond to the final formation of the ketene (4d).

In order to characterize the geometry of the $(S_1/S_0)_{x\text{-HT}}$ CI, the geometries at the time of the hop are averaged for all trajectories. The geometrical parameters more relevant to the ESHT are displayed in Fig. 5. As one can see bond distances and angles are in reasonable agreement with the values given in parentheses, which correspond to the $(S_1/S_0)_{x\text{-HT}}$ CI geometry optimized at the CAS(14,12) level of theory.[46]

Fig. 5 also displays the deviation with respect to the CI geometry in our swarm of trajectories, which amounts to 10%. A considerable planarization of the aldehyde and nitro groups can be observed. Even if both geometries are similar, it is worth to note that the crossing does not necessarily take place at the minimum energy CI geometry—a circumstance that has been already found in other theoretical studies.[75–78]

Three trajectories starting from the TS will be discussed in more detail in order to better understand the deactivation of *o*-NBA in the S_1 state and the progress of the reaction on S_0. One trajectory exemplifies the back reaction to the FC geometry (Fig. 6a); the other two evolve to the species where the H atom has been transferred from the aldehyde to the nitro group forming the ketene (Fig. 6b and 6c). In all cases, the relaxation to the ground state occurs extremely fast (in less than 5 fs) because the TS lies very close to the $(S_1/S_0)_{x\text{-HT}}$ CI and the passage through the CI is very efficient.

In the trajectory corresponding to the back reaction, the geometry snapshots only point to minor distortions of the ring and stretching motion of the C–H bond located at the aldehyde group (Fig. 6a). As we can see, the back transfer is complete and the equilibrium structure is recovered in about 50 fs. Regarding the trajectories evolving to the ketene intermediate, most of them behave as in the exemplary case depicted in Fig. 6b. Also here the decay to the ground state is very fast because the H atom is very close to the nitro group. After decay, the energy excess is employed in the rotation of the H atom around the N_2–O_9 bond and the linearization of the C_5–C_6–O_7 moiety, so that the system visits the biradical species, the *syn*-Ket, and finally the *anti*-Ket structure in *ca.* 40 fs. The corresponding change in the electronic configuration is confirmed by an examination of the configuration interaction coefficients and associated orbitals. We note that this particular trajectory is very effective; others remain trapped in the biradical structure for a longer time so that at the end of the propagation time (60 fs) the ketene is not formed yet. The trajectory of Fig. 6c shows that the transformation of the biradical to the ketene can also be subject to non-adiabatic effects. In this trajectory the hydrogen is transferred only after 1 fs and then a hop to S_0 takes place. However, after 8 fs ($t = 9$ fs) the molecule jumps back to S_1, and after another 11 fs ($t = 20$ fs) a further crossing to the ground state takes place. Interestingly, these recrossings do not involve the back transfer of the hydrogen, *i.e.*, they do not take place at the $(S_1/S_0)_{X\text{-HT}}$ region of intersection, but in the region of $(S_1/S_0)_{X\text{-Ket}}$. In the time scale of our simulation, the hydrogen atom continues rotating around the N_2–O_9 bond, which corresponds to an oscillation between the *syn*- and *anti*-Ket isomers. As in the previous example, the building of the ketene is complete in less than 50 fs.

4. Discussion

The results of the singlet relaxation mechanism of *o*-NBA at low excitation energy are summarized in Fig. 1. About 65% of the trajectories started at the hydrogen transfer TS relax back to $(n,\pi^*)_{Min}$, while only the remaining 35% evolve to the $(S_1/S_0)_{x\text{-HT}}$ CI. At this CI, the substituents are planarized with respect to the FC geometry, and the hydrogen is partially transferred. From the amount of trajectories which pass through
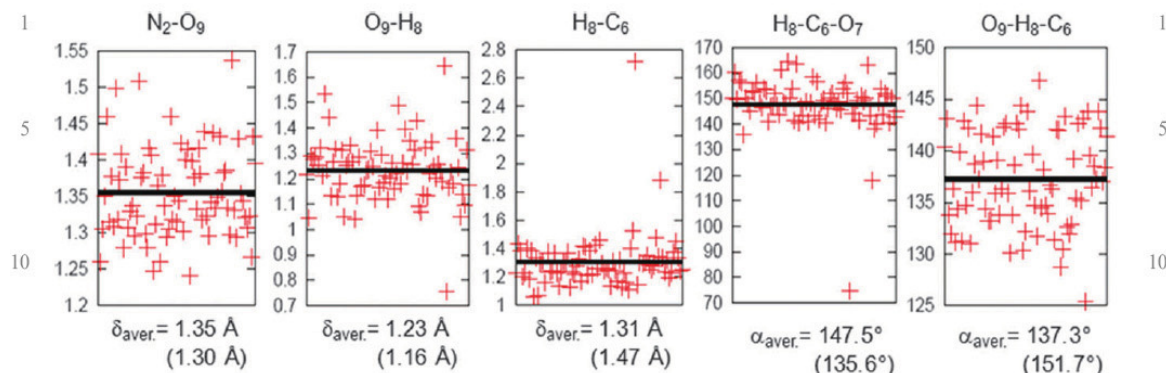
This journal is © the Owner Societies 2011

Phys. Chem. Chem. Phys., 2011, **❚❚❚**, 1–9 | 5

Fig. 5 Distribution of selected bond distances and bond angles at the time of the hopping at the $(S_1/S_0)_{x\text{-HT}}$ CI. The averaged value (solid line) is also indicated by δ_{aver}. Values in parentheses correspond to those obtained in the conical intersection calculated at the CASSCF(14,12) level of theory.[46] Distances in Å and angles in degrees. Atom numbering corresponds to the molecule depicted in Fig. 3.

the $(S_1/S_0)_{x\text{-HT}}$ CI, 69% returns back to the starting material, while 31% completes the hydrogen transfer. This is different from other aromatic compounds undergoing intramolecular ESHT, where the hydrogen transfer takes place before the decay to the ground state.[33–36,79–85] On the contrary, in *o*-NBA a CI for the decay to the ground state is found during the transfer, and part of the trajectories are reverted to the reactant before the transfer is complete, as in ref. 86. This mechanism corresponds to a partially aborted hydrogen transfer.[87] Moreover, because there is no back hydrogen transfer observed for the trajectories that reach Bir on S_0, the branching ratio at the CI gives an upper limit to the quantum yield of ketene formation. However, the estimated branching ratio at $(S_1/S_0)_{x\text{-HT}}$ is not consistent with the experimental yield of approximately 50% that has been recorded in various solvents.[40] The discrepancy is presumably due to two facts. On the one side, our calculations are in the gas phase and not in solution. On the other side, we underestimate the kinetic energy gained by the system when arriving at the $(S_1/S_0)_{x\text{-HT}}$ CI from the FC geometry because we start our trajectories from the TS; the TS is very close to the $(S_1/S_0)_{x\text{-HT}}$ CI and many molecules do not possess enough energy to keep the momentum towards the ketene. In most of the cases, the ketene formation takes place *via* a biradical structure that is formed in about 10 to 20 fs. The conversion of the biradical to the ketene corresponds to the passage through a second intersection region centered on the $(S_1/S_0)_{x\text{-Ket}}$ CI. In most trajectories this conversion is purely adiabatic and avoids the intersection, except for two trajectories where we observe a recrossing (recall Fig. 6c). Finally, we note that the complete conversion from the biradical to the ketene is observed for about one third of our simulations (see Fig. 4), which are limited to 60 fs because of the computational effort. For the remaining trajectories we can assume that the conversion to the ketene will take place in a slightly longer time, up to several hundreds of femtoseconds. Overall, the process is ultrafast, in agreement with experimental measurements which detect the ketene within 400 fs.[45,88]

5. Conclusions

Non-adiabatic quantum-classical simulations using on-the-fly state-average CASSCF electronic structure calculations have been performed in *o*-NBA to investigate the $S_1 \rightarrow S_0$ relaxation mechanism. Trajectories within two scenarios were considered. First, trajectories were propagated starting from the *o*-NBA equilibrium geometry. These simulations strongly underestimate the quantum yield of the ketene formation due to fact that CASSCF predicts a barrier which is refuted by MS-CASPT2. To avoid this problem, a second batch of trajectories was launched from the TS close to the CI responsible for the hydrogen transfer, $(S_1/S_0)_{x\text{-HT}}$. Without addition of momentum in any specific direction, only one third of the trajectories undergo internal conversion; the rest revert to a minimum located in the $n\pi^*$ state. In agreement with the CI $(S_1/S_0)_{x\text{-HT}}$ optimized with CASSCF, and also confirmed with high quality MS-CASPT2 calculations,[46] the geometry found at the time of the $S_1 \rightarrow S_0$ hopping is characterized by partial ESHT promoted by the planarity of the substituents of *o*-NBA. The hydrogen transfer leads to a biradical transient which is converted to the ketene after passing a second region of S_1/S_0 intersection. Once the hydrogen transfer is initiated, the tautomerization is completed on the femtosecond scale, in agreement with the experimental results which show that the phototautomerization is ultrafast after excitation at 388 and 260 nm.[40,44–46] The semiclassical propagations from the TS predict a quantum yield for the formation of the ketene of *ca.* 30%. The discrepancy with the 50% observed experimentally[40] is due to the initial conditions and the absence of solvent. Yet, the qualitative agreement confirms the assumption that the complete yield of the reaction is determined in its earliest step, with a CI governing the competition between the creation of the ketene and the regeneration of the starting material. Thus, the hydrogen transfer is irreversible for the trajectories that reach the biradical transient, *i.e.*, no back hydrogen transfer is observed at the biradical or ketene stage, as we proposed on the basis of our PES study.[46] The molecules that deactivate towards the ketene intermediate proceed *via* the formation of a biradical, which is vibrationally excited in the O–C–C group and the O–H bond. Recent transient pump–probe IR spectroscopy combined with Car-Parrinello *ab initio* (DFT) molecular dynamics show strong evidence that the ketene transforms directly into the nitroso acid, without the formation of intermediates.[89]
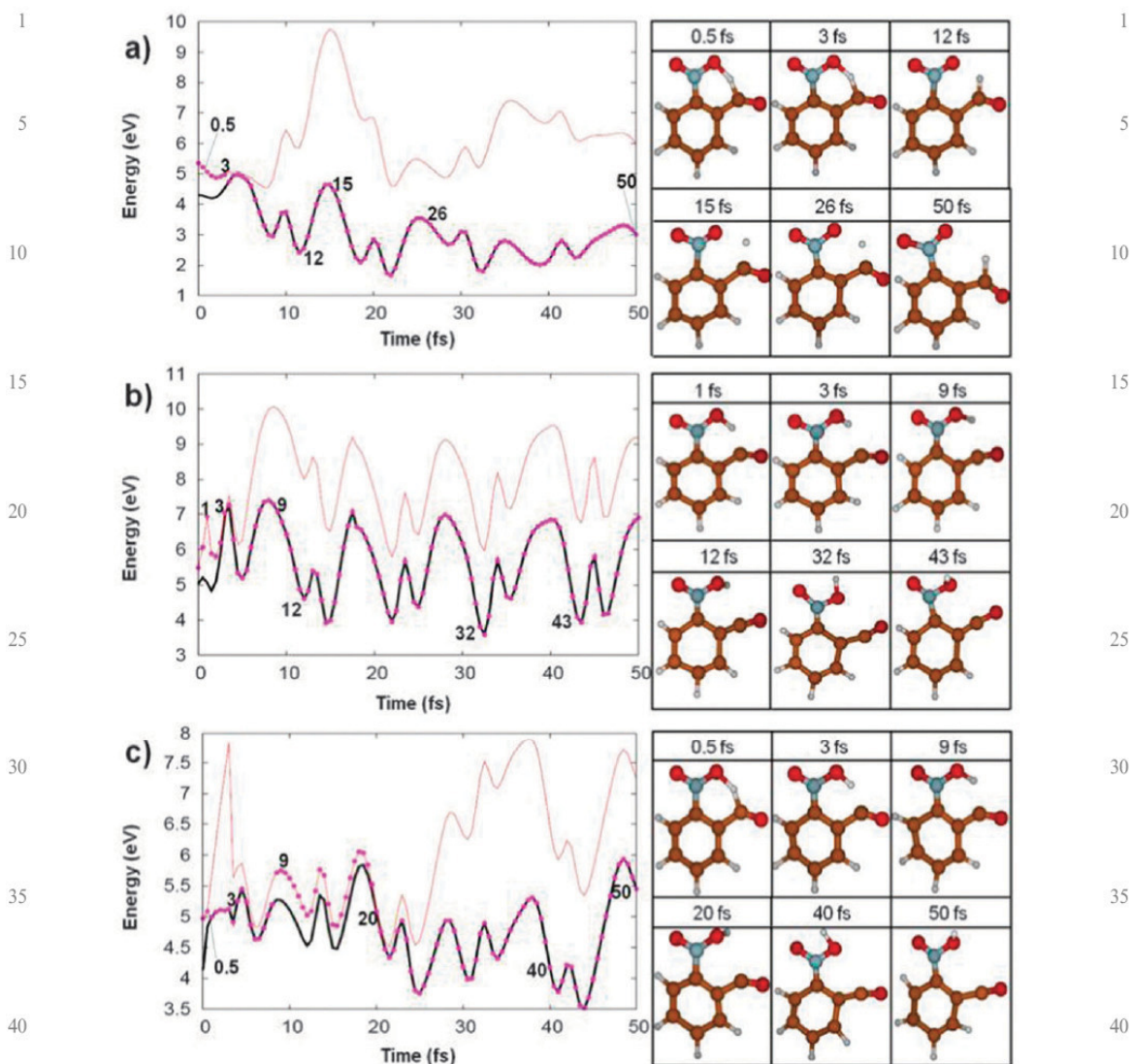
Fig. 6 Time evolution of the S_0 and S_1 potential energies and corresponding snapshots at selected times, as indicated. (a) Trajectory corresponding to the deactivation of o-NBA in the S_1 and recovery of the reactant. (b) and (c) Trajectories corresponding to the deactivation of o-NBA and formation of the ketene intermediate. Points along the potential energy curves symbolize at which potential the system is at the specific time.

In summary, the present simulations show that the deactivation from the S_1 state, which can be populated experimentally with excitation at 388 nm, is a very efficient channel for the ESHT reaction in o-NBA. Deactivation in o-NBA is also possible upon irradiation with 258 nm. In this case, a $\pi\pi^*$ state higher in energy is populated. The deactivation mechanism from this state is currently under investigation.

Acknowledgements

This journal is © the Owner Societies 2011
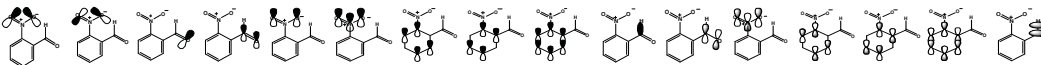
Phys. Chem. Chem. Phys., 2011, ▮▮▮, 1–9 | 7

122

References

1 M. Rini, B.-Z. Magnes, E. Pines and E. T. J. Nibbering, *Science*, 2003, **301**, 349–352.
2 P. L. Geissler, C. Dellago, D. Chandler, J. Hutter and M. Parrinello, *Science*, 2001, **291**, 2121.
3 W. W. Cleland and M. M. Kreevoy, *Science*, 1994, **264**, 1887–1890.
4 D. Lu and G. A. Voth, *J. Am. Chem. Soc.*, 1998, **120**, 4006–4014.
5 C. L. Perrin and J. B. Nielson, *Annu. Rev. Phys. Chem.*, 1997, **48**, 511–544.
6 L. G. Arnaut and S. J. Formosinho, *J. Photochem. Photobiol., A*, 1993, **75**, 1–20.
7 A. U. Acuña, A. Costela and J. M. Muñoz, *J. Phys. Chem.*, 1986, **90**, 2807–2808.
8 P. Chou, D. McMorrow, T. J. Aartsma and M. Kasha, *J. Phys. Chem.*, 1984, **88**, 4596–4599.
9 A. U. Khan and M. Kasha, *Proc. Natl. Acad. Sci. U. S. A.*, 1983, **80**, 1767–1770.
10 T. P. Smith, K. A. Zaklika, K. Thakur, G. C. Walker, K. Tominaga and P. F. Barbara, *J. Photochem. Photobiol., A*, 1992, **65**, 165–175.
11 T. Werner, *J. Phys. Chem.*, 1979, **83**, 320–325.
12 J. Catalán, F. Fabero, M. S. Guijarro, R. M. Claramunt, M. D. Santa-Maria, M. C. Foces-Foces, F. Hernández-Cano, J. Elguero and S. Sastre, *J. Am. Chem. Soc.*, 1990, **112**, 747.
13 J.-E. A. Otterstedt, *J. Chem. Phys.*, 1973, **58**, 5716–5725.
14 T. Nishiya, S. Yamauchi, N. Hirota, M. Baba and I. Hanazaki, *J. Phys. Chem.*, 1986, **90**, 5730–5735.
15 T. Schultz, E. Samoylova, W. Radloff, I. V. Hertel, A. L. Sobolewski and W. Domcke, *Science*, 2004, **306**, 1765–1768.
16 A. L. Sobolewski, W. Domcke and C. Hättig, *Proc. Natl. Acad. Sci. U. S. A.*, 2005, **102**, 17903–17906.
17 A. Douhal, F. Lahmani and A. H. Zewail, *Chem. Phys.*, 1996, **207**, 477–498.
18 Z. Lan, L. M. Frutos, A. L. Sobolewski and W. Domcke, *Proc. Natl. Acad. Sci. U. S. A.*, 2008, **105**, 12707–12712.
19 G. Groenhof, L. V. Schäfer, M. Boggio-Pasqua, M. Goette, H. Grubmüller and M. A. Robb, *J. Am. Chem. Soc.*, 2007, **129**, 6812–6819.
20 E. Kamarchik, O. Kostko, J. M. Bowman, M. Ahmed and A. I. Krylov, *J. Chem. Phys.*, 2010, **132**, 194311.
21 B. Chmura, Z. Lan, M. F. Rode and A. L. Sobolewski, *J. Chem. Phys.*, 2009, **131**, 134307.
22 J. M. Ortiz-Sánchez, R. Gelabert, M. Moreno and J. M. Lluch, *J. Phys. Chem. A*, 2006, **110**, 4649–4656.
23 J. M. Ortiz-Sánchez, R. Gelabert, M. Moreno and J. M. Lluch, *J. Chem. Phys.*, 2007, **127**, 084318.
24 C. Schriever, M. Barbatti, K. Stock, A. J. A. Aquino, D. Tunega, S. Lochbrunner, E. Riedle, R. de Vivie-Riedle and H. Lischka, *Chem. Phys.*, 2008, **347**, 446–461.
25 J. C. Tully, *J. Chem. Phys.*, 1990, **93**, 1061.
26 J. C. Tully, *Faraday Discuss.*, 1998, **110**, 407.
27 M. Richter, P. Marquetand, J. González-Vázquez, I. Sola and L. González, *J. Chem. Theory Comput.*, 2011, **7**, 1253–1258.
28 M. Barbatti, G. Granucci, M. Persico, M. Ruckenbauer, M. Vazdar, M. Eckert-Maksic and H. Lischka, *J. Photochem. Photobiol., A*, 2007, **190**, 228–240.
29 D. Shemesh and R. B. Gerber, *J. Phys. Chem. A*, 2006, **110**, 8401–8408.
30 M. Barbatti, A. J. A. Aquino, H. Lischka, C. Schriever, S. Lochbrunner and E. Riedle, *Phys. Chem. Chem. Phys.*, 2009, **11**, 1406–1415.
31 M. Ben-Nun and T. J. Martínez, *Adv. Chem. Phys.*, 2002, **121**, 439–512.
32 M. Ben-Nun, J. Quenneville and T. J. Martínez, *J. Phys. Chem. A*, 2000, **104**, 5161–5175.
33 J. D. Coe and T. J. Martínez, *J. Am. Chem. Soc.*, 2005, **127**, 4560–4561.
34 J. D. Coe and T. J. Martínez, *J. Phys. Chem. A*, 2006, **110**, 618–630.
35 J. D. Coe and T. J. Martínez, *Mol. Phys.*, 2008, **106**, 537–545.
36 J. D. Coe, B. G. Levine and T. J. Martinez, *J. Phys. Chem. A*, 2007, **111**, 11302–11310.
37 G. Ciamician and P. Silber, *Ber. Dtsch. Chem. Ges.*, 1901, **34**, 2040.
38 M. George and J. Scaiano, *J. Phys. Chem.*, 1980, **84**, 492.
39 S. Kuberski and J. Gebicki, *J. Mol. Struct.*, 1992, **275**, 105.
40 S. Laimgruber, W. J. Schreier, T. E. Schrader, F. O. Koller, W. Zinth and P. Gilch, *Angew. Chem., Int. Ed.*, 2005, **44**, 7901.
41 R. W. Yip and D. K. Sharma, *Res. Chem. Intermed.*, 1989, **11**, 109.
42 A. P. Pellicecioli and J. Wirz, *Photochem. Photobiol. Sci.*, 2002, **1**, 441.
43 X. L. Gao, E. Gulari and X. C. Zhou, *Biopolymers*, 2004, **73**, 579.
44 S. Laimgruber, T. Schmierer, P. Gilch, K. Kiewisch and J. Neugebauer, *Phys. Chem. Chem. Phys.*, 2008, **10**, 3872–3882.
45 T. Schmierer, W. J. Schreier, F. O. Koller, T. E. Schrader and P. Gilch, *Phys. Chem. Chem. Phys.*, 2009, **11**, 11596–11607.
46 A. Migani, V. Leyva, F. Feixas, T. Schmierer, P. Gilch, I. Corral, L. González and L. Blancafort, *Chem. Commun.*, 2011, **47**, 6383–6385.
47 V. Leyva, I. Corral, T. Schmierer, B. Heinz, F. Feixas, A. Migani, L. Blancafort, P. Gilch and L. González, *J. Phys. Chem. A*, 2008, **112**, 5046.
48 V. Leyva, I. Corral, T. Schmierer, P. Gilch and L. González, *Phys. Chem. Chem. Phys.*, 2011, **13**, 4269–4278.
49 S. Cheng, P. Song, S. Yang, H. Yin and K. Han, *Phys. Chem. Chem. Phys.*, 2010, **12**, 9067–9074.
50 L. Verlet, *Phys. Rev.*, 1967, **159**, 98.
51 L. Verlet, *Phys. Rev.*, 1968, **165**, 201.
52 H. Lischka, M. Dallos and R. Shepard, *Mol. Phys.*, 2002, **100**, 1647.
53 R. Shepard, *Int. J. Quantum Chem.*, 1987, **31**, 33.
54 R. Shepard, *Modern Electronic Structure Theory Part I*, ed. D. R. Yarkony, World Scientific, Singapore, 1995.
55 R. Shepard, H. Lischka, P. G. Szalay, T. Kovar and M. Ernzerhof, *J. Chem. Phys.*, 1992, **96**, 2085.
56 J. C. Butcher and H. Podhaisky, *Appl. Num. Math.*, 2006, **56**, 345.
57 G. Granucci and M. Persico, *J. Chem. Phys.*, 2007, **126**, 134114.
58 C. Zhu, S. Nangia, A. W. Jasper and D. G. Truhlar, *J. Chem. Phys.*, 2004, **121**, 7658.
59 A. D. Becke, *J. Chem. Phys.*, 1993, **98**, 5648–5652.
60 A. Schäfer, C. Huber and R. Ahlrichs, *J. Chem. Phys.*, 1994, **100**, 5829.
61 O. Treutler and R. Ahlrichs, *J. Chem. Phys.*, 1995, **102**, 346.
62 R. Ahlrichs, M. Bär, M. Häser, H. Horn and C. Kölmel, *Chem. Phys. Lett.*, 1989, **162**, 165.
63 H. Lischka, M. Dallos, P. G. Szalay, D. R. Yarkony and R. Shepard, *J. Chem. Phys.*, 2004, **120**, 7322.
64 M. Dallos, H. Lischka, R. Shepard, D. R. Yarkony and P. G. Szalay, *J. Chem. Phys.*, 2004, **120**, 7330.
65 S. Hammes-Schiffer and J. C. Tully, *J. Chem. Phys.*, 1995, **103**, 8528.
66 J. González-Vázquez and L. González, *ChemPhysChem*, 2010, **11**, 3617.
67 M. Barbatti, G. Granucci, M. Persico, M. Ruckenbauer, M. Vazdar, M. Eckert-Maksic and H. Lischka, *J. Photochem. Photobiol., A*, 2007, **190**, 228.
68 M. Barbatti, G. Granucci, M. Ruckenbauer, J. Pittner, M. Persico and H. Lischka, *NEWTONX: a package for Newtonian dynamics close to the crossing seam*, www.newtonx.org, 2007.
69 H. Lischka, R. Shepard, I. Shavitt, R. M. Pitzer, M. Dallos, T. Müller, P. G. Szalay, F. B. Brown, R. Ahlrichs, H. J. Boehm, A. Chang, D. C. Comeau, R. Gdanitz, H. Dachsel, C. Ehrhardt, M. Ernzerhof, P. Höchtl, S. Irle, G. Kedziora, T. Kovar, V. Parasuk, M. J. M. Pepper, P. Scharf, H. Schiffer, M. Schindler, M. Schüler, M. Seth, E. A. Stahlberg, J.-G. Zhao, S. Yabushita, Z. Zhang, M. Barbatti, S. Matsika, M. Schuurmann, D. R. Yarkony, S. R. Brozell, E. V. Beck and J.-P. Blaudeau, *COLUMBUS, an ab initio electronic structure program, release 5.9.1*, www.univie.ac.at/columbus, 2006.
70 W. J. Hehre, L. Radom, P. von R. Schleyer and J. Pople, *Ab initio Molecular Orbital Theory*, Wiley-Interscience, New York, 1986.
71 C.-M. Chang, Y.-H. Huang, S.-Y. Liu, Y.-P. Lee, M. Pombar-Pérez, E. Martínez-Núñez and S. A. Vázquez, *J. Chem. Phys.*, 2008, **129**, 224301.
72 J. González-Vázquez, E. Martínez-Núñez, A. Fernández-Ramos and S. A. Vázquez, *J. Phys. Chem. A*, 2003, **107**, 1398–1404.
73 D. Asturiol, B. Lasorne, M. A. Robb and L. Blancafort, *J. Phys. Chem. A*, 2009, **113**, 10211–10218.

8 | *Phys. Chem. Chem. Phys.*, 2011, **III**, 1–9

This journal is © the Owner Societies 2011

123

74 D. Chandler, in *Classical and Quantum Dynamics in Condensed Phase Simulations*, ed. G. C. a. D. F. C. B. J. Berne, World Scientific, Singapore, 1998, pp. 3–23.

75 T. Rozgonyi and L. González, *J. Phys. Chem. A*, 2008, **112**, 5573–5581.

76 B. G. Levine and T. J. Martínez, *Annu. Rev. Phys. Chem.*, 2007, **58**, 613–634.

77 M. J. Bearpark, F. Bernardi, M. Olivucci, M. A. Robb and B. R. Smith, *J. Am. Chem. Soc.*, 1996, **118**, 5254–5260.

78 O. Weingart, A. Migani, M. Olivucci, M. A. Robb, V. Buss and P. Hunt, *J. Phys. Chem. A*, 2004, **108**, 4685–4693.

79 A. J. A. Aquino, F. Plasser, M. Barbatti and H. Lischka, *Croat. Chem. Acta*, 2009, **82**, 105–114.

80 N. L. Doltsinis, *Mol. Phys.*, 2004, **102**, 499–506.

81 A. Migani, L. Blancafort, M. A. Robb and A. D. Debellis, *J. Am. Chem. Soc.*, 2008, **130**, 6932–6933.

82 M. J. Paterson, M. A. Robb, L. Blancafort and A. D. DeBellis, *J. Am. Chem. Soc.*, 2004, **126**, 2912–2922.

83 M. J. Paterson, M. A. Robb, L. Blancafort and A. D. DeBellis, *J. Phys. Chem. A*, 2005, **109**, 7527–7537.

84 A. L. Sobolewski and W. Domcke, *Phys. Chem. Chem. Phys.*, 2006, **8**, 3410–3417.

85 A. L. Sobolewski, W. Domcke and C. Hattig, *J. Phys. Chem. A*, 2006, **110**, 6301–6306.

86 A. Migani, M. J. Bearpark, M. Olivucci and M. A. Robb, *J. Am. Chem. Soc.*, 2007, **129**, 3703–3713.

87 W. M. Nau, G. Greiner, J. Wall, H. Rau, M. Olivucci and M. A. Robb, *Angew. Chem., Int. Ed.*, 1998, 37, 98–101.

88 B. Heinz, T. Schmierer, S. Laimgruber and P. Gilch, *J. Photochem. Photobiol., A*, 2008, **199**, 274.

89 M. L. Donten, P. Hamm and J. VandeVondele, *J. Phys. Chem. B*, 2011, **115**, 1075–1083.

This journal is © the Owner Societies 2011

Phys. Chem. Chem. Phys., 2011, **III**, 1–9 | 9

124

Active spaces used in this thesis for the Kasha and non-Kasha mechanisms at the QC calculations:

	n_{NO2}	n_{NO2}	n_{CO}	π_{CO}	P_{NO2}	π_{NO2}	π_{CC}	π_{CC}	π_{CC}	σ_{CH}	π^*_{CO}	π^*_{NO2}	π^*_{CC}	π^*_{CC}	π^*_{CC}	σ^*_{CH}
Vertical Spectrum o-NBA (16,12) in gas phase	X	X	X	X	X	X	X	X			X	X	X	X		
Vertical Spectrum o-NBA (12,11) in gas phase				X	X	X	X	X	X		X	X	X	X	X	
Vertical Spectrum m-NBA (16,12) in gas phase	X	X	X	X	X	X	X	X			X	X	X	X		
Vertical Spectrum m-NBA (12,11) in gas phase				X	X	X	X	X	X		X	X	X	X	X	
Vertical Spectrum p-NBA (16,12) in gas phase	X	X	X	X	X	X	X	X			X	X	X	X		
Vertical Spectrum p-NBA (12,11) in gas phase				X	X	X	X	X	X		X	X	X	X	X	
non-Kasha IRC and opt of stationary points	X		X	X	X		X	X		X	X	X	X	X		X
non-Kasha opt FC minimum (12,11)				X	X	X	X	X	X		X	X	X	X	X	
non-Kasha energy profiles (16,13)	X	X	X	X	X		X	X	X		X	X	X	X	X	
Kasha path IRC from S_5 (10,10)				X	X		X	X		X	X	X	X	X		X
Kasha path S_5/S_4 CI opt. (10,10)				X	X		X	X		X	X	X	X	X		X
Kasha path IRC from S_5/S_4 CI (12,10)	X	X			X		X	X	X			X	X	X	X	
Kasha path S_4/S_3 CI opt. (12,10)	X	X			X		X	X	X			X	X	X	X	
Kasha path IRC from S_4/S_3 CI (12,10)	X	X			X		X	X	X			X	X	X	X	
Kasha path minimum S_3 opt. (12,10)	X	X			X		X	X	X			X	X	X	X	
Kasha path LIIC to finde S_3/S_2 CI (14,12)	X	X		X	X		X	X		X	X	X	X	X		X
Kasha path S_3/S_2 CI opt. (14,12)	X	X		X	X		X	X		X	X	X	X	X		X
Kasha path IRC from S_3/S_2 CI (14,12)	X			X	X	X	X	X	X		X	X	X	X	X	
Kasha path S_2/S_1 CI opt. (14,12)	X			X	X	X	X	X	X		X	X	X	X	X	
Kasha path IRC from S_2/S_1 CI (14,12)	X			X	X	X	X	X	X		X	X	X	X	X	
Kasha energy profiles (16,13)	X	X	X	X	X		X	X	X		X	X	X	X	X	
MQCD Trajectories from the S_1 (10,8)	X		X	X	X		X				X	X	X			

Conclusions and Outlook

This thesis is a theoretical study on the H-transfer reaction of o-NBA. With the help of the highly accurate MS-CASPT2/CASSCF method for the description of the electronic excited states, the experimental UV-spectrum of o-NBA has been assigned.[106] The absorption spectrum of o-NBA consists of three experimental bands, peaking at 220, 250 and 300 nm. The weak tail at 300 nm arises from a series of weak $n\pi^*$ absorptions from the NO_2 and CHO groups. The strongest band in the energy region at 220 nm with its shoulder and 250 nm are, however, dominated by local or charge transfer $\pi\pi^*$ excitations, occurring mainly in the benzene and the nitro group. The experimental wavelength 260 nm used to initiate the H-transfer photoreaction has been assigned to populate the spectroscopic state the S_5, which presents local $\pi\pi^*$ transitions within the nitro group. The influence of solute-solvent interactions in the UV-spectrum of o-NBA and the relative position of the two functional groups CHO and NO_2 has also been analyzed considering the complex formed by 1:1 o-NBA-H_2O and the two positional isomers m-NBA and p-NBA. The shape of this spectrum is very similar to that obtained for o-NBA in the gas phase, although solvation was found to induce a shift to the blue of the spectrum.

Once the UV-spectrum has been characterized, the deactivation mechanism of o-NBA at molecular level has been deciphered by means of high level quantum chemical calculations. Particularly, two photodeactivation mechanisms connecting the spectroscopic state S_5 with the main intermediate ketene have been unravelled. The first path, a non-Kasha pathway, relaxes from the S_5 state through a cascade of conical intersections (CIs) along which a H-atom from the aldehyde is progressively transferred to the nitro group. This non-Kasha relaxation pathway involves three phases: planarization, H-transfer, and rotation of the newly formed enol. The second path, a Kasha path, directly relaxes by means of internal conversion from the S_5 to the S_1, state in which the H-transfer occurs. Along the H-transfer process, the system first reaches an intermediate syn-ketene structure which rotates the H atom around the N-O bond to finally yield the most stable $anti$-ketene tautomer. Both paths have in common that they require the planarization of the molecule so that the hydrogen can be transferred. In order to discern which of the two photoreaction mechanisms is preferred, molecular dynamics simulations using the surface hopping approach have been performed. These calculations have pursued to model the deactivation from two different experimental excitations, i.e. 260 and 388 nm. Molecular dynamics simulations from the high-lying S_5 spectroscopic state, simulating the 260 nm excitation, were performed at TD-DFT level of theory. None of the trajectories launched from the S_5 shows the transfer of the aldehyde hydrogen to the NO_2 group along the deactivation, confirming that the Kasha path is the operative one in the deactivation of o-NBA from the S_5. Nevertheless, the nature of the TD-DFT method prevents the description of the $S_1 \rightarrow S_0$ deactivation. For this reason, deactivation to the ground state from the S_1, describing photoreactions induced by 388 nm irradiation and the last stage of the Kasha path, has been simulated via molecular dynamics simulations at CASSCF level of theory. Semiclassical dynamics simulations from the S_1 predict that the complete yield of the reaction is

determined in its earliest step, with a CI governing the competition between the creation of the ketene (with 31% of quantum yield) and the regeneration of the starting *o*-NBA material (with 69% of quantum yield), both at the ground state. Moreover, the tautomerization is completed in the femtosecond time scale, which is in agreement with the experimental results.[33,35,36] Furthermore, and in contrast with other aromatic intramolecularly H-bonded systems, H-transfer is irreversible once the system reaches the biradical transient, i.e. the hydrogen does not go back to the CHO group.

Further aspects also interesting to be explored concern on how the solute-solvent interactions affect the photodeactivation of the *o*-NBA. This could be analyzed with molecular dynamics where the solvent effects are considered explicitly by means of one molecule of water, for example the quantum mechanical/molecular mechanics (QM/MM) proceedure. The resulting simulation in particular the quantum yield, should better explain the experimental results.

Additionally, the description at molecular level of the final transformation of the ketene transient into the final *o*-nitrobenzoic acid photoproduct would be interesting, since some authors believe is taking place *via* a lactone second intermediate.[33] Recently, VandeVondele et al. have obtained preliminary results[108] by transient pump probe IR experiments combined with Car-Parrinelllo DFT dynamics simulations. They have stated that the ketene transforms directly into the nitroso acid, without the formation of intermediates. Therefore, more accurate level of theory could be employed to discern the existence of a second intermediate.

A final outlook, worth to be investigated is the deactivation mechanisms of the non-reactive isomers: *m*-NBA and *p*-NBA, since although they show experimentally similar transient times and theoretically similar UV/Vis spectra on the o-NBA, they cannot undergo a H-transfer like the *o*-NBA.

Bibliography

(1)   Pelliccioli, A. P.; Wirz, J. *Photochem. Photobiol. Sci.* **2002**, *1*, 441.
(2)   Kornberg, A. *Biochem. J.* **1987**, *26*, 6888.
(3)   Ellis-Davies, G. C. R. *Nat. Meth.* **2007**, *4*, 619.
(4)   Engels, J.; Reidys, R. *Experientia* **1978**, *34*, 14.
(5)   Kaplan, J. H.; Forbush, B.; Hoffman, J. F. *Biochem. J.* **1978**, *17*, 1929.
(6)   Causgrove, T. P.; Dyer, R. B. *Chem. Phys.* **2006**, *323*, 2.
(7)   Abbruzzetti, S. *Biophys. J.* **2000**, *79*, 2714.
(8)   Gao, X.; Gulari, E.; Zhou, X. *Biopolymers* **2004**, *73*, 579.
(9)   McCray, J. A.; Trentham, D. R. *Annu. Rev. Biophys. Biophys. Chem.* **1989**, *18*, 239.
(10)   Amit, B.; Zehavi, U.; Patchornik, A. *J. Org. Chem.* **1974**, *39*, 192.
(11)   Wang, S. Y. *Photochemistry and Photobiology of Nucleic Acids, Vol. 2: Biology*; 1o ed. Academic Press Inc, 1976.
(12)   Lee, H.-M.; Larson, D. R.; Lawrence, D. S. *Chem. Bio.* **2009**, *4*, 409.
(13)   Adams, S. R.; Tsien, R. Y. *Annu. Rev. Physiol.* **1993**, *55*, 755.
(14)   Rubinstein, M.; Amit, B.; Patchornik, A. *Tetrah. Lett.* **1975**, *16*, 1445.
(15)   Patchornik, A.; Amit, B.; Woodward, R. B. *J. Am. Chem. Soc.* **1970**, *92*, 6333.
(16)   Mayer, G.; Heckel, A. *Angew. Chem. Int. Ed.* **2006**, *45*, 4900.
(17)   Davies, L. WHO | Environmental Health Criteria 230: Nitrobenzene.
(18)   Yip, R. W.; Sharma, D. K.; Giasson, R.; Gravel, D. *J. Phys. Chem.* **1985**, *89*, 5328.
(19)   Barltrop, J. A.; Schofield, P. *J. Chem. Soc.* **1965**, 4758.
(20)   Barltrop, J. A.; Plant, P. J.; Schofield, P. *Chem. Comm.* **1966**, 822.
(21)   Wettermark, G. *Nature* **1962**, *194*, 677.
(22)   Schaper, K.; Etinski, M.; Fleig, T. *Photochem. Photobiol.* **2009**, *85*, 1075.
(23)   Kasha, M. *Discuss. Faraday Soc.* **1950**, *9*, 14.
(24)   *IUPAC Compendium of Chemical Terminology*; Nič, M.; Jirát, J.; Košata, B.; Jenkins, A.; McNaught, A., Eds. 2.1.0 ed. IUPAC: Research Triangle Park, NC, **2009**.
(25)   Takezaki, M.; Hirota, N.; Terazima, M. *J. Chem. Phys.* **1998**, *108*, 4685.
(26)   Takezaki, M.; Hirota, N.; Terazima, M.; Sato, H.; Nakajima, T.; Kato, S. *J. Phys. Chem. A* **1997**, *101*, 5190.
(27)   Ciamician, G.; Silber, P. *Ber. Dtsch. Chem. Ges.* **1901**, *34*, 2040.
(28)   George, M. V.; Scaiano, J. C. *J. Phys. Chem.* **1980**, *84*, 492.
(29)   De Mayo, P.; Reid, S. T. *Q. Rev., Chem. Soc.* **1961**, *15*, 393.
(30)   Yip, R. W.; Sharma, D. K. *Res. Chem. Intermed.* **1989**, *11*, 109.
(31)   Yip, R. W.; Sharma, D. K.; Giasson, R.; Gravel, D. *J. Phys. Chem.* **1984**, *88*, 5770.
(32)   Yip, R. W.; Wen, Y. X.; Gravel, D.; Giasson, R.; Sharma, D. K. *J. Phys. Chem.* **1991**, *95*, 6078.
(33)   Laimgruber, S.; Schreier, W. J.; Schrader, T.; Koller, F.; Zinth, W.; Gilch, P. *Angew. Chem. Int. Ed.* **2005**, *44*, 7901.
(34)   McAllister, M. A.; Tidwell, T. T. *Can. J. Chem.* **1994**, *72*, 882.
(35)   Schmierer, T.; Schreier, W. J.; Koller, F. O.; Schrader, T. E.; Gilch, P. *Phys. Chem. Chem. Phys.* **2009**, *11*, 11596.
(36)   Laimgruber, S.; Schmierer, T.; Gilch, P.; Kiewisch, K.; Neugebauer, J. *Phys. Chem. Chem. Phys.* **2008**, *10*, 3872.
(37)   Donten, M. L.; Hamm, P.; VandeVondele, J. *J. Phys. Chem. B* **2011**, *115*, 1075.
(38)   Heinz, B.; Schmierer, T.; Laimgruber, S.; Gilch, P. *J. Photochem. Photobiol. A Chem.* **2008**, *199*, 274.

(39)   Laimgruber, S.; Schachenmayr, H.; Schmidt, B.; Zinth, W.; Gilch, P. *Appl. Phys. B* **2006**, *85*, 557.

(40)   Schmierer, T.; Laimgruber, S.; Haiser, K.; Kiewisch, K.; Neugebauer, J.; Gilch, P. *Phys. Chem. Chem. Phys.* **2010**, *12*, 15653.

(41)   Szabo, A.; Ostlund, N. S. *Modern Quantum Chemistry: Introduction to Advanced Electronic Structure Theory*; Dover Publications, **1996**.

(42)   Born, M.; Oppenheimer, R. *Ann. Phys.* **1927**, *389*, 457.

(43)   Reinhold, J. *Quantentheorie der Moleküle: Eine Einführung*; Vieweg +Teubner, 2006.

(44)   Chen, T. C. *J. Phys. Chem.* **1955**, *23*, 2200.

(45)   Roothaan, C. C. J. *J. Chem. Phys.* **1958**, *28*, 982.

(46)   Allen, L. C.; Karo, A. M. *Rev. Mod. Phys.* **1960**, *32*, 275.

(47)   Cramer, C. J. *Essentials of Computational Chemistry: Theories and Models*; 2o ed. Wiley, 2004.

(48)   Jensen, F. *Introduction to Computational Chemistry*; 2o ed. Wiley, 2006.

(49)   Hartree, D. R. *Proc. Cambridge Phil. Sc.* **1928**, *24*, 89-110.

(50)   Hartree, D. R. *Proc. Cambridge Phil. Sc.* **1928**, *24*, 111-132.

(51)   Roothaan, C. C. J. *Rev. Mod. Phys.* **1951**, *23*, 69.

(52)   Hall, G. G. *Proc. R. Soc. Lond. A* **1951**, *205*, 541 -552.

(53)   Pople, J. A.; Nesbet R.K. *J. Chem. Phys.* **1954**, *22*, 571.

(54)   McNaught, A. D.; IUPAC *Compendium of Chemical Terminology - IUPAC Recommendations*; 2o ed. Blackwell Science, **1997**.

(55)   Hehre, W. J.; Radom, L.; Schleyer, P. V.; Pople, J. *AB INITIO Molecular Orbital Theory*; 1o ed. Wiley-Interscience, **1986**.

(56)   Møller, C.; Plesset, M. S. *Phys. Rev.* **1934**, *46*, 618.

(57)   Shavitt, I. *Mol. Phys.* **1998**, *94*, 3.

(58)   Langhoff, S. R.; Davidson, E. R. *J. Quantum Chem.* **1974**, *8*, 61.

(59)   Roos, B. O.; Widmark, P.-O. *Multiconfigurational (MC) Self-Consistent (SCF) theory*; European Summer School in Quantum Chemistry; Lund, Sweden, **2005**.

(60)   Roos, B. O. *Notes in Quantum Chemistry · European Summer School in Quantum Chemistry* **1997**.

(61)   Olsen, J.; Roos, B. O.; Jørgensen, P.; Jensen, H. J. A. *J. Chem. Phys.* **1988**, *89*, 2185.

(62)   Andersson, K.; Malmqvist, P.-Å.; Roos, B. O. *J. Chem. Phys.* **1992**, *96*, 1218.

(63)   Finley, J.; Malmqvist, P.-Å.; Roos, B. O.; Serrano-Andrés, L. *Chem. Phys. Lett.* **1998**, *288*, 299.

(64)   Roos, B. O.; Andersson, K. *Chem. Phys. Lett.* **1995**, *245*, 215.

(65)   Roos, B. O.; Andersson, K.; Fülscher, M. P.; Malmqvist, P.-Å.; Serrano-Andrés, L.; Pierloot, K.; Merchán, M. *Multiconfigurational Perturbation Theory: Applications in Electronic Spectroscopy*, ed. Wiley & Sons, **2007**, 219.

(66)   Hättig, C.; Weigend, F. *J. Chem. Phys.* **2000**, *113*, 5154.

(67)   Vahtras, O.; Almlöf, J.; Feyereisen, M. W. *Chem. Phys. Lett.* **1993**, *213*, 514.

(68)   Weigend, F.; Häser, M. *Theor. Chim. Acta* **1997**, *97*, 331.

(69)   Hohenberg, P.; Kohn, W. *Phys. Rev.* **1964**, *136*, B864.

(70)   Kohn, W.; Sham, L. J. *Phys. Rev.* **1965**, *140*, A1133.

(71)   Slater, J. C. *The Self-consistent Field for Molecules and Solids. Quantum Theory of Molecules and Solids Volume 4. (Pure & Applied Physics)*; 1o ed. McGraw-Hill Inc.,US, **1974**.

(72)   Becke, A. D. *J. Chem. Phys.* **1993**, *98*, 1372.

(73)   Dobson, J. F.; Vignale, G.; Das, M. P. *Electronic Density Functional Theory: Recent Progress and New Directions*; 1o ed. Springer, **1998**.

(74)   Becke, A. D. *J. Chem. Phys.* **1993**, *98*, 5648.

(75)   Becke, A. D. *Phys. Rev. A* **1988**, *38*, 3098.

(76)   Lee, C.; Yang, W.; Parr, R. G. *Phys. Rev. B* **1988**, *37*, 785.

(77)   Vosko, S. H.; Wilk, L.; Nusair, M. *Can. J. Phys.* **1980**, *58*, 1200.

(78)   Runge, E.; Gross, E. K. U. *Phys. Rev. Lett.* **1984**, *52*, 997.

(79)   Marques, M. A. L.; Gross, E. K. U. *Annu. Rev. Phys. Chem.* **2004**, *55*, 427.

(80)   Koch, W.; Holthausen, M. C. *A Chemist's Guide to Density Functional Theory, 2nd Edition*; 2o ed. Wiley-VCH, **2001**.

(81)   Gross, E. K. U.; Kohn, W. *Density Functional Theory of Many-Fermion Systems*; ed. Academic Press, **1990**, Vol. *21*, 255.

(82)   Verlet, L. *Phys. Rev.* **1967**, *159*, 98.

(83)   Verlet, L. *Phys. Rev.* **1968**, *165*, 201.

(84)   Tully, J. C. *J. Chem. Phys.* **1971**, *55*, 562.

(85)   Tully, J. C. *J. Chem. Phys.* **1990**, *93*, 1061.

(86)   Hammes-Schiffer, S.; Tully, J. C. *J. Chem. Phys.* **1995**, *103*, 8528.

(87)   Butcher, J. C.; Podhaisky, H. *Appl. Num. Math.* **Marzo**, *56*, 345.

(88)   Granucci, G.; Persico, M. *J. Chem. Phys.* **2007**, *126*, 134114.

(89)   Doltsinis, N. L. *NIC Series* **2006**, *31*, 389.

(90)   Slater, J. C. *Phys. Rev.* **1930**, *36*, 57.

(91)   Boys, S. F. *Proc. Roy. Soc.* **1950**, *200*, 542.

(92)   Dunning, T. H. *J. Chem. Phys.* **1989**, *90*, 1007.

(93)   Frisch, M. J.; Trucks, G. W.; Schlegel, H. B.; Scuseria, G. E.; Robb, M. A.; Cheeseman, J. R.; Montgomery, J. A.; Vreven, J. T.; Kudin, K. N.; Burant, J. C.; Millam, J. M.; Iyengar, S. S.; Tomasi, J.; Barone, V.; Mennucci, B.; Cossi, M.; Scalmani, G.; Rega, N.; Petersson, G. A.; Nakatsuji, H.; Hada, M.; Ehara, M.; Toyota, K.; Fukuda, R.; Hasegawa, J.; Ishida, M.; Nakajima, T.; Honda, Y.; Kitao, O.; Nakai, H.; Klene, M.; Li, X.; Knox, J. E.; Hratchian, H. P.; Cross, J. B. ; Bakken, V.; Adamo, C.; Jaramillo, J.; Gomperts, R.; Stratmann, R. E.; Yazyev, O.; Austin, A. J.; Cammi, R.; Pomelli, C.; Ochterski, J. W.; Ayala, P. Y.; Morokuma, K.; Voth, G. A.; Salvador, P.; Dannenberg, J. J.; Zakrzewski, V. G.; Dapprich, S.; Daniels, A. D.; Strain, M. C.; Farkas, O.; Malick, D. K.; Rabuck, A. D.; Raghavachari, K.; Foresman, J. B.; Ortiz, J. V.; Cui, Q.; Baboul, A. G.; Clifford, S.; Cioslowski, J.; Stefanov, B. B.; Liu, G.; Liashenko, A.; Piskorz, P.; Komaromi, I.; Martin, R. L.; Fox, D. J.; Keith, T.; Al-Laham, M. A.; Peng, C. Y.; Nanayakkara, A.; Challacombe, M. Gill, P. M.; W. Johnson, B.; Chen, W.; Wong, M. W.; Gonzalez, C.; Pople, J. A. *Gaussian 03*; Gaussian 03; Gaussian, Inc., Wallingford CT, 2004.

(94)   Ahlrichs, R.; Bär, M.; Häser, M.; Horn, H.; Kölmel, C. *Chem. Phys. Lett.* **1989**, *162*, 165.

(95)   Schäfer, A.; Huber, C.; Ahlrichs, R. *J. Chem. Phys.* **1994**, *100*, 5829.

(96)   Aquilante, F.; De Vico, L.; Ferré, N.; Ghigo, G.; Malmqvist, P.-Å.; Neogrády, P.; Pedersen, T. B.; Pitoňák, M.; Reiher, M.; Roos, B. O.; Serrano-Andrés, L.; Urban, M.; Veryazov, V.; Lindh, R. *J. Comput. Chem.* **2010**, *31*, 224.

(97)   Almlöf, J.; Taylor, P. R. *J. Chem. Phys.* **1987**, *86*, 4070.

(98)   Combs, L. L. *International Journal of Quantum Chemistry* **1977**, *12*, 967.

(99)   Bolhuis, P. G. Chandler, D. Dellago, C.; Geissler, P. L. *Annu. Rev. Phys. Chem.* **2002**, *53*, 291.

(100)   Schlegel, H. B. *J. Comput. Chem.* **2003**, *24*, 1514-1527.

(101)   Heidrich, D. *The Reaction Path in Chemistry: Current Approaches and Perspectives*; 1o ed. Springer, **1995**.

(102)   Fukui, K. *Acc. Chem. Res.* **1981**, *14*, 363.

(103)   Bader, R. F. W. *Chem. Rev.* **1991**, *91*, 893.

(104)   Bader, R. F. W. *Atoms in Molecules: A Quantum Theory*; Oxford University Press, USA,

1994.

(105)   Coppens, P.; Schmidt, G. M. J. *Acta Cryst.* **1964**, *17*, 222.

(106)   Leyva, V.; Corral, I.; Schmierer, T.; Heinz, B.; Feixas, F.; Migani, A.; Blancafort, L.; Gilch, P.; González, L. *J. Phys. Chem. A* **2008**, *112*, 5046.

(107)   Leyva, V.; Corral, I.; Schmierer, T.; Gilch, P.; González, L. *Phys. Chem. Chem. Phys.* **2011**, *13*, 4269.

(108)   Donten, M. L.: Hamm, P.; VandeVondele, J. *The Journal of Physical Chemistry B* **2011**, *115*, 1075.

(109)   Migani, A.; Leyva, V.; Feixas, F.; Schmierer, T.; Gilch, P.; Corral, I.; González, L.; Blancafort, L. *Chem. Commun.* **2011**.

(110)   Leyva, V.; Corral, I.; Feixas, F.; Migani, A.; Blancafort, L.; González-Vázquez, J.; Gónzalez, L. *Physical Chemistry Chemical Physics*, in press.

List of publications which contains this thesis

1. **Leyva V.**; Corral I.; Schmierer T.; Heinz B.; Feixas F.; Migani A.; Blancafort L.; Gilch P.; González L. *"Electronic States of o-Nitrobenzaldehyde: A Combined Experimental and Theoretical Study" Journal of Physical Chemistry A*, **2008**; *112*, 5046-5053.
2. **Leyva V.**; Corral I.; González L. *"Ortho-Nitrobenzaldehyde 1:1 Water Complexes. The Influence of Solute Water Interactions in the Vertical Excited Spectrum" Zeitschrift für Physikalische Chemie*, **2008**, *222*, 1263-1278.
3. **Leyva V.**, Corral, I., Schreiber T., Gilch P., González L. *"A Comparative Analysis of the UV/Vis Absorption Spectra of Nitrobenzaldehydes."* Physical Chemistry Chemical Physics, **2011**, *13*, 4269-4278, (2011).
4. Migani A., **Leyva V.**, Feixas F., Corral I., Blancafort L., González L. *"Ultrafast irreversible phototautomerization of o-nitrobenzaldehyde"* Chemical Communications, **2011**, 47, 6383-6385.
5. **Leyva V.**, Corral I., Feixas F., Migani A., Blancafort L., González-Vázquez J., González L., *"A non-adiabatic quantum-classical dynamical study of the intramolecular excited state hydrogen transfer in ortho-Nitrobenzaldehyde"* Accepeted in Phys.Chem.Phys.

Curriculum Vitae

Verónica Leyva Novoa

Institut für Physikalische Chemie, Friedrich-Schiller-Universität Jena, Helmholtzweg 4, 07743, Jena, Germany.

Tel: +49 3641 9 48336 Fax: +49 3641 9 48302

http://www.theochem.uni-jena.de/people/groupmembers.php?ID=12

email: veronica.leyva@uni-jena.de

Personal Data

Date and Place of Birth   21st September 1980, Mexico, Mexico

Marital Status   Single

Nationality   Mexican

Degrees

October 2006   Master degree in Chemical Science by UNAM (Universidad Autónoma de México), Mexico City, Mexico (Grade: 9.08)

December 2004   Bachelor degree in Chemical Engineering by the La Salle University, Mexico City, Mexico (Grade: 8.2/10)

June 1999   High School degree Cristóbal Colón High School, Mexico State, Mexico (Grade: 8.9/10)

June 1996   Secondary Graduated in The Maddox Academy, Mexico State, Mexico (Grade: 9.1/10)

Studies

Since Nov. 2006   Doctoral studies in Chemistry.

Sept. 2004 – Oct. 2006   Master in Chemical Science at the Universidad Nacional Autónoma de México (UNAM), Mexico City, Mexico.

Sept. 1999 - July 2003   Bachelor in Chemical Engineering at the La Salle University, Mexico City, Mexico

Sept. 1996 - July 1999	High School at the Cristóbal Colón High School, Mexico State, Mexico
Sept. 1993 - July 1996	Secondary at The Maddox Academy, State of Mexico, Mexico

Fellowships and Awards

Jan. 2007 – Dec. 2009	Doctoral fellowship of CONACyT/DAAD for the project "Towards coherent control of non-adiabatic electron and hydrogen transfer in organic molecules"
Sept. 2004 - June 2006	Master scholarship of CONACyT for the project "Study of the participation of the stereoelectronic effects in the molecular stability through the evaluation of one-Bond Coupling Constants $^1J_{CH}$ and NBO in protoned Ciclohexanone and related molecules"
Jan. 2004 - Dec 2004	Scholarship of CONACyT for the project "Study of the Stereoelectronic effects in Sulfates, Sulfoxides and Sulfur"
Sept. 2002 - July 2003	Scholarship of La Salle for good grades.

Scientific Experience

Since Jan. 2009	Research in Theoretical Computational Chemistry with Prof. Dr. Leticia González, the Friedrich-Schiller-Universität Jena for the Doctoral Thesis theme "Towards coherent control of non-adiabatic electron and hydrogen transfer in organic molecules"
03 – 29 April 2011	Scientific stage in Madrid at Universidad Autónoma de Madrid, with Dr. Inés Corral. Funded by COST (European Cooperation in the field of Scientific and Technical Research) Thema: "MS-CASPT2/CASSCF calculations on the Kasha deactivation mechanism for excited *ortho*-nitrobenzaldehyde"
28 Feb – 21 March 2011	Scientific stage in Madrid at Universidad Complutense de Madrid, with Dr. Jesús González. Funded by COST (European Cooperation in the field of Scientific and Technical Research) Thema: "A mechanistic insight of excited state intramolecular hydrogen transfer in *ortho*-Nitrobenzaldehyde"
12 – 24 April 2010	Scientific stage in Madrid, at Universidad Complutense de Madrid, with Dr. Ignacio Solá
Oct. 2008 – Nov. 2008 and Oct. 2007 – Dec. 2007	Scientific stage in Gerona (Spain), at Universitat de Girona, with Dr. Lluís Blancafort funded by the DAAD (Acción Integrada Hispano.Alemana No 12786).

Nov. 2006 – Oct. 2008	Research in Theoretical Computational Chemistry with Prof. Dr. Manz group, guided/supervised by Prof. Dr. Leticia González, the Freie-Universität Berlin, for the Doctoral Thesis theme "Towards coherent control of non-adiabatic electron and hydrogen transfer in organic molecules"
Jan. 2005 – Oct. 2006	Research in Theoretical Computational Chemistry with Prof. Dr. Eduardo Cuevas, UNAM for the Master Thesis theme "Study of the participation of the stereoelectronic effects in the molecular stability through the evaluation of one-Bond Coupling Constants 1JCH and NBO in protoned Ciclohexanone and related molecules"
Jan. 2004 – Dec. 2004	Research in Theoretical Computational Chemistry Prof. Dr. Eduardo Cuevas, UNAM for the Bachelor Thesis theme "Study of the Stereoelectronic effects in Sulfates, Sulfoxides and Sulfur"

Teaching Experience

Teaching assistant at Friedrich-Schiller-Universität Jena:

Apr. 2008 – Sept. 2008 Theoretische Chemie/Computerchemie. (20 hours)

Jan. 2009 – Feb. 2009   Theoretische Chemie/Computerchemie. (8 hours)

Teaching assistant at Friedrich-Schiller-Universität Jena:

April 2010 – February 2011: Physikal Chemie Diplomarbeit: Caroline von Eiff "semi-empirical/ab initio methods over *ortho*-Nitrobenzaldehyde 1:2 Water Complexes"

Oct. 2008 – March 2009: Physikal Chemie Praktikum: Susanne Pahlow "Solvent Effects in *ortho*-Nitrobenzaldehyde 1:2 Water Complexes"

Oct. 2008 – March 2009: Phsysikal Chemie Praktikum: Caroline von Eiff "DFT calculations of *ortho*-Nitrobenzaldehyde 1:2 Water Complexes"

Complementary Training in Foreign Laboratories

1. "The 3rd Workshop of MOLCAS" at IDEON Beta, Lund (Sweden), April 14–18, 2008.

Theses:

1. Verónica Leyva (Bachelor Thesis) "Efectos estereoeléctricos en sulfonas, sulfóxicos y sulfuros." Universidad La Salle, México, 2004.
2. Verónica Leyva (Master Thesis) "Estudio del efecto de la protonación en la manifestación de efectos estereoelectrónicos en ciclohexanonas evaluado a través de las constantes de acoplamiento $^1J_{C-H}$". Universidad Autónoma de México, México, 2006.

Articles in refereed journal:

6. Martínez-Mayorga, K.; Cárdenas, J.; Colás-Herrerías, L.; **Leyva, V.**; Perrin C.L.; Juaristi, E.; Cuevas, G. *"Computational Study of 1,3-Dithiane 1,1-Dioxide (1,3- Dithiane Sulfone). Description of the Inversion Process and Manifestation of Stereoelectronic Effects on $_1J^{C-H}$ Coupling Constants" Journal of Physical Chemistry A*, **2006**; *110*, 7703-7712.
7. **Leyva V.**; Corral I.; Schmierer T.; Heinz B.; Feixas F.; Migani A.; Blancafort L.; Gilch P.; González L. *"Electronic States of o-Nitrobenzaldehyde: A Combined Experimental and Theoretical Study" Journal of Physical Chemistry A*, **2008**; *112*, 5046-5053.
8. **Leyva V.**; Corral I.; González L. *"Ortho-Nitrobenzaldehyde 1:1 Water Complexes. The Influence of Solute Water Interactions in the Vertical Excited Spectrum" Zeitschrift für Physikalische Chemie*, **2008**, *222*, 1263-1278.
9. Buendía-Atencio C., **Leyva V.**, González L. *"Thermochemistry and UV Spectroscopy of Alkyl Peroxynitrates" Journal Physical Chemistry A*, **2010**, 114 (35), 9537-9544*.*
10. **Leyva V.**, Corral, I., Schreiber T., Gilch P., González L. *"A Comparative Analysis of the UV/Vis Absorption Spectra of Nitrobenzaldehydes"* Physical Chemistry Chemical Physics, **2011**, *13*, 4269-4278, (2011).
11. Migani A., **Leyva V.**, Feixas F., Corral I., Blancafort L., González L. *"Ultrafast irreversible phototautomerization of o-nitrobenzaldehyde"* Chemical Communications, **2011**, 47, 6383-6385.
12. **Leyva V.**, Corral I., Feixas F., Migani A., Blancafort L., González-Vázquez J., González L., *"A non-adiabatic quantum-classical dynamical study of the intramolecular excited state hydrogen transfer in ortho-Nitrobenzaldehyde"* Accepted in Phys.Chem.Chem.Phys.

Oral Presentations:

1. Workshop Leipzig, February 26 – 27, 2009. Talk: "A mechanistic insight in the light-induced hydrogen transfer process of the *ortho*-Nitrobenzaldehyde". Invitation by Prof. B. Kirchner.

Poster Presentations:

1. ICP2007 – XXIII. International Conference on Photochemistry 2007 Köln, Germany, 29th Juli to 3rd August, 2007. **Leyva V.**; Corral I.; González L. "Hydrogen transfer in *ortho*-Nitrobenzaldehyde. A Theoretical Study."

2. XVII International Conference "Horizons in Hydrogen Bond Research" and Graduate Student Research School on "Hydrogen Bonding and Proton Transfer" St. Petesburg, Russia, 1st to 8th September, 2007. **Leyva V.**; Corral I.; González L. "Hydrogen transfer in *ortho*-Nitrobenzaldehyde. A Theoretical Study."

3. XXIInd IUPAC Symposium on Photochemistry. 28th July to 1st August, 2008 Gothenburg, Sweden. Feixas F.; Migani A.; Blancafort L.; **Leyva V.**; Corral I.; González L. "Mechanism of excited state intramolecular hydrogen transfer in *ortho*-Nitrobenzaldehyde by ab initio methods."

4. Computational Molecular Science 2008 Congress, London, England, 22th to 25th June, 2008. **Leyva V.**; Corral I.; Feixas F.; Migani A.; Blancafort L.; González L. "A computational insight in the hydrogen transfer mechanism of the *ortho*-Nitrobenzaldehyde."

5. 13th ICQC International Congress of Quantum Chemistry, Helsinki, Finland, 22th to 27th June, 2009. **Leyva V.**; Corral I.; Feixas F.; Migani A.; Blancafort L.; González L. "The deactivation mechanism of excited state intramolecular hydrogen transfer in *ortho*-Nitrobenzaldehyde explained by CASSCF and CASPT2 calculations."

6. First Principles Quantum Chemistry: from Elementary Reactions to Enzymes, Bad Herrenalb, Germany, 14th to 17th, April, 2010. Buendía-Atencioa C.; **Leyva V.**; González L. "Excited states and thermochemistry of alkyl peroxynitrates R-OONO$_2$ (R= CH$_3$, C$_2$H$_5$, C$_3$H$_7$)."

7. XXIV International Conference on Photochemistry (ICP 2009), Toledo, Spain, 19th to 24th July 2009. **Leyva V.**; Corral I.; Feixas F.; Migani A.; Blancafort L. , González-Vázquez J.; González L. "Photoreaction Mechanism of the Intramolecular Hydrogen Transfer in *ortho*-Nitrobenzaldehyde by ab initio Methods."

8. XXIIIth IUPAC Symposium on Photochemistry, Ferrara, Italy 11th to 16th July, 2010. **Leyva V.**; Corral I.; Feixas F.; Migani A.; Blancafort L. , González-Vázquez J.; González L. "Different excited state hydrogen transfer mechanisms in *ortho*-Nitrobenzaldehyde by ab initio quantum methods."

Languages

Spanish, native language.

English, fluent speaking and writing.

German, basic level

Acknowledgments

Selbständigkeitserklärung:

Ich erkläre, dass ich die vorliegende Arbeit selbst¨andig und unter Verwendung der angegebenen Hilfsmittel, persönlichen Mitteilungen und Quellen angefertigt habe.

Jena, den . . . .

Verónica Leyva Novoa